Model Complexes for Reactive Intermediates in NO_x Interconversions in Nature and Applications in Medicine

by

Elizabeth C. Manickas

A dissertation submitted in partial fulfillment
of the requirements for the degree of
Doctor of Philosophy
(Chemistry)
in the University of Michigan
2024

Doctoral Committee:

Professor Nicolai Lehnert, Chair
Professor Vincent L. Pecoraro
Professor Stephen W. Ragsdale
Professor Nathaniel Szymczak

Elizabeth C. Manickas

manickas@umich.edu

ORCID iD: 0000-0002-0257-0678

Dedication

To my family for believing in me.

To my friends for their support.

To Corey for the hugs.

And to our cat, Bjorn.

Acknowledgements

Nicolai, thank you for mentoring me throughout graduate school and being patient with me as I learned how to work with porphyrins. I appreciate that you let me be myself. To my committee, Prof Nate Szymczak, Prof Vincent Pecoraro, and Prof Stephen Ragsdale, I thank you for providing guidance at my major milestones and helping me to become a better scientist. To Prof Mark Meyerhoff for giving me an opportunity to learn something new. I am excited about working with you as a Post Doc.

I want to thank previous Lehnert Lab member, Dr. Andrew Hunt, for figuring out how to work with thiolate bound $\{FeNO\}^6$ complexes. Your hard work provided a strong foundation to build on and inspired me to take this thiolate chemistry to the next level.

Glorimar, thank you so much for helping me during my last semester of graduate school. I appreciate your hard work and value the fun we had (with more to come). I'm excited to see what you accomplish in your time here. Alivia and Cybele for helping me collect and plot the rRaman data I needed to finish my thiolate chapter. I want to also thank Benedict for solving my crystals and bouncing research ideas. Michael, for our constructive scientific discussion and the random laughs and memes. Daniel, for adding to the silly in the Lehnert Lab. A new era is coming. I am excited that you are taking over the porphyrin project. I might have some ideas for you (see Appendix A).

To the present and past lab members, thank you for making work a fun and happy place to be and going along with all my quirkiness, for I can be truly strange sometimes. Luis, you have

great energy. I am glad you brought in all of your Hawaiian shirts for our group picture to surprise Nicolai. He wasn't expecting it. Virginia, for being a great desk mate for most of my graduate school career. I miss having living plants at our desk. Mine are dead. Jill, for her unwavering emotional support and being a great friend, I could always count on throughout my whole time in graduate school. See also emotional support friend. I really see you as a role model and have learned a lot from you. I'm glad I got to know you.

To my cohort, Jessica, Virginia, Emily, and Isaac for all the fun memories throughout grad school between Friendsgiving's, random get-togethers, and now the occasional zoom calls we had/have a lot of fun.

To my family, thank you for your support over the last six years. I think I basically disappeared since I started graduate school except for the holidays. I'm so excited that our family is growing. It used to be just me, my sister and my brother and my parents but now we have in laws and multiple cats which makes for more fun when we get together. To my cat, Bjorn, I would make you co-author on all my papers if I could. He has been the best stress relief and I'm certain he's the softest cat I've ever met. I call him Corn. He also goes by Bjorno, Bjorb my orb, borb, and whatever else comes to my mind.

Corey, thank you for being by my side for my whole PhD. It's nice to come home and have someone there for you when you're having rough days in lab. Thank you for looking out for me throughout grad school and making sure that I was prioritizing self-care, especially at the end when I was writing my thesis. I am grateful for your support, and I look forward to resuming our adventures together.

Table of Contents

List of Tables

List of Figures

Abstract

Fungi consume nitric oxide (NO) using Cytochrome P450 nitric oxide reductase (Cyt P450nor) by reducing two molecules of NO to nitrous oxide (N_2O) – a potent greenhouse gas. The efficiency of this enzyme makes it difficult to study its reactive Intermediate *I*. For this reason, a bulky bis-picket fence porphyrin was synthesized to prevent the decomposition of an Intermediate *I* model complex for full vibrational characterization and reactivity studies with NO. Experimental conditions were designed analogous to the reaction in Cyt P450nor with hydride transfer to a Fe(II)-NO^+ species to form a ferrous heme nitroxyl species, [Fe(3,5-Me-BAFP)(MI)(HNO)]. This model was determined to be the most stable heme nitroxyl complex in organic solvents, with a half-life of 56 min at -30 C by UV-vis spectroscopy. This stability allowed me to perform the first detailed spectroscopic characterization of a heme-HNO model complex. In addition, this complex demonstrates high reactivity toward NO, exhibiting a 91% N_2O by IR spectroscopy that resulted in the formation of a ferric heme species. The obtained results indicate that heme-HNO complexes are catalytically competent intermediates for NO reduction to N_2O.

The proximal cysteinate in the Cyt P450nor active site is proposed to either stabilize the Fe^{III}-$NHO^{\bullet-}$ valence tautomer of the heme-HNO complex or increase the pKa of the bound nitroxyl in Intermediate *I*. Previous work has also shown that the presence of the axial thiolate makes the Fe(II)-NO^+ species less stable in synthetic model complexes. In this work, the bulky bis-picket fence porphyrin was used to stabilize a thiolate bound heme Fe(II)-NO^+ complex, [Fe(3,5-Me-BAFP)(NO)($SPhF_4CF_3$)] at low temperatures. The formation of this complex was verified by UV-

vis and NMR spectroscopy. Vibrational characterization of this complex by IR and rRaman spectroscopy demonstrated similar Fe-NO and N-O stretching frequencies in comparison to Cyt P450nor of 1853 and 543, and 1851 and 530 cm^{-1}, respectively. For the first time, hydride transfer reactions to a thiolate-bound ferrous nitrosonium synthetic model complex were conducted in this work, and followed by IR and NMR spectroscopy, to ultimately obtain a thiolate-bound Intermediate *I* model with direct relevance to the active site of Cyt P450nor.

Biomedical devices like IV catheters come with risks to patients, such as bacterial infections and blood clots. NO is known to prevent these risks. This part of my thesis focuses on catalyst development, inspired by copper nitrite reductase, for the electrochemical reduction of nitrite (NO_2^-) to NO for biomedical applications. The current limitation of these copper catalysts is their oxygen sensitivity, which reduces NO generation. The presence of O_2 cannot be avoided in IV catheters, which are in contact with oxygen rich blood. This issue is addressed by synthesizing two second coordination sphere (SCS) derivatives of the BMPA-Pr^- (BMPA-Pr^- = bis-(2-methylpyridyl)amine)propionate) ligands, Amide-BMPA-Pr^- and Amine-BMPA-Pr^-, to shuttle protons necessary for nitrite reduction and therefore decrease oxygen sensitivity. It was determined that [Cu(Amide-BMPA-Pr)(OAc)] is not capable of performing nitrite reduction due to poor substrate binding and low electrochemical stability of the complex. In contrast, [Cu(Amine-BMPA-Pr)(OAc)] can outperform the initially reported catalyst [Cu(BMPA-Pr)(OAc)] under inert atmosphere, showing that SCS H-bonding residues are able to accelerate nitrite reduction. However, the presence of a hydrogen bond donor does not reduce O_2 sensitivity as previously hypothesized.

Chapter 1 Introduction

Sections **1.1** and **1.3** of this chapter are based on the Chemistry Review and Comprehensive Coordination Chemistry III Book Chapter, and JACS paper referenced. The relevant sections included in this chapter were written by me.[1-3]

1.1 The Importance of HNO in Biology

Nitric oxide (NO) is a versatile biological molecule with established roles in immune defense in high (μM) concentrations, as well as vasodilation and nerve signal transduction in low (nM) concentrations in mammals.[4] Nitroxyl, HNO/NO^-, the one-electron reduced form of NO, is suggested to take part in its own distinct signaling pathways.[5-8] Proposed sources of HNO include peroxidation of hydroxylamine in globins and Cytochrome *c* oxidase (CcO), and L-arginine oxidation in nitric oxide synthase (NOS) in the absence of its tetrahydrobiopterin cofactor.[9-11] In addition, work by Doctorovich, Marti and coworkers has shown that simple alcohols like ascorbate and tyrosine, and thiols can reduce NO to HNO under physiologically-relevant conditions.[12,13] While HNO is difficult to study *in vivo*, recent investigations suggest endogenous HNO/NO^- production may aid in the protection from ischemia-related injuries as a result of cardiovascular events and strokes.[9,14,15] Similarly, HNO donors have been shown in animal studies to lessen tissue damage from ischemia when administered exogenously prior to ischemic/reperfusion events.[16,17] HNO, generated from the reaction of NO and H_2S, has also been proposed to activate the neuroendocrine HNO–TRPA1–CGRP signaling pathway that constitutes an essential element for the control of vascular tone throughout the cardiovascular system.[18] Additionally, HNO is a potent

anti-alcoholism drug due to its ability to irreversibly inhibit thiol-containing enzymes such as mitochondrial aldehyde dehydrogenase and glyceraldehyde-3-phosphate dehydrogenase.[19] Other research suggests that HNO can act as a potential anti-cancer agent by triggering cancer cell apoptosis and reducing tumor growth.[20-23] Recently, endogenous HNO production has been demonstrated to take part in redox cell signaling in plants.[24]

1.2 The Nitrogen Cycle

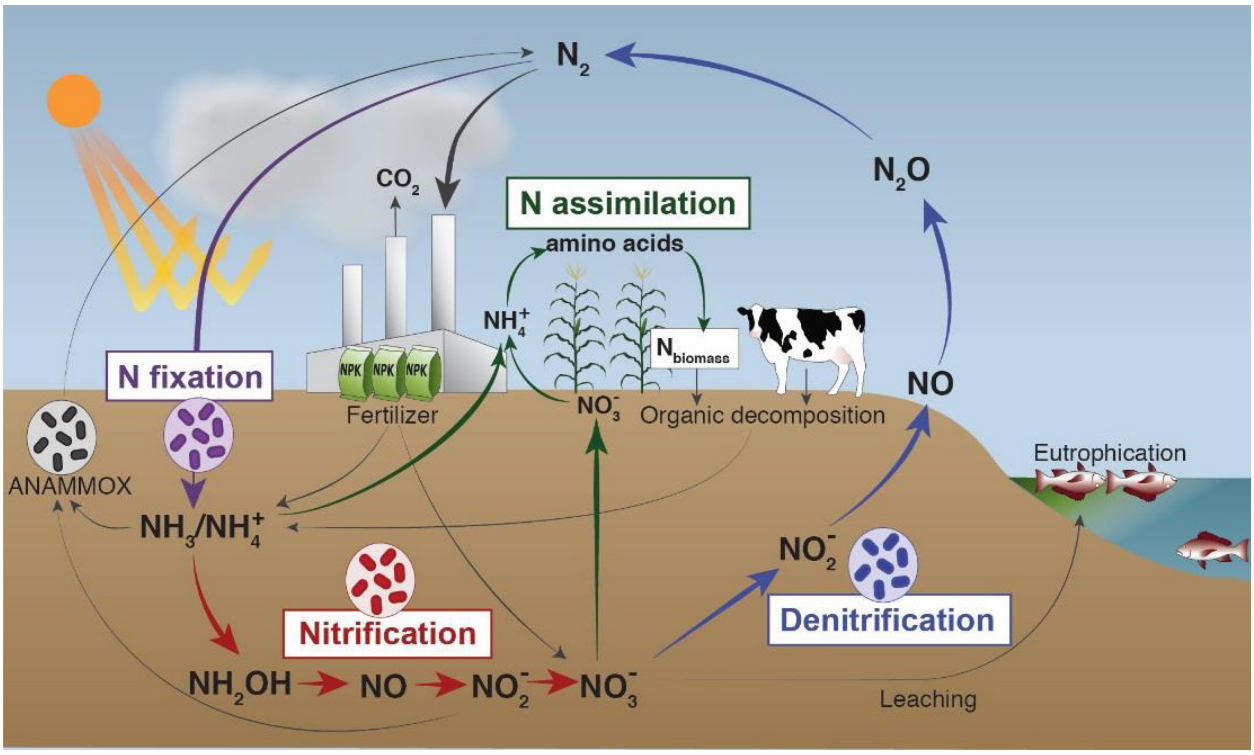

Figure 1.1 Overview of the nitrogen cycle. Adapted with permission from ref [25]. Copyright 2021 Royal Society of Chemistry.

Aside from its physiological roles mentioned above, HNO/NO^- is a proposed key intermediate in heme-enzyme mediated NO_x interconversions in the biogeochemical nitrogen (N_2) cycle, shown in **Figure 1.1**.[1] Dinitrogen makes up 78% of Earth's atmosphere and consists of a highly covalent triple bond making it a fairly inert molecule. Nitrogen fixation is performed by microbes symbiotic to leguminous plants that reduce N_2 to ammonia (NH_3)/ammonium (NH_4^+) as

a usable form of nitrogen for plants and microbes.[26] In addition to natural nitrogen fixation, NH_3/NH_4^+ based fertilizers are produced by the industrial Haber-Bosch process using an iron-based catalyst to convert hydrogen (H_2) and N_2 to NH_3 under high pressure and temperature (also referred to a synthetic nitrogen fixation). Since industrial fertilizers are both cheap and abundant, crops are typically overfertilized to produce enough food to support the Earth's growing population.[26] However, only 30-50% of fertilizers are absorbed by crops, leaving the rest to enter different microbial pathways. The NH_4^+ formed in nitrogen fixation pathway then undergoes nitrification, where ammonium is oxidized to nitrites (NO_2^-) and nitrates (NO_3^-). Soil-borne and seawater dwelling microbes known as autotrophic ammonia oxidizing bacteria and archaea carry out these reactions to support their respiratory function, forming hydroxylamine (NH_2OH) and NO as intermediates along the way. One notable heme-containing enzyme in this pathway is hydroxylamine oxidoreductase (HAO). In this case, a nitroxyl intermediate is proposed in the oxidation of NH_2OH to NO prior to further oxidation to NO_2^- and NO_3^-.[27] Here, the nitrogen cycle branches into three pathways. First, NO_2^- and NO_3^- have low soil retention, causing these compounds to act as pollutants by leaching into waterways, stimulating algal blooms in lakes and coastal waters as well as downstream eutrophication.[26] Second, nitrites and nitrates can undergo Dissimilatory Nitrate Reduction to Ammonia (DNRA), where nitrate is reduced back to ammonia by another heme-containing enzyme, Cytochrome *c* nitrite reductase (C*c*NIR) (**Figure 1.2**).[28-32] Similarly, assimilatory nitrite reductase is a heme-containing enzyme, and in both cases, nitroxyl intermediates are proposed in their catalytic cycles (**Figure 1.2**).[33] Lastly, NO_2^- and NO_3^- are reduced to N_2 in the denitrification pathway as the last step that closes the nitrogen cycle. Here, NO_2^- is reduced to NO by either a copper or heme-containing nitrite reductase (NIR). An important reaction in this pathway is the reduction of NO to nitrous oxide (N_2O), performed by nitric oxide

reductases (NOR). N_2O is the third most potent greenhouse gas behind carbon dioxide (CO_2) and methane (CH_4). It is estimated that 75% of N_2O emissions come from agriculture.[26] Sources of these emissions include fungal denitrification where N_2O is the final product and bacterial denitrification where N_2O escapes prior to further reduction to N_2 by nitrous oxide reductase (N2OR). The fungal enzyme responsible for N_2O production is Cytochrome P450 nitric oxide reductase (Cyt P450nor).[26] This enzyme is especially interesting as its reactive intermediate is proposed to be a nitroxyl species. For this reason, there is interest in modeling the active site of Cyt P450nor to elucidate the electronic structure and protonation state of its reactive intermediates and provide a full explanation of how N_2O is produced by this enzyme.

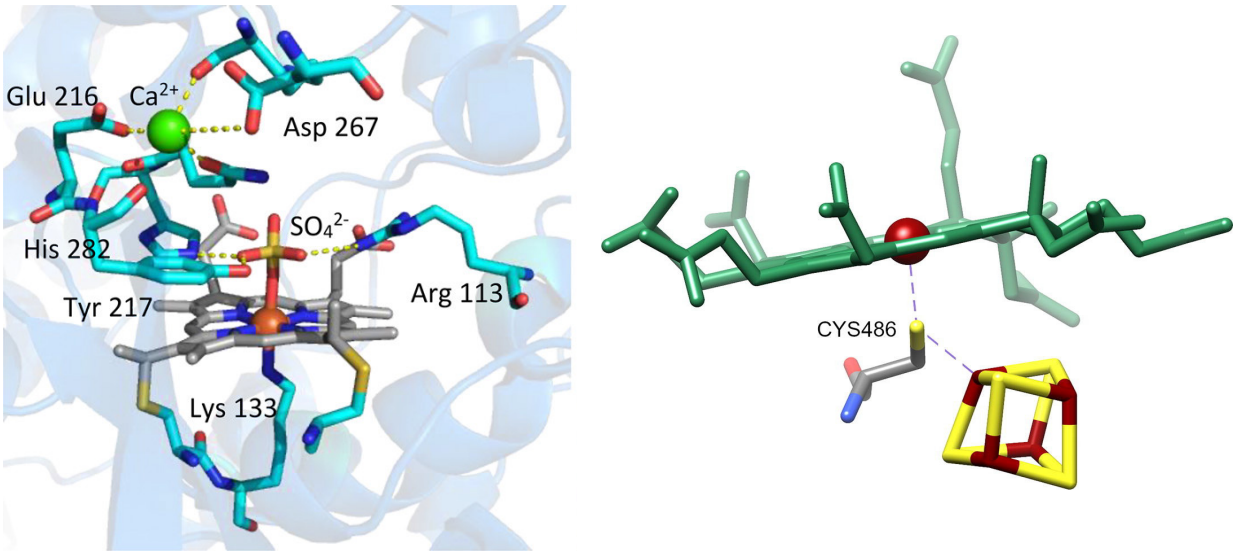

Figure 1.2 PyMOL generated images of the crystal structures of the active sites of C*c*NIR from *S. deleyianum* (left; PDB: 1QDB) Copyright 2021 Chemistry Reviews. Reprinted with permission from Ref [32]. The siroheme and [4Fe-4S] cluster in assimilatory nitrite reductase in *Spinacia oleracea* (right; PDB: 2AKJ) Copyright 2022 Elsevier. Reprinted with permission from Ref [33].

1.3 Cytochrome P450 Nitric Oxide Reductase (Cyt P45nor)

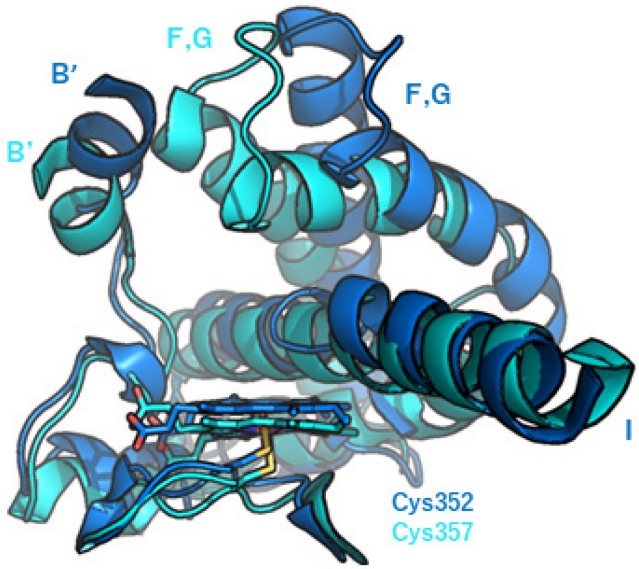

Figure 1.3 PYMOL generated overlay of the crystal structures of Cyt P450nor (blue, PDB: 1ROM) and Cyt P450cam (light blue, PDB: 1PHC), demonstrating the differences in the positioning of the F, G, and B' helices. Adapted with permission from ref [1]. Copyright 2021 American Chemical Society.

Cyt P450nor is found in soil-dwelling fungi, notably *Fusarium oxysporum*, *Trichoderma harzianum*, *Histoplamsa capulatum, Cylindrocarpon tonkinense,* as well as several strains of yeast. In *Fusarium oxysporum*, the enzyme is made up of 403 amino acids with a molecular weight of 46 kDa.[34] The overall fold of Cyt P450nor is similar to Cyt P450 monooxygenases, for example Cyt P450cam, as shown is **Figure 1.3**.[34-38] While the Cyt P450 superfamily of enzymes is generally known to oxidize its substrates through O_2 activation, Cyt P450nor is unique since it utilizes an NAD(P)H cofactor to reduce two molecules of NO to N_2O.[39] This enzyme is also the most efficient NOR to date, with a fast turnover rate of ~1200 s^{-1} at 10 °C.[40]

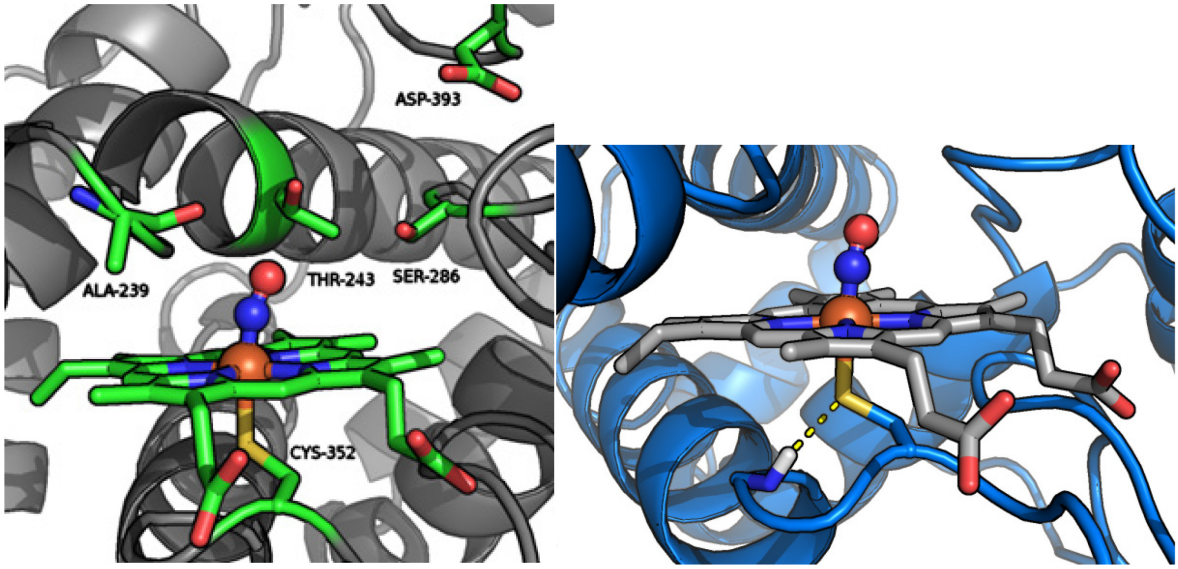

Figure 1.4 PyMOL generated images of the crystal structure of Cyt P450nor from *Fusarium oxysporum*. *Left*: A close-up of the NO-bound ferric active site and relevant residues for proton transfer. *Right*: Focused view on the proximal pocket and highlighting a key hydrogen bond (from the amide group of Ala354) to the heme-bound cysteinate ligand. PDB ID: 1CL6. Adapted with permission from ref [1]. Copyright 2021 American Chemical Society.

The active sites of Cyt P450 enzymes are conserved, utilizing a heme *b* cofactor with a proximally bound cysteinate/thiolate, Cys352 in *F. oxysporum* Cyt P450nor, as shown in **Figure 1.4**.[41] The figure also highlights the main hydrogen bonding network of the proximal Cys residue (the "Cys pocket") in the active site of Cyt P450nor. Recent work has shown that the strength of the hydrogen bonds to the cysteinate ligand tune enzyme reactivity in Cyt P450 monooxygenases by modulating the strength of the thiolate donation to the iron center,[42,43] and the same is expected here in the context of NO reduction. Additionally, the distal pocket of the enzyme contains a hydrogen bonding network formed between Ser286, Thr243, and Asp393 that is crucial for NO reduction by Cyt P450nor, since mutations of each residue either slow or halt N_2O production (see **Figure 1.4**).[35,38,44]

1.3.1 The Proposed Mechanism of Cyt P450nor

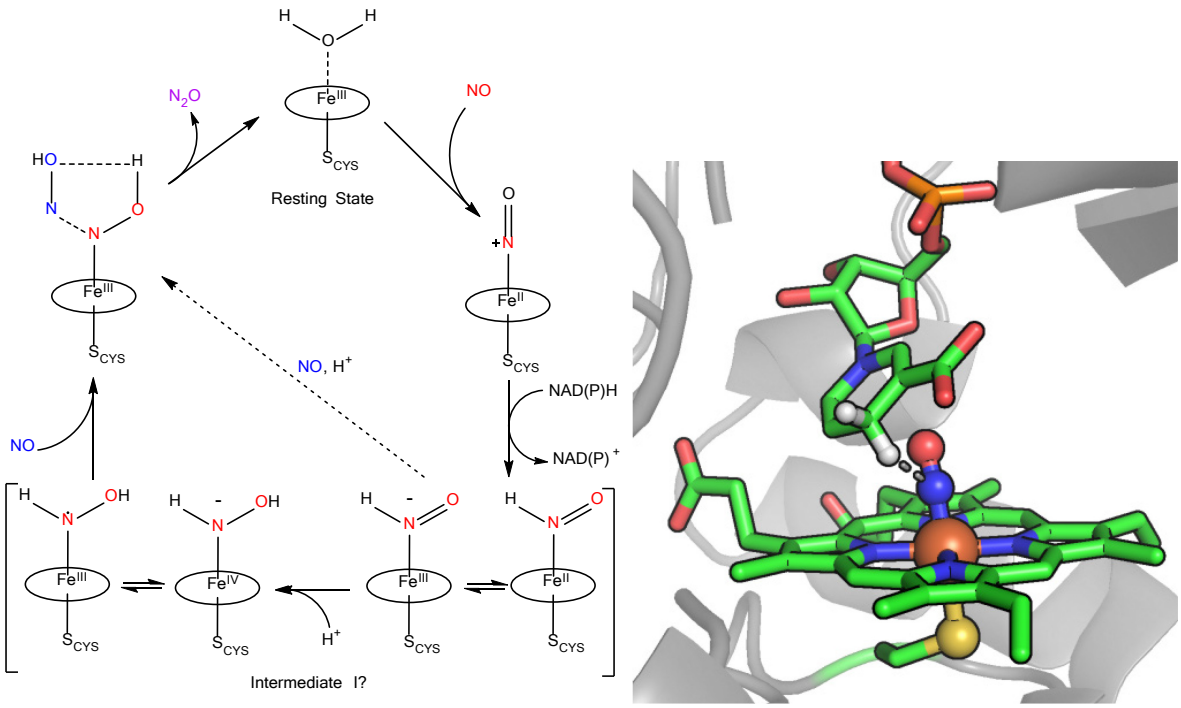

Figure 1.5 *Left*: The proposed reaction mechanism of Cytochrome P450nor. *Right*: Overlay of two structures from PDB ID: 1CL6 (NO bound to ferric heme) and PDB ID: 1XQD (NADPH analog, NAAD, bound in the active site). Adapted with permission from ref [1]. Copyright 2021 American Chemical Society.

Figure 1.5 shows the proposed reaction mechanism of Cyt P450nor.[1] In the resting state, the active-site heme of Cyt P450nor is in the ferric oxidation state with a weakly bound water molecule. The water molecule is easily displaced by NO to form an electrophilic low-spin (ls) Fe(II)-NO^+ species.[40,45-47] Because NO is a non-innocent ligand and forms unusually covalent bonds with metals, Enemark Feltham notation is used as an electron counting method to group nitrosyl complexes by the total number of electrons between the M-NO unit. Here, the Fe(II)-NO^+ is designated as ls-$\{FeNO\}^6$ in the Enemark-Feltham notation[48] ($\{FeNO\}^n$, where the exponent *n* corresponds to the sum of the number of Fe (d^5) and NO (1 π^*) electrons of the complex).[48] Here, the NAD(P)H cofactor performs a direct hydride transfer to the ls-$\{FeNO\}^6$ adduct, as shown in

the structural overlay in **Figure 1.5** to form the reactive species "Intermediate *I*".[40] Subsequent MCD experiments show no **C**-term signal at the 445 nm Soret band position of Intermediate *I*, indicating that this species is diamagnetic with $S_t = 0$.[49] The exact electronic structure and protonation state of Intermediate *I* is unclear due to its very short lifetime of about 100 ms.[40] As indicated in **Figure 1.5**, Intermediate *I* could either correspond to the initially formed HNO complex, with either a Fe(II)-NHO or Fe^{III}-$NHO^{\bullet-}$ type electronic structure, or the corresponding doubly-protonated species, which could exist in the form of two valence tautomers, either Fe(IV)-$NHOH^-$ or Fe(III)-$NHOH^{\bullet}$.[49-53] Recently, Shiro and coworkers studied the reaction of Cyt P450nor with NO using time-resolved spectroscopic techniques and DFT calculations.[54] In this work, the N-O stretching mode of Intermediate *I* was observed for the first time. Here, N-O stretching frequencies of 1330 cm^{-1} and 1290 cm^{-1} were obtained for the intermediate with and without NAD^+ present, respectively.[54] These results paired with DFT suggest that this species is likely singly protonated (potentially with the Fe^{III}-$NHO^{\bullet-}$ electronic structure).[51,54] However, as evident from **Figure 1.5**, more work is needed to ultimately identify the true nature of Intermediate *I* that reacts with a second equivalent of NO to generate N_2O to complete the catalytic cycle.

1.3.2 Theoretical and Experimental Models of Intermediate I

Since heme-HNO intermediates in the above-mentioned enzymes are very difficult to study, due to their high reactivity, model complexes have been found essential in determining most of what we know about heme-HNO species. In aqueous solution, the best spectroscopically characterized and most stable HNO complex is the ferrous Mb-HNO adduct, prepared by Farmer and coworkers.[55,56] The remarkable stability of the Mb(II)-NHO complex was attributed to steric shielding of the HNO ligand in the protein matrix and the presence of a hydrogen bonding network within the distal pocket of myoglobin.[57] Indeed, as first reported by Ryan and coworkers, heme-

HNO model complexes are susceptible to fast bimolecular decomposition, generating the corresponding ls-{FeNO}^{7} complexes and H_2, which is the main cause for the complexes instability.[58] Doctorovich and coworkers obtained further evidence that hydrogen-bonding interactions can increase the stability of heme-HNO complexes: they prepared the water-soluble complex [Fe(TPPS)(NHO)]$^{4-}$, where hydrogen bonding of water molecules with the bound HNO ligand is proposed to increase its stability and slow down its decomposition, with a reported half-life of 41 s at room temperature.[59]

In organic media, heme ls-{FeNO}^{8} complexes were prepared by both chemical and electrochemical reduction of the corresponding ls-{FeNO}^{7} precursors. These complexes have Fe(II)-NO$^-$ electronic structures, where a singlet NO$^-$ ligand is bound to a ls-Fe(II) center, with a very covalent Fe-NO bond.[2,60] Ryan and coworkers were able to obtain the complex [Fe(OEP)(NHO)] (OEP^{2-} = octaethylporphyrin dianion) upon treatment of the corresponding nitroxyl complex [Fe(OEP)(NO)]$^-$ with phenols (PhOH) as weak acids. Here, the [Fe(OEP)(NHO)] complex seems to form an equilibrium with the hydrogen bonded complex [Fe(OEP)(NO---HOPh)].[61,62] Similarly, our group utilized electrochemical reduction followed by protonation with acetic acid to prepare a five-coordinate (5C) HNO complex, [Fe(3,5-Me-BAFP)(NHO)], using a bulky bis-picket fence porphyrin.[63] Unfortunately, [Fe(3,5-Me-BAFP)(NHO)] could not be isolated for spectroscopic characterization due to the large excess of electrolyte salt present from bulk electrolysis. On the other hand, Richter-Addo and coworkers prepared a six-coordinate (6C) HNO derivative, [Fe(OEP)(5-MeIm)(NHO)], using a method that is analogous to the reaction catalyzed by Cyt P450nor, where a hydride is added to the electrophilic ls-{FeNO}^{6} complex, [Fe(OEP)(5-MeIm)(NO)]$^+$.[64] Despite the low yield (11%), the HNO complex showed qualitative N_2O upon addition of NO gas. However, because the yield of N_2O

could not be determined, the catalytic competency of the heme-HNO as Intermediate *I* in Cyt P450nor remains unclear.

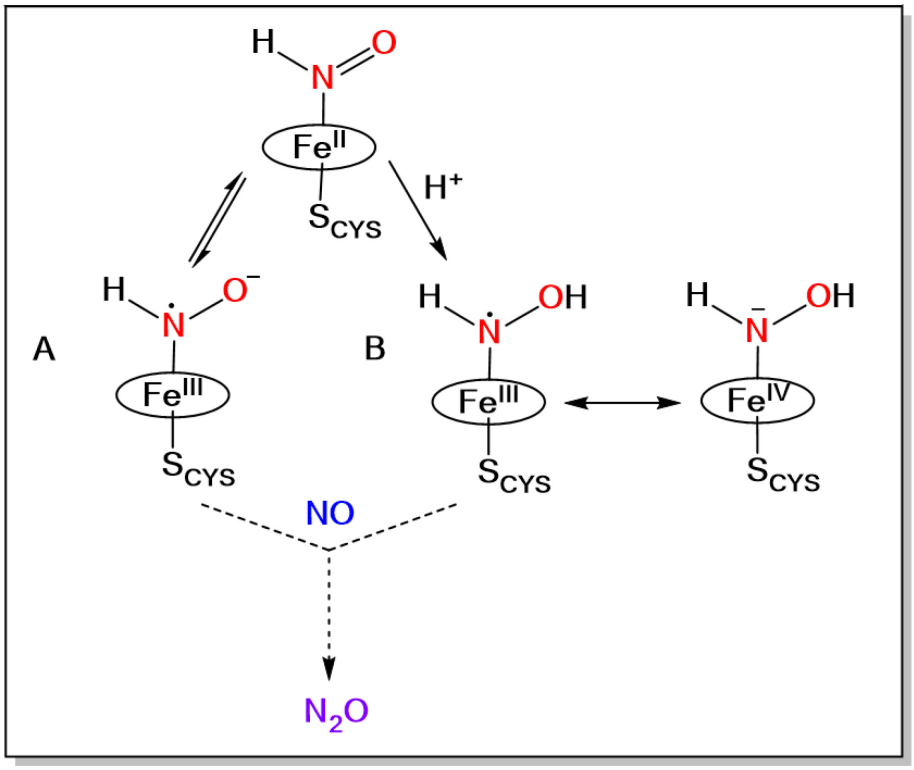

Figure 1.6 Possible geometric and electronic structures of Intermediate *I* in Cyt P450nor. Scheme adapted from ref. [1]. Copyright 2021 American Chemical Society.

One important question in the context of Cyt P450nor is how the axial thiolate ligand affects the electronic properties of Intermediate *I*. Based on DFT studies by the Neese group, it was proposed that the anionic nature of the thiolate could promote the formation of a valence tautomer, with an Fe^{III}-$HNO^{\bullet-}$ type electronic structure (see **Figure 1.6**).[51] The formation of such a radical species can be expected to aid in the following reaction with the incoming NO•, corresponding to a radical-radical type coupling reaction, which generally have very low activation barriers. Alternatively, DFT calculations predict that the strong electron donation from the axial thiolate ligand increases the basicity of the bound HNO ligand, leading to its further protonation. In this case, the Fe-NHO species could be protonated at neutral pH, forming an Fe-NHOH type

species (see **Figure 1.6**).[50] This is analogous to later work by Green and coworkers, where it was shown that the proximal thiolate ligand in Cyt. P450s increases the basicity of Compound II by 9 log units (compared to Mb), which drives the H-atom abstraction from a substrate C-H bond.[43,51,65] Experimental support for a Fe-NHOH complex comes from pulse radiolysis experiments with H_2NOH, which is known to generate the •NHOH radical under these conditions.[66] When H_2NOH is irradiated in the presence of ferric P450nor, the Soret band shifts to ~444 nm, which is identical to the position of the Soret band in Intermediate *I*.[67]

With these considerations in mind, the ferric complex [Fe(3,5-Me-BAFP)(NHOMe)] was prepared, where O-methylhydroxylamide is used as a substitute for hydroxylamide (to increase the stability of the complex) in combination with the sterically shielding 3,5-Me-BAFP^{2-} porphyrin ligand.[53] One-electron oxidation of this species at -80 ºC then generates [Fe(3,5-Me-BAFP)(NHOMe)]$^{+}$ as a model for Intermediate *I*. Spectroscopic studies (especially rRaman and Mössbauer) show that in this complex, the iron center is still in the Fe^{III} state, which means that the complex indeed corresponds to the Fe^{III}-NHOMe• valence tautomer. Reactivity studies of this intermediate with stoichiometric NO• demonstrated fast attack on the coordinated NHOMe• within ~35 s, likely leading to N-N bond formation. These results indicate that a Fe^{III}-NHOMe• type species is indeed highly reactive towards NO•, even at -80 ºC, which is in agreement with a radical-radical type reaction.[49,53]

In summary, based on spectroscopic studies on Cyt. P450nor, model complex studies, and DFT calculations, there are two possible structures for Intermediate *I*, the key intermediate in Cyt. P450nor catalysis. This species could either correspond to the Fe^{II}-HNO adduct, proposed to have an Fe^{III}-$HNO^{\bullet-}$ electronic structure, or the corresponding protonated species, Fe^{III}-NHOH•, as

shown in **Figure 1.6**.[45,49,50,53] Further studies are necessary to fully elucidate the true nature of Intermediate *I*, and to shed more light on the second half of the catalytic cycle of Cyt. P450nor.

1.4 Scope of Chapters 2 and 3

In this work, the electronic structure and protonation state of the reactive Intermediate *I* were investigated within the context of Cytochrome P450nor's reaction mechanism. **Chapter 2** focuses on the stabilization of a six-coordinate Fe(II)-HNO complex, [Fe(3,5-Me-BAFP)(MI)(HNO)] (MI = N-methylimidazole), using a sterically hindered bis-picket fence porphyrin, 3,5-Me-BAFP^{2-} = 3,5-dimethyl-bisaryloxyfence porphyrin, to prolong the stability of the HNO complex for spectroscopic characterization. The formation of this complex mimics the reaction in the enzyme itself, where the conversion of a ls-{FeNO}^{6} precursor to the corresponding ls-{FeHNO}^{8} complex is complete upon addition of 1 equivalent of a hydride source. The formation of the ls-{FeHNO}^{8} complex was monitored *in situ* using UV-vis and ^{1}H-NMR spectroscopy. Excitingly, this heme-HNO model complex is stable enough to be isolated from the reaction mixtures as a solid for further characterization by IR, temperature-dependent ^{1}H-NMR, and nuclear resonance vibrational spectroscopy (NRVS). Reaction of the 6C heme-HNO complex with NO gas leads to the formation of quantitative amounts of N_2O by gas headspace IR spectroscopy. This chapter has been adapted from the manuscript: **Manickas, E. C.**; LaLonde, A. B.; Hu, M. Y.; Alp, E. E.; Lehnert, N. *J. Am. Chem. Soc.,* 2023, 145, 42, 23014.

Despite the increased stability of [Fe(3,5-Me-BAFP)(MI)(HNO)], this complex is not a perfect analog of Intermediate *I* of Cyt P450nor since the active site of the enzyme contains a proximally bound anionic thiolate rather than a neutral imidazole as the axial ligand. **Chapter 3** focuses on using the bis-picket fence porphyrin to generate select thiolate-bound ls-{FeNO}^{6} complexes [Fe(3,5-Me-BAFP)(SR)(NO)]. This expands on previous work from our laboratory that

used the tetraphenylporphyrin scaffold (TPP^{2-}) in combination with a number of different thiolate ligands to form thiolate-bound ls-{FeNO}^{6} complexes.[45,46] The stability of each ls-{FeNO}^{6} complex was initially accessed by UV-Vis spectroscopy and compared to the analogous [Fe(TPP)(SR)(NO)] complexes reported previously. Of these complexes, [Fe(3,5-Me-BAFP)($SPhF_4CF_3$)] generated the cleanest ls-{FeNO}^{6} complex with the lowest equivalents of NO gas added, and therefore, my work focused on this complex that was subsequently fully characterized by UV-Vis, ^{1}H-NMR, IR and rRaman spectroscopy. The reactivity of this complex was further studied by hydride addition to observe a thiolate-bound nitroxyl intermediate to determine how the identity of the proximal ligand affects the electronic structure and reactivity of the Fe-HNO unit.

1.5 Electrocatalytic NO Generation by Copper Catalysts for Biomedical Applications

Biomedical devices, such as intravascular catheters, play an integral role in medical care, enabling hospital staff to monitor patients' blood as well as deliver drugs and nutrients. Two major complications of such devices include microbial infections and thrombosis/clotting. Considering catheter-related bloodstream infections (CR-BSIs) alone, about 80,000 patients are infected in intensive care units (ICU) in the United States, leading to 28,000 deaths and an additional $2.3 billion in medical costs each year.[68] NO can be used to mitigate microbial infections and blood clotting at the surface of these blood contacting devices since it is already produced endogenously in humans and plays several physiological roles depending on its local concentration. At higher (μM) concentrations, NO can act as an antimicrobial agent in our immune system against invading pathogens, while at low (nM) concentrations, NO can provide therapeutic effects that enhance vasodilation, prevent platelet aggregation, aid in wound healing, and prevent angiogenesis.[69-73]

Previously, catheters were equipped with a polymeric coating capable of NO release at the outer surface of the device to prevent infections and blood clotting.[74,75] Limitations of this method include lack of control over NO release that varies by patient to patient, resulting in inconsistent NO fluxes. In collaboration with Prof. Mark E. Meyerhoff at the University of Michigan, current research is aimed at electrochemical NO production via a copper-based catalyst within a dual-lumen catheter as shown in **Figure 1.7**. This method ensures a controlled rate of NO release by applying an electrochemical potential to an aqueous nitrite solution with a copper catalyst inside of a multi-lumen catheter.

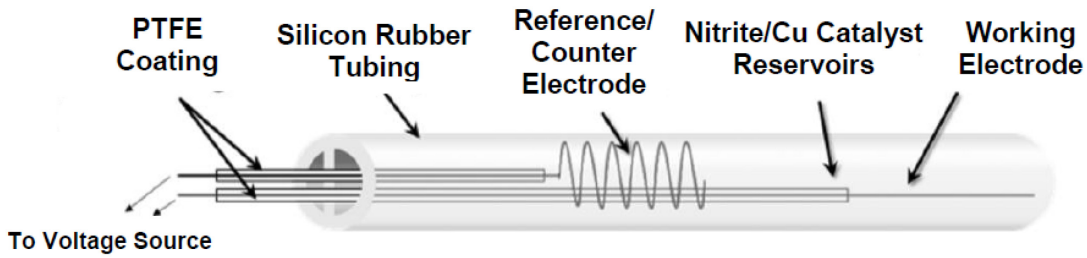

Figure 1.7. Schematic of a dual-lumen intravascular catheter for electrochemical NO production. Scheme adapted from ref.[76]. Copyright 2014 American Chemical Society.

Copper nitrite reductase (CuNIR) is an enzyme that plays a key role in the nitrogen cycle (**Figure 1.1**) in the denitrification pathway where nitrite is reduced to NO anaerobically.[77] These enzymes are homotrimers with typically 36 kDa subunits, as shown in **Figure 1.8**.[78] CuNIRs facilitate nitrite reduction using a Type 1 and Type 2 copper center as shown in **Figure 1.8**, where the Type 1 copper center, coordinated by two histidine, a cysteine and a methionine residue, is responsible for electron transfer and the Type 2 copper center, coordinated by three histidine residues, is the active site responsible for catalysis.[79,80] These centers are 12.6 Å apart and are covalently linked via a Cys-His sequence between the metal sites, which allows for facile electron

transfer from the Type 1 copper site to the Type 2 copper active site for nitrite reduction.[79] With inspiration from CuNIR, catalysts can be designed to model the Type 2 copper active site responsible for nitrite reduction. With the application of a constant electrochemical potential, electrons can be supplied to the catalyst to generate NO to combat bacterial infections and blood clots at the surface of a catheter.

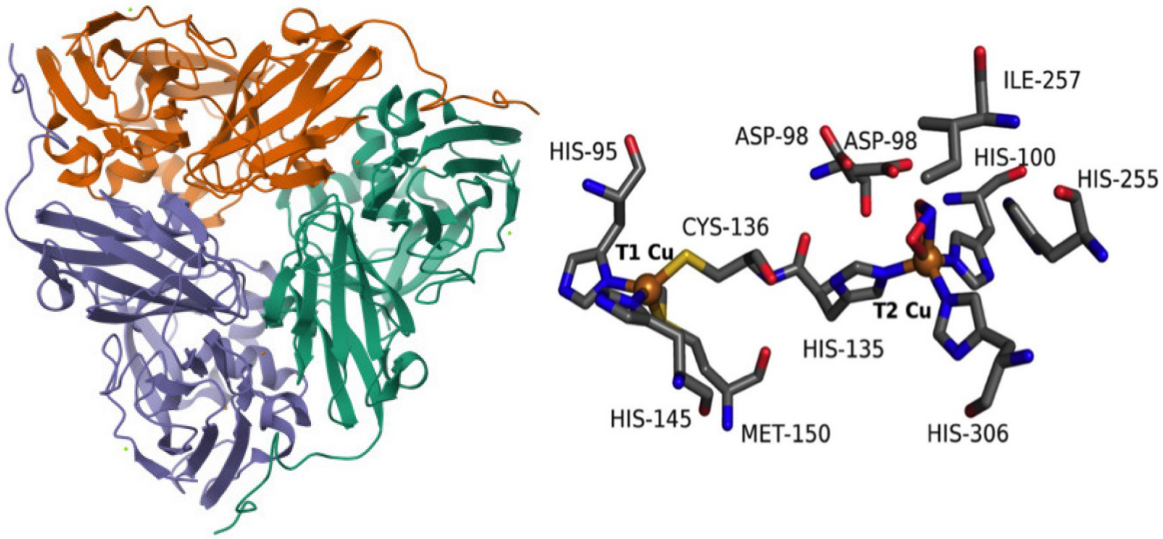

Figure 1.8 Crystal structure of CuNIR of *Rhodobacter sphaeroides*, PDB: 2A3T (left).[78] Reproduced with permission of the International Union of Crystallography. The active site of CuNIR during the catalytic process in *Achromobacter cycloclastes*, PDB: 2BWD (right). Adapted with permission from ref.[80]. Copyright 2015 American Chemical Society.

Several water-soluble catalysts have been tested for electrochemical NO production demonstrating reproducible, controlled NO release under an N_2 atmosphere, as shown in **Figure 1.9**.[76,81-83] Initial electrochemical experiments were performed with copper(II) tris(2-pyridylmethyl)amine, $[Cu(TMPA)]^+$, which was determined to have a reduction potential of -380 mV (vs Ag/AgCl) displaying a Faradaic efficiency of 6.3%.[76] A significant improvement was observed when experiments were repeated with copper(II) 1,4,7-trimethyl-1,4,7-triazacyclononane, $[Cu(Me_3TACN)]^+$, which has a reduction potential of -340 mV (versus Ag/AgCl) and shows Faradaic efficiencies for nitrite reduction ranging from 57-84%, depending

on the applied potential.[81] Despite the improved catalysis observed with $[Cu(Me_3TACN)]^+$, NO generation decreased by 75% when changing the sparge gas from N_2 to 3% O_2. Given that catheters are placed in arteries and veins where oxygen content is 5 and 12%, respectively, decreasing O_2 sensitivity is crucial in successfully designing catalysts for this application. Additionally, electrochemical experiments with $[Cu(Me_3TACN)]^+$ indicated catalyst disproportionation of the Cu(I) center to Cu(II) and Cu(0), where the latter plates onto the surface of the working electrode and lowers NO production over time.[81]

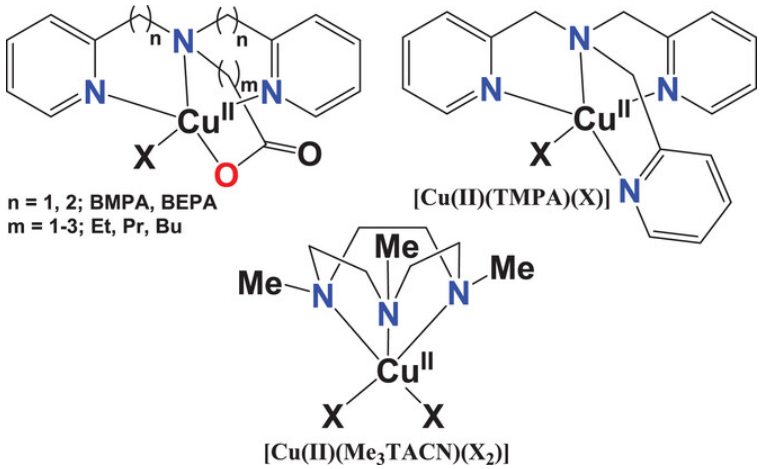

Figure 1.9 Chemdraw scheme of current copper complexes capable of electrochemical nitrite reduction to NO in aqueous solvent. Scheme adapted with permission from ref.[84]. Copyright 2021 Wiley.

To address the O_2 sensitivity and disproportionation observed with these catalysts, a series of BEPA/BMPA carboxylate catalysts were synthesized to tune the reduction potential of the Cu(II)/Cu(I) couple and study its role in nitrite reduction to nitric oxide, as shown in **Figure 1.9**.[82] Based on this work, it was determined that copper complexes with more positive reduction potentials, for example $[Cu(BEPA\text{-}Bu)]^+$, were favored for selective NO generation without disproportionation to N_2O. This complex shows a reduction potential of +10 mV with a Faradaic efficiency for nitrite reduction of 91%.[82] Additionally, complexes with more negative reduction potentials are more O_2 sensitive, resulting in inhibition of nitrite reduction upon reduction from

Cu(II) to Cu(I) in the presence of air. While catalysts with more positive reduction potentials lead to selective NO generation, overall nitrite reduction slows, which is less optimal in terms of desired catalyst performance. For example, $[Cu(TMPA)]^+$ which demonstrates a more negative reduction potential of -380 mV, shows a turnover frequency (TOF) of 13.42 s^{-1}, in contrast to $[Cu(BEPA\text{-}Bu)]^+$ which shows a TOF of 1.18 s^{-1}.[82]

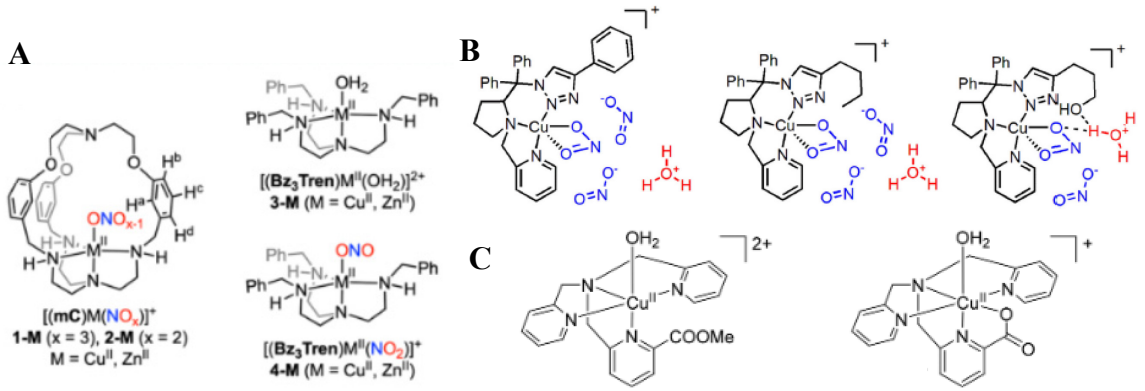

Figure 1.10 Previously reported copper catalysts with hydrogen bond donors in the second coordination sphere for nitrite reduction. (A) Adapted with permission from ref. [85]. Copyright 2022 American Chemical Society. (B) Adapted with permission from ref.[86]. Copyright 2023 Royal Society of Chemistry. (C) Adapted with permission from ref.[87]. Copyright 2018 American Chemical Society.

One strategy to increase the rate of nitrite reduction as reduction potentials become more positive is to append hydrogen bond donors in the second coordination sphere (SCS) of these copper catalysts. There are several examples in the literature that demonstrate improved nitrite reduction in nonaqueous solvents with catalysts containing intramolecular hydrogen bond donors , as shown in **Figure 1.10**. Kundu and coworkers demonstrated nitrite binding to tripodal copper complexes equipped with a protonated amine in the SCS, demonstrating that the formation of a HONO species facilitates NO_2 reduction.[85,88] Similar observations were discussed by Netto and coworkers where a copper catalyst equipped with a propanol group in the SCS doubled in

efficiency toward nitrite reduction, in comparison to two control complexes.[86] Symes and coworkers designed TMPA derivatives containing an appended carboxylate or ester in the SCS. It was determined that the carboxylate complex was twice as effective for nitrite reduction in comparison to the ester complex, suggesting that there is a proton relay that facilitates catalysis.[87]

1.6 Scope of Chapter IV

In this work, the oxygen sensitivity of these catalysts was addressed by employing hydrogen bond donors within the second coordination sphere (SCS) of water-soluble copper complexes. The goal of **Chapter 4** was to increase the affinity of nitrite binding and allow facile proton transfer to the nitrite prior to reduction to NO. Here, the synthesis of two asymmetric hydrogen bonding derivatives of [Na(BMPA-Pr)] = sodium 3-(bis(pyridin-2-ylmethyl)amino)propanoate are reported. These derivatives include the ligands [Na(Amide-BMPA-Pr)] and [Na(Amine-BMPA-Pr)], which were synthesized according to two synthetic methods. Each corresponding copper complex was characterized by X-ray crystallography, UV-vis spectroscopy and cyclic voltammetry (CV). The effect of the hydrogen-bonds in these copper catalysts was assessed by bulk electrolysis where the amount of nitric oxide produced was quantified using a nitric oxide analyzer (NOA). The Faradaic efficiencies of these complexes were compared between sparge gases with varying oxygen and nitrogen compositions, from pure nitrogen to air, to assess oxygen sensitivity in comparison to the parent complex (that lacks the SCS groups). These results provide a foundation for assessing the effect of SCS hydrogen bond donors in copper complexes and how they affect nitrite reduction to NO.

Chapter 2 Stabilization of a Six Coordinate Heme-HNO Model Complex using a Bulky Bis-Picket Fence Porphyrin and Reactivity Studies with NO

In this Chapter, a stable heme-HNO complex was isolated and spectroscopically characterized using a bulky bis-picket fence porphyrin. Reactivity studies were performed with NO to assess its competency toward NO reduction in the context of Cyt P450nor. The following chapter was adapted from the referenced publication.[3]

2.1 Introduction

Since heme-HNO intermediates in native enzymes are very difficult to study, due to their high reactivity. Protein and synthetic model complexes have been found essential in determining most of what we know to date about heme-HNO species. In aqueous solution, two notable models include the ferrous Mb-HNO adduct prepared by Farmer and coworkers[55,56] and the water-soluble complex $[Fe(TPPS)(NHO)]^{4-}$ prepared by Doctorovich and coworkers.[59] The prolonged stability of the former was attributed to either the steric shielding of the HNO ligand in the protein matrix and the presence of a hydrogen bonding network with the distal pocket of myoglobin, while the latter was proposed to form hydrogen bonds with water to slow decomposition.[57,59]

In organic solvents, heme ls-$\{FeNO\}^8$ complexes were prepared by both chemical and electrochemical reduction of the corresponding ls-$\{FeNO\}^7$ precursors. Our group utilized electrochemical reduction to prepare a five-coordinate (5C) HNO complex, [Fe(3,5-Me-BAFP)(NHO)], using the same bulky bis-picket fence porphyrin used in this work.[63] Unfortunately, the complex could not be isolated due to the presence of large amounts of electrolyte in solution. On the other hand, Richter-Addo and coworkers prepared a low yielding

six-coordinate (6C) HNO derivative, [Fe(OEP)(5-MeIm)(NHO)], using a method that is analogous to the reaction catalyzed by Cyt P450nor.

This chapter focuses on the formation of a 6C heme-HNO complex using a sterically hindered bis-picket fence porphyrin to enhance its half-life in organic solvents for isolation, thorough spectroscopic characterization, and reactivity studies with NO gas. This porphyrin scaffold was chosen to slow the known bimolecular decomposition pathway of the heme-HNO complex to $\{FeNO\}^7$ complex and H_2, as discussed in **Chapter 1**. The formation of the heme-HNO complex *in situ* was confirmed based on characteristic features provided in the literature. Kinetic studies were performed at different temperatures to confirm that the heme-HNO species is indeed more stable than other synthetic heme-HNO model complexes previously reported in the literature. Precipitation of the complex from solution at low temperatures allowed for spectroscopic studies at room temperature. Reactivity studies of the heme-HNO complex with NO indicates competence toward N_2O formation, making it a potential intermediate in the Cyt P450nor reaction mechanism.

2.2 Synthesis and Characterization of Precursor Compounds

As described in the Introduction, a sterically hindered bis-picket fence porphyrin was used in this work to stabilize a six-coordinate (6C) heme-HNO model complex for isolation and thorough spectroscopic characterization. The syntheses of the porphyrin, [H_2(3,5-Me-BAFP)], and the complex, [Fe(3,5-Me-BAFP)(Cl)], are based on published procedures.[63] The ligand and metalated complex were characterized by elemental analysis and ^{1}H-NMR spectroscopy.

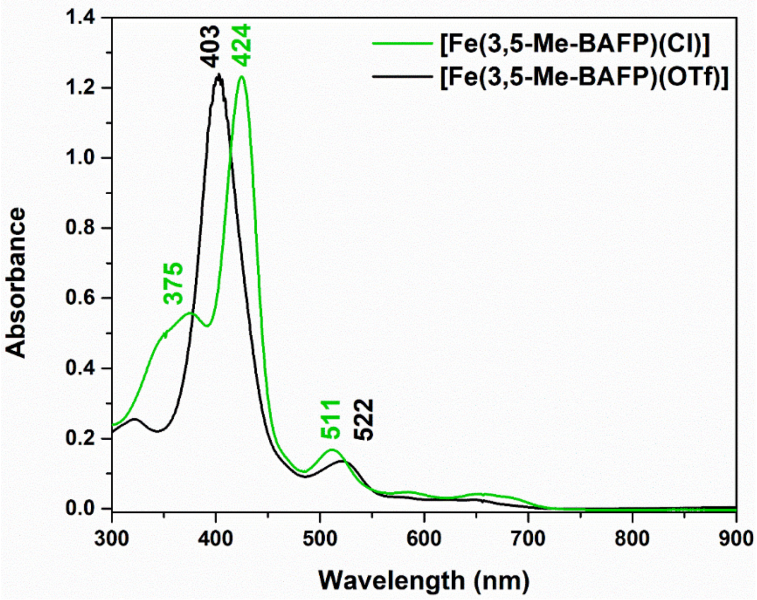

Figure 2.1 Normalized UV-vis spectral overlay of the [Fe(3,5-Me-BAFP)(Cl)] & [Fe(3,5-Me-BAFP)(OTf)].

Prior to nitrosylation, the bound chloride ligand of the metalated complex, [Fe(3,5-Me-BAFP)(Cl)], was exchanged using a silver salt, typically AgOTf to form [Fe(3,5-Me-BAFP)(OTf)]. Once the reaction was complete according to UV-vis spectroscopy (see **Figure 2.1**), the reaction mixture was filtered to remove silver chloride and the product was collected from the filtrate following precipitation with hexanes. This complex was exposed to NO gas to form the five-coordinate (5C) low-spin (ls) $\{FeNO\}^6$ complex, [Fe(3,5-Me-BAFP)(NO)](OTf) (see **Figure 2.2**). In the process of nitrosylation, a sixth (axial) ligand was added as well, which is critical for the following reaction with hydride donors, as shown by Richter-Addo and coworkers.[89] Without the axial ligand, it was shown that 5C ls-$\{FeNO\}^6$ complexes add hydride to the iron center, not the NO^+ ligand, ultimately leading to decomposition. Here, we chose 1-methylimidazole (MI) as the sixth ligand, as a model for the proximal histidine ligand in heme proteins. Preparation of the 6C complex, [Fe(3,5-Me-BAFP)(MI)(NO)](OTf), includes the addition of one equivalent of MI to the metathesized complex in dichloromethane, either before or after exposing the reaction solution to excess NO gas, as shown by UV-vis and solution IR spectroscopy in **Figure 2.2**.

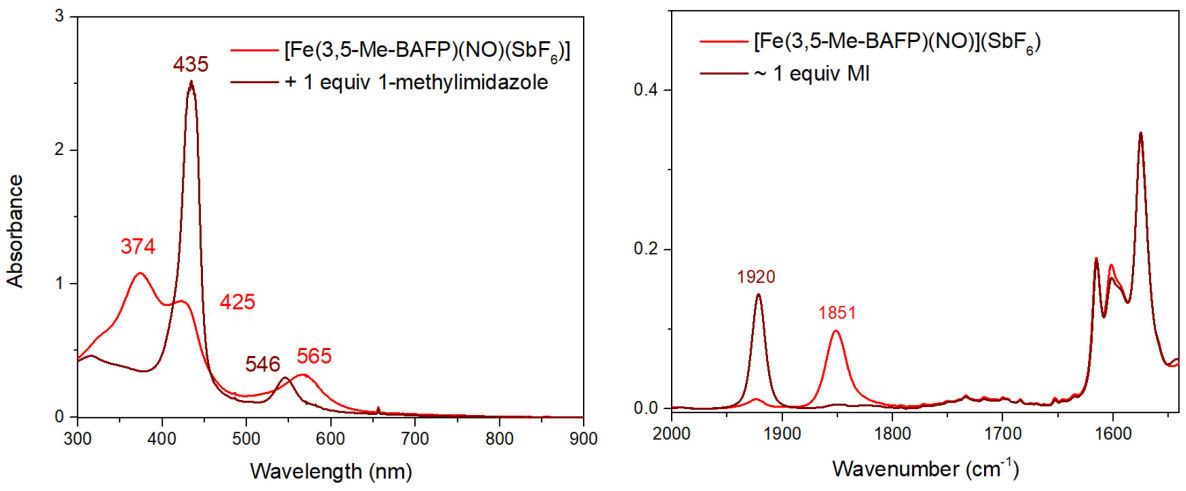

Figure 2.2 Spectral overlay of $[Fe(3,5\text{-Me-BAFP})(NO)]^+$ before (red) and after (maroon) addition of 1 equivalent of 1-methylimidazole in dichloromethane. Left: UV-vis spectra. Right: Solution IR spectra in dichloromethane.

The successful preparation of the ls-{FeNO}^{6} complex, [Fe(3,5-Me-BAFP)(MI)(NO)](OTf), was confirmed by UV-vis, IR, NRVS , and ^{1}H NMR spectroscopy (see **Figure 2.2, Figure 2.3, and Figure 2.4.** This complex showed the Soret and Q bands at 436 and 545 nm and was characterized by N-O (from IR spectroscopy) and Fe-NO (from NRVS) vibrational frequencies of 1912 and 593 cm^{-1}, respectively. The latter values compare well with those of the 6C complex, [Fe(TPP)(MI)(NO)](SbF$_6$), which has N-O and Fe-NO stretching frequencies of 1920 and 589 cm^{-1}, respectively.[90]

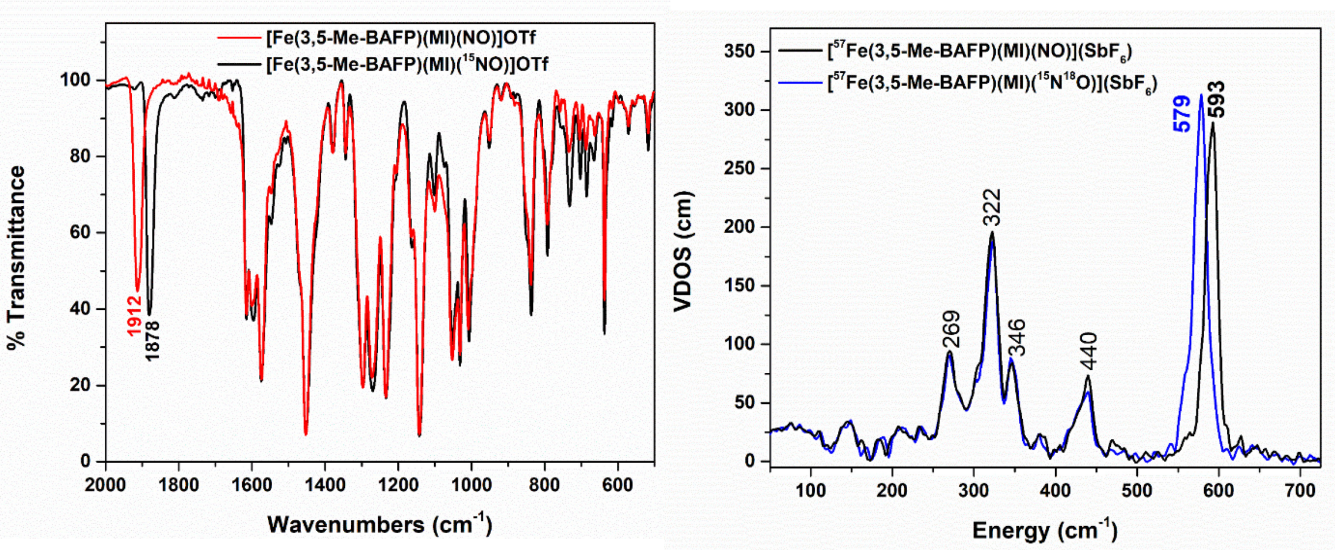

Figure 2.3 Left: FT-IR spectral overlay of the 6C {FeNO}^{6} complex, [Fe(3,5-Me-BAFP)(MI)(NO)](OTf) (red) and [Fe(3,5-Me-BAFP)(MI)(^{15}NO)](OTf). Both prepared as KBr pellets. Right: NRVS-derived vibrational density of states (VDOS) for solid samples of [^{57}Fe(3,5-Me-BAFP)(MI)(NO)](SbF$_6$) (black) and [^{57}Fe(3,5-Me-BAFP)(MI)(^{15}N^{18}O)](SbF$_6$) (blue).

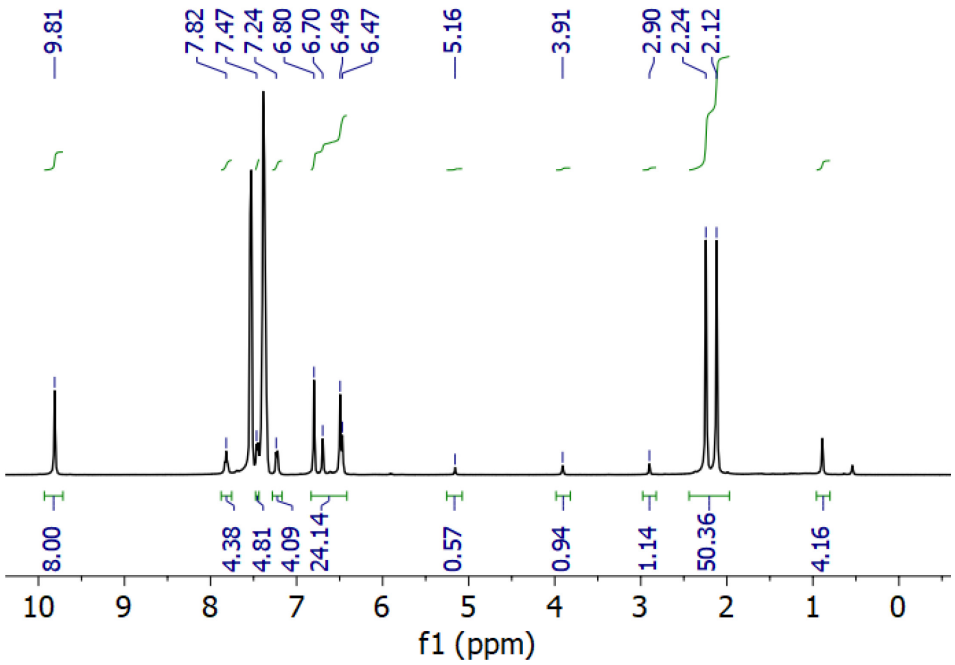

Figure 2.4 NMR spectrum of ~12 mM [Fe(3,5-Me-BAFP)(MI)(NO)](OTf) in chlorobenzene-d_5 at room temperature, ^{1}H-NMR. The chlorobenzene-d_5 signals were referenced at 7.37, 7.39, and 7.54 ppm.

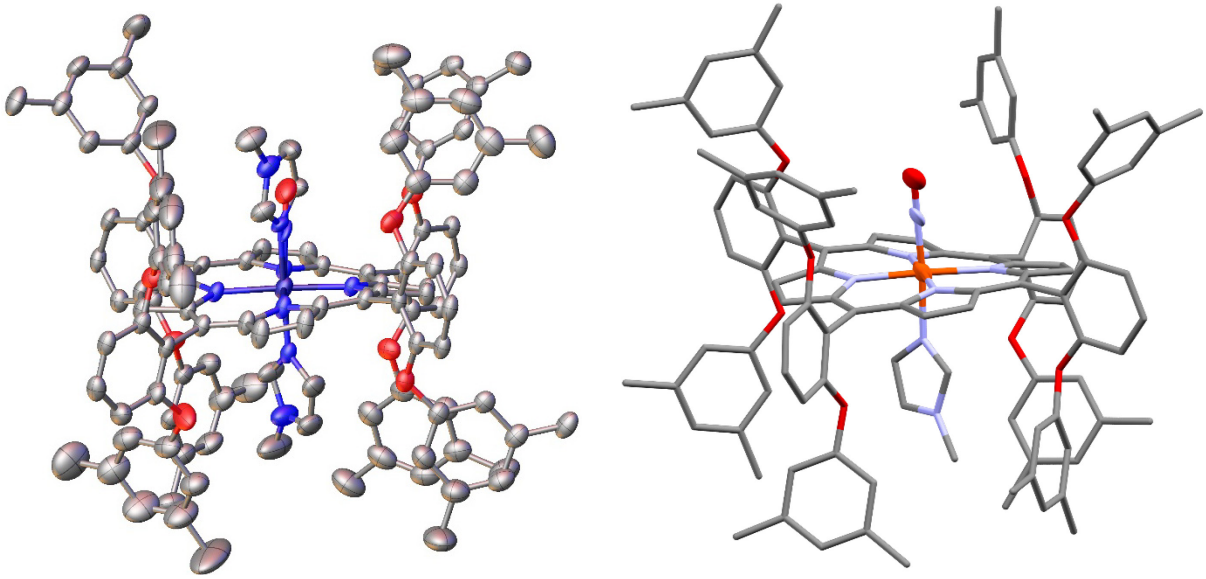

Figure 2.5 The molecular structure of the 6C $\{FeNO\}^6$ complex, [Fe(3,5-Me-BAFP)(MI)(NO)](BArF$_{24}$), contains two species: 70.6% bis-imidazole and 29.4% 6C $\{FeNO\}^6$ (left) and the minor species is represented in a capped stick model (right). R_{int}= 0.0483 and R= 0.0558. Color scheme: C, gray; N, blue; O, red; Fe, orange. All thermal ellipsoids are shown at 50% probability. The hydrogen atoms and the BArF$_{24}^-$ counterion were omitted for clarity.

The [Fe(3,5-Me-BAFP)(MI)(NO)](BArF$_{24}$) was analyzed by single crystal X-ray diffractometry. The obtained molecular structure exhibits two co-crystallized species of 70.6 and 29.4%, where the major species represents the bis-imidazole bis-picket fence porphyrin, [Fe(3,5-Me-BAFP)(MI)$_2$], and the minor species is the desired 6C {FeNO}^{6} complex. Due to the significant overlap of the electron density of the nitrogen from the NO and the imidazole, restraints were placed on the coordinated NO of the 6C {FeNO}^{6}. For this reason, the bond lengths and angles for the FeNO unit can only be discussed qualitatively. Typical Fe-N and N-O bond distances of 6C {FeNO}^{6} complex reported in the literature are typically 1.63-1.65 and 1.13-1.15 Å, respectively.[1] The [Fe(3,5-Me-BAFP)(MI)(NO)]$^+$ shows Fe-N and N-O bond lengths of 1.677 and 1.21 Å which are slightly elongated compared to the literature.[1]

Table 2.1 Geometric parameters of [Fe(3,5-Me-BAFP)(MI)(NO)]$^+$ obtained by X-ray crystallography. Bond distances are reported in Å.

*Fe-N	*N-O	*∠Fe-N-O	Fe-N_{MI}	Fe-$N_{porphyrin}$
1.677	1.21	175.8°	1.9855	1.9901

*Due to restraints on the Fe-N-O unit, values listed are only for qualitative discussion.

2.3 Stabilization and Isolation of [Fe(3,5-Me-BAFP)(MI)(NHO)]

2.3.1 Formation of [Fe(3,5-Me-BAFP)(MI)(NHO)].

The formation of [Fe(3,5-Me-BAFP)(MI)(NHO)] was monitored by UV-vis and ^{1}H-NMR spectroscopy in chlorobenzene-d_5 between -20 and -40 °C. Upon addition of ~1 equivalent of [TBA](BH$_4$) to a solution of [Fe(3,5-Me-BAFP)(MI)(NO)](OTf), two new peaks initially appeared at 14.59 and 14.66 ppm, indicating the formation of at least two HNO species (see **Figure 2.6).** We ascribe the observation of multiple HNO signals in the spectra to the formation of

rotational isomers within the pocket of the sterically hindered porphyrin scaffold. After ~25 minutes, the two major species equilibrate to a 1:1 ratio at 14.59 and 14.68 ppm (**Figure 2.6 and Figure 2.8**). When repeated with the ^{15}N-labeled ls-{FeNO}^{6} complex, both peaks split into doublets with resonances at 14.51 and 14.65, and 14.58 and 14.73 ppm, respectively, after reaching equilibrium (**Figure 2.7 and Figure 2.8**). The second HNO species is likely a rotational isomer which has been previously observed in both heme HNO model complexes and in protein HNO adducts.[64,91] For example, Richter-Addo and coworkers observed a minor amount of a second isomer (~9%) of their HNO complex, [Fe(OEP)(5-MI)(NHO)], and discussed the possibility that these isomers are simple rotamers. The J_{NH} coupling constant of each species was determined to be 75 and 70 Hz, which are within the range of those reported for [Fe(OEP)(5-MI)(NHO)] and Mb(II)-NHO (see **Table 2.2**).[55,64]

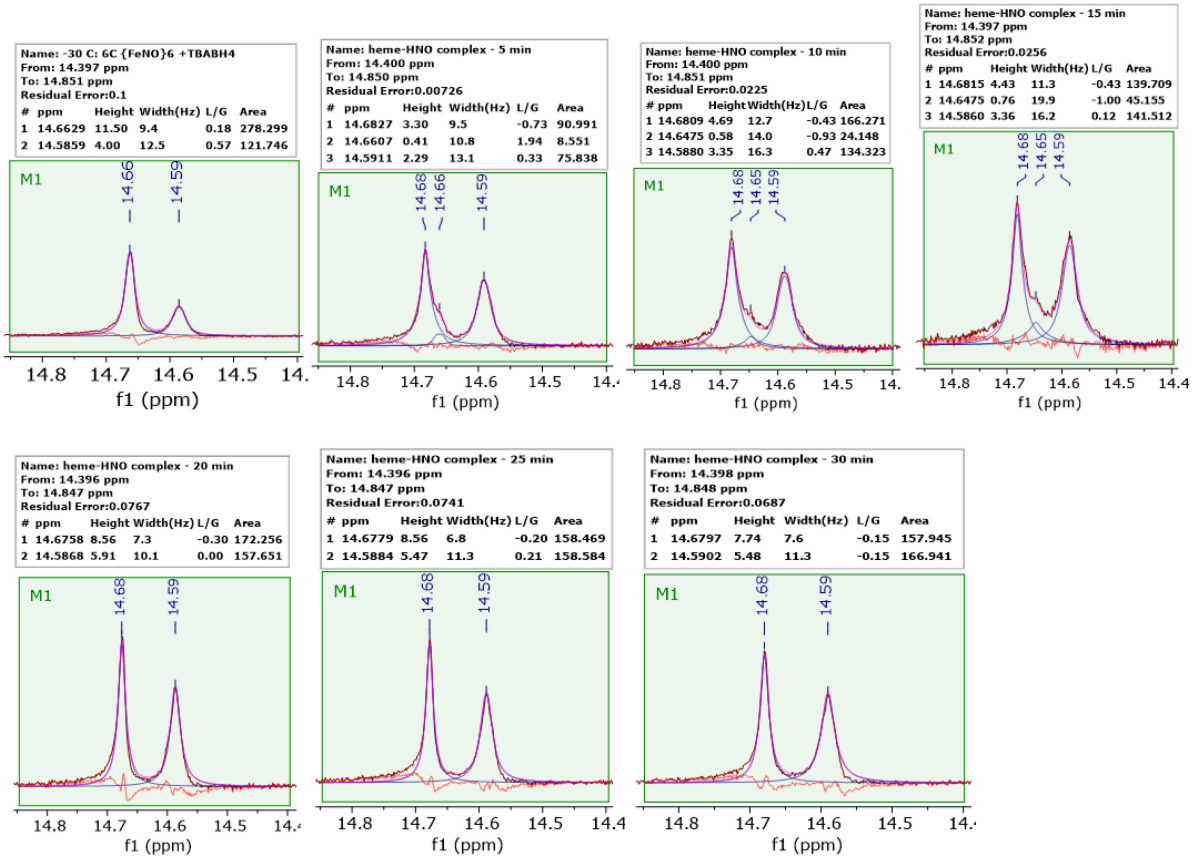

Figure 2.6 Low temperature (-30 °C) ^{1}H-NMR spectra of [Fe(3,5-Me-BAFP)(MI)(NHO)] taken every 5 minutes for 30 minutes. Multiple heme-HNO species appear to equilibrate around 25 minutes.

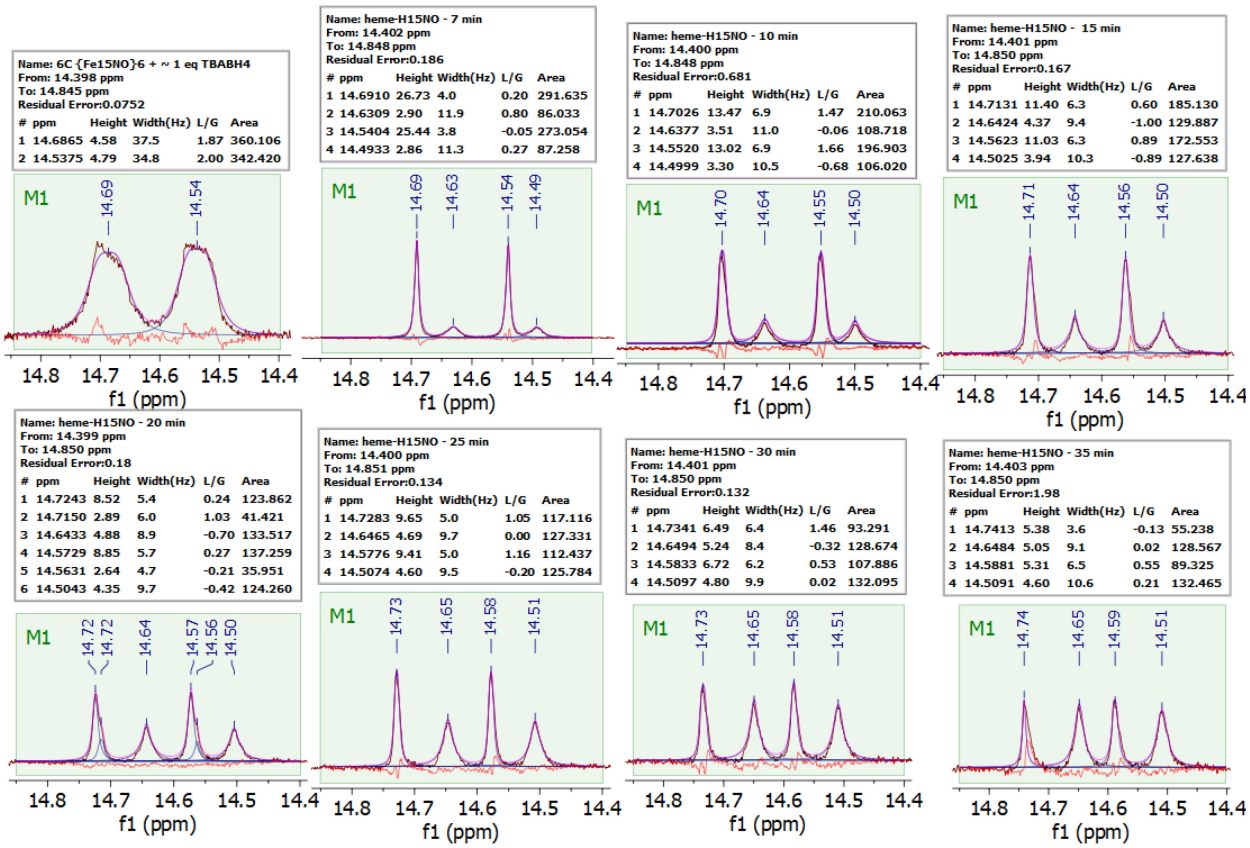

Figure 2.7 Low temperature (-30 °C) ^{1}H-NMR spectra of [Fe(3,5-Me-BAFP)(MI)(^{15}NHO)].

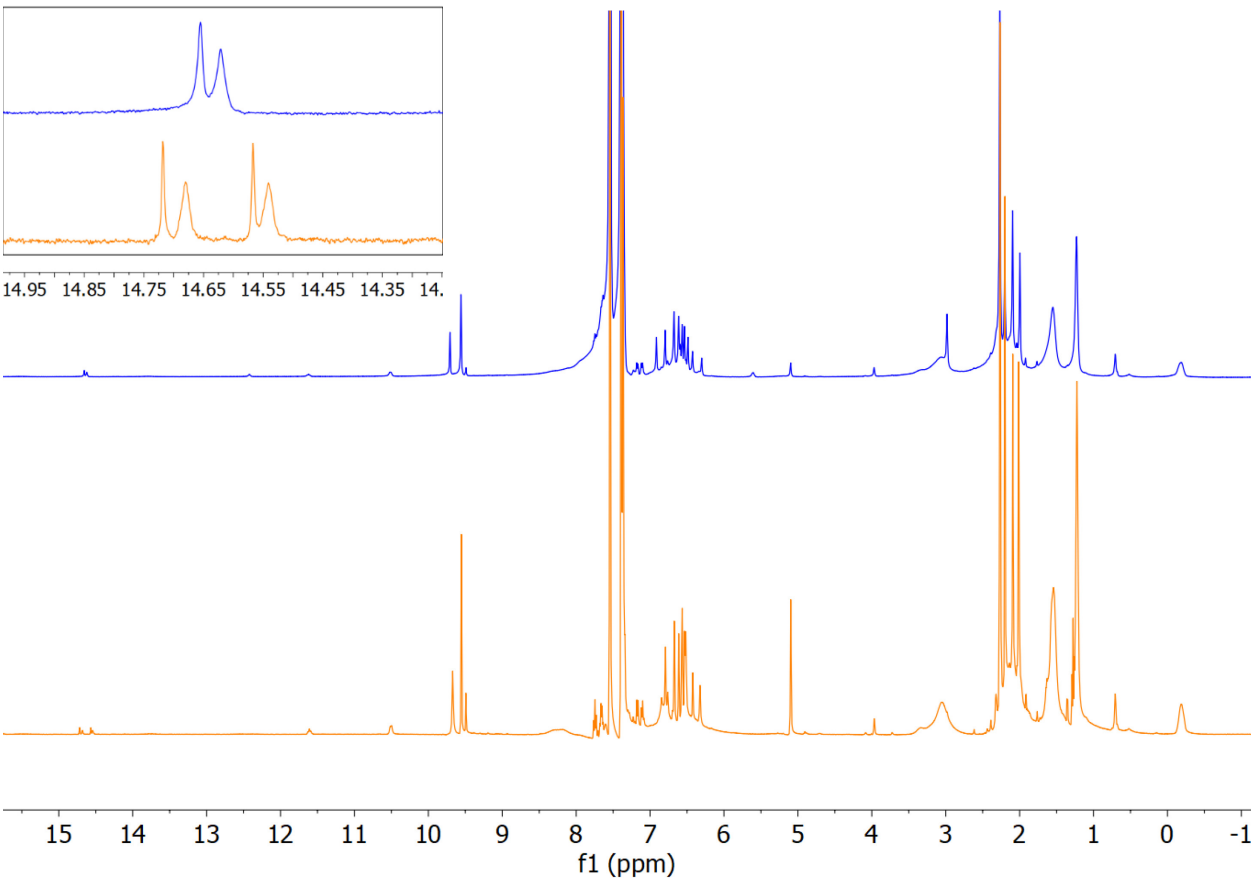

Figure 2.8 ^{1}H-NMR spectra of [Fe(3,5-Me-BAFP)(MI)(NHO)](OTf) (blue) and [Fe(3,5-Me-BAFP)(MI)(^{15}NHO)](OTf) (orange), generated by the addition of ~1 equivalent of [TBA](BH$_4$) to the corresponding ls-{FeNO}^{6} precursor. Both spectra were taken after 25 minutes of reaction time at -25 °C in chlorobenzene-d$_5$. Inset: Two singlets at 14.59 and 14.68 ppm associated with the heme-HNO complex (likely two conformations; blue) are observed that split into two signals each with ^{15}N labeling (14.51 and 14.65 ppm, and 14.58 and 14.73 ppm, respectively). The J-coupling constants associated with the two species are 75 and 70 Hz, respectively.

The temperature-dependence of the ^{1}H-NMR signals of the rotational isomers was further examined using variable-temperature NMR experiments. As shown in **Figure 2.9**, after initial generation of the heme-HNO complex at -30 ^{o}C, a lowering of the temperature to -40 °C leads to further separation of the peaks. Warming to -20 °C, on the other hand, leads to a coalescence of the signals, and subsequent cooling to -40 ^{o}C separates the signals again, in a fully reversible process. These results demonstrate that [Fe(3,5-Me-BAFP)(MI)(NHO)] contains two major conformations of the heme-HNO complex that slowly interconvert at low temperature. Interestingly, when the HNO complex was warmed from -30 ^{o}C to room temperature over the course of 35 minutes, ~30% of the complex remained initially, and then further decomposed within 30 minutes (see **Figure 2.10**). The resulting decomposition product was isolated and investigated by IR spectroscopy. The IR data show a strong N-O stretching band at 1685 cm^{-1} (**Figure 2.11**; confirmed by ^{15}N-labeling), indicating the formation of the corresponding 5C ls-{FeNO}^{7} complex, [Fe(3,5-Me-BAFP)(NO)], as the decomposition product of [Fe(3,5-Me-BAFP)(MI)(NHO)]. This is in line with previous reports of heme-HNO model complexes, which were found to decompose rapidly due to a bimolecular disproportionation reaction:[1,61,63,64]

$$2\ \text{Fe(II)-NHO} \rightarrow 2\ \text{Fe(II)-NO} + \text{H}_2 \qquad (1)$$

resulting in the formation of the corresponding ls-{FeNO}^{7} complex. In the case of [Fe(3,5-Me-BAFP)(MI)(NHO)], this decomposition pathway is greatly slowed down due to the bulky H_2[3,5-Me-BAFP] ligand, generating a heme-HNO model complex with unprecedented stability.

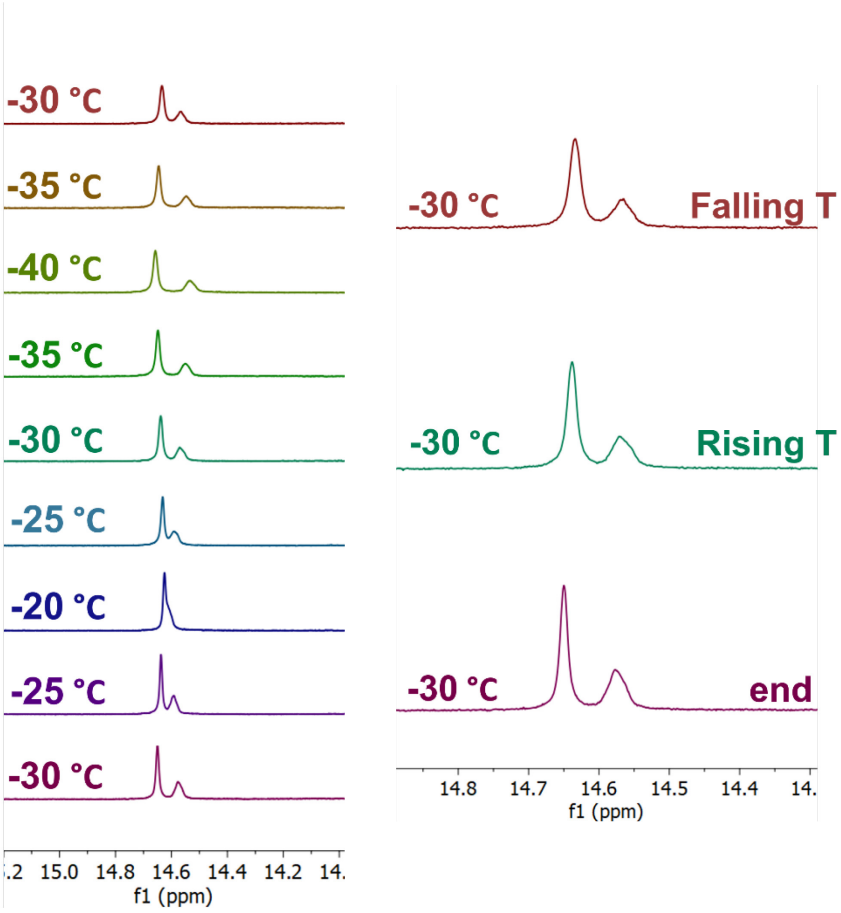

Figure 2.9 Variable temperature ^{1}H-NMR spectra of the HNO signal in [Fe(3,5-Me-BAFP)(MI)(HNO)]. Left: Changes in the signal as the temperature was lowered and raised. Right: Direct comparison of the three individual spectra of the HNO complex at -30 °C, demonstrating that the shifts were fully reversible after the temperature was varied.

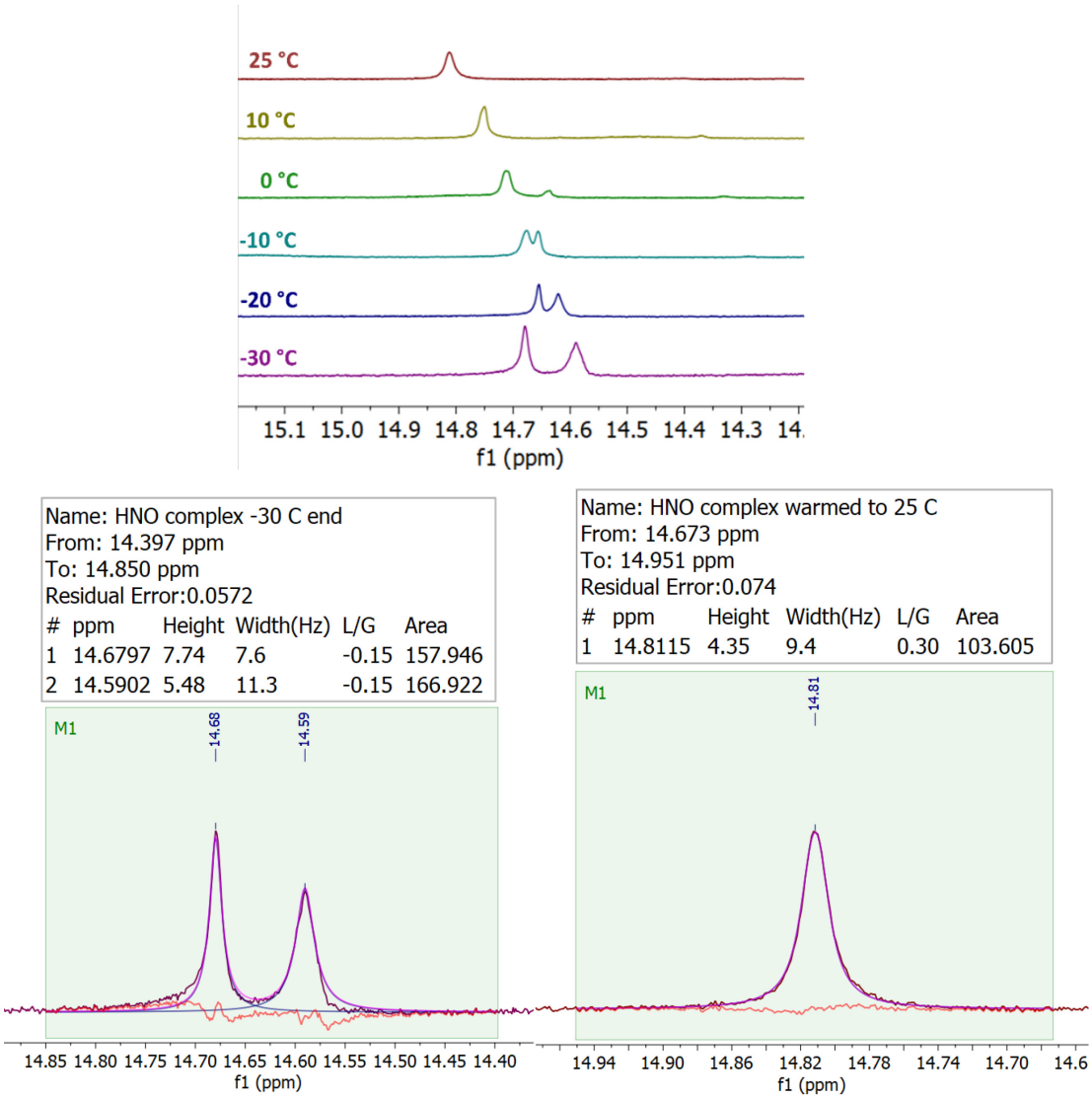

Figure 2.10 Variable temperature ^{1}H-NMR spectra of the HNO signal of [Fe(3,5-Me-BAFP)(MI)(NHO)]. Top: Changes in the signal as the sample was warmed to room temperature. Bottom: Integration of the HNO signal at -30 and 25 °C. These results showed that ~30% of the HNO complex persist initially when the sample was warmed to room temperature.

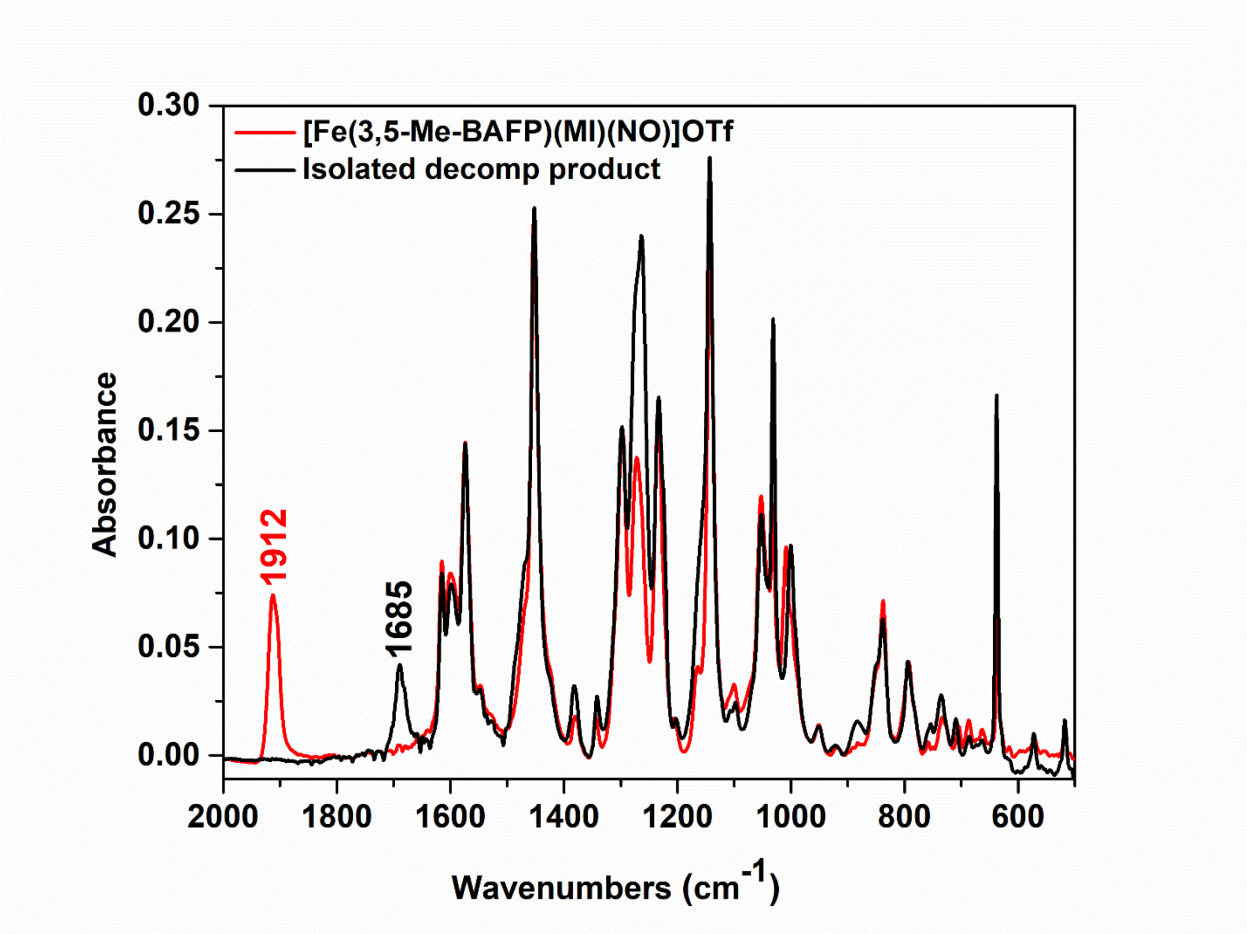

Figure 2.11 Overlay of the IR spectra of the starting complex, [Fe(3,5-Me-BAFP)(MI)(NO)](OTf) (red), and the isolated decomposition product, [Fe(3,5-Me-BAFP)(NO)] (black), after warming the reaction mixture of the ls-{FeNO}^{6} complex and [TBA](BH_4) to room temperature. Both complexes were measured in KBr pellets.

The addition of 1 equivalent of a hydride source to [Fe(3,5-Me-BAFP)(MI)(NO)](OTf) was also monitored by UV-vis spectroscopy, under the same conditions. After the addition of 1 equivalent of [TBA](BH_4), the Soret band of the heme shifts from 436 to 431 nm, indicating the successful formation of the HNO complex (see **Figure 2.12**). The UV-vis spectrum of [Fe(3,5-Me-BAFP)(MI)(NHO)] was comparable to that of Mb(II)-NHO, which had a Soret band at 423 nm and a broad Q band around 550 nm.[55] When the same experiment was performed at room

temperature, the crisp 431 nm Soret band of the heme-HNO complex was not observed. Instead, the 436 nm Soret band of the ls-{FeNO}^{6} precursor shifted to 421 nm, and a small shoulder appeared at 479 nm, indicating formation of the 5C ls-{FeNO}^{7} complex, in agreement with the ^{1}H-NMR results described above (see **Figure 2.12**). Maintaining the temperature of the hydride transfer experiment at -30 °C resulted in a fairly stable heme-HNO complex in solution, with very slow decay of the complex, which was monitored over the course of 5 hours (**Figure 2.13**). This decay process has a first-order rate constant k = 2.05x10^{-4} s^{-1}, corresponding to a half-life of 56 minutes, making [Fe(3,5-Me-BAFP)(MI)(NHO)] the by far most stable heme-HNO model complex (in organic solvents) reported to date.

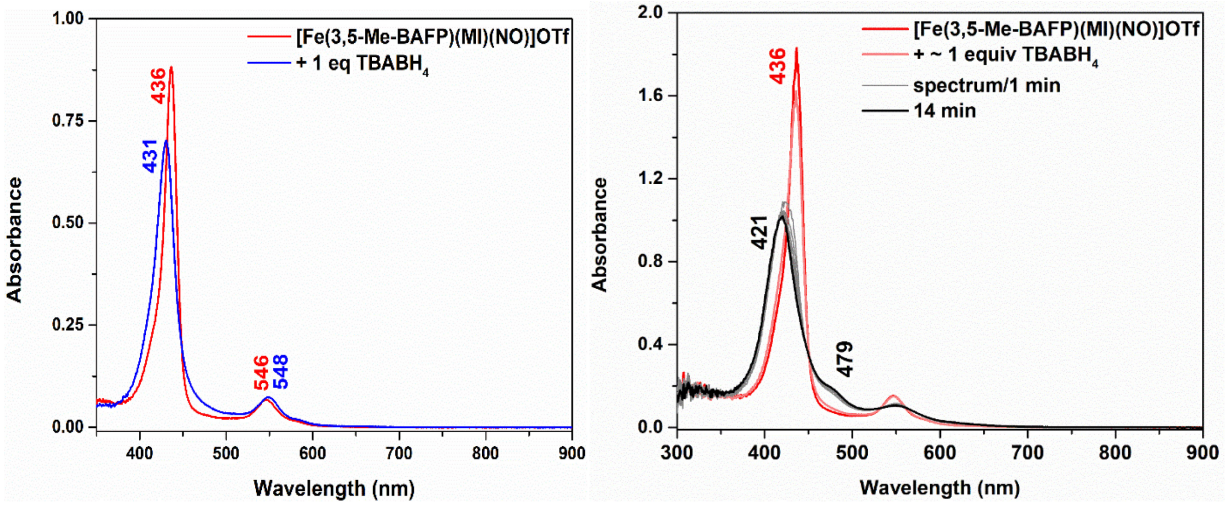

Figure 2.12 UV-vis spectra at -30 °C in chlorobenzene. Left: [Fe(3,5-Me-BAFP)(MI)(NO)](OTf) before (red) and after (blue) addition of ~1 equivalent of [TBA](BH$_4$). Right: ~5 µM [Fe(3,5-Me-BAFP)(MI)(NO)](OTf) before (red) and after (black) addition of ~1 equivalent of [TBA](BH$_4$) at room temperature in chlorobenzene.

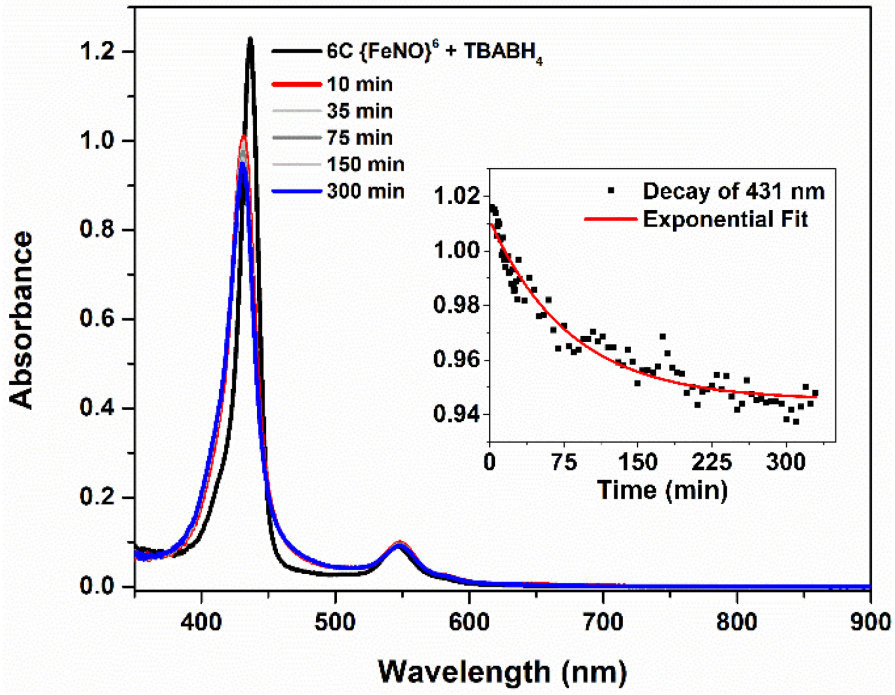

Figure 2.13 UV-vis data monitoring the stability of [Fe(3,5-Me-BAFP)(MI)(NHO)] at -30 ºC over the course of ~5 hours. Inset: a slow decay of the 431 nm Soret band of the heme-HNO complex was observed over 5 hours, with a rate constant of 2.05×10^{-4} s^{-1} and a half-life of 56 minutes.

Due to the remarkable stability of [Fe(3,5-Me-BAFP)(MI)(NHO)] below 0 °C, the decay of the HNO complex was also investigated at 4 °C, to obtain full decomposition to the 5C ls-{FeNO}^{7} complex. At 4 °C, the heme-HNO complex decays with a first-order rate constant k = 1.73×10^{-3} s^{-1} over the course of 30 min, corresponding to a half-life of 6.7 minutes (see **Figure 2.14**). Kinetic decay parameters for previously reported heme-HNO model complexes in organic media could not be determined due to instability, even at lower temperatures. Mb(II)-NHO shows much better stability, likely due to the fact that the HNO ligand is again sterically protected from decomposition.[55] The water-soluble model complex [Fe(TPPS)(NHO)] is stabilized by hydrogen bonding from surrounding water molecules, but still decomposes with a half-life of 41seconds at room temperature, with a first-order rate constant of k = 1.7×10^{-2} s^{-1}.[59]

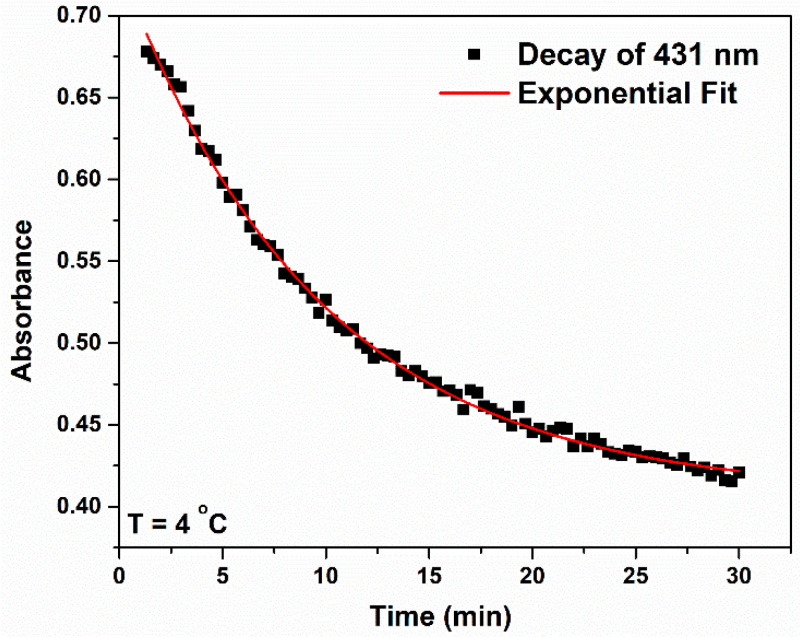

Figure 2.14 UV-vis kinetic decay curve of the complex [Fe(3,5-Me-BAFP)(MI)(NHO)] to yield [Fe(3,5-Me-BAFP)(NO)] at 4 °C in chlorobenzene over the course of 30 m. The decomposition reaction had a first-order rate constant of $k = 1.73 \times 10^{-3}$ s^{-1}, corresponding to a half-life of 6.7 m.

Previously, our group showed the formation of [Fe(3,5-Me-BAFP)(NHO)] by protonation of the corresponding ls-{FeNO}^{8} complex [Fe(3,5-Me-BAFP)(NO)]$^-$, obtained by electrochemical reduction. Despite differences in solvent, coordination number, and method of HNO formation, the 5C complex [Fe(3,5-Me-BAFP)(NHO)] showed a very similar UV-vis absorption spectrum compared to the 6C complex [Fe(3,5-Me-BAFP)(MI)(NHO)] obtained here, with the Soret and Q bands located at 426 and 545 nm, respectively.[63] The complex [Fe(3,5-Me-BAFP)(MI)(NHO)] can be reversibly deprotonated, further confirming that the species obtained after hydride transfer is indeed a heme-HNO complex (see **Figure 2.15**). Upon addition of the base, 1,8-Diazabicyclo[5.4.0]undec-7-ene (DBU), the corresponding ls-{FeNO}^{8} complex [Fe(3,5-Me-BAFP)(NO)]$^-$ was formed, as evident from the split Q band at 535 and 560 nm. The complex can then be reversibly protonated with acetic acid, and the Q band returns to its original

position at 548 nm. In **Figure 2.15**, the UV-vis spectrum of the HNO complex before the addition of DBU is overlaid with the spectrum after treatment with DBU and acetic acid, revealing recovery of the heme-HNO complex, with a small amount of 5C ls-{FeNO}^{7} decomposition product observed in the final spectrum.

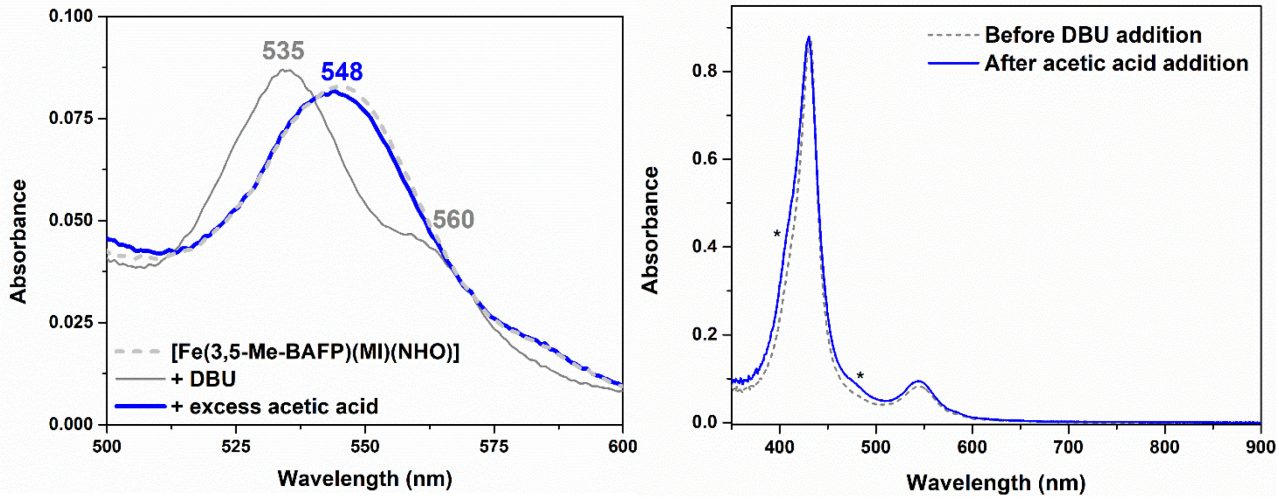

Figure 2.15 Reversible deprotonation of [Fe(3,5-Me-BAFP)(MI)(NHO)] monitored by UV-vis spectroscopy at -30 °C in chlorobenzene. Left: Addition of the base DBU; gray) to the complex [Fe(3,5-Me-BAFP)(MI)(NHO)] (dotted light gray) and reprotonation with acetic acid (blue). Right: The starting heme-HNO complex (dotted light gray) and the resulting complex after reprotonation by acetic acid (blue). The asterisks indicate signals from a small amount of decomposition product, the 5C ls-{FeNO}^{7} complex.

2.3.2 Vibrational Characterization of [Fe(3,5-Me-BAFP)(MI)(NHO)] and DFT Analysis.

Isolation of the heme-HNO complex as a solid was typically achieved by cooling the precursor complex [Fe(3,5-Me-BAFP)(MI)(NO)](OTf) to temperatures between -30 and -40 °C and adding 1 equivalent of [TBA](BH_4). After 1 minute, the resulting heme-HNO complex was precipitated with dry pentanes, allowing about 30 minutes for the process to complete. The precipitated complex was then filtered at room temperature and collected for rigorous spectroscopic characterization and solid-state stability studies. The heme-HNO complex was in

fact quite stable in the solid state at room temperature under anaerobic conditions, as the 431 nm Soret band persists over the course of one month (see **Figure 2.16**).

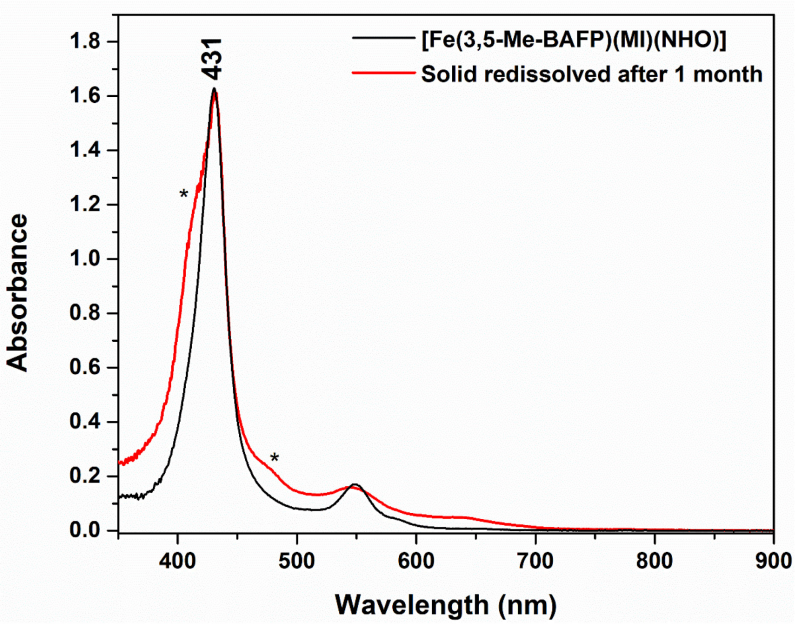

Figure 2.16 UV-vis spectrum of [Fe(3,5-Me-BAFP)(MI)(NHO)] at -30 °C, taken before and after storing the solid material for one month. The asterisks indicate the presence of the decomposition product, [Fe(3,5-Me-BAFP)(NO)].

Immediately after isolation, solid [Fe(3,5-Me-BAFP)(MI)(NHO)] was characterized by IR spectroscopy. As shown in **Figure 2.17**, three new signals appear at 1685, 1420, and 1393 cm^{-1}, which shifted to 1654 and 1378 cm^{-1} upon ^{15}N labeling. As previously stated, the 1685 cm^{-1} signal corresponds to the N-O stretch of the 5C ls-$\{FeNO\}^7$ decomposition product. More exciting was the observation of the new signals at 1393 and 1420 cm^{-1}, which were assigned to the N-O stretch of the coordinated HNO ligand in [Fe(3,5-Me-BAFP)(MI)(NHO)]. The splitting of the N-O stretch in the natural abundance isotopes compound into two components is either caused by Fermi resonance or is due to accidental, weak mixing with some other normal mode that is very close in energy, evident from the fact that the two signals collapse into one band at 1378 cm^{-1} in the ^{15}N-labeled compound and at 1405 cm^{-1} in the deuterated (DNO) complex (see **Figure 2.17**). The N-

O stretching frequency of [Fe(3,5-Me-BAFP)(MI)(NHO)] was consistent with those of other HNO complexes reported in the literature, as shown in **Table 2.2**, which were typically observed in the 1380-1400 cm^{-1} range.

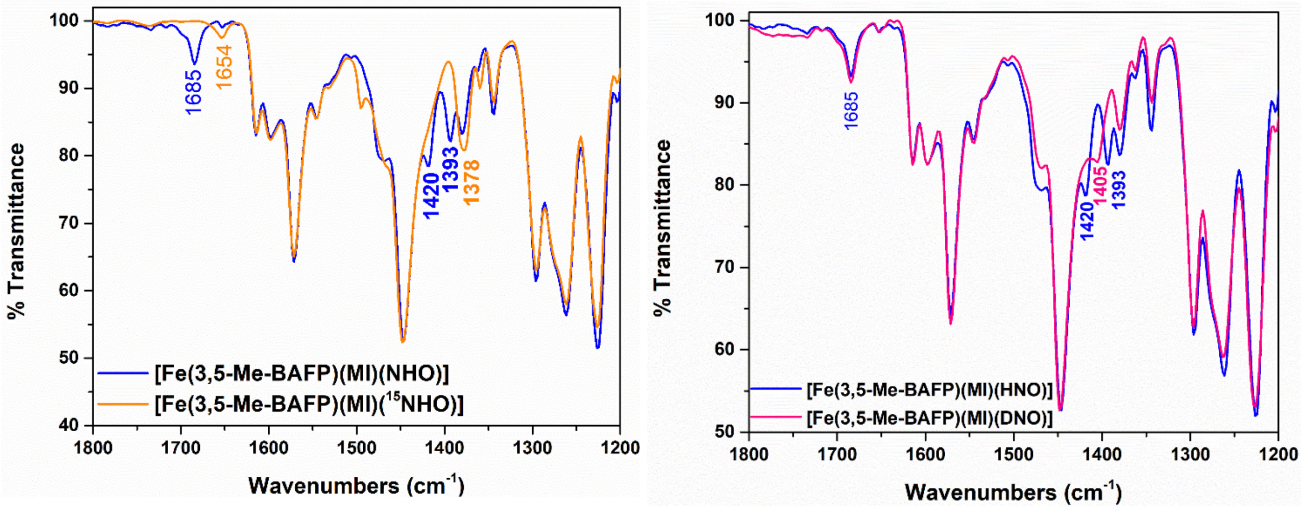

Figure 2.17 ATR-FTIR of isotopically labeled heme-HNO complexes as a solid, measured at room temperature. Left: [Fe(3,5-Me-BAFP)(MI)(NHO)] (blue) and [Fe(3,5-Me-BAFP)(MI)(^{15}NHO)] (orange). Right: Overlay of [Fe(3,5-Me-BAFP)(MI)(NHO)] (blue) and the deuterated complex [Fe(3,5-Me-BAFP)(MI)(NDO)] (pink). The latter complex was generated according to the procedure, using [TBA](BD$_4$) in the reaction with the ls-{FeNO}^{6} complex.

Table 2.2. Spectroscopic properties of heme-HNO complexes

Complex	δ (J_{NH}) [ppm]	νFe-N(O) [cm^{-1}]	δFe-N-O [cm^{-1}]	νN-O [cm^{-1}]	Ref.
[Fe(3,5-Me-BAFP)(MI)(NHO)]	14.59 (75)/ 14.68 (70)	644	461	1393/(1420)	*t.w.*
Mb(II)-NHO	14.99 (72)	651	-	1385	55,92
[Fe(OEP)(5-MI)(NHO)]	13.99 (76)	-	-	1383	64,89
[Fe(OEP)(MI)(NHO)]	13.72 (77)	-	-	1388	89
[Fe(PPDME)(5-MI)(NHO)]	13.93 (77)	-	-	1382	89
[Fe(PPDME)(MI)(NHO)]	13.64 (77)	-	-	1384	89
[Fe(TTP)(5-MI)(NHO)]	14.26 (76)	-	-	1381	89
[Fe(TTP)(MI)(NHO)]	14.02 (76)	-	-	1389	89

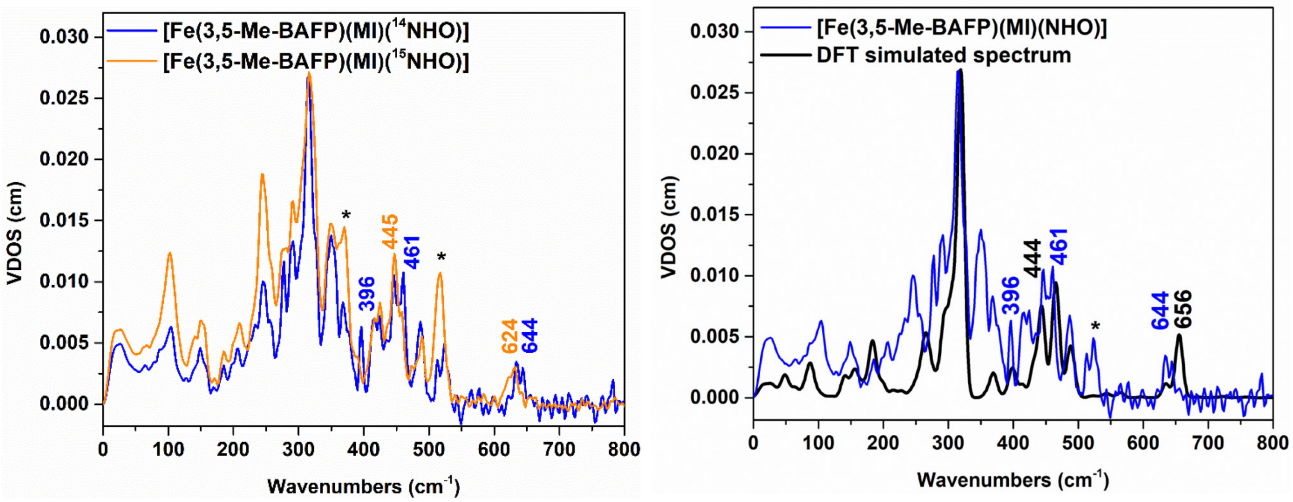

Figure 2.18 Left: NRVS-derived vibrational density of states (VDOS) for [^{57}Fe(3,5-Me-BAFP)(MI)(NHO)] (blue) and [^{57}Fe(3,5-Me-BAFP)(MI)(^{15}NHO)] (orange), both isolated as a solid. Right: Calculated (BP86/TZVP) NRVS VDOS (black), overlaid with the experimental data for [^{57}Fe(3,5-Me-BAFP)(MI)(NHO)] (blue). Signals belonging to [^{57}Fe(3,5-Me-BAFP)(^{15}NO)] are indicated with asterisks in both panels.

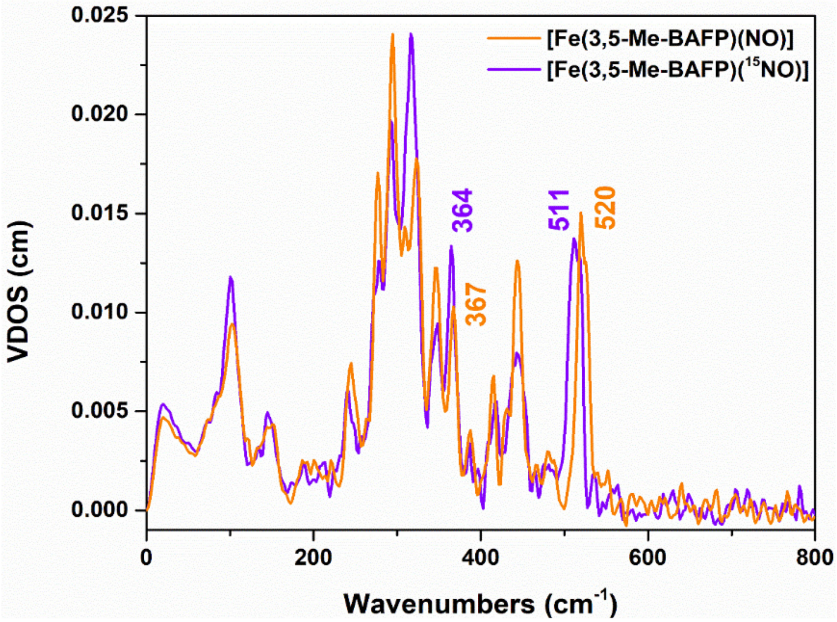

Figure 2.19 NRVS-derived vibrational density of states (VDOS) for solid samples of [^{57}Fe(3,5-Me-BAFP)(NO)] (orange) and [^{57}Fe(3,5-Me-BAFP)(^{15}NO)] (purple).

Further vibrational characterization of [Fe(3,5-Me-BAFP)(MI)(NHO)] was performed using NRVS, to determine the Fe-N stretch of the complex. In previous work, Farmer and coworkers had reported the Fe-N stretch of Mb(II)-NHO at 651 cm^{-1}, based on resonance Raman data, but the rather weak signal observed in this case necessitates confirmation by measurements on other compounds and/or using other techniques.[92] As shown in **Figure 2.18**, two ^{15}N-isotope sensitive signals were observed in the NRVS data of [^{57}Fe(3,5-Me-BAFP)(MI)(NHO)] at 461 and 644 cm^{-1}, which shifted to 444 and 624 cm^{-1} in [^{57}Fe(3,5-Me-BAFP)(MI)(^{15}NHO)]. There appeared to be an additional signal at 396 cm^{-1} that disappears upon isotopic labeling. Unfortunately, the heme-HNO complex cannot be isolated without the presence of some amount of the decomposition product, [Fe(3,5-Me-BAFP)(NO)]. This complex showed intense signals at 520 and 367 cm^{-1} (511 and 364 cm^{-1} in the ^{15}NO compound) that correspond to the Fe-NO stretch and Fe-N-O bend, respectively (see **Figure 2.19**). This is a particular problem for the ^{15}N-labeled compound, and the corresponding signals in **Figure 2.18**, top are indicated with an asterisk.

To assign the low-energy vibrational features of [Fe(3,5-Me-BAFP)(MI)(NHO)], DFT calculations were employed. For this purpose, the H_2[3,5-Me-BAFP] ligand was simplified by removing the bottom pickets surrounding the bound 1-methylimidazole ligand and including the top pickets shielding the bound HNO moiety. This structure was then fully optimized using BP86/TZVP, and the resulting optimized structure is shown in **Figure 2.20**. With respect to the Fe-HNO unit, the Fe-NHO, HN-O, H-NO bond lengths are predicted to be 1.79, 1.24, 1.05 Å, respectively, with an Fe-N-O angle of 131°. These values agree well with EXAFS data obtained for Mb(II)-NHO, which display Fe-NHO and HN-O bond distances of 1.82 and 1.24 Å, respectively, with an Fe-N-O angle of 131°. The average Fe-N(porphyrin) and Fe-N(MI) bond lengths are calculated to be 2.01 and 2.10 Å, respectively, again very similar to those reported for

Mb(II)-NHO, 2.00 and 2.09 Å, respectively. Frequency calculations performed on this optimized structure predict an N-O stretching frequency of 1456 cm^{-1} that shifts to 1428 cm^{-1} upon ^{15}N-isotopic labeling. These values are in good agreement with the experimental N-O stretch of [Fe(3,5-Me-BAFP)(MI)(NHO)], observed at 1393/(1420) cm^{-1} and 1378 cm^{-1} with ^{15}N. As shown in **Figure 2.18**, bottom, the calculations also reproduce the experimental NRVS data well. In the calculations, the Fe-N stretch and the Fe-N-O bend are predicted to be 656 and 444 cm^{-1} respectively. Upon isotopic labeling, the Fe-N stretch shifts to 630 cm^{-1}, while the Fe-N-O bend splits into multiple modes between 413 and 430 cm^{-1}. Based on these results, the experimental features at 644 and 461 cm^{-1} can be assigned to the Fe-N stretch and the Fe-N-O bend, respectively, of the bound HNO ligand. The experimental band at 396 cm^{-1} could correspond to the out of plane N-H bend of the bound HNO ligand, since it appears to be shifting upon isotope labeling, but this assignment remains tentative.

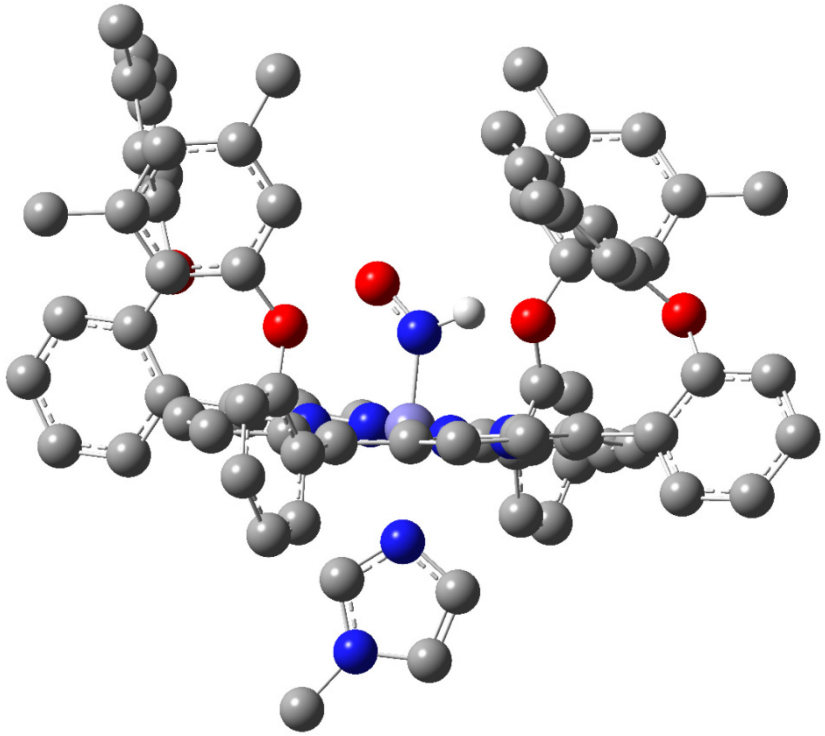

Figure 2.20 BP86/TZVP optimized structure of a simplified version of [Fe(3,5-Me-BAFP)(MI)(NHO)], where the pickets on the face of the heme where MI binds have been omitted.

2.3.3 Reactivity of [Fe(3,5-Me-BAFP)(MI)(NHO)] with NO Gas: Quantification of N_2O.

Gas headspace N_2O yield measurements were performed to evaluate the reactivity of [Fe(3,5-Me-BAFP)(MI)(NHO)] with excess NO gas at -30 °C in chlorobenzene. For N_2O analysis, the reaction mixture of [Fe(3,5-Me-BAFP)(MI)(NHO)] and NO gas was stirred at -30 °C for 15 minutes before warming to room temperature, followed by extraction of the gas headspace of the reaction flask. An analogous experiment was followed with UV-vis spectroscopy, as shown in **Figure 2.21**, to ensure that 15 minutes is an appropriate reaction time between the heme-HNO complex and excess NO gas at low temperature. Measurements were taken in quadruplicate and converted into μmols of N_2O using an appropriate calibration curve (see **Figure 2.22**). In these experiments, N_2O is detected in the gas headspace in 91±10% yield (see **Figure 2.23**), showing that the heme-HNO complex is catalytically competent to mediate quantitative N_2O formation when reacted with NO gas. This N_2O yield is indirectly supported by EPR where 30% of the signal accounts for the $\{FeNO\}^7$ decomposition product, as shown in **Figure 2.24**. Using IR spectroscopy, an isotope scrambling experiment was performed to provide further evidence that the heme-HNO complex plays a role in N_2O formation. As shown in **Figure 2.25**, [Fe(3,5-Me-BAFP)(MI)(^{15}NHO)] reacts with excess ^{14}NO gas, which generated singly labeled N_2O gas (either ^{15}NNO or N^{15}NO, or both), demonstrating that NO attacks the coordinated HNO ligand. This reaction was repeated at room temperature (including the generation of the heme-HNO complex), showing a 28±8% yield of N_2O (see **Figure 2.26**). The reason for the significantly lower N_2O yield at room temperature is the reduced stability of [Fe(3,5-Me-BAFP)(MI)(NHO)] under these conditions. This is in agreement with the ^{1}H-NMR experiments, which show that up to ~30% of the heme-HNO complex are present right after warming the sample to room temperature (see **Figure 2.10**).

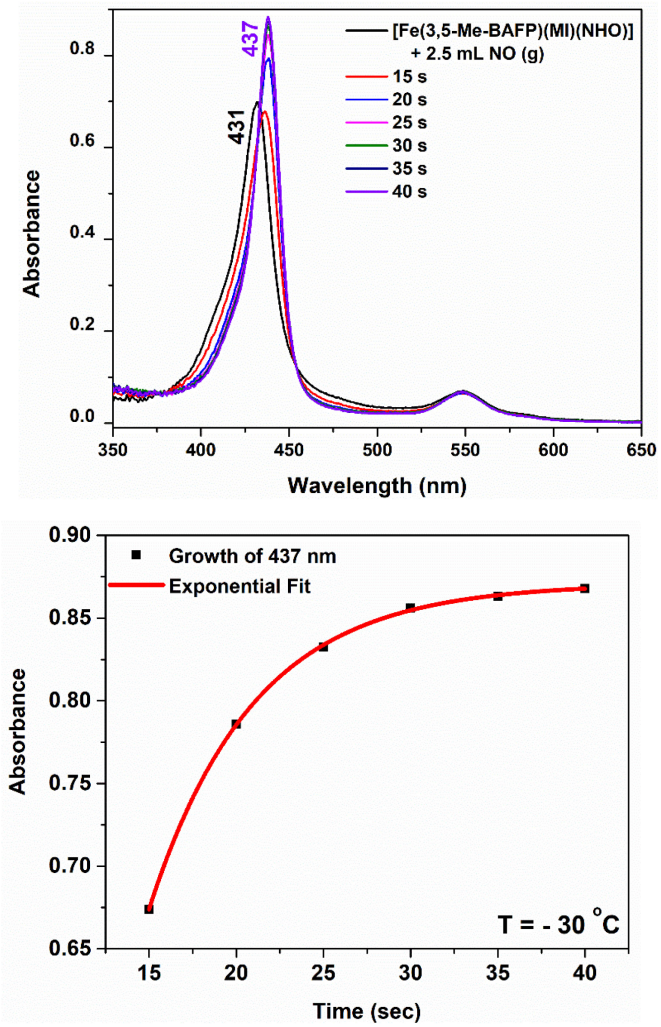

Figure 2.21 Top: Overlay of the UV-vis spectra of ~5 μM [Fe(3,5-Me-BAFP)(MI)(NHO)] before and after reaction with excess NO gas. Bottom: kinetic trace at 437 nm and single-exponential fit.

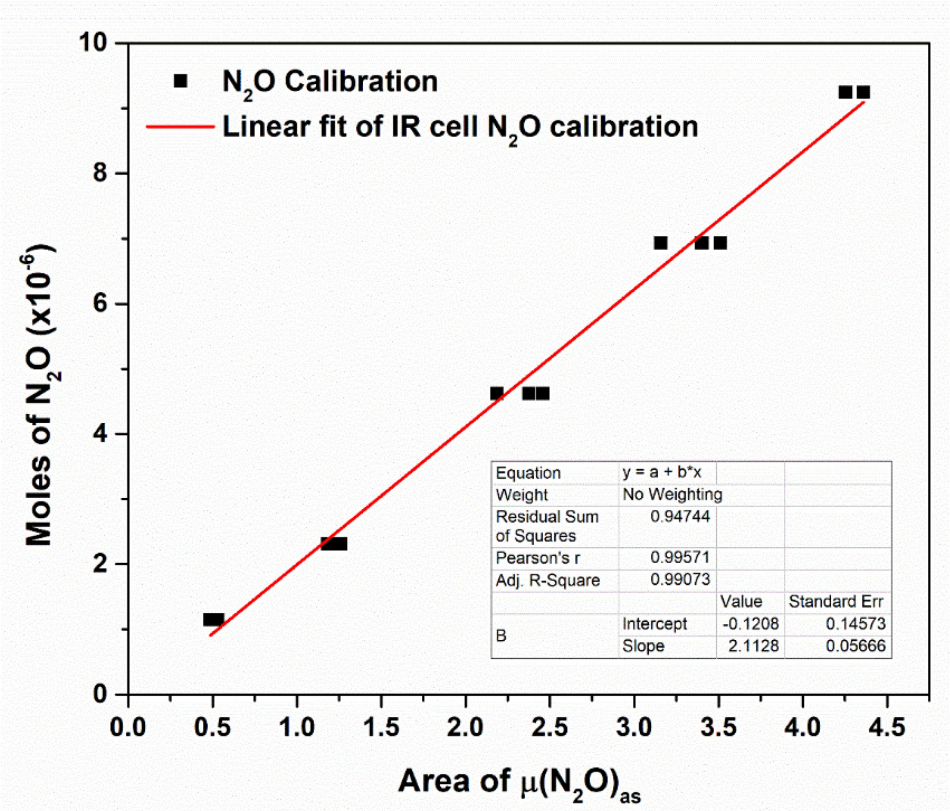

Figure 2.22 N_2O calibration curve generated using Piloty's acid (see Experimental Section for details).

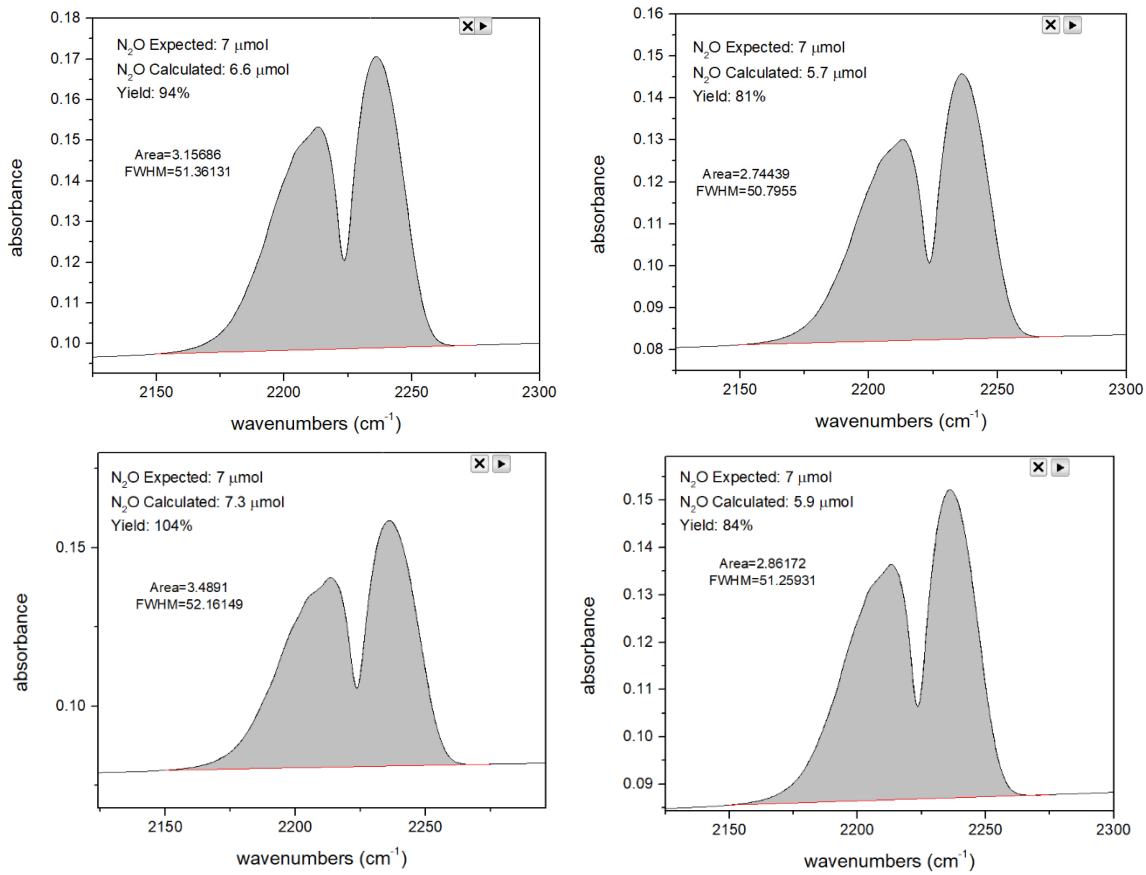

Figure 2.23 Gas headspace IR spectra of the reaction of 7 µM (based on the ls-{FeNO}^{6} starting material) [Fe(3,5-Me-BAFP)(MI)(NHO)] with excess NO gas at -30 °C. After stirring the heme-HNO complex with excess NO gas at low temperature for 15 minutes and warming to room temperature for 35 minutes, N_2O was detected with an average yield of 91±10%.

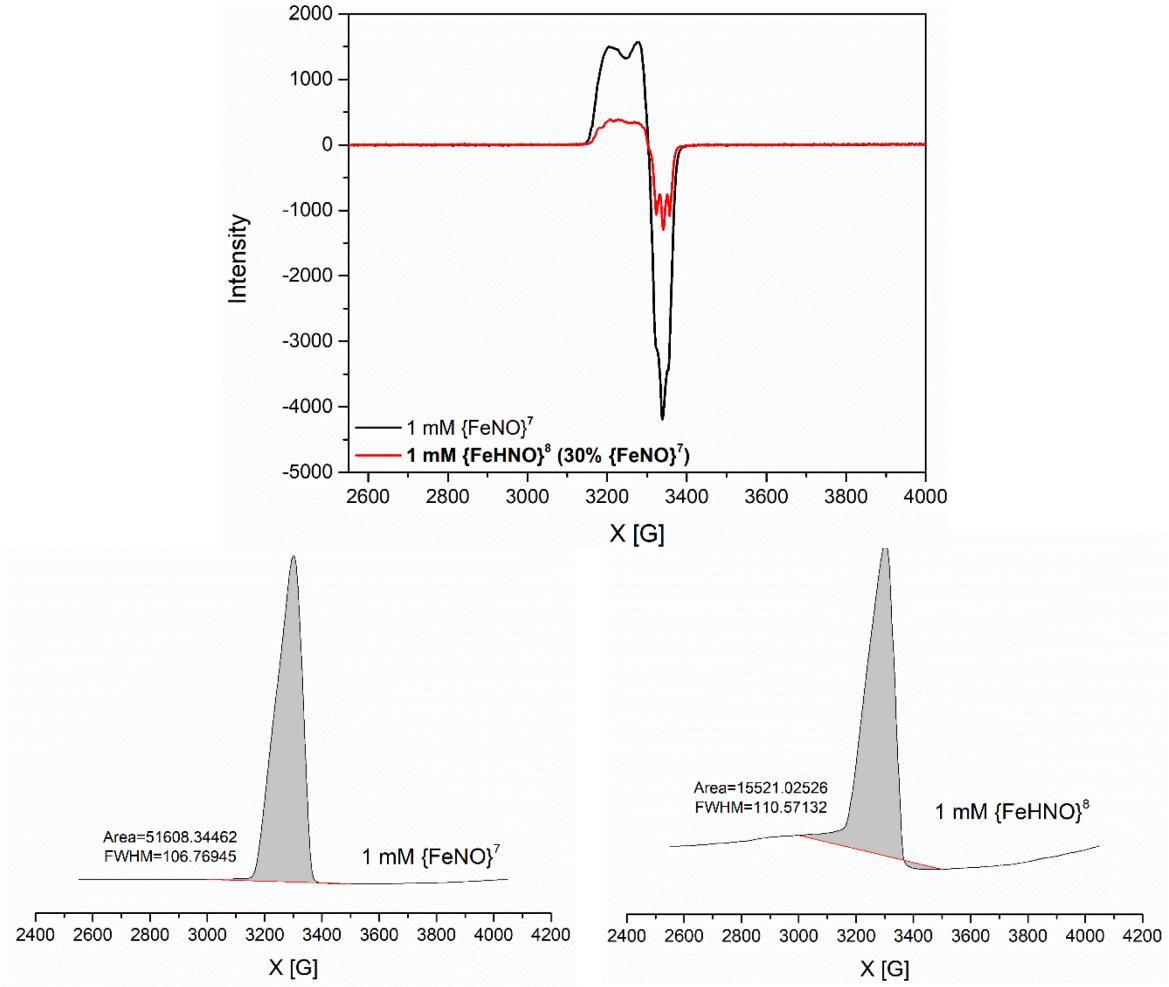

Figure 2.24 EPR quantification of the ls-{FeNO}^{7} decomposition product after addition of 1 equivalent of [TBA](BH$_4$) to the 6C ls-{FeNO}^{6} starting complex at -30 °C. Top: Overlay of the EPR spectra of the 1 mM ls-{FeNO}^{7} standard and 1 mM {FeHNO}^{8} reaction product ~50 seconds after hydride addition. Bottom: Integration of the EPR signal of each complex to quantify the amount of ls-{FeNO}^{7} present after the reaction with [TBA](BH$_4$). The amount of ls-{FeNO}^{7} decomposition product present in the sample of the heme-HNO complex (30%) is somewhat inflated compared to the UV-vis and ^{1}H-NMR measurements, due to warming of the EPR sample in the process of removing it from the glovebox, which facilitates decomposition.

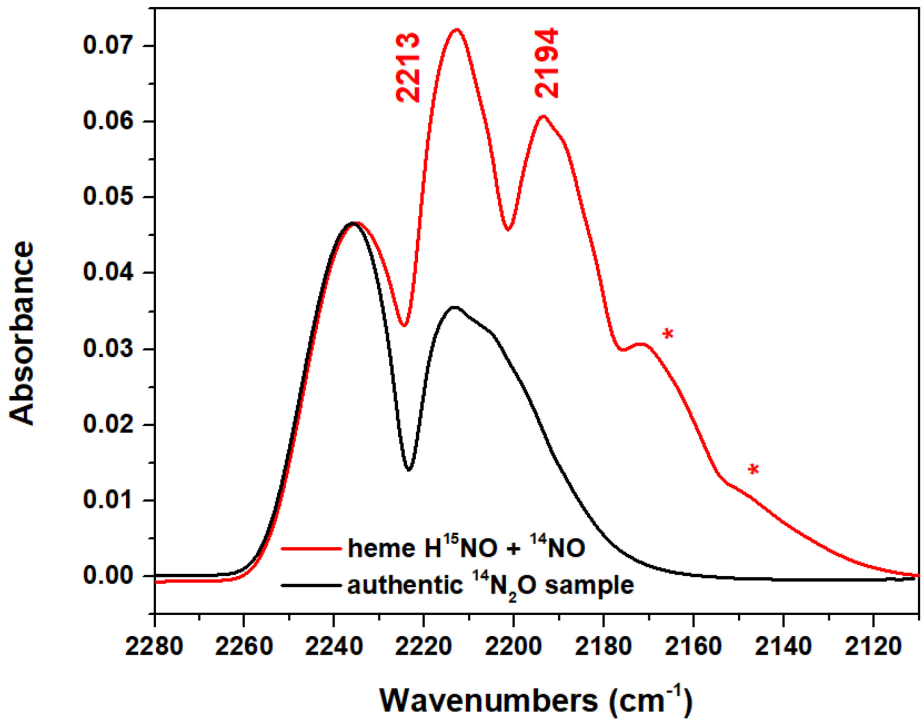

Figure 2.25 Gas headspace IR spectral overlay of the reaction of [Fe(3,5-Me-BAFP)(MI)(^{15}NHO)] with excess ^{14}NO gas at -30 °C (red) and natural abundance N_2O (black). The asterisks indicate some $^{15}N_2O$ formation.

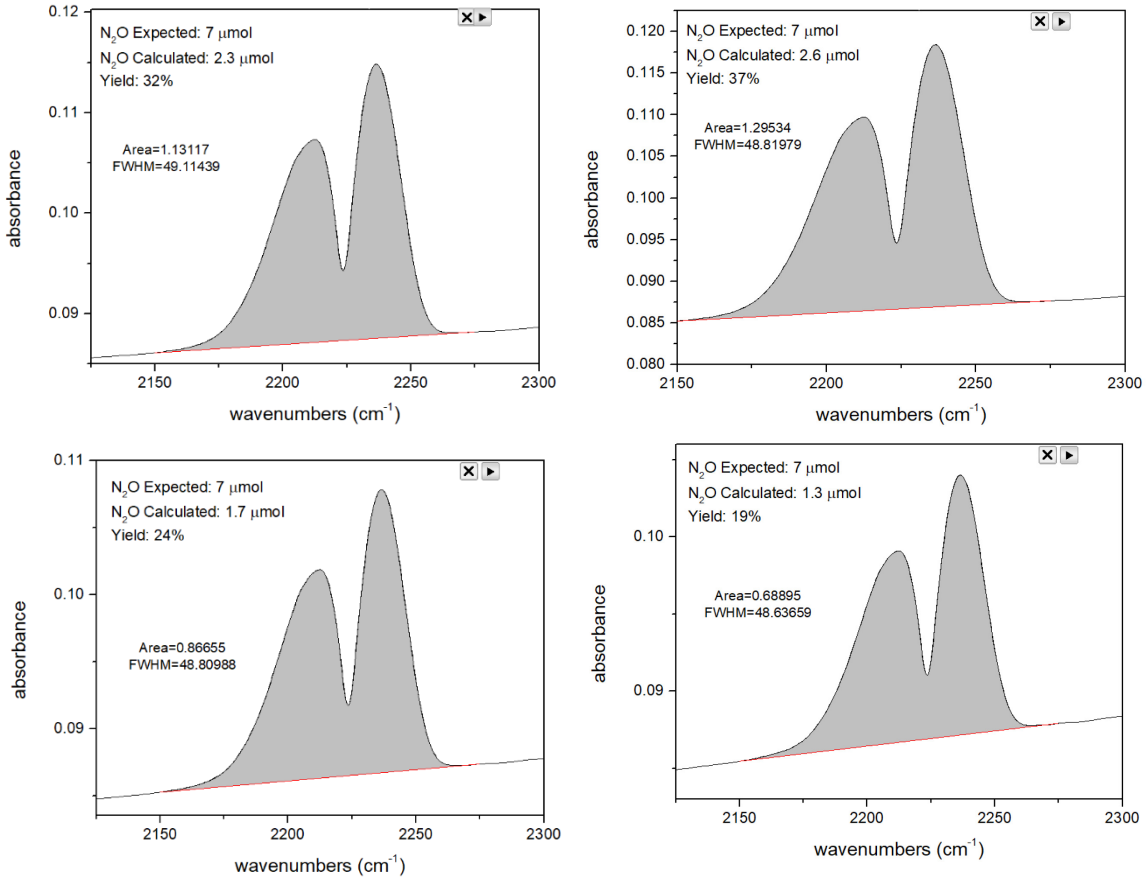

Figure 2.26 Gas headspace IR spectra of the reaction of 7 µM (based on the ls-{FeNO}^{6} starting material) [Fe(3,5-Me-BAFP)(MI)(NHO)] with excess NO gas at room temperature. After stirring the heme-HNO complex with excess NO gas at room temperature for 50 m, N_2O is made with an average yield of 28±8%. This result is in agreement with the ^{1}H-NMR data in **Figure 2.10**, showing that after warming the reaction mixture of the ls-{FeNO}^{6} complex and [TBA](BH_4) to room temperature, about 30% of the heme-HNO complex persist (before further decomposing over time).

A series of control experiments were conducted to ensure that the heme-HNO complex is the only species to react with NO gas to form N_2O. No N_2O was formed during heme-HNO decomposition, nor when excess NO is added to either the 6C ls-{FeNO}^{6} starting complex or the ls-{FeNO}^{7} decomposition product. To account for over addition of [TBA](BH_4), an additional experiment was conducted with 1 equivalent of [TBA](BH_4) and NO gas, resulting in 24±8% of N_2O formed (see **Figure 2.27**). This shows that even in the case where a small amount of excess

[TBA](BH4) would be present, for example an extra 10%, this would only minimally contribute to the total N_2O produced (in this example, this would add an additional 2-3% to the total N_2O yield).

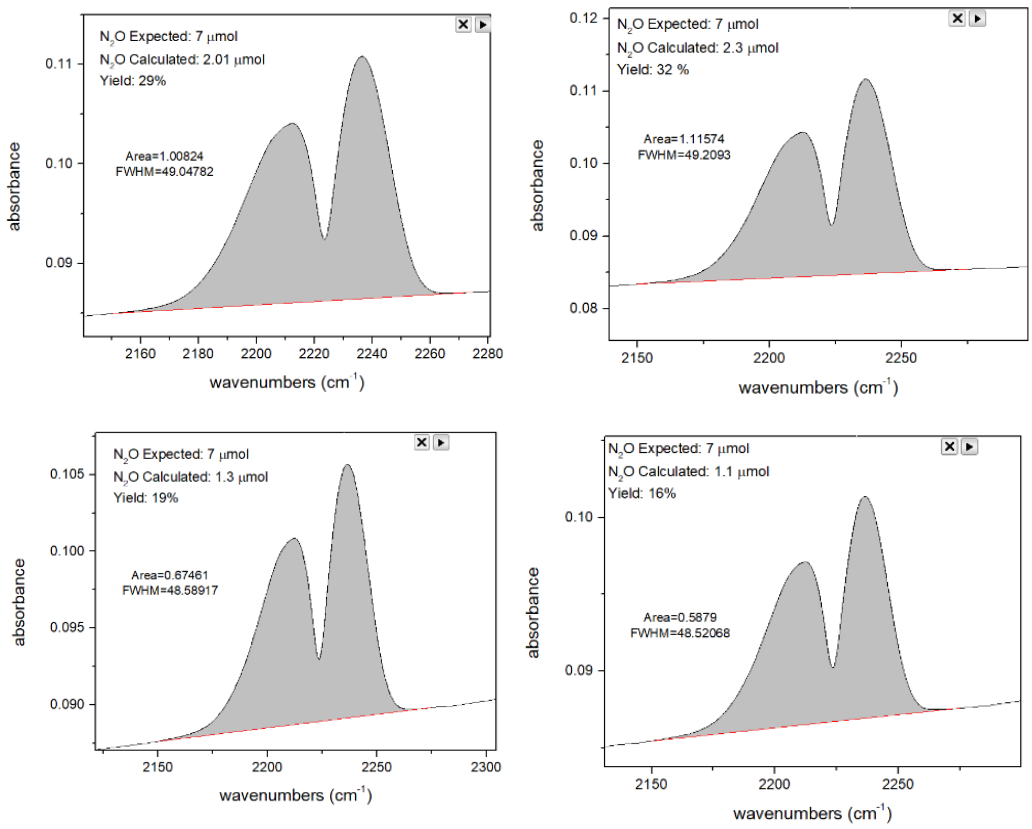

Figure 2.27 Gas IR spectra of the reaction of 7 μM [TBA](BH4) with NO gas for 50 minutes at room temperature. N_2O is made with an average yield of 24±8%.

The reaction of [Fe(3,5-Me-BAFP)(MI)(NHO)] and NO gas was further investigated using UV-vis spectroscopy, using either excess or stoichiometric amounts of NO gas, added to the reaction mixture about 1 minute after hydride addition. Upon the addition of excess NO, the 431 nm Soret band of the HNO complex shifts to 437 nm, indicating that the product of the reaction of [Fe(3,5-Me-BAFP)(MI)(NHO)] and NO gas is the ferric heme, which has a high affinity for NO and binds excess NO in solution to reform a six-coordinate ls-$\{FeNO\}^6$ complex. We suspect that

after the reaction, N_2O is released, and the ferric heme-OH complex forms. This complex then reacts with NO to form either [Fe(3,5-Me-BAFP)(OH)(NO)] or $[Fe(3,5\text{-Me-BAFP})(MI)(NO)]^+$. Assuming that MI does not displace the hydroxo ligand at the low equivalents of MI present in the reaction mixtures, the initial product would be [Fe(3,5-Me-BAFP)(X)(NO)]. Due to this uncertainty, we do not specify the sixth ligand (X) in the ls-$\{FeNO\}^6$ product in **Figure 2.28**. Interestingly, when the experiment was repeated with the addition of exactly 1 equivalent of NO gas, the reaction only proceeded minimally and instead, HNO decomposition became the dominant process over time at low temperature. Further experiments show that it takes about 4 equivalents of NO under our reaction conditions to observe the clean shift of the Soret band to 437 nm, indicating formation of the 6C ls-$\{FeNO\}^6$ complex (**Figure 2.29**). This interesting result is further analyzed in the Discussion section.

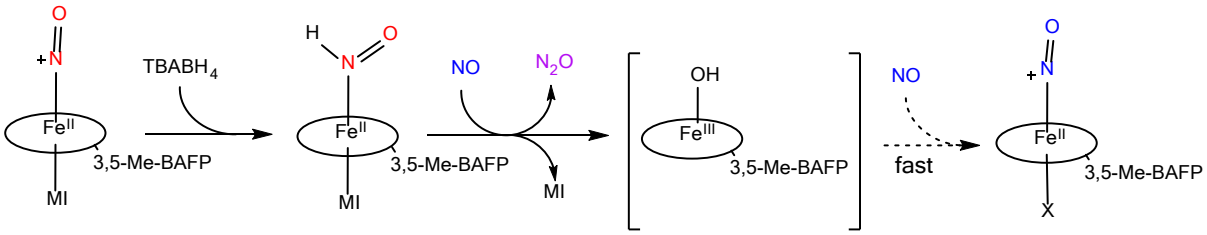

Figure 2.28 Reaction scheme of [Fe(3,5-Me-BAFP)(MI)(NO)](OTf) with ~1 equivalent of [TBA](BH_4) to form [Fe(3,5-Me-BAFP)(MI)(NHO)], followed by the addition of excess NO to reform the 6C ls-$\{FeNO\}^6$ complex and produce N_2O.

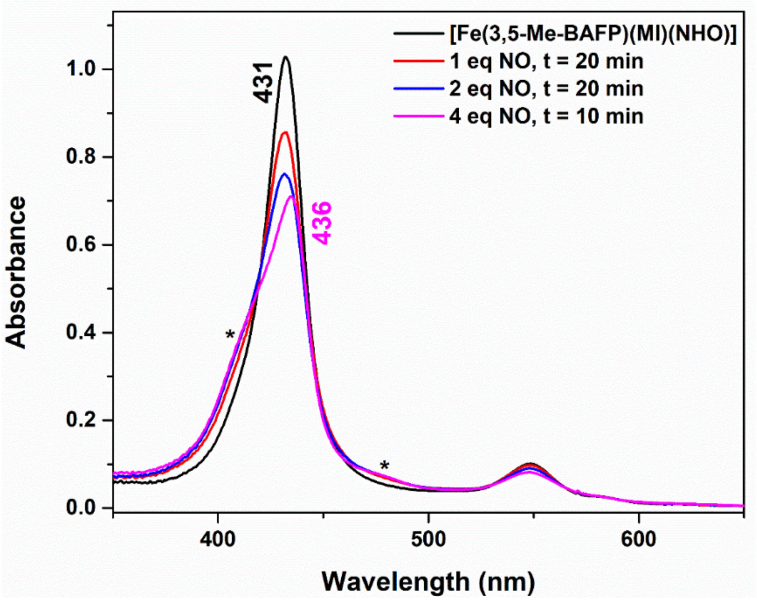

Figure 2.29 Overlay of the UV-vis spectra of ~5 μM [Fe(3,5-Me-BAFP)(MI)(NHO)] reacted with a stoichiometric amount of NO gas at -30 °C in chlorobenzene. Up to 4 equivalents of NO gas are needed for the heme-HNO complex to react. Prior to reaction with NO gas, the complex shows some decomposition, to form [Fe(3,5-Me-BAFP)(NO)], as indicated by the asterisks. The 4 equivalents spectrum shows the Soret band at 436 nm (not 437 nm, likely due to the presence of multiple species with overlapping Soret bands in the sample).

2.4 Discussion

In this work, the formation of [Fe(3,5-Me-BAFP)(MI)(NHO)] was accomplished by the addition of a moderately strong hydride donor, [TBA](BH_4), to the low-spin (ls) $\{FeNO\}^6$ complex [Fe(3,5-Me-BAFP)(MI)(NO)](OTf) in organic solvent at -30 °C. This complex has the typical Fe(II)-NO^+ type electronic structure of ls-$\{FeNO\}^6$ heme complexes with an electrophilic NO^+ ligand.[1,47,93-96] This reaction is analogous to the mechanism of Cyt P450nor, where NAD(P)H performs hydride transfer to an electrophilic Fe(II)-NO^+ complex formed in the first step of the reaction.[40] In the literature, this method has shown limited success when applied to model complexes with hemes like H_2[TPP] and H_2[OEP] and their simple derivatives, as heme-HNO complexes are quite unstable towards bimolecular disproportionation (see eqn. 1) and therefore often only form in low

yields.[64,89] Hence, a detailed characterization and reactivity studies of heme-HNO complexes have been difficult to carry out. In contrast, we were able to make the desired heme-HNO complex cleanly and in high yield at -30 °C, with a half-life of about 1 hour under these conditions, and good stability at room temperature in the solid state. The high stability of this complex is due to the bulky bis-picket fence porphyrin scaffold which prevents the prompt bimolecular decomposition of the heme-HNO complex to the five-coordinate (5C) ls-{FeNO}^{7} analog and H_2, as reported in the literature.[64,89] The identity of the complex was confirmed by UV-vis and ^{1}H-NMR spectroscopy, the latter showing a slow interconversion of multiple heme-HNO conformers (rotamers) as the temperature is varied between -20 to -40 °C for both the natural abundance and ^{15}N labeled complex. Therefore, whereas Mb(II)-NHO is the most stable heme-HNO adduct in aqueous media, our complex is the most stable heme-HNO model complex in organic solvents.

With the new compound [Fe(3,5-Me-BAFP)(MI)(NHO)] in hand, we were able to address a couple of key questions with respect to the spectroscopic properties and the reactivity of heme-NHO complexes. First, the vibrational properties of heme-HNO complexes were not well defined. Whereas the N-O stretch had been reported for a number of compounds, not much was known about the Fe-N stretching and Fe-N-O bending modes of the coordinated HNO ligand. In Mb(II)-NHO, a weak, isotope sensitive feature had been observed at 651 cm^{-1} by resonance Raman spectroscopy.[92] This mode was automatically assigned to the Fe-N stretch; however, without further computational and/or vibrational analysis such assignments can be problematic, as demonstrated, for example, for the assignment of the Fe-NO stretching vs the Fe-N-O bending mode in six-coordinate (6C) ferrous-heme nitrosyl complexes.[1,50,97] Taking advantage of the enhanced stability of [Fe(3,5-Me-BAFP)(MI)(NHO)], we were able to obtain the first NRVS data for any heme-HNO complex, which provided detailed insight into the assignments of the low-

energy Fe-NHO stretching and bending vibrations. Our analysis shows that the Fe-N stretch of [Fe(3,5-Me-BAFP)(MI)(NHO)] is located at 644 cm^{-1}, which finally confirms the assignment of this mode for the Mb(II)-HNO complex at 651 cm^{-1}. The Fe-N-O bending mode of [Fe(3,5-Me-BAFP)(MI)(NHO)] is identified at 461 cm^{-1}.

The reactivity studies performed here provided useful insight into the protonation state and iron oxidation state of Intermediate *I* in Cyt P450nor. Upon the addition of excess NO gas to [Fe(3,5-Me-BAFP)(MI)(NHO)] at -30 °C, the HNO complex reacts with NO within 5 minutes, resulting in the conversion of the heme to the ferric, likely hydroxyl bound complex and ultimately to the 6C ls-$\{FeNO\}^6$ complex [Fe(3,5-Me-BAFP)(OH)(NO)], and quantitative formation of N_2O. Since heme-HNO complexes with axial (proximal) imidazole coordination have an electronic structure that is best described as an Fe(II)-NHO complex (where the HNO ligand serves as a relatively weak σ-donor and moderate π-acceptor),[60,98] this result indicates that one-electron oxidation of the ferrous heme center in the HNO complex takes place upon reaction with NO. The resulting ferric heme complex then rapidly rebinds NO and regenerates a ls-$\{FeNO\}^6$ complex, as shown in **Figure 2.28**. The use of gas headspace IR studies confirms that this reaction directly models the chemistry of Cyt P450nor, by indicating quantitative N_2O production under these conditions (yield: 91±10%). Similar chemistry was previously reported by Richter-Addo and coworkers, but due to the fact that their compound, [Fe(OEP)(5-MeIM)(NHO)], can only be obtained with ~11% yield, N_2O generation could be detected, but the amount of N_2O formed could not be quantified, the fate of the heme after the reaction could not be determined, and hence, no further conclusions about the mechanism of the reaction could be drawn. Our work demonstrates that NO is quite reactive towards a heme-bound HNO ligand, generating quantitative amounts of N_2O and a ferric heme product. The alternative mechanism, where NO would first coordinate to

the heme in trans position to HNO and then cause HNO loss, would only generate a 50% N_2O yield (from dimerization of free HNO: 2 HNO → $N_2O + H_2O$) and the five-coordinate (5C) ls-{FeNO}^{7} complex as the product. This alternative mechanism can therefore safely be ruled out.

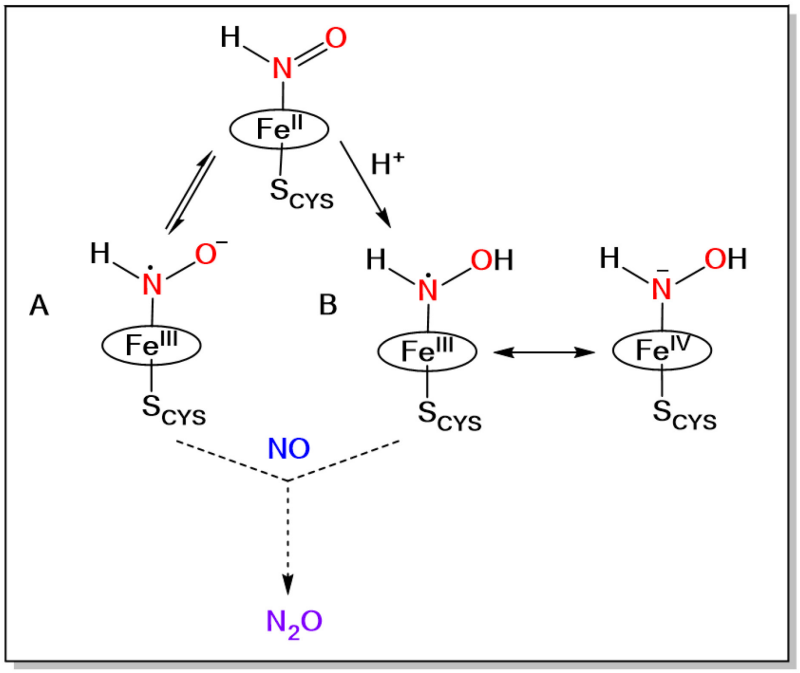

Figure 2.30 Scheme of possible geometric and electronic structures of Intermediate *I* in Cyt P450nor. Scheme adapted from ref.[2]. Copyright 2021 American Chemical Society.

Based on these new results, we have demonstrated that a heme-HNO complex is a catalytically competent intermediate for reaction with a second equivalent of NO to generate N_2O, according to the mechanism of Cyt P450nor. In other words, the key intermediate of this enzyme, termed Intermediate *I*, could correspond to the heme-HNO adduct. Further support for this conclusion comes from recent transient IR-spectroscopic measurements on the enzyme by Shiro and coworkers. Here, it was possible to obtain the N-O stretching frequency of Intermediate *I*, observed at 1330 and 1290 cm^{-1} with and without $NADP^+$, respectively.[54] These N-O stretches are located close to the typical range of 1380 – 1400 cm^{-1} for reported heme-HNO complexes (see **Table 1**). The authors further posit that the somewhat lower N-O stretching frequencies observed

for Intermediate *I* compared to these other heme-HNO complexes could be due to the presence of a unique thiolate (cysteinate) donor as the proximal ligand in the enzyme, which gives this intermediate an electronic structure that is better described as an Fe^{III}-$NHO^{\bullet-}$ complex, where the reduction of the HNO ligand would cause a drop in the N-O stretch. In addition, the radical character on the HNO ligand in this case would promote fast reactivity with the incoming NO radical in the enzyme.

The effect of HNO radical character on the reaction with NO can be further probed by comparison to previous work from our laboratory. As shown in **Figure 2.30**, another possible description of Intermediate *I* would be a Fe(III)-$NHOH^{\bullet}$ type species,[51] where the presence of the axial cysteinate ligand would increase the basicity of the HNO ligand, allowing for its further protonation under physiological conditions.[50] We were able to prepare such a model system for Intermediate *I*, using the same bis-picket fence porphyrin that was applied in this study. By one-electron oxidation of the precursor complex, [Fe(3,5-Me-BAFP)(NHOMe)], we obtained the analogous Fe(III)-$NHOMe^{\bullet}$ complex $[Fe(3,5\text{-Me-BAFP})(NHOMe)]^{+}$, the electronic structure of which was confirmed by resonance Raman and Mössbauer spectroscopy. $[Fe(3,5\text{-Me-BAFP})(NHOMe)]^{+}$ reacts with slight excess NO at -80 °C in under one minute to form the analogous starting material, $[Fe(3,5\text{-Me-BAFP})(SbF_6)]$, with a first order rate constant of 5×10^{-2} s^{-1}.[53] Considering the temperature difference (-80 vs -30 °C), this reaction is actually much faster than that of [Fe(3,5-Me-BAFP)(MI)(NHO)] with NO at -30 °C, which has a first order rate constant of 0.17 s^{-1} and requires a larger excess of NO. This comparison demonstrates that a radical-type species like Fe(III)-$NHOH^{\bullet}$ is more reactive towards NO than a heme-HNO complex. Hence, in revising the previous mechanistic proposal for Cyt P450nor,[52] the role of the axial cysteinate ligand would **not** be to increase the basicity of the bound HNO to allow for its further

protonation, but to generate a heme-HNO complex with a Fe^{III}-$NHO^{\bullet-}$ type electronic structure, which would then be much more reactive towards NO compared to the analogous Fe(II)-NHO complex in the presence of an axial histidine (imidazole) ligand. The assignment of Intermediate *I* to an Fe^{III}-$NHO^{\bullet-}$ type species, potentially in the presence of hydrogen bonding, is in agreement with the N-O stretching frequency of the intermediate recently determined by Shiro and coworkers (see above). Future work is now focused on generating a heme-HNO model complex with axial thiolate coordination, to better model Intermediate *I* and determine the electronic structure of such a species, and to investigate its reactivity towards NO.

2.5 Experimental Section

General Considerations

All chemicals were purchased from commercial sources, including Sigma Aldrich, Fisher Scientific, and Cambridge Isotopes, and used without further purification unless noted below. Reactions were performed under inert atmosphere via Schlenk techniques. All solvents were dried and distilled from CaH_2 and freeze pump thawed four times to remove water and dioxygen. Preparation and handling of air-sensitive materials were performed under a dinitrogen atmosphere in an MBraun glovebox, equipped with a circulating purifier (O_2, H_2O <0.1 ppm). H_2[3,5-Me-BAFP], [Fe(3,5-Me-BAFP)(Cl)][63], and [Co(TPP)][99] were synthesized according to published procedures. Nitric oxide (Cryogenic Gases Inc., 99.95%) was first passed through an Ascarite II column and then a -80 °C cold trap to remove higher nitrogen oxide impurities prior to use. Complexes and solvents were then exposed to NO via a Schlenk line. Isotopically labeled ^{15}NO was synthesized according to previously reported procedures.[100] ^{57}Fe complexes were metalated analogous to the iron natural abundance isotopes complexes using $^{57}FeCl_2$•2MeOH, which was

synthesized from ^{57}Fe powder.[101] Reactivity studies were typically performed with excess NO gas from a bomb flask. Stoichiometric additions of NO were carried out by NO-saturation of chlorobenzene in a Schlenk flask under an N_2 atmosphere. The NO concentration of the solution was quantified by UV-vis titration of the NO(g)/chlorobenzene solution into a ~40 μM solution of [Co(TPP)] in tetrahydrofuran. Reactions are complete after observing a Q band shift from 527 to 538 nm. Typical concentrations are 5-6 mM NO(g)/chlorobenzene.

Physical Measurements

UV-vis Spectroscopy/Immersion Probe. All spectra were recorded using an Analytic Jena Specord S-600 Spectrometer. Using the same spectrometer, dip probe measurements were conducted using a Hellma low temperature immersion probe with a 10 mm pathlength.

^{1}H NMR Spectroscopy. A Varian MR 600 instruments was used to record all NMR spectra at temperatures between -40 and 25 °C.

Elemental Analysis. Elemental analyses were conducted by Atlantic Microlabs (Norcross, GA)

Infrared Spectroscopy (ATR/KBr/Gas). Solid state IR spectra were recorded using a Bruker Alpha-E FT-IR spectrometer. IR data for KBr disks were obtained on PerkinElmer BX and GX spectrometers. The same instruments were used to conduct gas headspace measurements using a 10 cm Pike HT gas cell with CaF_2 windows. The calibration curve for N_2O quantification was generated using 2-18 μmol of Piloty's acid in 2.5 mL of water at pH 13 in a 25 mL round bottom flask. After 3 hours of reaction time, the gas headspace of the reaction mixture was extracted for

exactly 20 seconds and IR measurements were immediately conducted. The amount of N_2O produced from the reaction was correlated with the integrated area of the asymmetric N-N stretch of N_2O between 2150 and 2275 cm^{-1}. Experiments were conducted in triplicate (**Figure 2.22**).

Nuclear Resonance Vibrational Spectroscopy (NRVS). NRVS data were obtained at Sector 3ID at the Advanced Photon Source (APS) at Argonne National Laboratory. For each sample, 20-40 mg of compound were packed into a copper cell containing a 4x7x1 mm sample well. All spectra were taken from 0 to 100 meV. Further experimental details are described in ref. [102].

Electron Paramagnetic Resonance (EPR). X-Band EPR spectra were collected using a Bruker X-band EMX spectrometer with an Oxford Instruments liquid helium cryostat. Samples were frozen and consisted of 300 μL of ~1 mM solutions. All spectra were obtained at 77 K, 1.0 G modulation amplitude, and 2 mW microwave power.

Crystal Structure Determination

[Fe(3,5-Me-BAFP)(MI)(NO)](BArF$_{24}$). Red needles of [Fe(3,5-Me-BAFP)(MI)(NO)](BArF$_{24}$) were grown by vapor diffusion of pentanes into a concentrated diethyl ether solution of the compound in a sealed vial at room temperature (20 °C). A crystal of dimensions 0.093 x 0.133 x 0.143 mm was mounted on a Rigaku AFC10K Saturn 944+ CCD-based X-ray diffractometer equipped with a low temperature device and a Micromax-007HF Cu-target micro-focus rotating anode (λ = 1.54187 A) operated at 1.2 kW power (40 kV, 30 mA). The X-ray intensities were measured at 85(2) K with the detector placed at a distance of 42.00 mm from the crystal. A total of 2028 images were collected with an oscillation width of 1.0° in ω. The exposure times were 1 second for the low angle images, 5 seconds for high angle. Rigaku d*TREK images were exported to CrysAlisPro 1.171.43.112a (Rigaku OD,

2024) for processing and corrected for absorption.[103] The integration of the data yielded a total of 194636 reflections to a maximum 2θ value of 137.97° of which 25255 were independent. Analysis of the data showed negligible decay during data collection. Five reflexes were identified as clear outliers and omitted. The structure was solved using SHELXT 2018[104] and refined with SHELXL-2019/2 (Sheldrick, 2019).[104,105] The obtained molecular structure features two different species co-crystallized. The major species (70.6%) has two N-methylimidazoles coordinated to the central iron ion, while the minor species (29.4%) has one N-methylimidazole and one NO bound. The co-crystallized species was treated as disorder and restrained using SIMU and DELU. The counterion (BArF24) exhibited severe disorders which were restrained using SADI, SIMU and DELU. After refinement of the disorder, the following formula for the mixed crystalized species was obtained: C146.82 H114.24 B F24 Fe N7.71 O8.29. All non-hydrogen atoms were refined anisotropically with the hydrogen atoms placed in a combination of idealized and refined positions using the riding model. The molecular structure featured four solvent molecules (diethyl ether) disordered over several positions identified by the electron density in the respective voids in combination with the crystallization conditions. These solvent molecules could not be refined and were squeezed using Platon.[106] Full matrix least-squares refinement based on F2 converged at R1 = 0.0558, wR2 = 0.1531 [based on $I > 2\sigma(I)$], R1 = 0.0645, wR2 = 0.1658 for all data. Additional details are presented in .

Density Functional Theory Calculations. All calculations were performed using the program Gaussian 09.[107] All geometry optimizations and frequency calculations were performed using BP86 as the functional and TZVP as the basis set. Calculated frequencies were inspected to ensure the absence of any imaginary frequencies, to confirm that true energy minima were obtained.

Synthetic Procedures

Synthesis of [Fe(3,5-Me-BAFP)(OTf)]. [Fe(3,5-Me-BAFP)(Cl)] (244.1 mg, 0.147 mmol) and silver trifluoromethanesulfonate (36.8 mg, 0.143 mmol) were added to an oven-dried round bottom flask equipped with a stir bar. The solids were dissolved in 15 mL of 2-Me-THF, resulting in an immediate color change of the solution from brown to brown/red. Once the reaction was complete as determined by UV-vis spectroscopy, the reaction was filtered to remove insoluble silver chloride. The resulting filtrate was layered with hexanes and placed in the glovebox freezer overnight. The light brown solid product was collected by vacuum filtration the next day and dried vigorously under vacuum at 120 °C. Yield: 225.5 mg (0.127 mmol, 86%). UV-Vis (2-Me-THF): 401, 520 nm; (CH_2Cl_2): 410, 520 nm. Elemental analysis: cald (found) for $C_{109}H_{92}F_3FeN_4O_{11}S$•0.5 CH_2Cl_2: C, 72.30 (72.41); N, 3.07 (3.11); H, 5.13 (5.24).

Synthesis of [Fe(3,5-Me-BAFP)(MI)(NO)](OTf). Under an inert atmosphere, [Fe(3,5-Me-BAFP)(OTf)] (186.4 mg, 0.105 mmol) and 8 μL (0.100 mmol) of 1-methylimidazole (MI) were dissolved in 5 mL of dichloromethane. The reaction mixture was then exposed to NO gas, resulting in a bright red solution. The reaction mixture was brought into the glovebox and precipitated with 30-40 mL of hexanes, and then stored at -33 °C in the glovebox freezer overnight. The next day, the reaction mixture was vacuum filtered in the glovebox through a frit. The resulting bright purple powder was washed with hexanes. Yield: 173.3 mg (0.092 mmol, 87%). UV-vis (CH_2Cl_2): 435, 545 nm. IR (KBr): ν(N-O) = 1912 cm^{-1}. Elemental analysis: cald (found) for $C_{113}H_{98}F_3FeN_7O_{12}S$•0.5 CH_2Cl_2: C, 70.60 (70.69); N, 5.06 (4.93); H, 5.15 (5.07).

Synthesis of [Fe(3,5-Me-BAFP)(MI)(NHO)]. Under an inert atmosphere, a 10-15 mM solution of [Fe(3,5-Me-BAFP)(MI)(NO)](OTf), dissolved in either chlorobenzene or toluene, was

precooled in a copper block to -40 °C using a dry ice/acetonitrile bath. One equivalent of (TBA)[BH_4] was added to the solution to form the HNO complex. After ~1 minute of stirring, the desired complex was precipitated with dry pentanes. The complex was allowed to precipitate at -40 °C for 30 minutes and the solid was filtered and collected for further characterization.

Chapter 3 Synthesis, Characterization, and Hydride Reactivity Studies with a Thiolate Bound {FeNO}^{6} Cyt P450nor Mimic Utilizing the Bulky Bis-Picket Fence Porphyrin

3.1 Introduction

Although the heme-HNO complex was successfully stabilized in **Chapter 2**, this complex is not an ideal model for Intermediate *I* of Cytochrome P450nor.[3] As discussed in **Chapter 1**, NO reduction in Cyt P450nor begins with NO binding to a thiolate-bound ferric heme, resulting in a ls-{FeNO}^{6} complex by Enemark-Feltham notation, **Figure 1.5**[40,48] As shown in **Chapter 2**, the neutral imidazole axial ligand is crucial for heme-nitroxyl formation. The presence of the axial ligand guides hydride attack to the nitrosonium ligand rather than the ferric heme center.[45,89] By replacing the imidazole with a thiolate, hydride addition to the corresponding ls-{FeNO}^{6} complex would provide a comparable heme-nitroxyl model to the active site of the native enzyme. While the formation of the ls-{FeNO}^{6} is made easily in the enzyme, the opposite is observed in synthetic model complexes.[40,45] In the presence of a thiolate bound ferric heme, autoreduction occurs upon NO addition, resulting in the ls-{FeNO}^{7} complex and disulfide, and/or the unwanted side reaction between NO and the thiolate, resulting in the formation of an RSNO (**Figure 3.1**).[45,46,108,109]

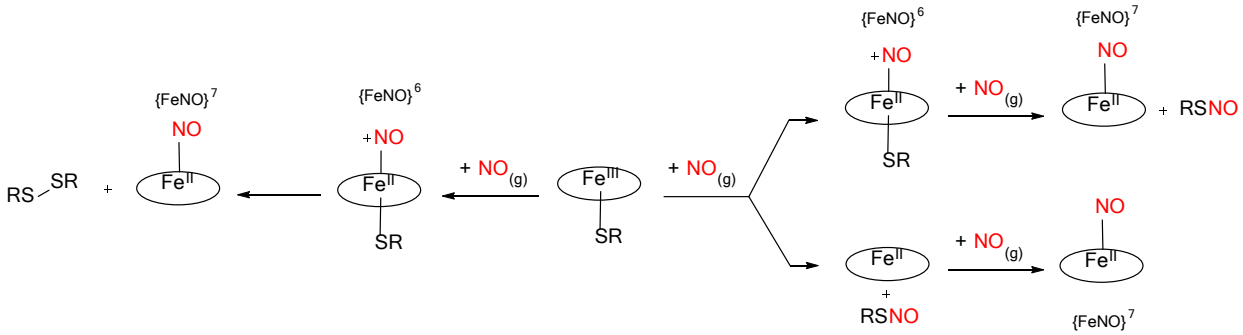

Figure 3.1 Potential reaction pathways of thiolate ferric heme complexes with NO to from the ls-{FeNO}^{7} complex with stoichiometric (left) and excess NO addition (right).

Despite these challenges, a series of thiolate-bound heme ls-{FeNO}^{6} complexes using tetraphenylporphyrin, [Fe(TPP)(SR)(NO)], was previously synthesized at low temperatures (-80 °C) with stoichiometric additions of NO to the thiolate-bound ferric heme precursor complexes. The thiolate-donor strength was tuned by either the presence of electron withdrawing substituents (-SPh-X, where X = NO_2, CF_3, or F) or via an electronically tuned intramolecular hydrogen bond to modulate the strength of the donor (-SPhNHPh-R, where R = CH_3, H, Cl, CF_3, NO_2), as shown in **Figure 3.2**.[45,46] It was determined that the ls-{FeNO}^{6} thiolate complexes generated with a intramolecular hydrogen bond were more stable with warming with warming up to -40 °C before beginning to decompose. This is in contrast to the smaller electronically tuned thiolates which rely solely on the electronic tuning of the phenol thiolate to prevent decomposition.[46] Between both series, the tuning of the thiolate strength was evident in the vibrational data collected, revealing a direct correlation between the Fe-NO and N-O bonds in these complexes, which occurs due to the strong σ donation from the thiolate ligand that imparts a σ-trans effect on the Fe-N-O unit.[110] Based on the correlation plot in **Figure 3.2**, stronger thiolate donors result in weaker Fe-NO and N-O bonds. This strong donation also causes the Fe-N-O unit to deviate from linearity, with an angle of 161°.[111] The opposite trend is observed for ls-{FeNO}^{6} complexes with a neutral imidazole donor, where the Fe-NO and N-O bond strengths show an inverse correlation with respect to the imidazole donor strength, and the Fe-N-O bond is linear.[111-113] It was determined that the Fe(II)-NO^+ unit is isoelectronic to Fe(II)-CO, and therefore dominated by π-backbonding, causing the inverse correlation (and a weakened N-O bond compared to free NO^+).[114,115] Based on the vibrational data, Cyt P450nor contains a strongly donating cysteine-thiolate in comparison to other heme-thiolate containing enzymes.[110] However, the role of this strong thiolate donation in the context of NO reduction has remained unclear.

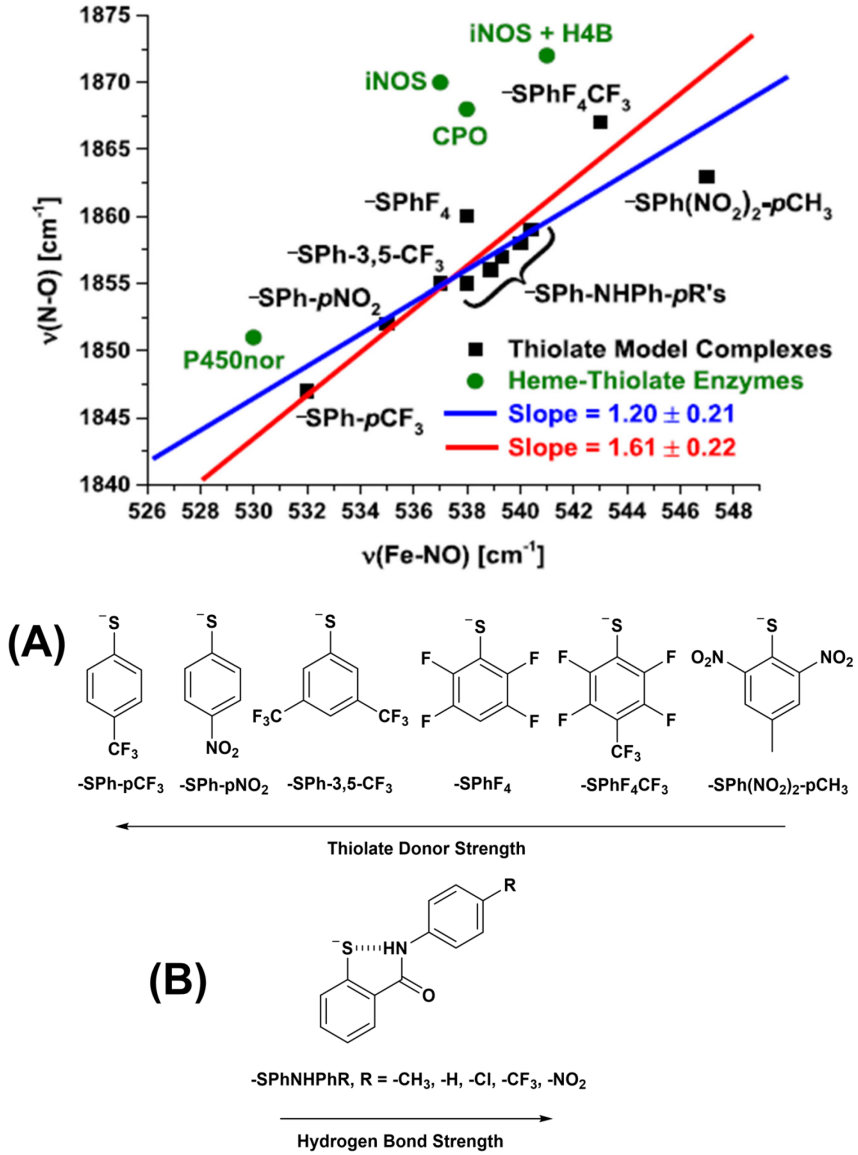

Figure 3.2 Correlation plot of the Fe-N versus N-O stretching frequencies for synthetic model complexes (black) and native enzymes (red) (top). Thiolate donors listed in order of increasing strength from right to left where (A) lists the electronically tuned phenol thiolates and (B) lists the thiolates equipped with an electronically tunable hydrogen bond.[45,46]

The proximal thiolate in Cytochrome P450s play two roles to support the key reactivity of these enzymes. First, the donating nature of the proximal thiolate causes a "push effect" where the electron donation of this axial ligand facilitates O-O bond cleavage of the hydroperoxo intermediate to result in Compound I.[42,45,116,117] Additionally, the presence of the proximal thiolate was found to increase the pKa of Compound II, aiding H-atom abstraction.[43,65] These roles cannot

be extended to the thiolate donor of Cyt P450nor, as this enzyme is a reductase rather than an oxygenase.

In the context of Cyt P450nor, there are two possible electronic structures that could describe the heme-HNO complex with thiolate ligation (see **Figure 1.6**).[1] DFT calculations predict that strong donation from the axial anionic thiolate increases the basicity of the HNO ligand (analogous to Compound II), leading to protonation and formation of an Fe^{III}-$NHOH^{\bullet}$ type species.[45,49-52] Alternatively, DFT studies have also shown that the anionic nature of the thiolate aids in forming an elusive ferric heme HNO radical intermediate, Fe^{III}-$HNO^{\bullet-}$.[51,54] This intermediate is predicted to be highly reactive towards $NO^{\bullet}$ to quickly form an N-N bond to generate N_2O.[49] Recently, Shiro and coworkers studied the reaction of Cyt P450nor with NO using time-resolved spectroscopic techniques and DFT calculations.[54] Here, the N-O stretching mode of Intermediate *I* was observed for the first time. N-O stretching frequencies of 1330 cm^{-1} and 1290 cm^{-1} were obtained for the intermediate with and without NAD^+ present, respectively.[54] These results paired with DFT calculations suggest that this species is likely singly protonated (potentially with the Fe^{III}-$NHO^{\bullet-}$ electronic structure).[51,54]

This chapter focuses on the stabilization of the thiolate-bound ls-$\{FeNO\}^6$ complex with the bulky bis-picket fence porphyrin of **Chapter 2**, 3,5-dimethyl-bisaryloxyfence porphyrin ([H_2(3,5-Me-BAFP)], to prevent facile decomposition to the corresponding ls-$\{FeNO\}^7$ complex and disulfide. The thiolate chosen for the synthetic model of the active site of Cyt P450nor was selected based on the cleanest formation of the thiolate complex and the thiolate-bound ls-$\{FeNO\}^6$. This model was compared to the active site of Cyt P450nor based on the N-O and Fe-NO stretching frequencies obtained from IR and rRaman spectroscopy, respectively. With complete characterization of the ls-$\{FeNO\}^6$ complex by UV-vis, NMR, IR and rRaman

spectroscopy, ~1 equivalent of hydride was added to the complex to observe the putative thiolate-bound heme-nitroxyl complex, [Fe(3,5-Me-BAFP)(SR)(NHO)]$^{-}$, using the bulky bis-picket porphyrin. This work acts as a foundation for future research on thiolate-bound heme nitroxyl complexes within the context of Cyt P450nor.

3.2 Synthesis of Thiolate-Bound Precursors

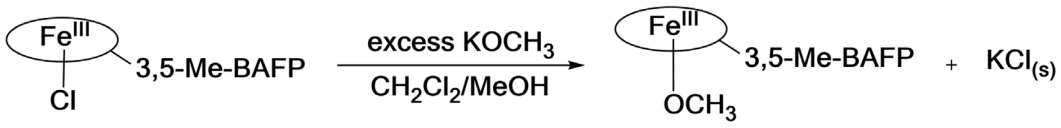

Figure 3.3 Synthetic scheme for the five-coordinate ferric heme methoxide complex, [Fe(3,5-Me-BAFP)(OCH_3)].

First, the axial chloride of the [Fe(3,5-Me-BAFP)(Cl)] complex exchanged to a bound methoxide to form [Fe(3,5-Me-BAFP)(OCH_3)], as shown in **Figure 3.3**. This was accomplished by dissolving the chloride complex in dichloromethane and with excess $KOCH_3$ solubilized in methanol.[45] This reaction was allowed to stir for 1 hour before all solvent was removed by vacuum. The resulting residue was redissolved in dry dichloromethane and filtered to remove excess $KOCH_3$ and KCl salts formed from the reaction product. Next, the filtrate was evaporated, the resulting solid was resuspended in dry methanol, and collected for vacuum filtration. The black solid was washed with additional methanol to wash away excess $KOCH_3$. The success of this reaction was assessed by UV-vis spectroscopy, as shown in **Figure 3.4**, where the chloride shoulder at 375 nm disappears with a new feature at 378 nm and a shifted Q band to 584 nm, indicating that Cl^{-} was successfully displaced by OCH_3^{-}. These results are analogous to those observed for the [Fe(TPP)(OCH_3)] complex.[45] It should be noted that by changing the porphyrin

from TPP^{2-} to the bis-picket fence porphyrin, 3,5-Me-$BAFP^{2-}$, the complex becomes partially soluble in nonpolar solvents, such as hexanes and pentanes, which was previously used to precipitate the methoxide complex and wash away any unreacted [Fe(3,5-Me-BAFP)(Cl)]. Based on elemental analysis, no chloride ions remained in the sample under these work-up conditions. The methoxide complex was further characterized by ^{1}H NMR spectroscopy in CD_2Cl_2. This spectrum shows a peak at 79.61 ppm, which is indicative of the β-pyrrole protons of high-spin ferric heme porphyrins as shown in **Figure 3.5**.

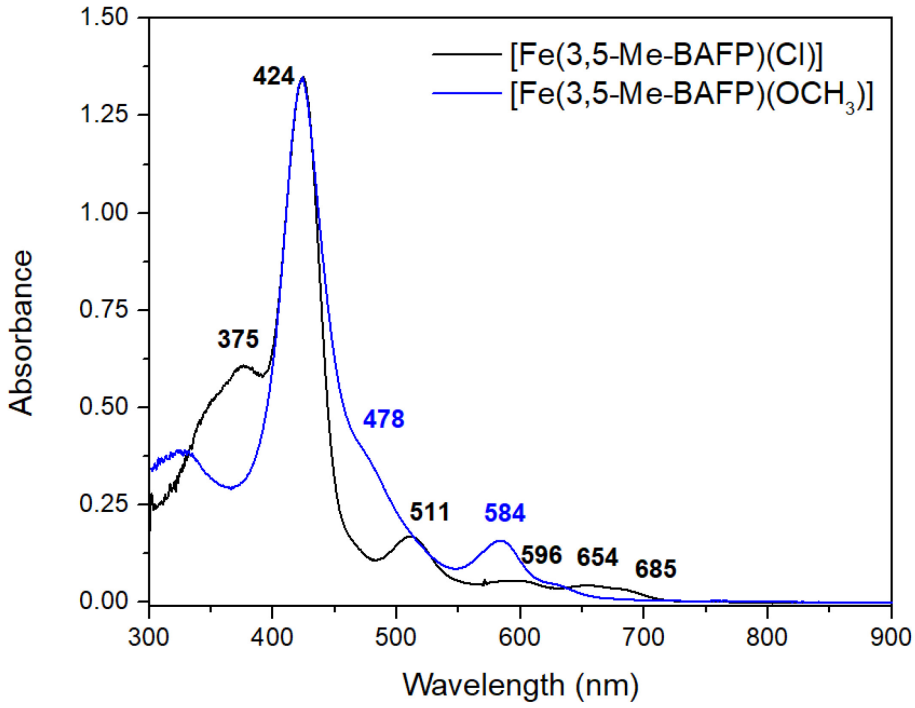

Figure 3.4 Normalized UV-vis spectral overlay of [Fe(3,5-Me-BAFP)(Cl)] in dichloromethane (black) and [Fe(3,5-Me-BAFP)(OCH_3)] in toluene (blue).

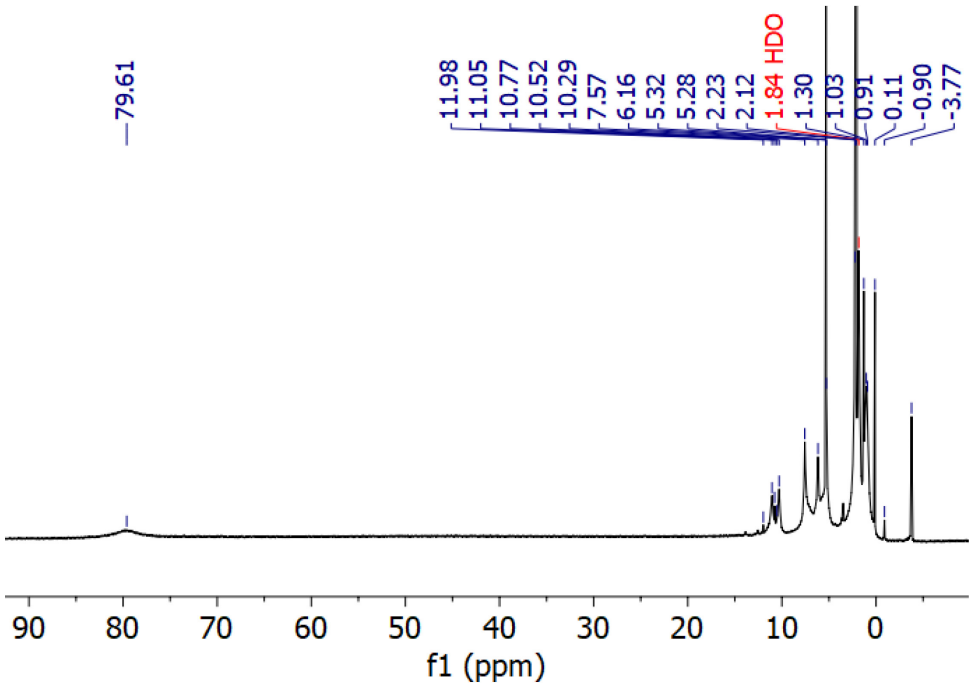

Figure 3.5 ^{1}H NMR spectrum of [Fe(3,5-Me-BAFP)(OCH_3)] in CD_2Cl_2.

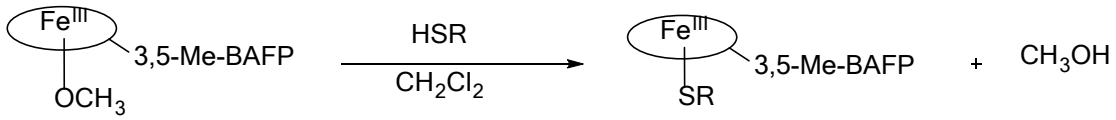

Figure 3.6 Synthetic scheme for five-coordinate ferric heme thiolate complexes, [Fe(3,5-Me-BAFP)(SR)].

Next, the methoxide-bound ferric heme is mixed with 1 equivalent of the desired thiol in dichloromethane to perform an acid base reaction and form the desired five coordinate thiolate-bound ferric heme complex and methanol, as shown in **Figure 3.6**.[45] This complex was isolated by removing the dichloromethane and methanol and the resulting solid was suspended in pentanes and collected by vacuum filtration.

Based on previous work with tetraphenylporphyrin, the thiolate donors containing an intramolecular hydrogen bond produced the most robust ls-{FeNO}^{6} complexes with stability up to -40 °C.[46] The presence of the hydrogen bond prevents the known tautomerization of the ferric heme thiolate to the unfavored ferrous thiyl radical complex, shown in equation 1, and thus helps prevent unwanted side reactions upon NO addition.[118]

$$[Fe^{III}(porphyrin)(SR)] \leftrightarrow [Fe^{II}(porphyrin)](^{\bullet}SR)] \quad (1)$$

Due to the inherent steric hinderance between the intramolecular hydrogen bond-containing thiolate ligands and the bis-picket fence porphyrin, poor thiolate binding to the ferric center was not unexpected. Therefore, the success of the reaction was studied as a function of thiolate donor strength, using a strong (–SPhNHPhCH$_3$) and a weak (–SPhNHPhCF$_3$) thiolate donor chosen from the correlation plot in **Figure 3.2**. As shown in the ^{1}H NMR spectrum in **Figure 3.8**, the –SPhNHPhCH$_3$ ligand does in fact bind to the ferric bis-picket fence porphyrin to form [Fe(3,5-Me-BAFP)(SPhNHPhCH$_3$)]. This is evident from the signal of the β-pyrrole protons, which shifts from 79.61 ppm of the [Fe(3,5-Me-BAFP)(OCH$_3$)] (**Figure 3.5**) to 73.48 ppm for the thiolate bound complex, [Fe(3,5-Me-BAFP)(SPhNHPhCH$_3$)] (**Figure 3.7** and **Figure 3.8**). Additional signals also appear at 80.10, 66.89 and -91.70 ppm, representing the meta and ortho protons of the axially bound thiolate, further indicating the successful binding of the thiolate to the ferric heme.[46,119]

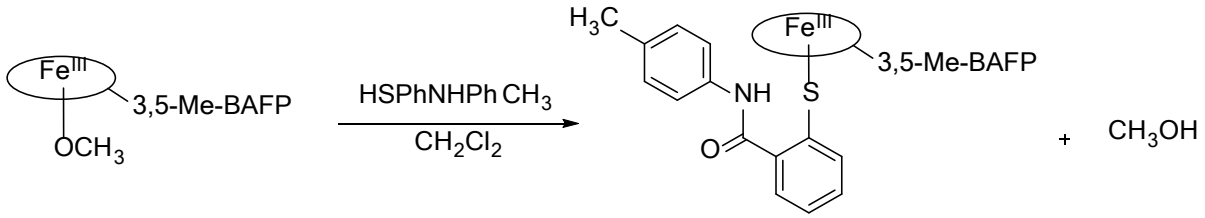

Figure 3.7 Synthetic scheme for [Fe(3,5-Me-BAFP)(SPhNHPhCH$_3$)].

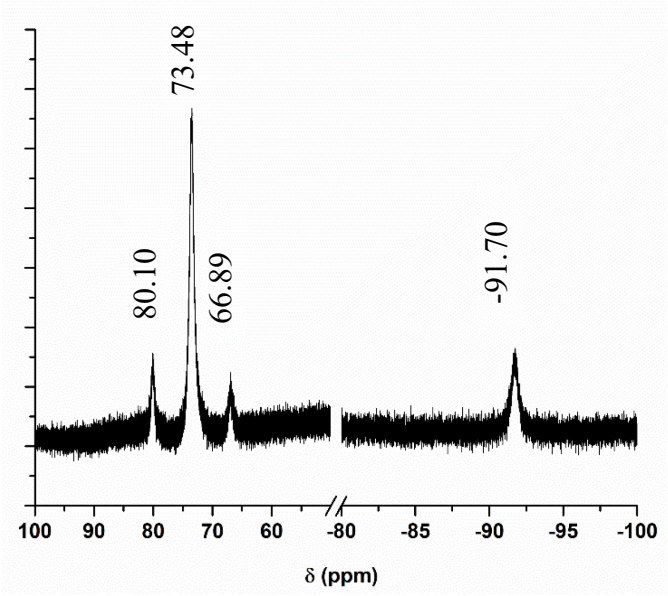

Figure 3.8 Key regions of the ^{1}H NMR spectrum of [Fe(3,5-Me-BAFP)(SPhNHPhCH$_3$)] in CD_2Cl_2. The full spectrum is shown in the experimental section.

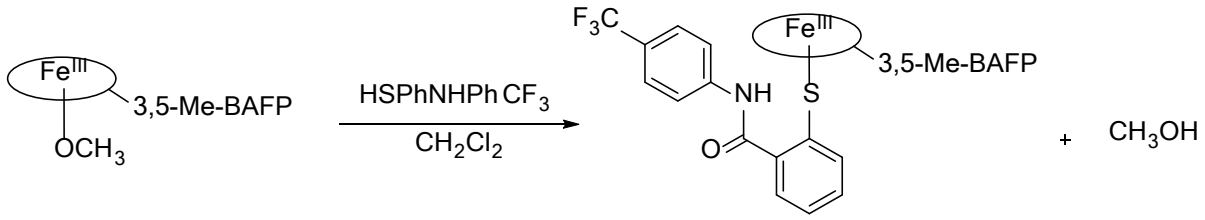

Figure 3.9 Synthetic scheme for [Fe(3,5-Me-BAFP)(SPhNHPhCF$_3$)].

Similar results were obtained with the weaker –SPhNHPhCF$_3$ thiolate (**Figure 3.9**), where the β-pyrrole protons shifted to 73.00 ppm. Unfortunately, the ^{1}H NMR spectrum shows an incomplete conversion to the bound thiolate complex as evident from a residual signal at 79.61 ppm, as shown in **Figure 3.10**. These results are in agreement with those observed for the ^{19}F NMR spectrum, where a new signal appears at -57.43 ppm corresponding to the formation of the desired ferric heme thiolate complex, as well as the original signal at -61.53 ppm indicating unbound thiol despite the addition of slight excess (1.66 equivalents) thiol. To purify the thiolate

complex from the methoxide complex, the reaction was filtered to remove insoluble $HSPhNHPhCF_3$ as the first step. After repeating both ^1H and ^{19}F NMR experiments, the changes in the integration of the ferric heme thiolate complex and free thiol suggest a shift in the reaction towards the starting methoxide complex. This result was likely caused by filtering off excess thiol. Attempts to optimize this reaction were unsuccessful due to a combination of the low solubility of $–SPhNHPhCF_3$, weak thiolate donation and steric hindrance resulted in loss of the axial ligand after the desired complex was formed. For this reason, this complex was not brought forward in the formation of the ls-$\{FeNO\}^6$ complex.

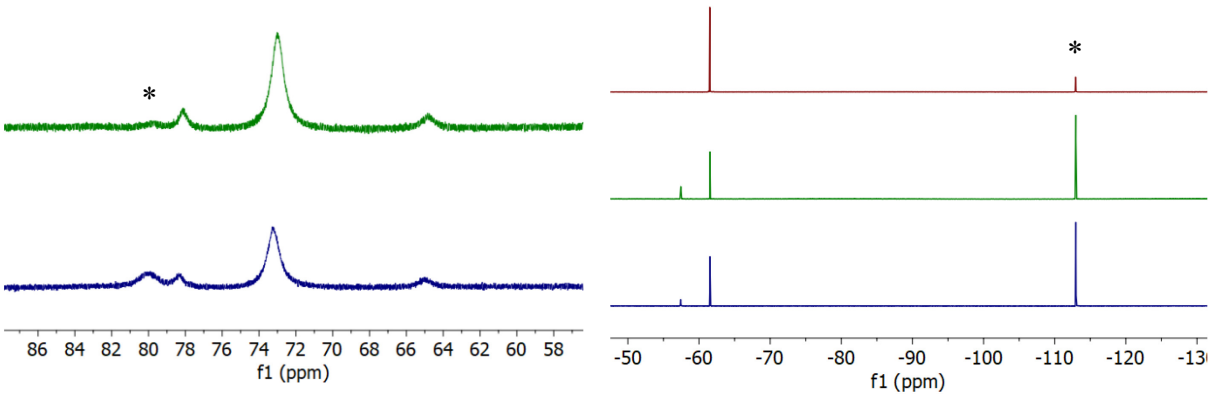

Figure 3.10 (left) Key regions of the ^1H NMR spectrum of [Fe(3,5-Me-BAFP)($SPhNHPhCF_3$)] before (green) and after filtering off excess thiol (blue). The asterisk represents unreacted [Fe(3,5-Me-BAFP)(OCH_3)]. The full spectrum is in the experimental section. (right) ^{19}F NMR of free thiol, $HSPhNHPhCF_3$ (red) [Fe(3,5-Me-BAFP)($SPhNHPhCF_3$)] in before (green) and after filtering off excess thiol (blue). The asterisk represents the fluorobenzene reference. All spectra were taken in CD_2Cl_2.

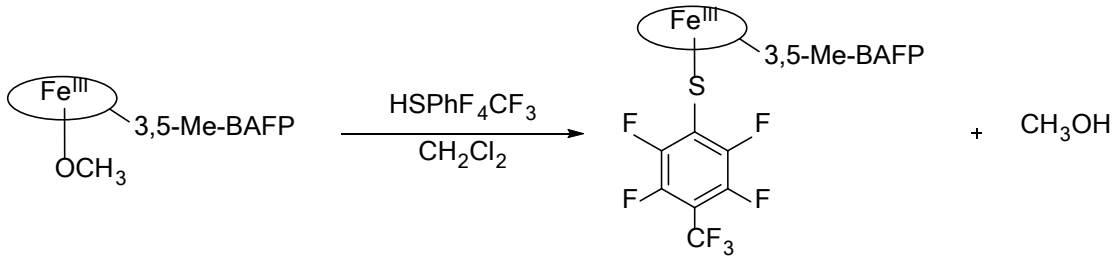

Figure 3.11 Synthetic scheme for [Fe(3,5-Me-BAFP)($SPhF_4CF_3$)].

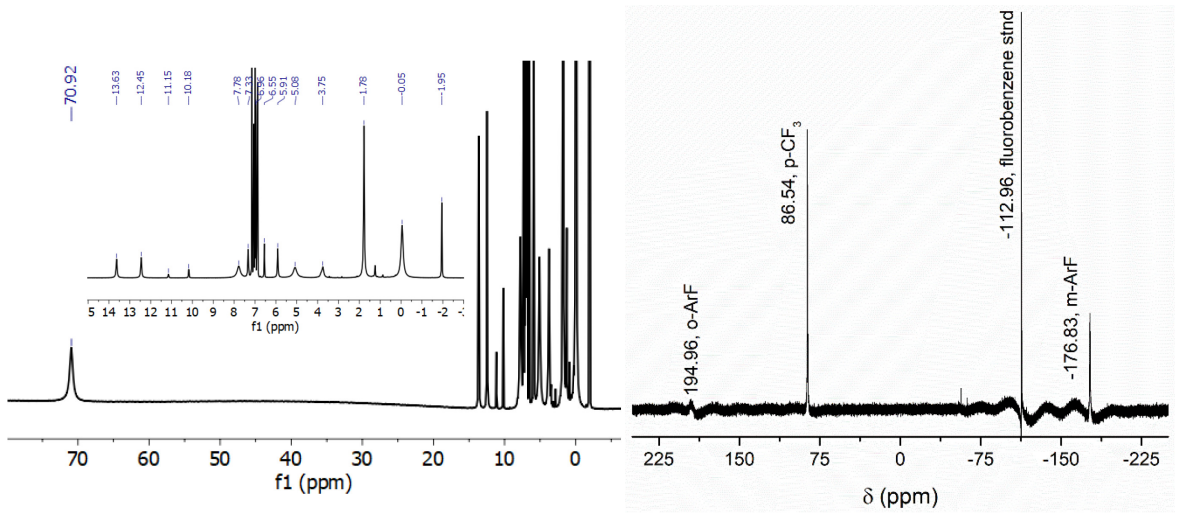

Figure 3.12 NMR spectrum of [Fe(3,5-Me-BAFP)(SPhF$_4$CF$_3$)] in chlorobenzene-d$_5$ with a drop of fluorobenzene (left) ^{1}H NMR spectrum (right) ^{19}F NMR spectrum.

Alternatively, one of the smaller electronically tuned phenolthiolates was considered for the formation of the ls-{FeNO}^{6} complex, using again the bulky bis-picket fence porphyrin. Despite the absence of the intramolecular hydrogen bond, the bi-spicket fences were thought to aid in preventing side reactions between the bound thiolate with NO. Based on the vibrational data in **Figure 3.1**, the phenolthiolate deemed to form the best electronic model for the Cyt P450nor active site was –SPh-pCF$_3$. Unfortunately, previous work by Dr. Andrew Hunt demonstrated challenges in getting NO to fully bind to [Fe(TPP)(SPh-pCF$_3$)] prior to ls-{FeNO}^{6} decomposition, making this a less attractive choice for future reactivity studies with the bis-picket fence porphyrin.[45] To ensure maximum NO binding to the ferric heme thiolate complex, the thiolate –SPhF$_4$CF$_3$ was chosen due to its success in forming the [Fe(TPP)(SPhF$_4$CF$_3$)(NO)] analog (**Figure 3.11**). As shown in **Figure 3.12**, [Fe(3,5-Me-BAFP)(SPhF$_4$CF$_3$)] was formed quantitatively based on the shift of the β-pyrrole protons at 70.92 ppm by ^{1}H NMR spectroscopy. The data obtained by ^{19}F NMR spectroscopy show three new signals at 194.96, 85.54, and -176.83

ppm representing the ortho-F, para-CF_3, and meta-F signals of the bound thiolate, respectively. The temperature dependence of this complex is observed in **Figure 3.13**.

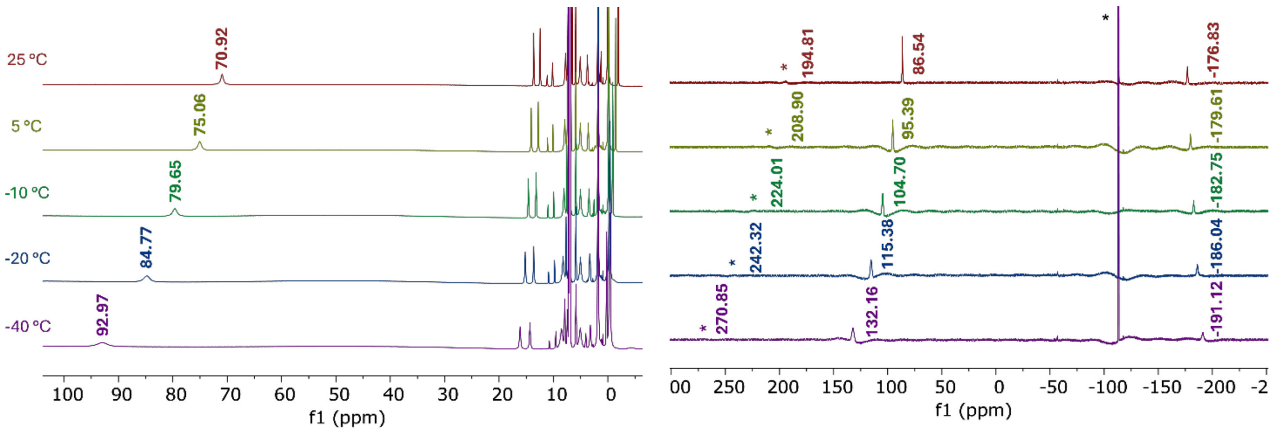

Figure 3.13 VT NMR spectra of [Fe(3,5-Me-BAFP)($SPhF_4CF_3$)] in chlorobenzene-d_5 with fluorobenzene (left) ^1H NMR (right) ^{19}F NMR. The asterisk represents the fluorobenzene reference.

The successful formation of [Fe(3,5-Me-BAFP)($SPhNHPhCH_3$)] and [Fe(3,5-Me-BAFP)($SPhF_4CF_3$)] as evident from NMR spectroscopy provides two models for subsequent ls-{FeNO}^{6} complex formation. The UV-vis data of these complexes in CH_2Cl_2 have Soret bands of 421 and 423 nm, respectively, as shown in **Figure 3.14**. Additionally, both complexes show a shoulder analogous to [Fe(3,5-Me-BAFP)(Cl)] at 378 and 381 nm, respectively. Since no chloride was found in the elemental analysis of [Fe(3,5-Me-BAFP)(OCH_3)] prior to the reaction with the thiols, it is safe to assume that the shoulders belong to the LMCT transitions between the thiolate ligand and the ferric heme center.[120]

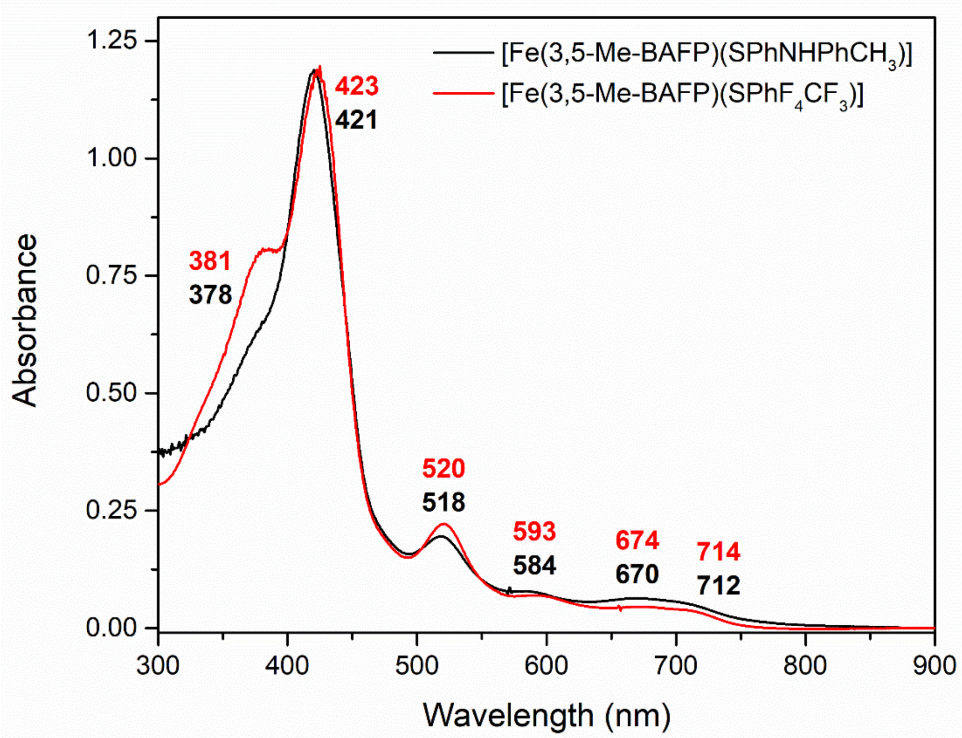

Figure 3.14 UV-vis spectral overlay of [Fe(3,5-Me-BAFP)(SPhNHPhCH$_3$)] (black) and [Fe(3,5-Me-BAFP)(SPhF$_4$CF$_3$)] (red).

3.3 Low Temperature Formation of [Fe(3,5-Me-BAFP)(SR)(NO)] Complexes

The formation of the ls-{FeNO}^{6} complexes using [Fe(3,5-Me-BAFP)(SPhNHPhCH$_3$)] and [Fe(3,5-Me-BAFP)(SPhF$_4$CF$_3$)] as precursors was initially observed by low temperature UV-vis dip-probe experiments. The goal of these experiments was to observe the clean formation of the corresponding ls-{FeNO}^{6} complex without unwanted side reactions, namely the formation of the ls-{FeNO}^{7} decomposition product and disulfide. Upon successful formation, the stability of the ls-{FeNO}^{6} complexes was assessed at the given temperature to determine the accessible time-frame for future reactivity studies. Based on the conditions used in these experiments, the ls-{FeNO}^{6} complexes were prepared for further characterization by NMR, solution IR, and resonance Raman spectroscopy.

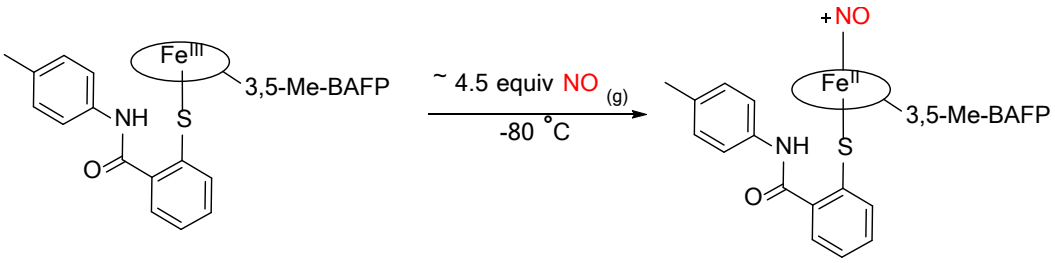

Figure 3.15 Synthetic scheme for the desired complex [Fe(3,5-Me-BAFP)(SPhNHPhCH$_3$)(NO)].

Initial work was performed with [Fe(3,5-Me-BAFP)(SPhNHPhCH$_3$)], which possessed the thiolate with the intramolecular hydrogen bond. Here, the reaction was performed at -80 °C where the limits of NO binding were tested by the addition of 4.5 equivalents of NO gas to a 10 μM solution of the precursor in toluene to form the ls-{FeNO}^{6} complex, [Fe(3,5-Me-BAFP)(SPhNHPhCH$_3$)(NO)] (**Figure 3.15**). As shown in **Figure 3.16**, a new Soret band grew in at 439 nm upon NO addition, which agrees with the UV-vis data obtained for the ls-{FeNO}^{6} tetraphenylporphyrin analog.[46] Unfortunately, this reaction was not clean due to the lack of isobestic points over the course of the reaction. Additionally, it was clear that some ls-{FeNO}^{7} complex had formed as evidenced by the shoulder at 476 nm, which grew simultaneously with the Soret band of the ls-{FeNO}^{6} complex. The complexity of this reaction is likely due to the strong donation of –SPhNHPhCH$_3$, which results in an equilibrium between the thiolate bound heme and valence tautomerizes to the ferrous thiyl radical, as shown in equation 1. Despite being equipped with an intramolecular hydrogen bond, the steric bulk between the porphyrin scaffold and the axial ligand may strain the hydrogen bonding interaction that would prevent tautomerization to the ferrous heme thiyl radical complex. Interestingly, as the solution was warmed from -80 °C, the absorbance of the 439 nm band continued to increase until -48 °C where the complex decayed to the expected decomposition product, [Fe(3,5-Me-BAFP)(NO)]. Unfortunately, several iterations of this experiment consistently displayed a mixture of these species at different temperatures and

equivalents of NO gas added. Due to unwanted side reactions observed in these experiments, this complex was deemed an unsuitable model for the active site of Cyt P450nor for the generation of the ferric heme NO adduct.

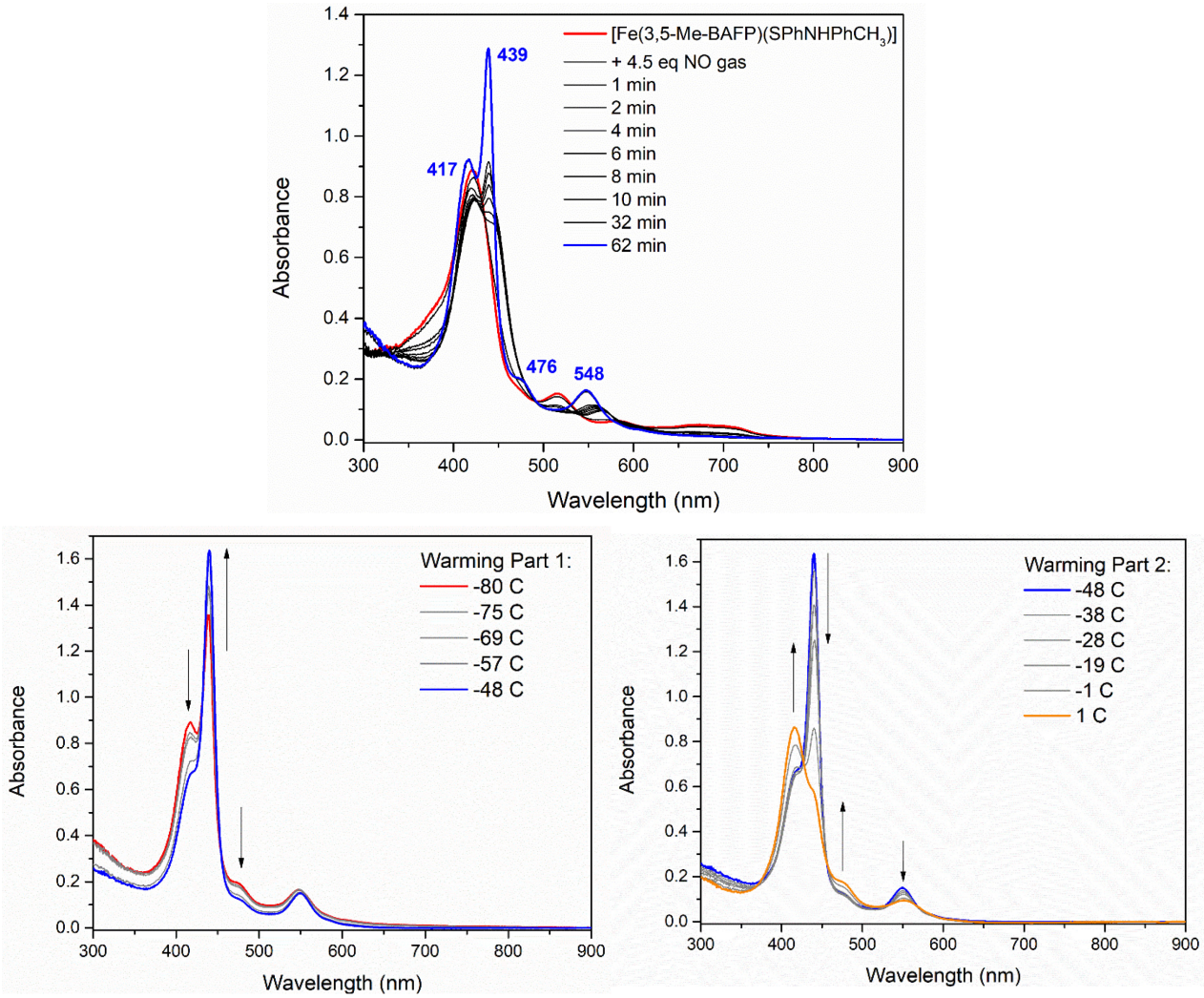

Figure 3.16 UV-vis spectral overlay of NO addition to the [Fe(3,5-Me-BAFP)(SPhNHPhCH$_3$)] at -80 °C in toluene. (top) Addition of 4.5 eq of NO gas over the course of 60 min. (bottom) Warming of the solution from -80 °C to the decomposition of the {FeNO}^{6} complex.

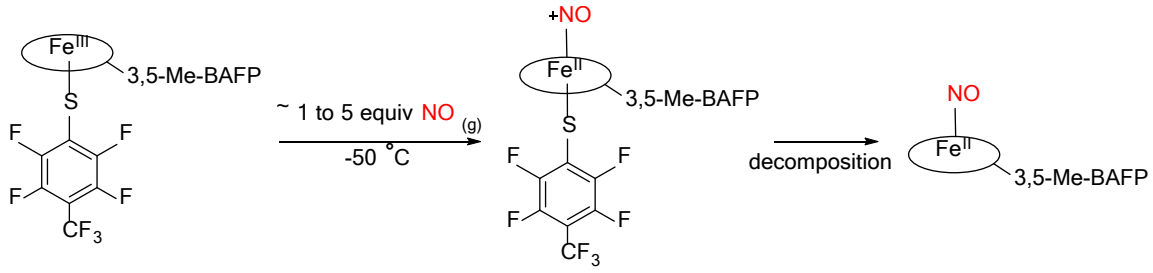

Figure 3.17 Synthetic scheme for the desired complex [Fe(3,5-Me-BAFP)(SPhNHPhCH$_3$)(NO)], followed by decomposition to the ls-{FeNO}^{7} complex, [Fe(3,5-Me-BAFP)(NO)] in two steps.

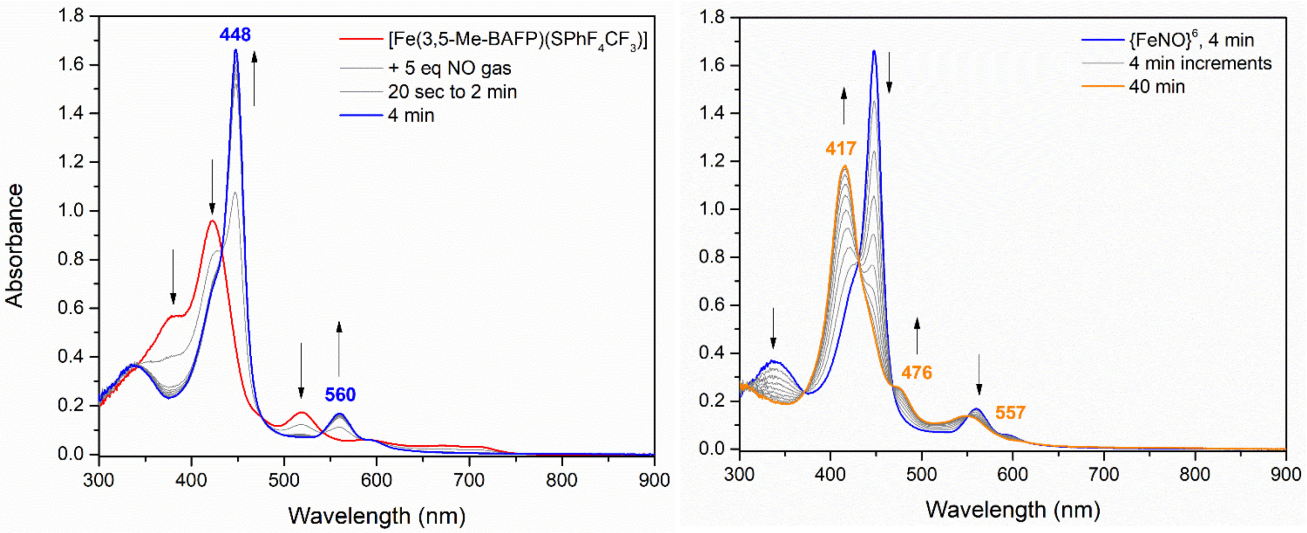

Figure 3.18 UV-vis spectral overlay of [Fe(3,5-Me-BAFP)(SPhF$_4$CF$_3$)] and 5 equivalent of NO gas at -50 °C in toluene. (left) formation of the {FeNO}^{6}, [Fe(3,5-Me-BAFP)(SPhF$_4$CF$_3$)(NO)] (right) decay to the {FeNO}^{7}, [Fe(3,5-Me-BAFP)(NO)].

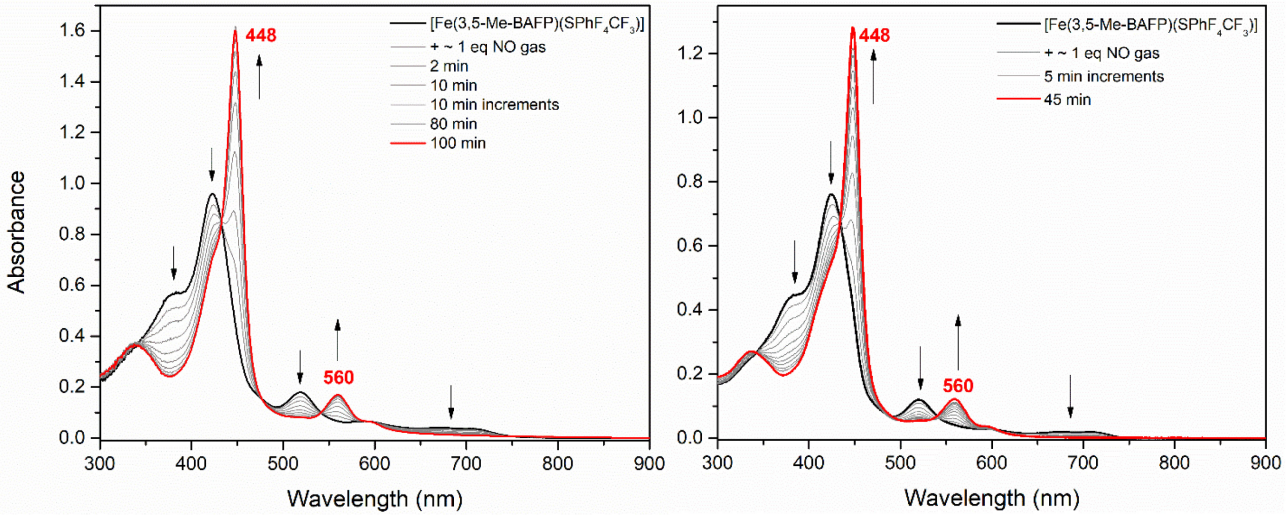

Figure 3.19 Overlay of the UV-vis spectra of [Fe(3,5-Me-BAFP)($SPhF_4CF_3$)] before and after addition of ~ 1 equivalent of NO gas at -50 °C in toluene (left) and at -40 °C in chlorobenzene (right).

On the other hand, repeating the reaction with [Fe(3,5-Me-BAFP)($SPhF_4CF_3$)] and 5 equivalents of NO gas at -50 °C in toluene led to successful formation of the ls-$\{FeNO\}^6$ adduct within 4 minutes, as shown in **Figure 3.18**. Additionally, this complex formed the ls-$\{FeNO\}^6$ complex and decayed to the expected ls-$\{FeNO\}^7$ complex in two distinct steps within 40 minutes, suggesting clean formation without side reactions. While this experiment yielded promising results, the formation of this complex needed to be optimized with ~1 equivalent of NO rather than 5 equivalents to lengthen the lifetime of the ls-$\{FeNO\}^6$ adduct for reactivity studies. As shown in **Figure 3.19**, the successful nitrosylation of the precursor was observed over the course of 1 hour to form the ls-$\{FeNO\}^6$ complex. Similar observations were made when this experiment was repeated in chlorobenzene. Once formed, the ls-$\{FeNO\}^6$ complex was stable for a few hours with minimal decay at temperatures of -50 °C and below, as shown in **Figure 3.20**. As expected,

[Fe(3,5-Me-BAFP)(SPhF$_4$CF$_3$)(NO)] decayed slowly with substantial decomposition between -30 and -10 °C. This is in comparison to the [Fe(TPP)(SPhF$_4$CF$_3$)(NO)] analog where significant decay is observed around -50 °C as the solution is warmed.[45]

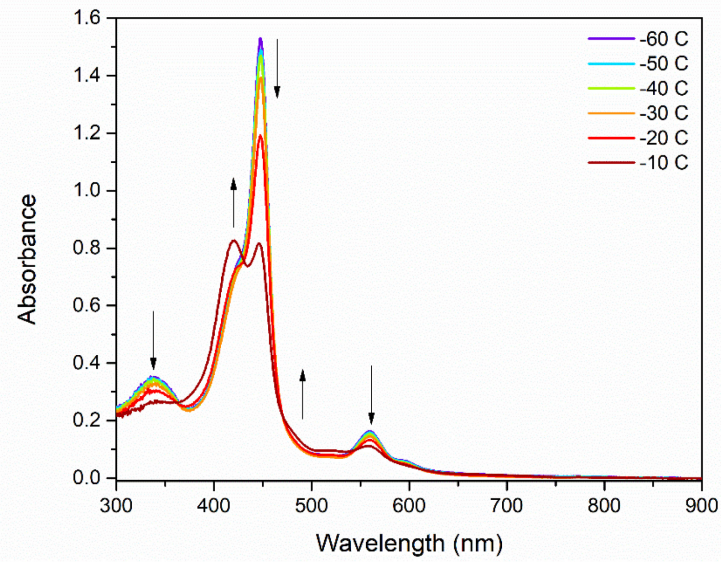

Figure 3.20 UV-vis spectral overlay of the thermal decay to the {FeNO}^{7}, [Fe(3,5-Me-BAFP)(NO)] in toluene. The temperature starts at -60 °C due to the accidental over addition of dry ice.

Next, [Fe(3,5-Me-BAFP)(SPhF$_4$CF$_3$)(NO)] was characterized by NMR spectroscopy. For these experiments, a ~ 10 mM solution of [Fe(3,5-Me-BAFP)(SPhF$_4$CF$_3$)] in toluene-d$_8$, or a mixture of toluene-d$_8$/chlorobenzene-d$_5$ was transferred to a 10 mL Schlenk finger and cooled to -60 to -65 °C. Because the reaction between the precursor and NO gas could not be monitored directly for completion, the solution was freeze, pump, thawed four times prior to NO addition to ensure all NO dissolved in solution. The reaction mixture was stirred for 30 to 40 minutes to allow ls-{FeNO}^{6} formation before being transferred to an NMR tube in a cold copper block. The tube was transported from the glovebox to the NMR in an isopropanol/dry ice bath.

As shown in the ^{1}H NMR spectrum in **Figure 3.21**, several sharp peaks appear in the spectrum associated with a new diamagnetic species, which supports the successful formation of

the ls-{FeNO}^{6} adduct. Notably, the appearance of a new peak at 9.43 ppm correlates with the β-pyrrole proton signals of the porphyrin, further supporting this conclusion. This peak decays upon warming, completely disappearing by 0°C, which is in agreement with the results obtained by UV-vis spectroscopy shown in **Figure 3.20**. Once warmed to -10 °C, the appearance of a broad peak at ~8 ppm suggests the formation for the ls-{FeNO}^{7} complex, as expected with warming, as shown in **Figure 3.23**. The results from ^{19}F NMR experiments are in agreement with the formation of the thiolate bound ls-{FeNO}^{6} complex with three new peaks present at -56.41, -127.68, and -145.58 ppm, that disappear at the same temperature, **Figure 3.22**. With decomposition of this complex, three additional peaks appear at -56.78, -130.32, and -139.29 ppm consistent with disulfide formation, known to form alongside the ls-{FeNO}^{7} complex.

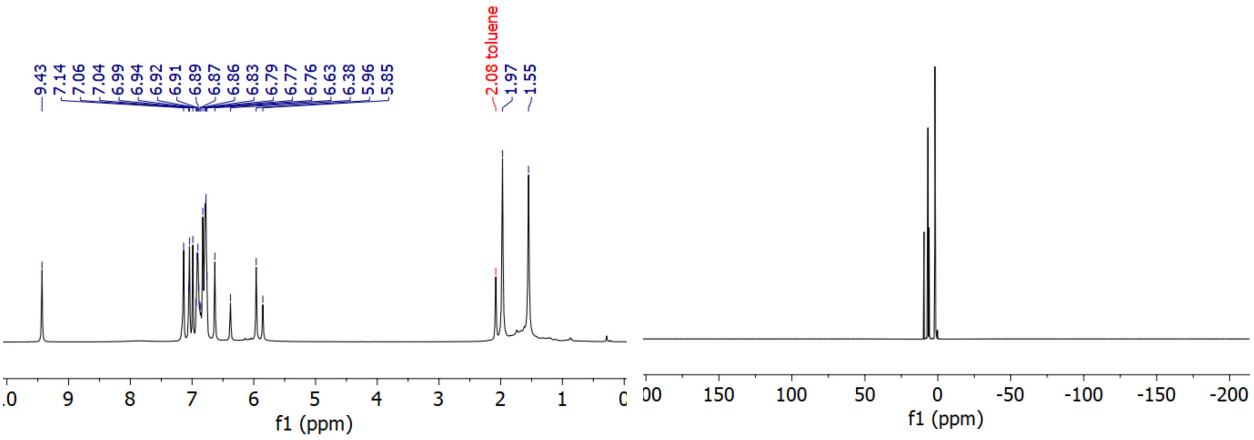

Figure 3.21 ^{1}H NMR spectrum of [Fe(3,5-Me-BAFP)(SPhF$_4$CF$_3$)(NO)] in toluene-d$_8$:chlorobenzene-d$_5$, zoomed in (left) and full spectrum (right). Most of the signals between 6.76 and 7.14 ppm correspond to solvent peaks: chlorobenzene-d$_5$, toluene-d$_8$, and fluorobenzene.

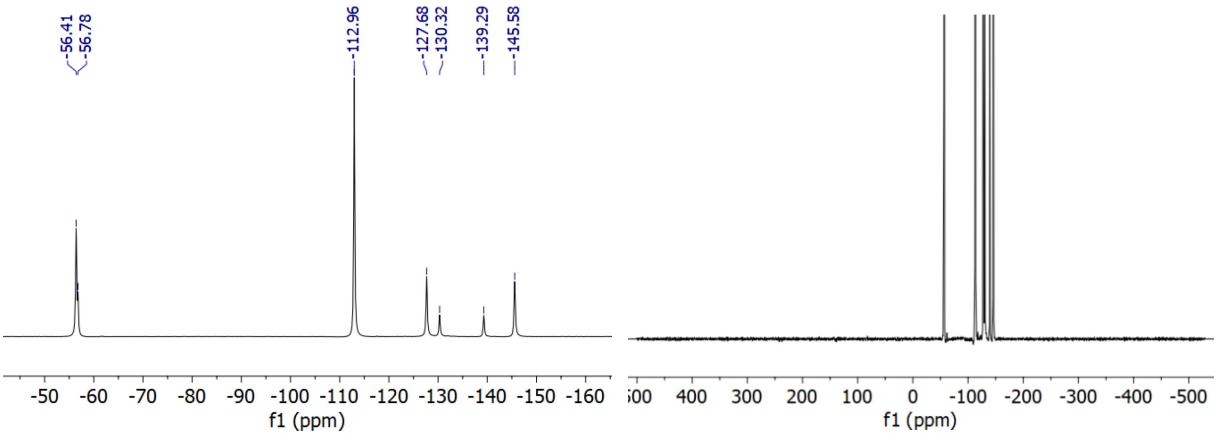

Figure 3.22 ^{19}F NMR spectrum of [Fe(3,5-Me-BAFP)(SPhF$_4$CF$_3$)(NO)] in toluene-d$_8$:chlorobenzene-d$_5$, zoomed in (left) and full spectrum (right). Referenced to fluorobenzene at -112.96 ppm.

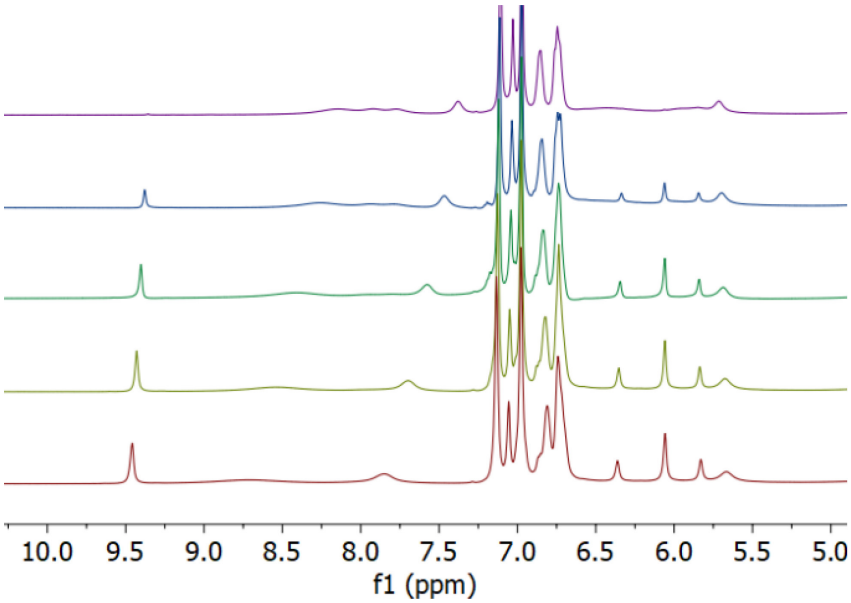

Figure 3.23 ^{1}H NMR spectra of [Fe(3,5-Me-BAFP)(SPhF$_4$CF$_3$)(NO)] in toluene-d$_8$:chlorobenzene-d$_5$.

3.4 Vibrational Characterization of [Fe(3,5-Me-BAFP)(SPhF$_4$CF$_3$)(NO)]

Complex [Fe(3,5-Me-BAFP)(SPhF$_4$CF$_3$)(NO)] was vibrationally characterized by IR and rRaman spectroscopy to determine the N-O and Fe-NO stretching frequencies for comparison to the vibrational data of the ferric NO adduct of Cyt P450nor. Depending on the technique, a 20 mM (IR) or 1 mM (rRaman) solution of the precursor was prepared in a mixture of dichloromethane and toluene. The solution was transferred to a 10 mL Schlenk finger, which underwent four freeze, pump, thaw cycles prior to NO addition and was allowed to stir for 30 to 40 minutes. The solution was then transferred cold to either the precooled solution IR cell or an EPR tube for rRaman analysis.

As shown in **Figure 3.24**, [Fe(3,5-Me-BAFP)(SPhF$_4$CF$_3$)(NO)] shows an N-O stretching frequency of 1860 cm^{-1} that shifts to 1823 cm^{-1} upon ^{15}N isotopic labeling. As the complex is warmed, the ls-{FeNO}^{6} decays to the ls-{FeNO}^{7} complex with an N-O stretching frequency of 1685 cm^{-1} (1656 cm^{-1} upon ^{15}N isotopic labeling). Additionally, the Fe-NO stretching frequency of the ls-{FeNO}^{6} complex was determined to be 544 cm^{-1} that shifts to 533 cm^{-1} upon ^{15}N isotopic labeling, as shown in **Figure 3.25**. Interestingly, the Fe-NO and N-O stretching frequencies of WT Cyt P450nor were reported to be 530 and 1851 cm^{-1}, respectively, as shown in **Table 3.1**. It must be noted that the Fe-NO and N-O stretches obtained for [Fe(3,5-Me-BAFP)(SPhF$_4$CF$_3$)(NO)] are closer to those reported for the WT enzyme than those reported for the analogous tetraphenylporphyrin complex, [Fe(TPP)(SPhF$_4$CF$_3$)(NO)], which are 543 and 1867 cm^{-1}, respectively.[40,45]

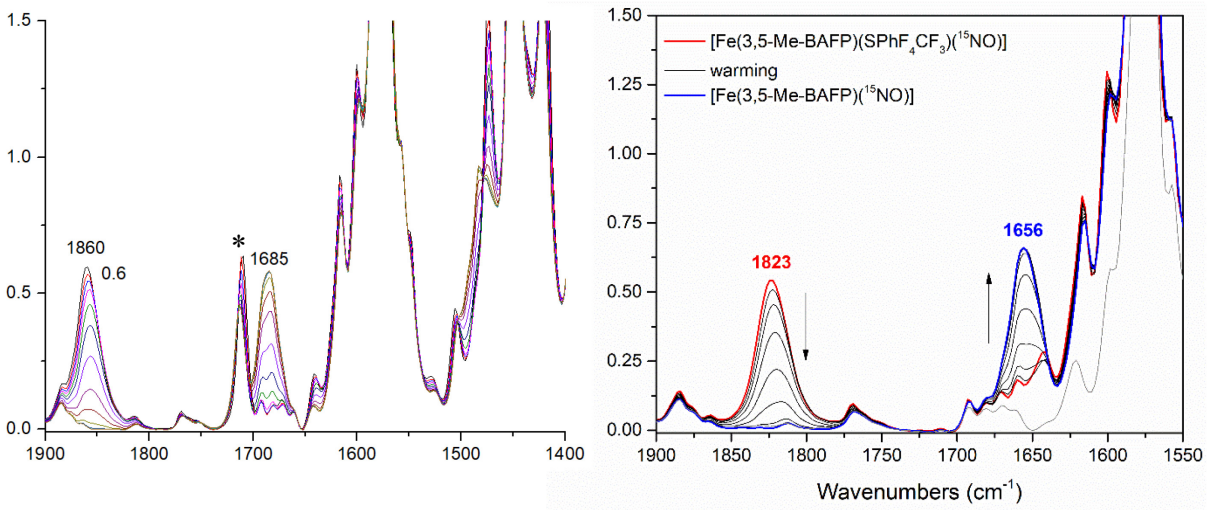

Figure 3.24 Solution IR spectra of [Fe(3,5-Me-BAFP)($SPhF_4CF_3$)(NO)] in 1:1 CH_2Cl_2. The * indicates acetone contamination (left) natural abundance isotopic complex (right) ^{15}N isotopically labeled complex.

Table 3.1 Vibrational Data for Relevant $\{FeNO\}^6$ Complexes

	νFe-N (cm^{-1})	νN-O (cm^{-1})	Ref.
Cytochrome P450nor	530	1851	[40]
[Fe(TPP)($SPhF_4CF_3$)(NO)]	543	1867	[45]
[Fe(3,5-Me-BAFP)($SPhF_4CF_3$)(NO)]	535/544	1860	t.w.

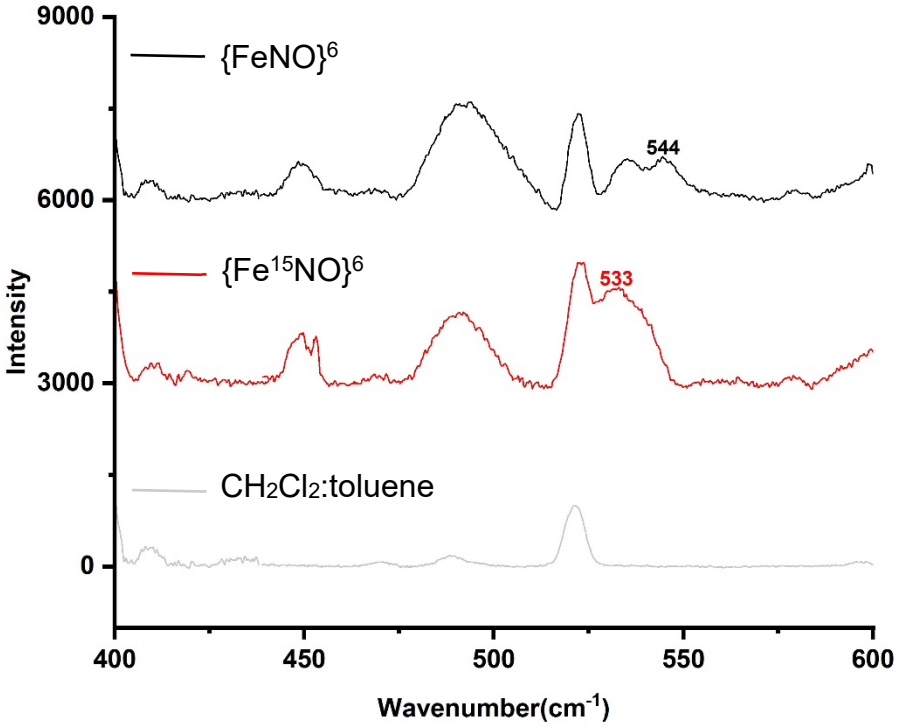

Figure 3.25 rRaman spectra of [Fe(3,5-Me-BAFP)(SPhF$_4$CF$_3$)(NO)] in 1:1 CH_2Cl_2. Natural abundance (black) ^{15}N isotopically labeled complex (red) CH_2Cl_2:toluene background (gray).

Based on the characterization discussed above, [Fe(3,5-Me-BAFP)(SPhF$_4$CF$_3$)(NO)] was determined to be a promising model for the active site of Cyt P450nor. In comparison to other thiolate bound heme {FeNO}^{6} complexes reported in the literature, this complex appears to be the most stable based on the extended lifetime of this species by UV-vis spectroscopy, coupled with the ability to obtain the first NMR spectrum of a thiolate-bound ferric heme-NO complex. Additionally, the vibrational characterization obtained by IR and rRaman spectroscopy indicates that this complex provides a good electronic model for the FeNO unit in the active site of Cyt P450nor.

3.5 Hydride Addition to [Fe(3,5-Me-BAFP)(SPhF$_4$CF$_3$)(NO)]

With the [Fe(3,5-Me-BAFP)(SPhF$_4$CF$_3$)(NO)] in hand, reactivity studies were conducted with a hydride source, [TBA](BH$_4$), with the intent to form the thiolate bound heme nitroxyl complex. Initial experiments were monitored by solution IR spectroscopy using the same procedure described on page 83 in 1:1 chlorobenzene-d$_5$:toluene-d$_8$. If hydride transfer is successful, the resulting IR spectrum should show the absence of the NO stretch of the {FeNO}^{6} complex at 1853 cm^{-1} (**Figure 3.26**).

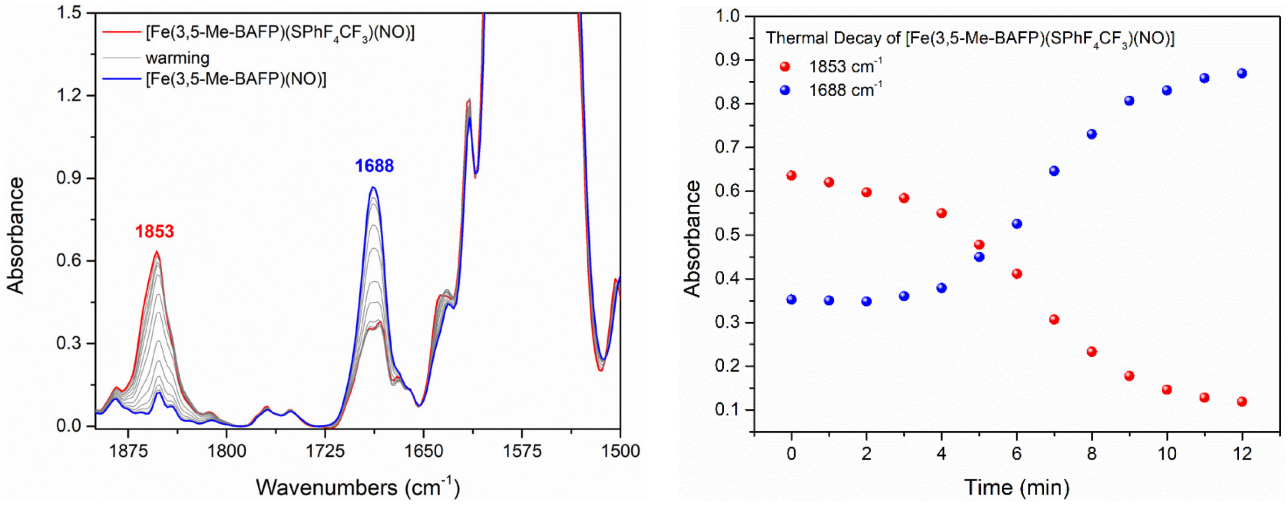

Figure 3.26 Solution IR spectra of the thermal decay of [Fe(3,5-Me-BAFP)(SPhF$_4$CF$_3$)(NO)] in chlorobenzene-d$_5$:toluene-d$_8$.

The decay of the {FeNO}^{6} was monitored to establish a baseline absorbance of the 1853 cm^{-1} peak at maximum nitrosylation. Based on the solution IR data shown in **Figure 3.26**, the NO stretch of the [Fe(3,5-Me-BAFP)(SPhF$_4$CF$_3$)] demonstrated an absorbance of ~ 0.64 that decayed to ~ 0.1. The decay of the {FeNO}^{6} complex is directly correlated with the growth of the 1688 cm^{-1} peak, indicating formation of the {FeNO}^{7} complex, [Fe(3,5-Me-BAFP)(NO)]. The reaction was repeated with a 25 mM solution of [Fe(3,5-Me-BAFP)(SPhF$_4$CF$_3$)(NO)] assuming full NO binding. The reaction was diluted to 20 mM with the addition of 1 equivalent of

tetrabutylammonium borohydride, [TBA](BH$_4$) and allowed to stir for 2 minutes (**Figure 3.27**). The solution was transferred cold to a precooled solution IR cell where measurements were taken every minute until the reaction was complete. As shown in **Figure 3.28**, the NO stretch at 1853 cm^{-1} decreased by ~ 2/3 upon hydride addition. As the IR cell was warmed, the resulting {FeNO}^{6} in solution decayed to {FeNO}^{7}, indicating an incomplete reaction with the hydride. This reaction was repeated to ensure that the results were reproducible, as shown in **Figure 3.28**.

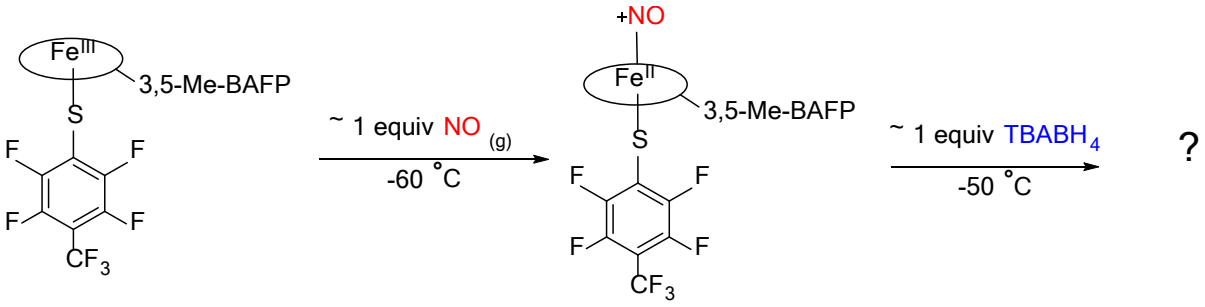

Figure 3.27 Synthetic scheme demonstrating *in situ* generation of the ls-{FeNO}^{6} complex, followed by hydride addition.

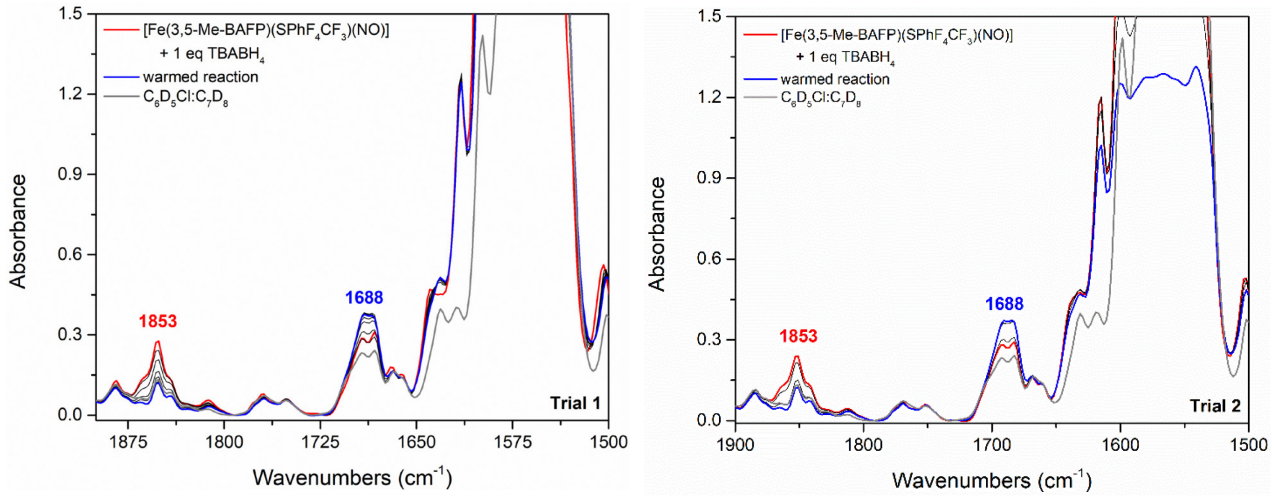

Figure 3.28 Solution IR spectra of the reaction of [Fe(3,5-Me-BAFP)(SPhF$_4$CF$_3$)(NO)] and 1 equivalent of [TBA](BH$_4$) in chlorobenzene-d$_5$:toluene-d$_8$.

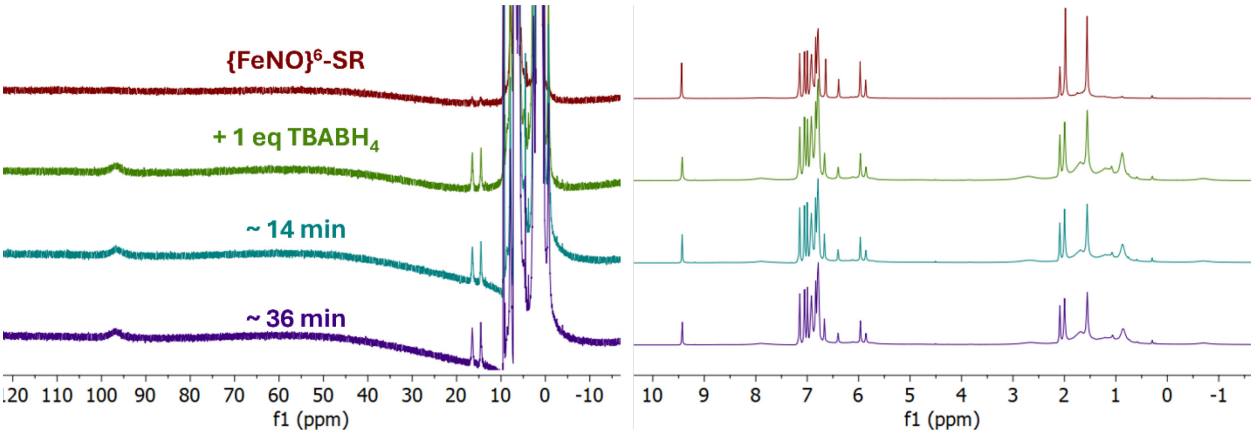

Figure 3.29 ^{1}H NMR spectra of the addition of 1 equivalent of [TBA](BH$_4$) to [Fe(3,5-Me-BAFP)(SPhF$_4$CF$_3$)(NO)] in 1:1 chlorobenzene-d$_5$:toluene-d$_8$ -50 °C. Full spectrum (left) and zoomed spectrum (right).

The reaction between [Fe(3,5-Me-BAFP)(SPhF$_4$CF$_3$)(NO)] and [TBA](BH$_4$) was monitored by both ^{1}H and ^{19}F NMR spectroscopy to directly monitor the{FeNO}^{6} upon hydride addition at -50 °C. As shown in **Figure 3.29**, most of the initial spectrum demonstrates full nitrosylation of the thiolate ferric heme, as evidenced by the absence of the β-pyrrole protons around 97 ppm. Upon hydride addition, there was a notable decrease in intensity of the 9.43 ppm indicating a reaction with the {FeNO}^{6} complex. This result agrees with the data obtained by solution IR, where the {FeNO}^{6} does not react completely with the hydride added to the reaction. Additionally, new peaks appear around 96.91, 14.54 and 16.55 ppm upon hydride addition indicating the formation of the ferric heme thiolate complex at -50 °C (**Figure 3.30**).

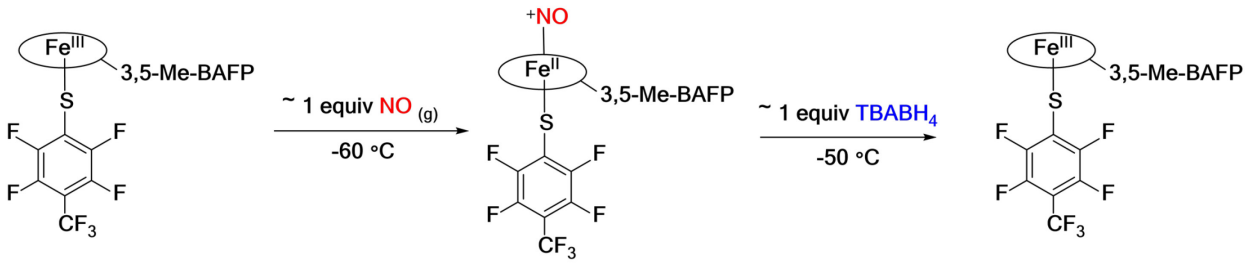

Figure 3.30 Synthetic Scheme demonstrating reformation of the ferric heme-thiolate complex, [Fe(3,5-Me-BAFP)(SPhF$_4$CF$_3$)] upon [TBA](BH$_4$) addition to [Fe(3,5-Me-BAFP)(SPhF$_4$CF$_3$)(NO)].

The ^{19}F NMR spectra provide more information about this reaction, as shown in **Figure 3.31**. Here, the formation of the ferric heme thiolate was confirmed with signals at 142.20 and -193.18 ppm. The third signal associated with this complex between 200 and 300 ppm was too broad to be observed in this spectrum. It should be noted that the disulfide peaks present in the $\{FeNO\}^6$ spectrum disappear upon hydride addition to form two new peaks associated with the para-CF_3 at -53.89 and -55.31 ppm, as well as aryl-F peaks at -135.45, -138.22, -146.94, and -150.28 ppm, indicating the formation of two new species. Based on these results, the reaction scheme was redrawn to include the presence of the disulfide in the reaction, as shown in **Figure 3.32**.

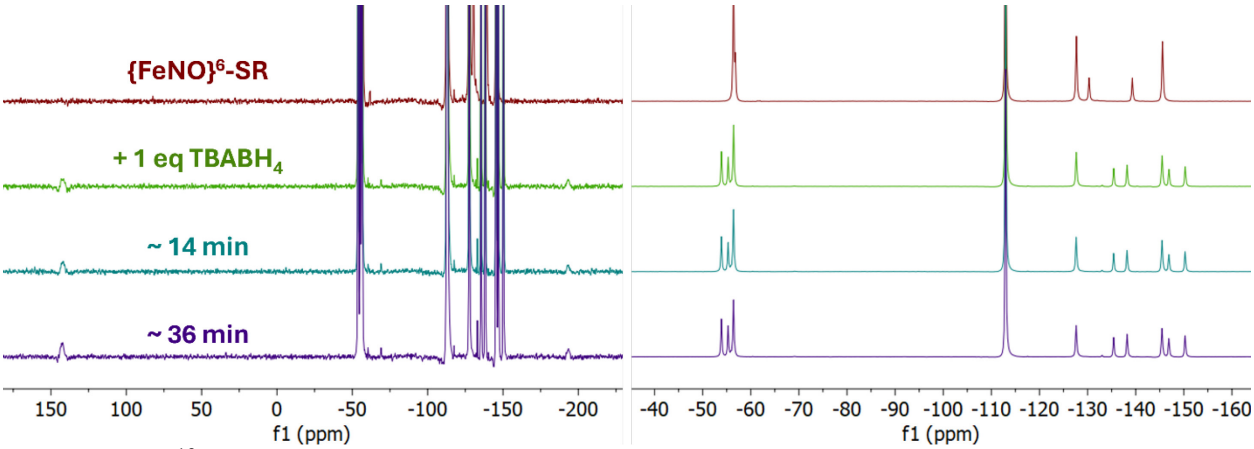

Figure 3.31 ^{19}F NMR spectra of the addition of 1 equivalent of [TBA](BH_4) to [Fe(3,5-Me-BAFP)($SPhF_4CF_3$)(NO)] in 1:1 chlorobenzene-d_5:toluene-d_8 at -50 °C. Full spectrum (left) and zoomed spectrum (right). Spectra were referenced to fluorobenzene at -112.96 ppm.

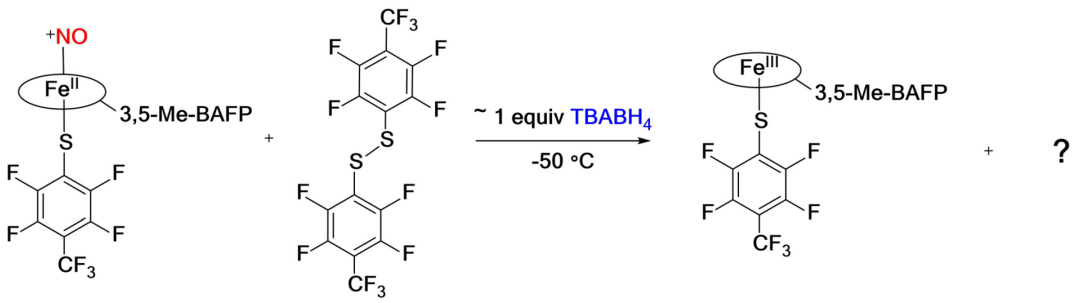

Figure 3.32 Synthetic Scheme demonstrating the presence of disulfide prior to [TBA](BH_4) addition. The reaction between the hydride and disulfide lead to unknown products. The presence of the ls-{FeNO}^{7} complex, [Fe(3,5-Me-BAFP)(NO)], was excluded for clarity.

Since no changes were observed by either the ^{1}H or ^{19}F spectra over the course of 36 minutes, the reaction was warmed in 10 °C increments. As shown in the ^{1}H NMR spectra in **Figure 3.33**, the remaining {FeNO}^{6} showed full decay at 0 °C. This is further confirmed by ^{19}F NMR as shown in **Figure 3.34**. It must be noted that a new peak was observed at 4.5 ppm as early as -30 °C. Based on both ^{1}H and ^{19}F NMR, the amount of ferric heme thiolate shows slight increase with warming in addition to the appearance of a broad doublet ~ 8 ppm indicates decomposition to the {FeNO}^{7} complex. Based on the ^{19}F NMR in **Figure 3.34**, the new peaks observed upon hydride addition grew as the temperature increased indicating that these species are stable at room temperature.

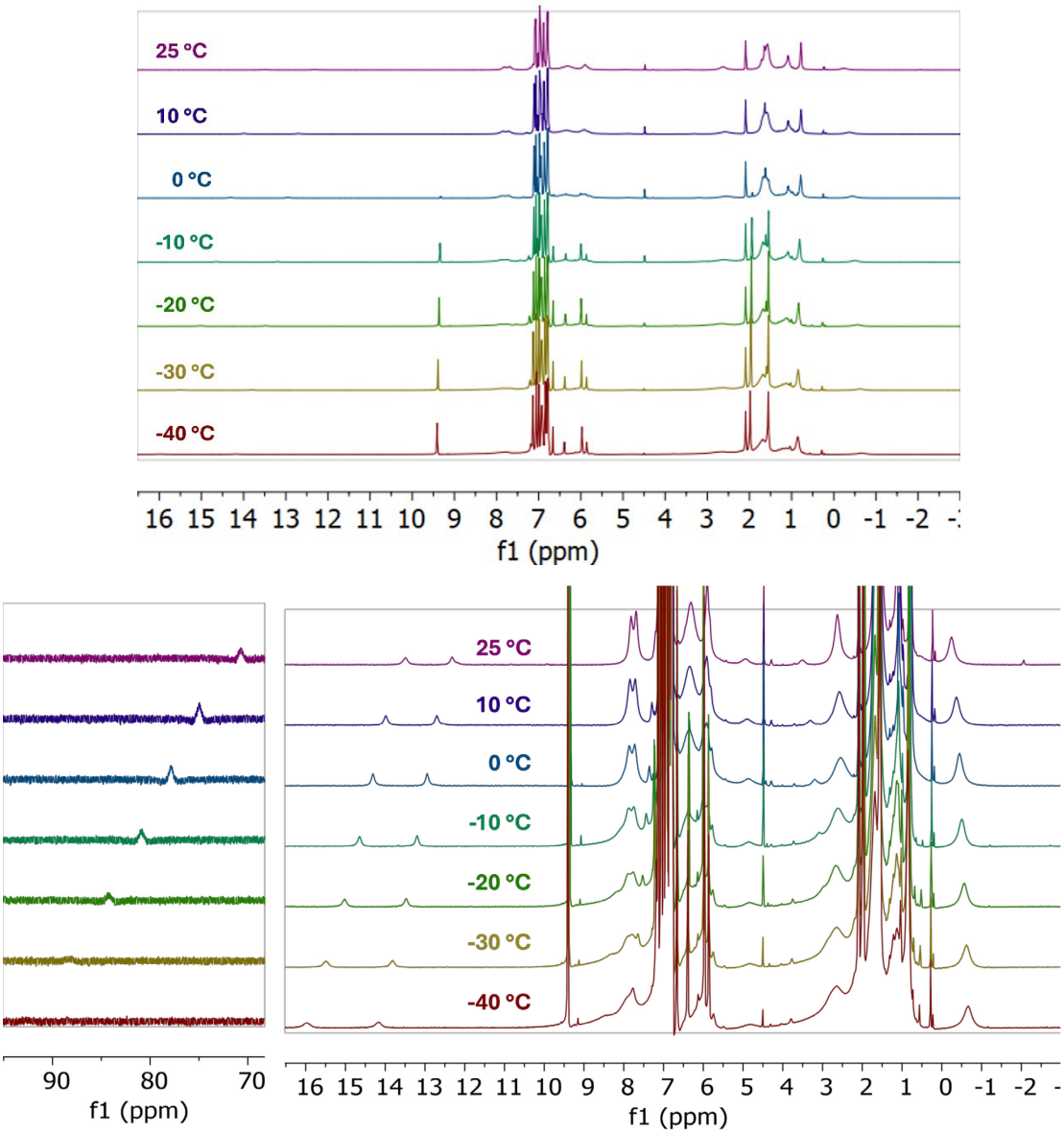

Figure 3.33 VT ^{1}H NMR spectra of the reaction between [Fe(3,5-Me-BAFP)(SPhF$_4$CF$_3$)(NO)] and 1 equivalent of [TBA](BH$_4$) to in 1:1 chlorobenzene-d$_5$:toluene-d$_8$. The diamagnetic spectrum (top) shows the decay of the {FeNO}^{6} complex at 9.43 ppm and the appearance of a new species around 4.5 ppm. The paramagnetic spectrum (bottom) shows prominent growth of the {FeNO}^{7} around 8 ppm. The amount of ferric heme thiolate complex appears to increase with warming.

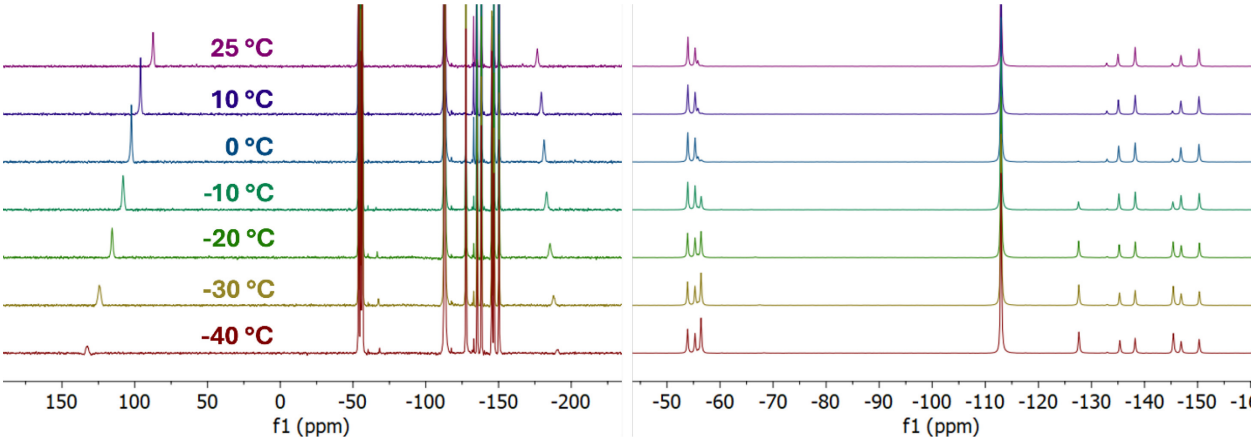

Figure 3.34 VT ^{19}F NMR spectra of the reaction between [Fe(3,5-Me-BAFP)($SPhF_4CF_3$)(NO)] and 1 equivalent of [TBA](BH_4) to in 1:1 chlorobenzene-d_5:toluene-d_8. The full spectra (left) confirmed a slight increase in the ferric heme thiolate complex with warming. The zoomed spectra (right) confirmed the decay of the $\{FeNO\}^6$ complex with the growth of two stable species with respect to temperature. Spectra were referenced to fluorobenzene at -112.96 ppm.

As discussed above, the disulfide appears to react with the hydride source to form two new species by ^{19}F NMR spectroscopy. Given the reducing nature of [TBA](BH_4), the disulfide was likely reduced to the corresponding thiol and thiolate species, $HSPhF_4CF_3$ and [TBA]($SPhF_4CF_3$), generating strong nucleophiles in solution. Since the $\{FeNO\}^6$ complex contains an electrophilic nitrosonium, these nucleophilic species could scavenge the bound NO^+ to form the corresponding RSNO, $ONSPhF_4CF_3$, as well as the starting ferric heme thiolate complex, [Fe(3,5-Me-BAFP)($SPhF_4CF_3$)] observed by NMR (**Figure 3.35**). This possibility was examined by preparing an authentic $ONSPhF_4CF_3$ species by reaction of the thiol and isoamyl nitrite. As shown in **Figure 3.36**, the $ONSPhF_4CF_3$ shows signals at -56.58, -129.41, and -139.46 ppm by ^{19}F NMR spectroscopy and was therefore not observed upon hydride addition to the $\{FeNO\}^6$ reaction solution, **Figure 3.31** and **Figure 3.34**.

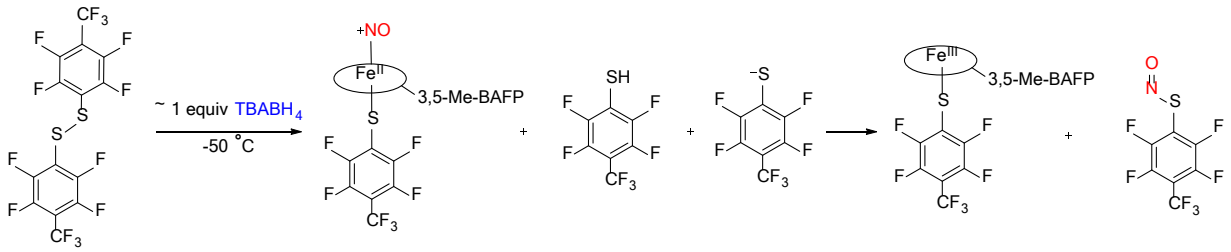

Figure 3.35 Proposed reaction scheme for RSNO, $ONSPhF_4CF_3$ formation.

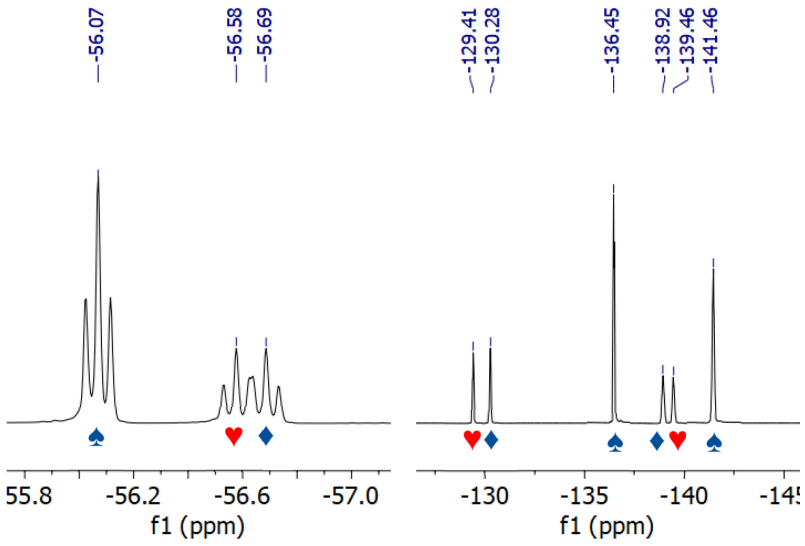

Figure 3.36 ^{19}F NMR spectrum of $ONSPhF_4CF_3$ (red hearts) in toluene-d_8:chlorobenzene-d_5 at room temperature. Thiol (blue spades) and disulfide (blue diamonds) are also present in the spectrum. Spectrum was referenced to fluorobenzene at -112.96 ppm (not shown).

Due to the formation of multiple species over the course of the reaction, the formation of a thiolate bound heme nitroxyl complex could not be confirmed. Therefore, another experiment was performed using PPh_3 as a selective trap for free nitroxyl species formed in the reaction according to equation (2).[6,121-123]

$$Ph_3 + HNO \rightarrow HN{=}PPh_3 + O{=}PPh_3 \quad (2)$$

The reaction was repeated by sequentially forming the [Fe(3,5-Me-BAFP)(SPhF$_4$CF$_3$)(NO)] prior to hydride addition using [THA](BH$_4$). After addition of the hydride source the reaction was stirred for two minutes and was subsequently diluted in an air free NMR tube containing excess PPh$_3$. As shown in **Figure 3.37**, triphenyl phosphene persisted in the NMR tube at -50 and 25 °C, indicating that no free HNO is formed in this reaction.

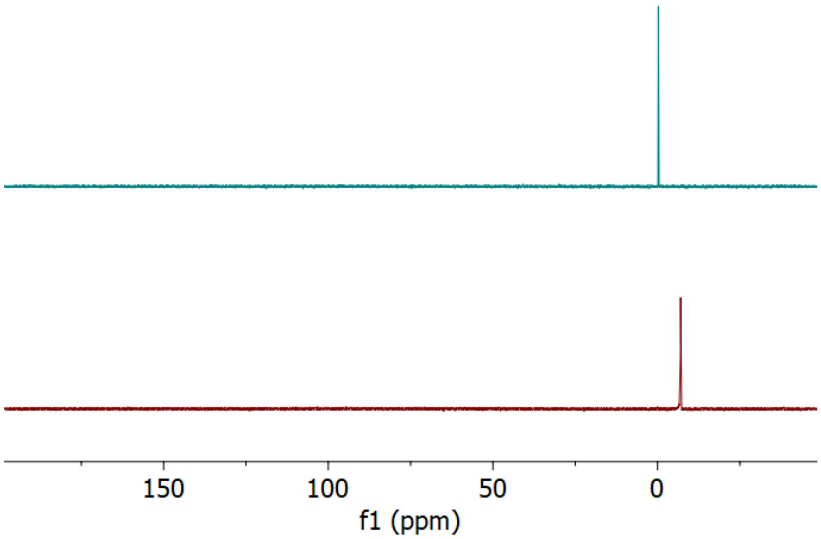

Figure 3.37 ^{31}P NMR spectrum of the [Fe(3,5-Me-BAFP)(SPhF$_4$CF$_3$)(NO)] and [THA](BH$_4$) followed by addition of PPh$_3$ after 2 minutes of reaction time. 25 °C (teal) and -50 °C (red).

3.6 Discussion

In this chapter, the bulky bis-picket fence porphyrin was used to synthesize a thiolate bound {FeNO}^{6} complex, [Fe(3,5-Me-BAFP)(SPhF$_4$CF$_4$)(NO)]. The formation of the {FeNO}^{6} was monitored by UV-vis spectroscopy at -50 °C. With the addition of ~5 equivalents of NO gas, the formation and decay of the {FeNO}^{6} occurred in two distinct steps within 40 minutes indicating a clean formation of the desired complex prior to its decomposition to the {FeNO}^{7} complex. The optimization of this reaction with ~ 1 equivalent of NO shows full NO binding within 45 minutes to an hour depending on the solvent. This data demonstrates that there is a prolonged window of

stability of the [Fe(3,5-MeBAFP)(SPhF$_4$CF$_3$)(NO)] with full decay between -10 and 0 °C. The decay of this complex begins ~ 10 °C higher than the previously generated phenol thiolate [Fe(TPP)(SR)(NO)] complexes which fully decay between -20 and -10 °C.[45] With this increase in stability, the first NMR spectra was obtained for a thiolate bond {FeNO}^{6} synthetic model complex. By solution IR and rRaman spectroscopy, the [Fe(3,5-Me-BAFP)(SPhF$_4$CF$_3$)(NO)] was determined to be a good electronic model for the Cyt P450nor active site with N-O and Fe-N stretching frequencies of 1860 and 544 cm^{-1} in toluene:CH_2Cl_2 which are comparable to those reported for the Cyt P450nor with N-O and Fe-N stretching frequencies of 1851 and 530 cm^{-1}.

Initial reactivity between the [Fe(3,5-Me-BAFP)(SPhF$_4$CF$_3$)(NO)] and hydride [TBA](BH$_4$) was monitored by solution IR spectroscopy. After stirring the reaction for ~ 2 minutes, the spectrum demonstrates a significant decrease in the NO stretch at 1853 cm^{-1}, where it was estimated that ~ 1/3 of the {FeNO}^{6} remained post reaction. As the reaction was warmed, the intensity of the NO stretch at 1688 cm^{-1} was also significantly lower than observed for the control reaction. Based on this result, the {FeNO}^{6} appears to react with the added hydride source where the product formed does not decay to the {FeNO}^{7} complex. This reaction was reproducible, further confirming this conclusion.

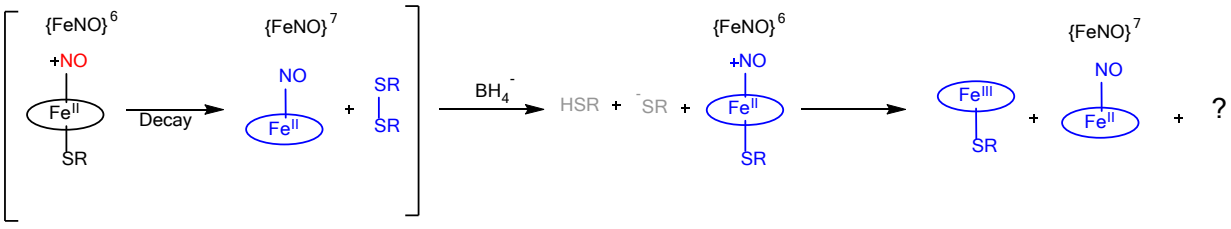

Figure 3.38 Proposed reaction scheme for the reaction of [Fe(3,5-Me-BAFP)(SPhF$_4$CF$_3$)(NO)] and the borohydride salt. The species in brackets are present prior to hydride addition due to the sensitive conditions required to synthesize the ls-{FeNO}^{6} complex. SR = -SPhF$_4$CF$_3$.

The reaction was directly monitored by NMR spectroscopy to observe the species formed with hydride addition. According to the NMR results, the reaction sequence summarized in **Figure 3.38** is proposed. The initial spectrum shows full nitrosylation of the ferric heme thiolate complex with an apparent overaddition of NO, based on the disulfide signals present in the ^{19}F NMR spectrum. Since these signals were not present in the ^{19}F NMR spectrum of the ferric heme thiolate precursor prior to NO addition, it is safe to assume some of the ls-{FeNO}^{6} complex decomposed to the disulfide and the corresponding ls-{FeNO}^{7} complex. Upon hydride addition, features associated with the ls-{FeNO}^{6} complex appear to decrease immediately, based on both the ^{1}H and ^{19}F NMR data, in agreement with the observations of the solution IR experiment. Notably, disulfide consumption was observed in the ^{19}F NMR spectrum, indicating possible reduction upon hydride addition, resulting in the corresponding unbound thiolate and thiol. It is known that thiolates and thiols are highly reactive towards nitrosonium (NO^+) and nitroxyl (HNO) and can therefore act as an internal scavenger. Accordingly, the initial formation of a thiolate bound heme nitroxyl complex cannot be ruled out in these reactions.[6] The less sterically hindered free thiolate species, produced from the disulfide after hydride addition, might scavenge both free and bound nitroxyl species, before the more sterically hindered triphenylphosphine is able to react with the newly formed species, as shown by the lack of reactivity of PPh_3 in the ^{31}P NMR spectrum. Free nitroxyl in solution was ruled out by gas headspace IR spectroscopy, where no N_2O gas could be detected after warming the reaction solution.

On the other hand, the NMR data also indicates possible thiol and/or thiolate attack on the bound nitrosonium ligand of the ls-{FeNO}^{6} complex, resulting in its incomplete consumption and immediate formation of the ferric heme thiolate precursor complex, as discussed above

The identity of the two new species observed by ^{19}F NMR is currently unknown and is therefore represented in **Figure 3.38** as a question mark, "?". It is known that thiolates will also react with nitroxyl to form an N-hydroxylsulfenamide.[6,124,125] Alternatively, the potential thiolate or thiol formed upon disulfide reduction could attack the bound NO^+ of the ls-{FeNO}^{6} complex and result in RSNO formation, $ONSPhF_4CF_3$.[126] Though this species was not observed by ^{19}F NMR spectroscopy, RSNO compounds can be reductively cleaved by electron-rich organometallic complexes[127] Considering the electron withdrawing nature of this thiolate, the N-S bond of the $ON\text{-}SPhF_4CF_3$ could be weaker compared to electron donating thiolates and therefore cleavage of the N-S bond could be possible in this reaction due to the electron rich nature of the bis-picket fence porphyrin.[63,128] This reactivity could result in more side reactions after RSNO formation, increasing the complexity of the products made in the inital reaction between the disulfide and the borohydride. More work is needed to fully characterize the unknown products generated after hydride addition to the {FeNO}^{6}/disulfide reaction mixture, since the current proposed reaction in **Figure 3.38** is based on the major species observed by ^1H and ^{19}F NMR spectroscopy. With respect to HNO formation in this system, future work should focus on forming ls-{FeNO}^{6} complexes *without the formation of disulfides* in solution, so hydride transfer to the ls-{FeNO}^{6} can be assessed properly without a number of unwanted and possibly deleterious side reactions.

3.7 Experimental Section

General Considerations

All chemicals were purchased from commercial sources, including Sigma Aldrich, Fisher Scientific, and Cambridge Isotopes, and used without further purification unless noted below. Reactions were performed under inert atmosphere via Schlenk techniques. All solvents were dried

and distilled from CaH_2 and freeze pump thawed four times to remove water and dioxygen. Preparation and handling of air-sensitive materials were performed under a dinitrogen atmosphere in an MBraun glovebox, equipped with a circulating purifier (O_2, H_2O <0.1 ppm). H_2[3,5-Me-BAFP], [Fe(3,5-Me-BAFP)(Cl)][63]. Nitric oxide (Cryogenic Gases Inc., 99.95%) was first passed through an Ascarite II column and then a -80 ºC cold trap to remove higher nitrogen oxide impurities prior to use. Complexes and solvents were then exposed to NO via a Schlenk line. Isotopically labeled ^{15}NO was synthesized according to previously reported procedures.[100]

Physical Measurements

UV-vis Spectroscopy/Immersion Probe. All spectra were recorded using an Analytic Jena Specord S-600 Spectrometer. Using the same spectrometer, dip probe measurements were conducted using a Hellma low temperature immersion probe with a 10 mm pathlength. A 10 μM solution of the desired ferric heme thiolate bound complex was cooled between -40 and -45 °C in either toluene or chlorobenzene.

^{1}H NMR Spectroscopy. A Varian MR 500 and 600 instruments was used to record all NMR spectra at temperatures between -60 and 25 °C.

Elemental Analysis. Elemental analyses were conducted by Atlantic Microlabs (Norcross, GA)

Infrared Spectroscopy (ATR/KBr/Gas). Solid state and solution IR spectra were recorded using a Bruker Alpha-E FT-IR spectrometer. IR data for KBr disks were obtained on PerkinElmer BX and GX spectrometers. Solution IR experiments were conducted using a thin-layer solution cell

equipped with CaF_2 windows. The same instruments were used to conduct gas headspace measurements using a 10 cm Pike HT gas cell with CaF_2 windows.

Solution IR experiments were conducted with 0.35 mL of a 20 mM [Fe(3,5-Me-BAFP)($SPhF_4CF_3$)] in 1:1 toluene-d_8/chlorobenzene-d_5 for an appropriate solvent window. The solution was transferred to a 10 mL Schlenk finger which was sealed with a 14/20 septum and copper wire. The solution was freeze, pump, thawed four times to increase the solubility of the NO at low temperatures (-60 to -65 °C). The reaction was allowed to stir for 30 minutes prior to breaking the vacuum seal and septum removal. The solution was transferred to the precooled solution IR cell using a precooled plastic syringe. Measurements were taken every minute until full decomposition to the $\{FeNO\}^7$ complex.

Resonance Raman (rRaman). Experiments were performed using a INNOVA with a 457 nm excitation line from a Cobolt 08-DPL diode pumped laser and the laser power was set to 20 mW. Samples were prepared at 1mM in 1:1 CH_2Cl_2:toluene and frozen as a glass. Prior to data collection, samples were transferred to liquid nitrogen inside an EPR cold finger to keep samples frozen during measurements. The light scattered from the samples was focused on a Acton two-stage TriVista 555 monochromator and detected by a liquid N_2 cooled Princeton Instruments Spec-10:400B/LN CCD camera. The accumulation and exposure time for each sample was 12 acquisitions for 4 minutes, repeated three times to improve signal to noise. Spectra were plotted and baseline corrected using OriginPro 2024.

Sample concentration was 1mM in 1:1 CH_2Cl_2:toluene and were prepared in a 10 mL Schlenk finger sealed with a septum and copper wire. The solution was prepared for NO addition by four freeze, pump, thawed cycles to aid in NO solubility at low temperatures. The Schlenk

finger was cooled to -60 to -65 °C for 15 minutes. Next, ~1.2 eq of NO gas was added above the reaction solution and allowed to stir at low temperature for 30 minutes. The vacuum seal of the flask was carefully broken, and the solution was transferred to a precooled EPR tube in a copper block using a precooled glass pipette. The tube was removed from the glovebox and frozen in liquid nitrogen resulting in a glass for further measurements.

Synthetic Procedures

Synthesis of [Fe(3,5-Me-BAFP)(OCH_3)]. [Fe(3,5-Me-BAFP)(Cl)] (314.5 mg, 0.19 mmol) and potassium methoxide (65.3 mg, 0.93 mmol) were added to an oven-dried schlenk flask equipped with a stir bar. The solids were dissolved in 7 mL of dry dichloromethane and 1.5 mL of methanol, resulting in an immediate color change of the solution from brown to green. Once the reaction was complete as determined by UV-vis spectroscopy, the solvent was removed by vacuum. The resulting solid was redissolved in dry dichloromethane and filtered to remove excess potassium methoxide and KCl formed during the reaction. The filtrate was added to a round bottom flask and all solvent was removed by vacuum. The resulting black complex was suspended in dry methanol and collected by vacuum filtration and dried vigorously under vacuum at 120 °C. Yield: 286.4 mg (0.173 mmol, 91%). UV-vis (CH_2Cl_2): 424, 478, 584 nm. Elemental analysis: cald (found) for $C_{109}H_{92}F_3FeN_4O_{11}S•H_2O$: C, 77.98 (77.97); N, 3.34 (3.24); H, 5.82 (5.83); Cl, 0.00 (0.00).

General Synthesis of [Fe(3,5-Me-BAFP)(SR)] Complexes. The synthesis was adapted from a literature procedure. Under an inert atmosphere, [Fe(3,5-Me-BAFP)(OCH_3)] and desired thiol (1 equivalent) were dissolved in minimal dichloromethane causing the solution to change from brown to brown/red. The reaction was completed immediately by UV-vis spectroscopy. Next, all solvent

was removed, and the resulting black powder was suspended in pentanes and collected by vacuum filtration. The solid was washed with more pentanes and dried under vacuum over 100 °C overnight.

Synthesis of [Fe(3,5-Me-BAFP)(SPhF$_4$CF$_3$)]. Yield: 148.8 mg (0.079 mmol, 90%). UV-vis (CH_2Cl_2) 381, 423, 520, 593, 674, 714 nm; (toluene) 378, 423, 520, 589, 671, 706 nm; (chlorobenzene) 378, 425, 520, 594, 674, 709 nm. ^{1}H NMR (C_6D_5Cl): 70.92, 13.63, 12.45, 11.15, 10.18,7.78, 7.73, 6.55, 5.91, 5.08, 3.75, 1.78, -0.05, -1.95 ppm. ^{19}F NMR (C_6D_5Cl, fluorobenzene): 194.96 (O-ArF), 86.54 (p-CF_3), -176.83 (m-ArF) ppm. Elemental analysis: cald (found) for $C_{115}H_{92}F_7FeN_4O_8S$: C, 73.51 (73.47); N, 2.98 (2.96); H, 4.94 (4.90); S, 1.71 (1.58).

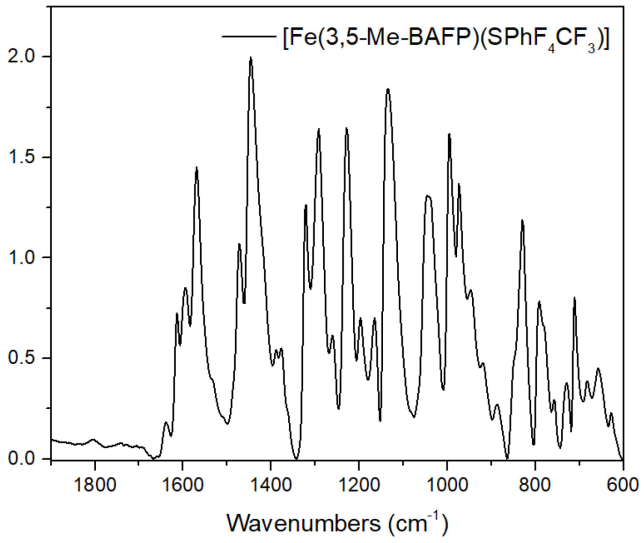

Figure 3.39 IR spectrum of [Fe(3,5-Me-BAFP)(SPhF$_4$CF$_3$)] (KBr).

Synthesis of [Fe(3,5-Me-BAFP)(SPhNHPhCH$_3$)]. Yield: 52 mg (0.028 mmol, 87%). UV-vis (CH_2Cl_2) 378, 421, 518, 584, 670, 712 nm; (toluene) 371, 421, 517, 583, 670, 706 nm. ^{1}H NMR (CD_2Cl_2): 80.10, 73.48, 66.89, -91.70 ppm. Elemental analysis: cald (found) for $C_{122}H_{104}FeN_5O_9S$: C, 78.27 (77.57); N, 3.74 (3.77); H, 5.60 (5.70); S, 1.71 (1.63).

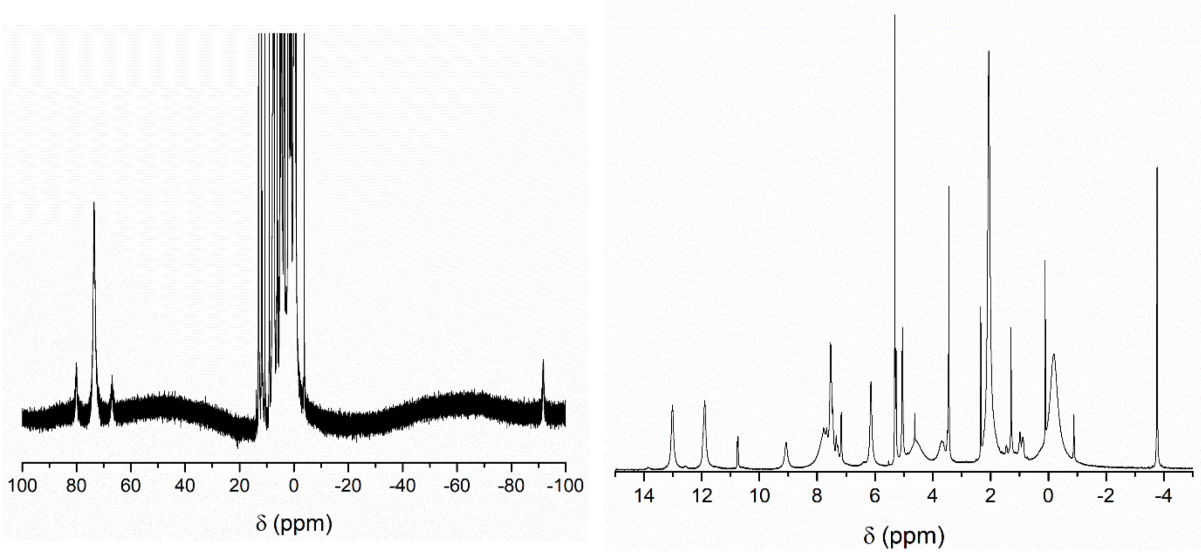

Figure 3.40 ^{1}H NMR spectrum of [Fe(3,5-Me-BAFP)(SPhNHPhCH$_3$)] in CD_2Cl_2.

Synthesis of [Fe(3,5-Me-BAFP)(SPhNHPhCF$_3$)]. Yield: DNR. UV-vis (CH_2Cl_2) nm. ^{1}H NMR (CD_2Cl_2): 78.25, 73.27, 64.98, -89.89 ppm. ^{19}F NMR (CD_2Cl_2, fluorobenzene): -57.43 (p-CF_3) ppm.

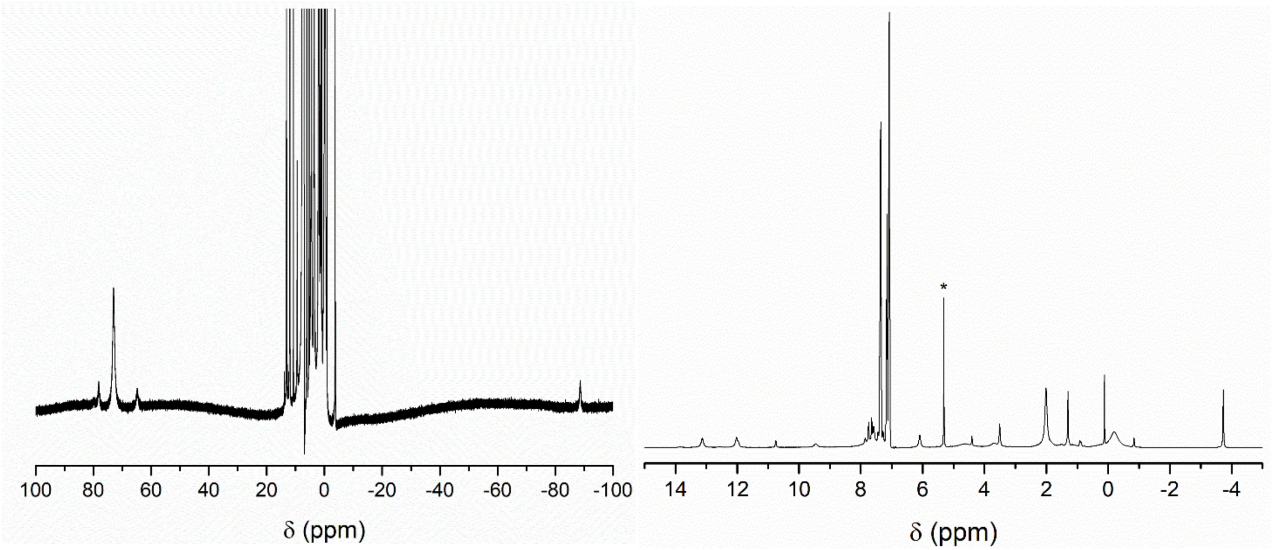

Figure 3.41 ^{1}H NMR spectrum of [Fe(3,5-Me-BAFP)(SPhNHPhCF$_3$)] in CD_2Cl_2.

Chapter 4 Second Coordination Sphere Hydrogen-Bonding Copper Complexes for Electrochemical Nitric Oxide Generation for Applications in Biomedical Devices

The development and execution of Route 2, as well as the [Cu(Amine-BMPA-Pr)(OAc)] and the NOA experiments were performed by rotation student Glorimar Miranda-Mendez.

4.1 Introduction

Nitric oxide (NO) is an endogenous gas that is known to play several physiological roles that are dependent on concentration and location within the human body.[69,129] For example, the endothelium continuously releases NO at low nM concentrations to control arteriolar tone and prevent platelet aggregation, while higher μM concentrations of NO are released in nasal endothelial cells and macrophages as an antimicrobial agent to fight infections.[70,130] Additionally, physiological NO aids in blood vessel vasodilation, wound healing, and promoting angiogenesis.[71-73,130-134] For these reasons, the use of NO in biomedical devices can help to prevent significant risk factors associated with IV catheters, which include blood clots and bacterial infections.[68]

Despite the physiological benefits of NO, the uncontrolled production of NO in the body leads to toxic effects. Therefore, it is essential to develop a controlled method of NO delivery to achieve the desired anti-microbial and anti-clotting effects without harm to the patient. To accomplish this task, NO can be produced electrochemically via nitrite reduction by a copper catalyst.[76] The inspiration for the catalyst comes from the active site of copper nitrite reductase (CuNIR), an enzyme which efficiently reduces NO_2^- to NO.[77] Electrochemical nitrite reduction to NO occurs in two steps as shown in equations 1 and 2, where L represents the ligand of the complex.

$$Cu^{II}(L) + e^- \rightarrow Cu^{I}(L) \quad (1)$$

$$Cu^{I}(L) + NO_2^- + 2H^+ \rightarrow Cu^{II}(L) + NO + H_2O \quad (2)$$

In collaboration with Professor Meyerhoff's laboratory at the University of Michigan, a series of water-soluble copper catalysts were synthesized using BMPA and BEPA carboxylate ligands that can generate controlled amounts of NO on demand in IV catheters.[82] These catalysts were analyzed by bulk electrolysis for electrochemical NO generation as a function of linker length of the BMPA and BEPA arms, as well as the length of the carboxylate arm, as shown in **Figure 4.1**.

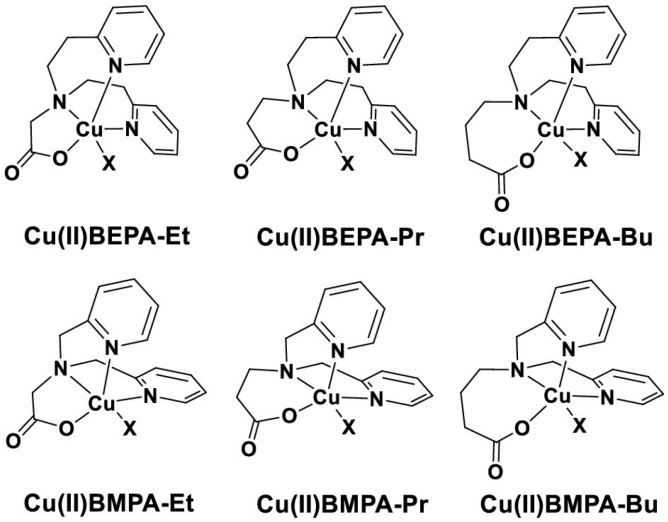

Figure 4.1 Previous BMPA and BEPA carboxylate complexes tested for electrochemical nitrite reduction to NO. X = OH_2, Cl, acetate, or nitrite depending on the conditions.

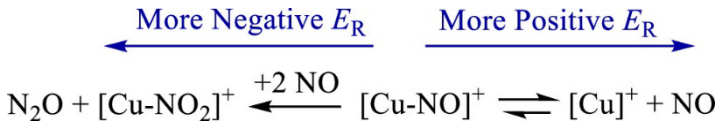

Figure 4.2 Reaction scheme summarizing selective NO generation by catalysts with more positive reduction potentials. Catalysts with more negative reduction potentials result in disproportionation of the generated NO to N_2O.

This series was used to tune the reduction potential of the Cu(II)/Cu(I) couple and study its role in nitrite reduction to nitric oxide. Based on this work, it was determined that copper complexes with more positive reduction potentials, for example $[Cu(BEPA\text{-}Bu)]^+$, were favored for selective NO generation without disproportionation to N_2O (**Figure 4.2**).[82] Additionally, complexes with more negative reduction potentials are more O_2 sensitive, resulting in inhibition of nitrite reduction upon reduction from Cu(II) to Cu(I) in the presence of air. Because IV catheters come in contact with O_2 rich blood, catalysts with more negative reduction potentials become less than ideal for this biomedical application.

In addition to synthesizing complexes with more positive reduction potentials, an alternative strategy is to tune the complexes to have a higher affinity for NO_2^- and increase the rate of reduction to NO. One way to achieve this would be to synthesize derivatives that include hydrogen bond donors in the second coordination sphere (SCS) that can interact with the Cu(I)-NO_2 moiety, allowing for facile proton donation, making nitrite reduction more efficient.[88,135] Multiple examples in the literature show that nitrite reduction to NO improves in the presence of hydrogen bond donors in the SCS in nonaqueous solutions.[85-87,136-140] A notable example was reported by Symes and coworkers where a tetradentate tris(2-methylpyridyl)amine (TMPA) derivative was synthesized with a pendent carboxylate group, as shown in **Figure 4.3**. It was determined that the pendent carboxylate acts as a proton donor to the bound nitrite that facilitates its reduction to NO. In fact, this catalyst was twice as effective in comparison to the pendent ester TMPA analog, further highlighting the importance of the proton donation in the SCS.[87]

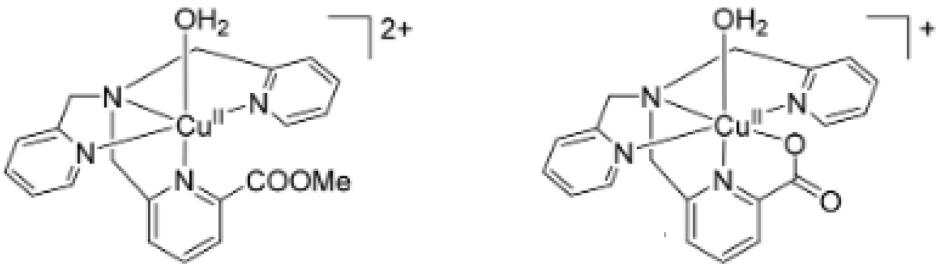

Figure 4.3 Derivative copper TMPA catalysts with appended carboxylate or ester groups for electrocatalytic nitrite reduction to NO in nonaqueous solvents.

In this chapter, two derivatives of $[Cu(BMPA\text{-}Pr)]^+$ were synthesized containing an amine and amide in the second coordination sphere in aqueous solutions for biomedical applications. Here, the synthesis of each ligand was optimized via two synthetic routes. The ligands were synthesized using the most efficient synthetic route and were metalated with $Cu(OAc)_2 \bullet H_2O$. Next, the [Cu(Amide-BMPA-Pr)(OAc)] and [Cu(Amine-BMPA-Pr)(OAc)] were characterized by UV-vis spectroscopy and CV with and without nitrite. Additionally, these complexes were characterized by X-ray crystallography. The performance of these catalysts for nitrite reduction was analyzed by bulk electrolysis coupled with NO quantification to determine their respective Faradaic efficiencies. The O_2 sensitivity of the complexes was studied by performing these experiments under inert conditions with nitrogen gas, as well as oxygen/nitrogen mixtures with 3 and 10% O_2. The results of these studies are presented and discussed here.

4.2 Synthesis and Characterization of Hydrogen Bonding BMPA-Pr Ligands

With the goal of synthesizing BEPA/BMPA carboxylate derivatives capable of hydrogen bond donation, DFT was used to optimize potential synthetic targets. As proof of concept, the BMPA-Pr$^-$ scaffold was chosen due to the commercially available chemicals needed to synthesize derivatives. As shown in **Figure 4.4**, the hydrogen bonding derivative, [Cu(Amine-BEPA-Pr)(NO_2)]$^-$ was optimized using BP86/TZVP. Here, the structure contains a Cu(I) center with bound NO_2^- to determine the hydrogen bond distance from an appended amine to the copper-bound nitrite, prior to reduction to NO. Based on the optimized structure, this hydrogen bonding group appears to form a very strong hydrogen bond between the primary amine and the bound nitrite with a distance of 1.85 Å, which can both increase affinity for nitrite binding over oxygen, as well as act as a proton shuttle to aid in facile nitrite reduction.

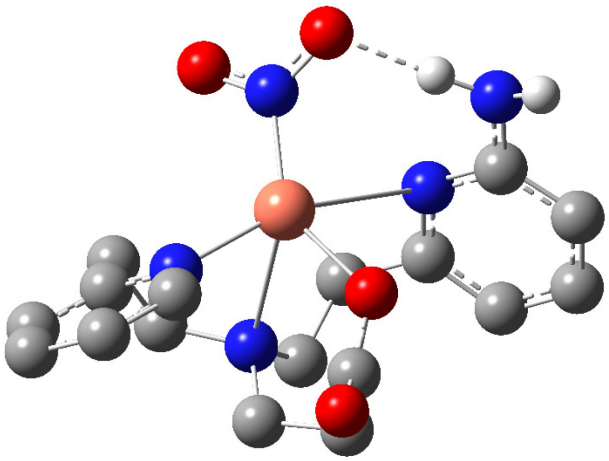

Figure 4.4 DFT optimized (BP86/TZVP) structure of [Cu(Amine-BEPA-Pr)(NO_2)]$^-$

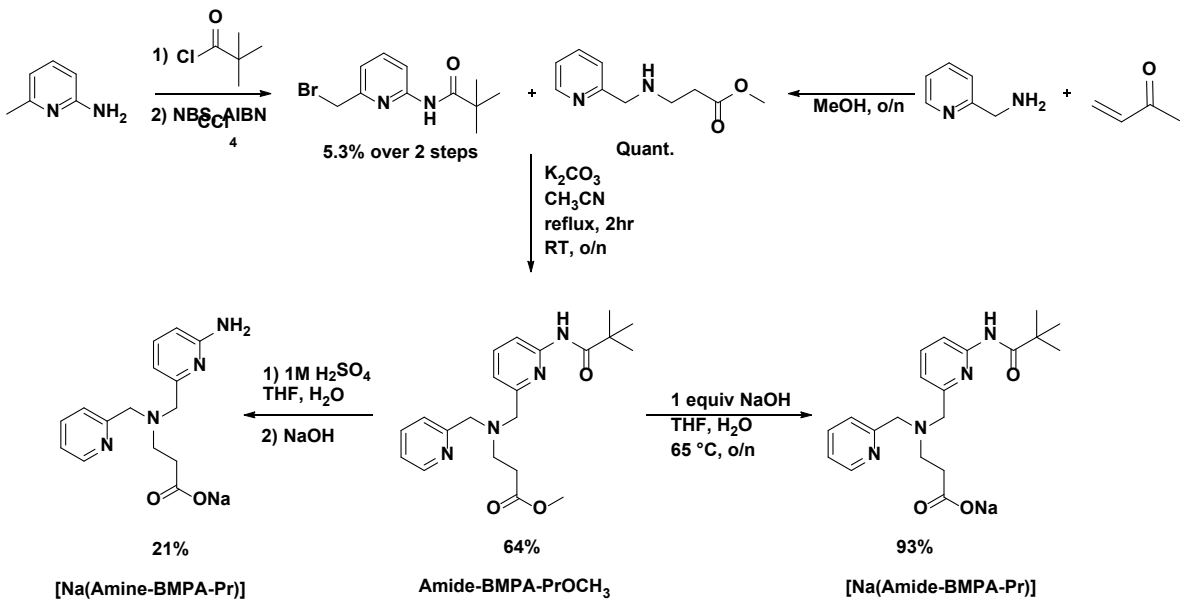

Figure 4.5 Route 1 to synthesize [Na(Amide-BMPA-Pr)] and [Na(Amine-BMPA-Pr)].

Initial attempts to synthesize the [Na(Amine-BMPA-Pr)] ligand are shown in **Figure 4.5** and labeled as Route 1. Here, half of the BMPA-Pr^{-} ligand was synthesized as shown on the top right of **Figure 4.5**, by reaction of 2-picoloyl amine and methyl acrylate to form the first half of BMPA-PrOCH$_3$, labeled as MPA-PrOCH$_3$.[82] This reaction was quantitative and provided a foundation for synthesizing BMPA analogs with hydrogen bonding moieties in the second coordination sphere. Next, the derivatized BMPA arm was prepared using 6-methylpyridin-2-amine which was equipped with the primary amine, as shown on the top left of **Figure 4.5**. First, the amine was protected to form the amide using picolyl chloride, prior to bromination of the 6-methylpyridine.[141,142] Despite the success of the amine protection in the first step, the subsequent bromination results in a mixture consisting of unreacted starting material, as well as the mono- and di-brominated products. This product mixture was difficult to column purify due to the poor separation of the components, resulting in a very low yield of 7.5% for this step. The overall yield for protection and bromination steps was 5.3% (**Figure 4.5**). Nevertheless, the product was taken

forward to perform an S_N2 reaction with the MPA-PrOCH_3 component to form the Amide-BMPA-PrOCH_3 derivative with a 64% yield.

Because amides are also considered hydrogen bond donors, the hydrolysis conditions to obtain the sodium salts of my target ligands branch at this point. To obtain the Amide-BMPA-Pr^- scaffold, the ester was hydrolyzed by addition of 1 equivalent of NaOH to form the corresponding carboxylate salt, [Na(amide-BMPA-Pr)]. This hydrolysis reaction was straight forward: the reaction mixture was heated overnight, and the product was purified by washing with organic solvents to remove unreacted starting material and dried under vacuum, to obtain the product with a 93% yield. The success of this reaction was confirmed from the missing methyl ester in the ^{1}H NMR spectrum in **Figure 4.6**.

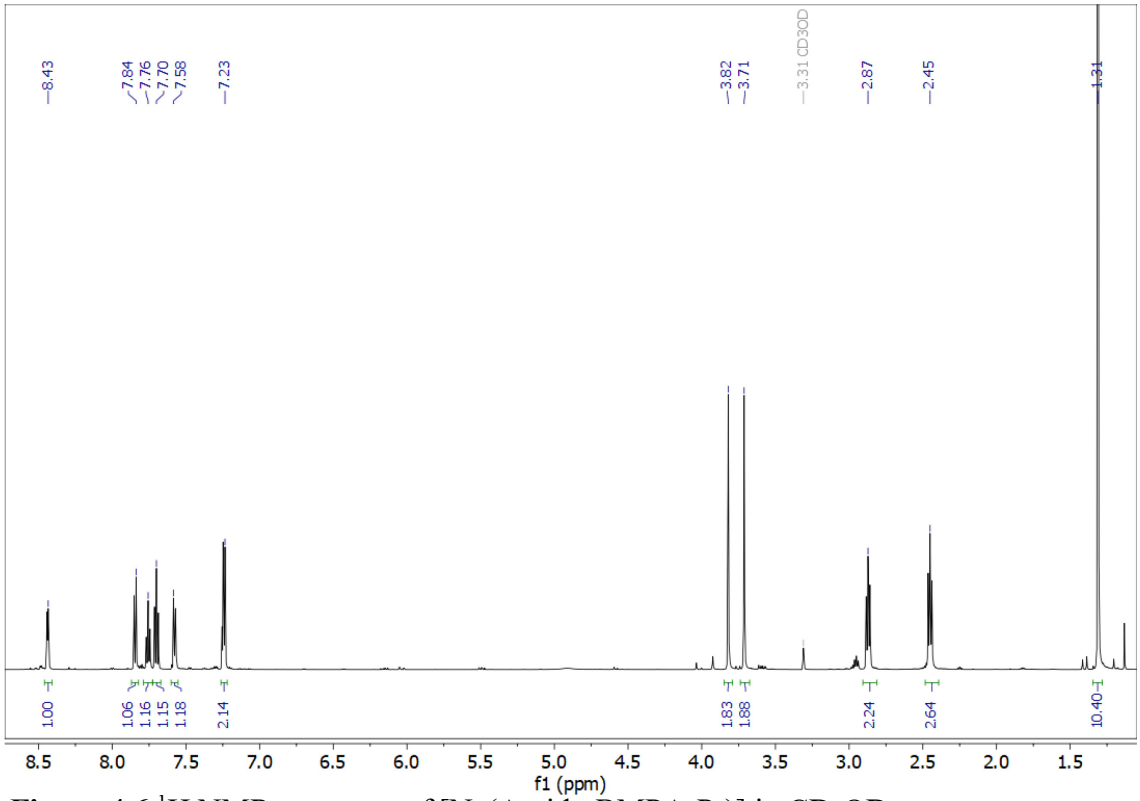

Figure 4.6 ^{1}H NMR spectrum of [Na(Amide-BMPA-Pr)] in CD_3OD.

Next, the [Na(Amine-BMPA-Pr)] ligand was synthesized by acid hydrolysis of the amide, which was performed with either [Na(Amide-BMPA-Pr)] or Amide-BMPA-PrOCH_3 as starting material. As shown in **Figure 4.7**, excess 1M HCl shows hydrolysis of the amide over the course of 32 hours. After the first hour, no significant changes were observed, suggesting that the amide was still fully intact. After 4 hours, new peaks appeared in the spectrum indicating the formation of a second species. Notably, the amide peak at 1.17 ppm decreased in intensity with the appearance of a new peak at 0.99 ppm, indicating hydrolyzed amide. After 32 hours, the reaction stopped progressing, and the ligand was purified by pH adjustment above 13 to fully deprotonate the primary amine. Unfortunately, the pH adjustment resulted in excess NaCl and NaOH, making it difficult to purify the [Na(Amine-BMPA-Pr)] ligand, as it is only soluble in water and methanol. For this reason, the acid was changed to H_2SO_4 so that neutralization would result in the formation of Na_2SO_4. The reaction mixture was dried after pH adjustment, under vacuum, to remove as much water as possible. The resulting solid was redissolved in anhydrous methanol to precipitate the Na_2SO_4. In changing the acid, the reaction was much faster resulting in more hydrolyzed amine with reaction times of ~ 5 hours. Unfortunately, the corresponding copper complex could not be obtained cleanly, as ligand decomposition was observed over the course of the reaction, resulting in a low yield. Based on these results, an alternative route was needed to successfully synthesize the [Na(Amine-BMPA-Pr)] scaffold.

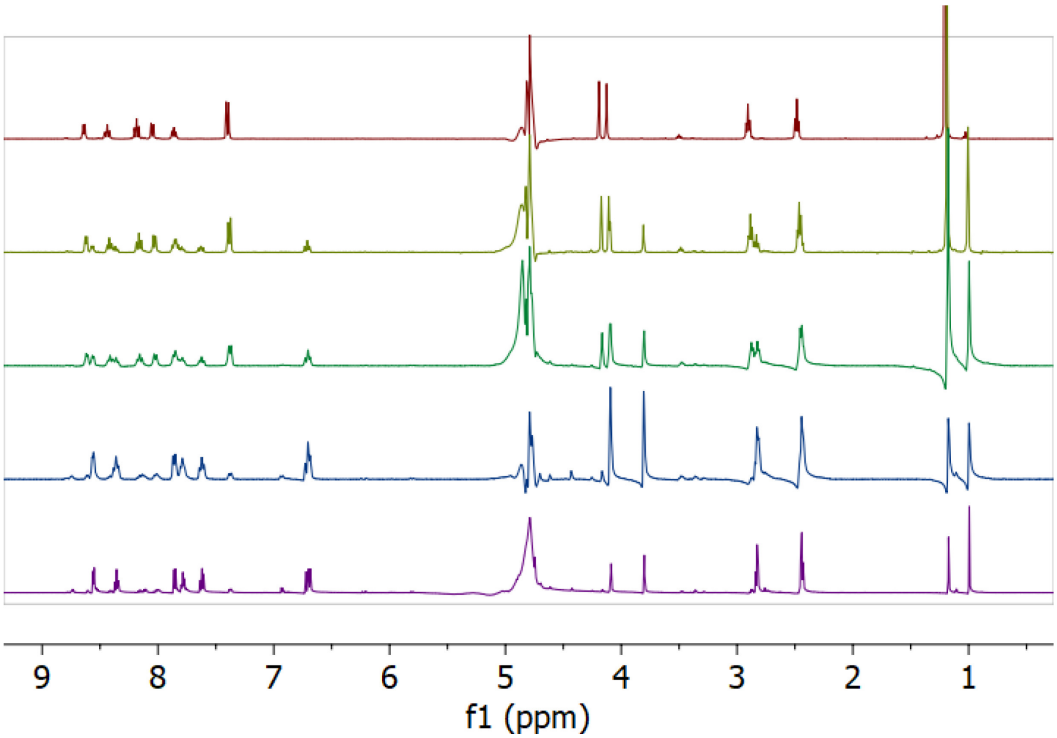

Figure 4.7 Reaction progress of acid hydrolysis by ^{1}H NMR of [Na(Amide-BMPA-Pr)] with HCl at 1 hour (red), 4 hours (yellow), 8 hours (green), 28 hours (blue), and 32 hours (purple). The sample was diluted in D_2O and excess water was solvent suppressed to reduce the signal.

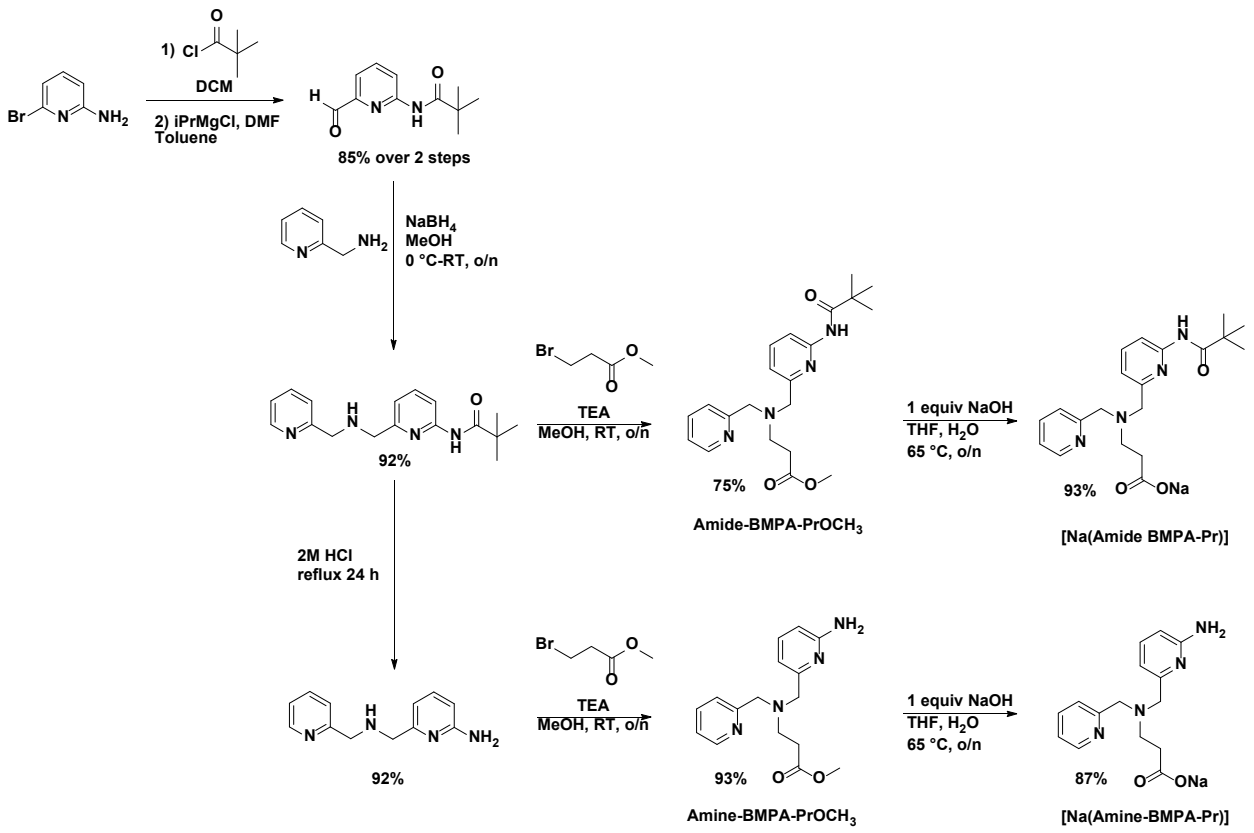

Figure 4.8 Route 2 to synthesize [Na(Amide-BMPA-Pr)] and [Na(Amine-BMPA-Pr)].

To synthesize the [Na(Amine-BMPA-Pr)] salt, Route 2 was developed and executed by rotation student, Glorimar Miranda-Mendez as shown in **Figure 4.8**. Here, the focus is placed on first synthesizing the derivatized BMPA arm containing either an Amide or Amine group. This was accomplished by repeating the amine protection of the 6-bromopyridin-2-amine which is commercially available. The resulting product underwent a Grignard reaction to form an aldehyde in place of the bromo substituent.[143] The yield of the first two steps was determined to be 85% in comparison to Route 1, which had an overall yield of 5.3%. Next, the Amide-BMPA arm was synthesized by reductive amination with 2-picolylamine. The amide was further hydrolyzed by refluxing with 2M HCl over the course of 24 hours to obtain the Amine-BMPA arm.[144] At this point, either the Amide-BMPA-$PrOCH_3$ or Amine-BMPA-$PrOCH_3$ unit was synthesized by

performing an S_N2 reaction with either the Amide- or Amine-BMPA arm and methyl 3-bromopropanoate in methanol.[82] The hydrolysis of both ligands was performed as described for [Na(Amide-BMPA-Pr)] in Route 1. Here, unreacted starting material was washed away, and the aqueous layer was dried under vacuum to provide both the [Na(Amide-BMPA-Pr)] and [Na(Amine-BMPA-Pr)] salts.[82] While [Na(Amine-BMPA-Pr)] was initially difficult to synthesize, Route 2 demonstrates a high yielding and clean formation of the sodium salt, as shown in **Figure 4.9**.

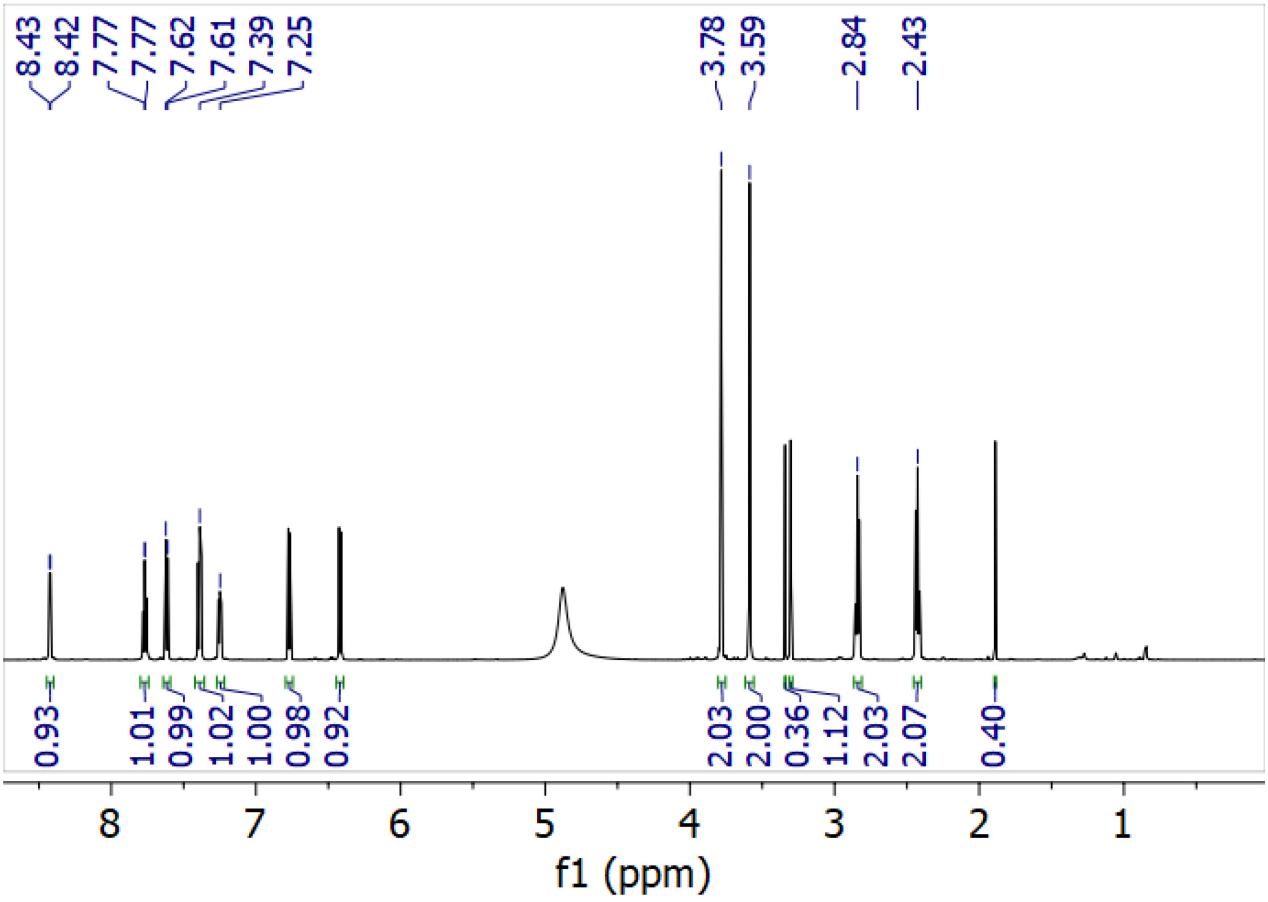

Figure 4.9 ^{1}H NMR spectrum of [Na(Amine-BMPA-Pr)] in CD_3OD.

4.3 UV-vis Spectroscopy of $[Cu(Amide\text{-}BMPA\text{-}Pr)]^+$ and $[Cu(Amine\text{-}BMPA\text{-}Pr)]^+$ Complexes

With the [Na(Amide-BMPA-Pr)] and [Na(Amine-BMPA-Pr)] ligands in hand, the corresponding copper complexes were characterized by titrating $Cu(OAc)_2 \bullet H_2O$ with the respective ligand and following the reaction by UV-vis spectroscopy. The titrations were performed in milli-Q water with 5 mM of the copper salt. As shown on the left in **Figure 4.10**, [Cu(Amide-BMPA-Pr)(OAc)] appears fully formed after the addition of 2 equivalents of ligand with a λ_{max} of 600 nm. Similar results are observed for [Cu(Amine-BMPA-Pr)(OAc)] shown on the right in **Figure 4.10**. Here, full copper binding appears at ~ 1 equivalent of ligand. In this case, the λ_{max} for [Cu(Amine-BMPA-Pr)(OAc)] appears at 637 nm. To ensure full copper binding during electrochemical experiments, 1.5 equivalents of the respective ligand were added to the copper solutions in all experiments.

Additionally, both complexes were further characterized in the presence of 1M $NaNO_2$ to observe changes to the spectrum upon nitrite binding to the Cu(II) center (**Figure 4.11**). The addition of nitrite to the [Cu(Amide-BMPA-Pr)(OAc)] complex results in no changes in the λ_{max}, which remains at 600 nm, suggesting that nitrite does not bind to the Cu(II) complex. When repeated with [Cu(Amine-BMPA-Pr)(OAc)], the λ_{max} shifts from 637 nm to 628 nm, indicating the formation of $[Cu(Amide\text{-}BMPA\text{-}Pr)(NO_2)]$.

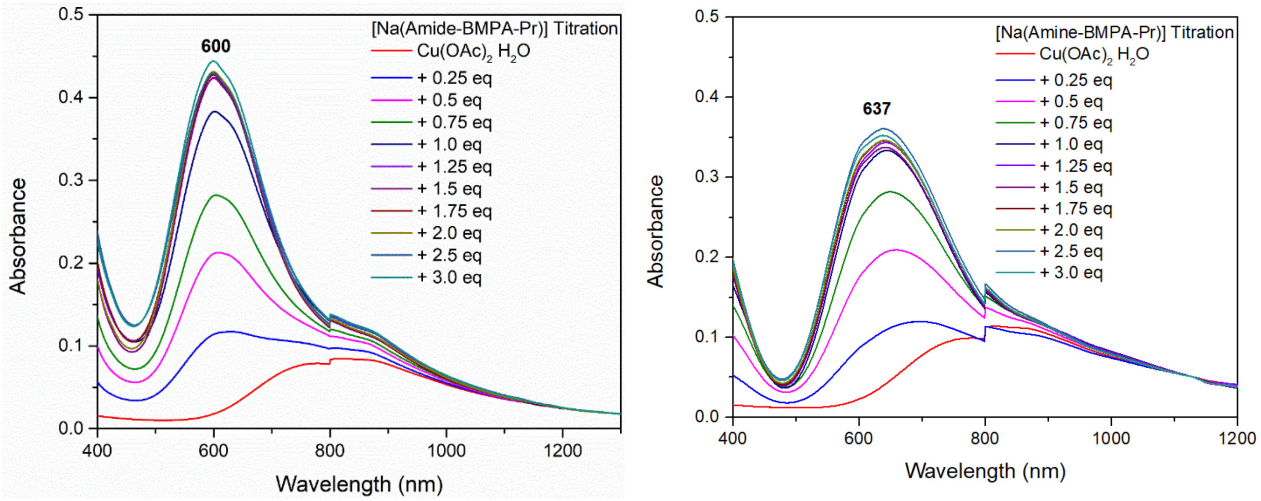

Figure 4.10 UV-vis spectra for the titration of 5 mM $Cu(OAc)_2 \cdot H_2O$ with the indicated ligand in milli-Q water, with [Na(Amide-BMPA-Pr)] (left) and [Na(Amine-BMPA-Pr)] (right).

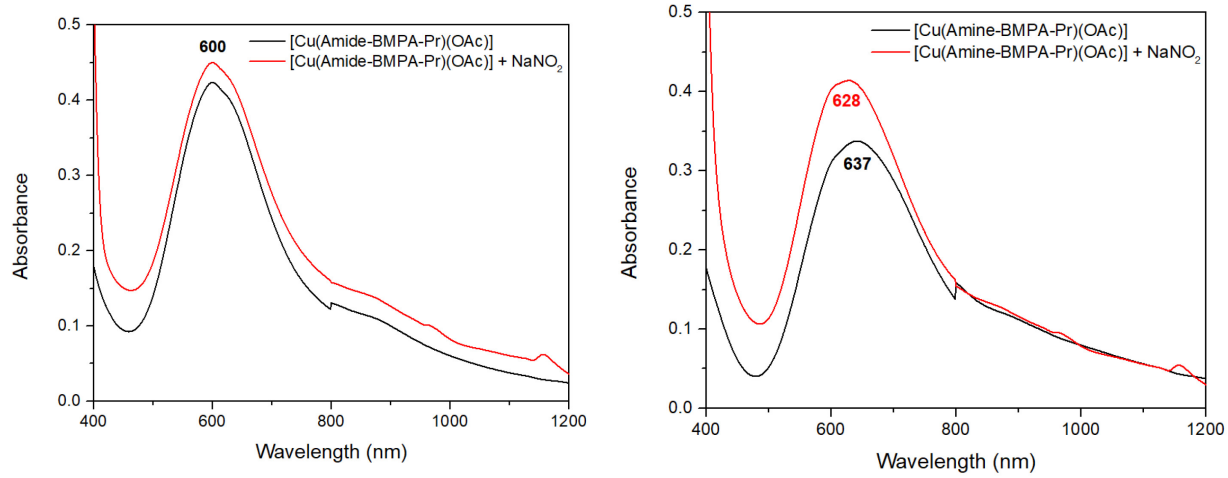

Figure 4.11 UV-vis spectral overlay of 5 mM [Cu(Amide-BMPA-Pr)(OAc)] (1:1.5 Cu(II):ligand ratio) (left) and [Cu(Amine-BMPA-Pr)(OAc)] (right) in the presence and absence of 1 M $NaNO_2$.

4.4 Crystallographic Characterization of Hydrogen Bond Derivatives of [Cu(BMPA-Pr)(OAc)]

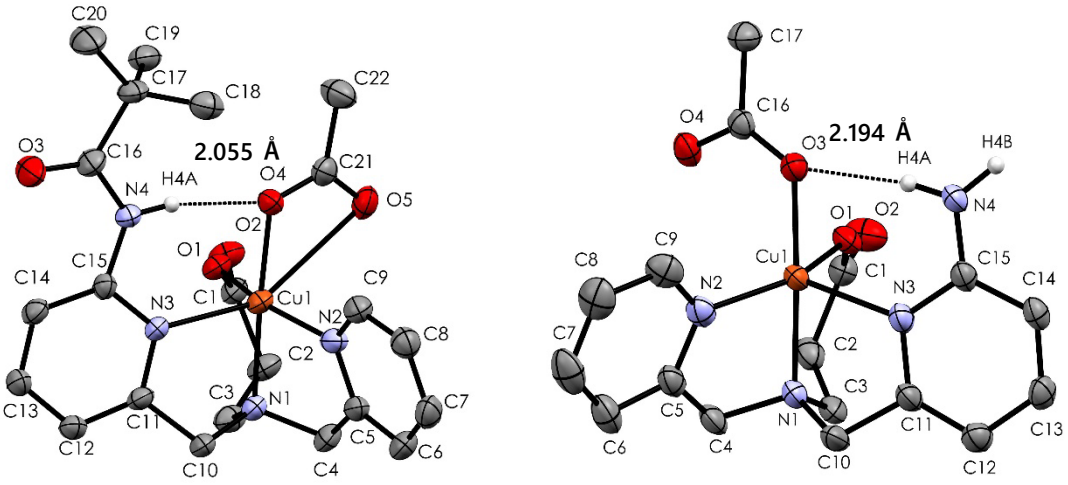

Figure 4.12 Crystal structure representation of [Cu(Amide-BMPA-Pr)(OAc)] (left) and [Cu(Amine-BMPA-Pr)(OAc)] (right). Thermal ellipsoids are shown at 50% probability. All hydrogen atoms and solvent molecules have been omitted for clarity. Color scheme: C, gray; N, blue; O, red; Cu, orange.

The [Cu(Amide-BMPA-Pr)(OAc)] and [Cu(Amine-BMPA-Pr)(OAc)] complexes were further characterized by X-ray crystallography, as shown in **Figure 4.12**. Here, both structures reveal that the acetate counter ion is bound to the Cu(II) center with bond distances of 1.964 and 2.779 Å for [Cu(Amide-BMPA-Pr)(OAc)] and 1.958 Å for [Cu(Amine-BMPA-Pr)(OAc)], which essentially corresponds to a monodentate binding mode. Additionally, the amide/amine group present in the second coordination sphere is involved in a strong hydrogen bonding interaction with the O atom of the bound acetate that is only weakly interacting with the copper center, with H4A–O4/H4A–O3 distances of 2.055 and 2.194 Å for the [Cu(Amide-BMPA-Pr)(OAc)] and [Cu(Amine-BMPA-Pr)(OAc)], respectively. Based on the UV-vis data, nitrite does not bind to the Cu(II) center, therefore the [Cu(Amide-BMPA-Pr)(NO_2)] complex could not be structurally characterized. Additional geometric parameters are summarized in **Table 4.1**.

Table 4.1 Geometric parameters of $[Cu(BMPA\text{-}Pr)]^+$ derivatives obtained from X-ray crystallography. Bond distances are reported in Å.

Bond Distance (Å)	Cu-X	Cu-O_{Pr}	Cu-$N_{pyr\ (H\text{-}bond\ donor)}$	Cu-N_{pyr}	Cu-$N_{tert\ amine}$
[Cu(Amide-BMPA-Pr)(OAc)]	1.962/2.779	1.964	2.254	2.019	2.040
[Cu(Amine-BMPA-Pr)(OAc)]	1.958	1.981	2.230	2.023	2.039

4.4.1 Cyclic Voltammetry (CV) in the Absence and Presence of Nitrite

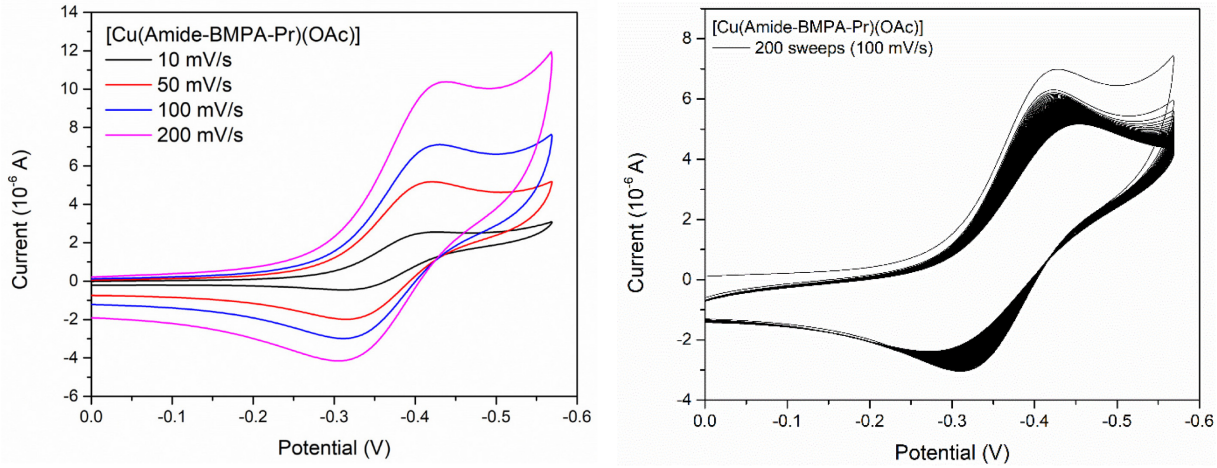

Figure 4.13 CV of $[Cu(Amide\text{-}BMPA\text{-}Pr)]^+$ at pH 7.4 in 0.1 M HEPES buffer and 0.1 M NaCl at varying scan rates (left). Catalyst stability over the course of 200 sweeps 100 mV/s (right).

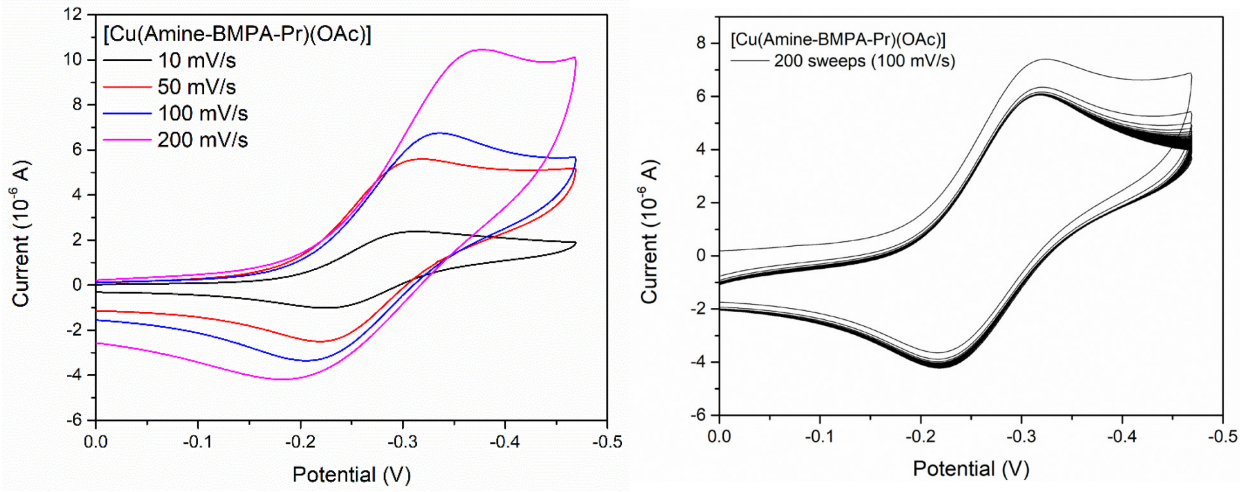

Figure 4.14 Cyclic voltammogram of $[Cu(Amine\text{-}BMPA\text{-}Pr)]^+$ at pH 7.4 in 0.1 M HEPES buffer and 0.1 M NaCl at varying scan rates (left). Catalyst stability over the course of 200 sweeps at 100 mV/s (right).

Table 4.2 Comparison of the reduction potentials (E_R) and $E_{1/2}$ for both derivatives of the $[Cu(BMPA\text{-}Pr)]^+$ complex in comparison to the parent complex. All potentials are reported vs Ag/AgCl in mV and were obtained from CVs measured with a scan rate of 50 mV/s. TOF were determined with a scan rate of 100 mV/s.

	E_R (mV)	$E_{1/2}$ (mV)	TOF (s^{-1})	Ref
[Cu(BMPA-Pr)(OAc)]	-380	-335	4.78	[82]
[Cu(Amide-BMPA-Pr)(OAc)]	-420	-367	n/a	*t.w.*
[Cu(Amine-BMPA-Pr)(OAc)]	-324	-280	6.51	*t.w.*

The $[Cu(Amide\text{-}BMPA\text{-}Pr)]^+$ and $[Cu(Amine\text{-}BMPA\text{-}Pr)]^+$ complexes were characterized by CV to determine their Cu(II)/Cu(I) reduction potentials in comparison to the $[Cu(BMPA\text{-}Pr)]^+$ parent complex. As shown in **Figure 4.13**, the $[Cu(Amide\text{-}BMPA\text{-}Pr)]^+$ complex has a semi-reversible redox couple with a reduction potential of -420 mV and an $E_{1/2}$ of -367 mV at a scan rate of 50 mV/s. Alternatively, the complex $[Cu(Amine\text{-}BMPA\text{-}Pr)]^+$ exhibits a fully reversible redox couple with a reduction potential of -324 mV and an $E_{1/2}$ of -280 mV, as shown in **Figure 4.14**. These data are summarized in **Table 4.2** in comparison to the parent complex, $[Cu(BMPA\text{-}Pr)]^+$, which has a reduction potential and $E_{1/2}$ of -380 and -335 mV, respectively. The addition of the hydrogen bond donor in the second sphere appears to induce a slight positive shift in reduction potential. Based on previous work in our laboratory, it was determined that more positive reduction potentials lead to selective NO generation and prevent further reduction to N_2O.

Next, each complex was titrated with $NaNO_2$ to observe catalysis at the cathodic wave, indicating NO_2^- reduction by the copper(I) center. Unfortunately, the $[Cu(Amide\text{-}BMPA\text{-}Pr)]^+$ complex decays with 200 consecutive sweeps, indicating catalyst decomposition during long term electrochemical experiments. Since the amide-complex does not bind nitrite and is electrochemically unstable, this complex was not tested for bulk nitrite reduction by controlled potential electrolysis (CPE). On the other hand, $[Cu(Amine\text{-}BMPA\text{-}Pr)]^+$ shows catalysis upon

addition of nitrite as shown in **Figure 4.15**. This is also evident when compared to [Cu(BMPA-Pr)]$^{+}$, which has a TOF of 4.78 s^{-1} at a scan rate of 100 mV/s, whereas the amine complex demonstrates a TOF of 6.51 s^{-1} at this scan rate.

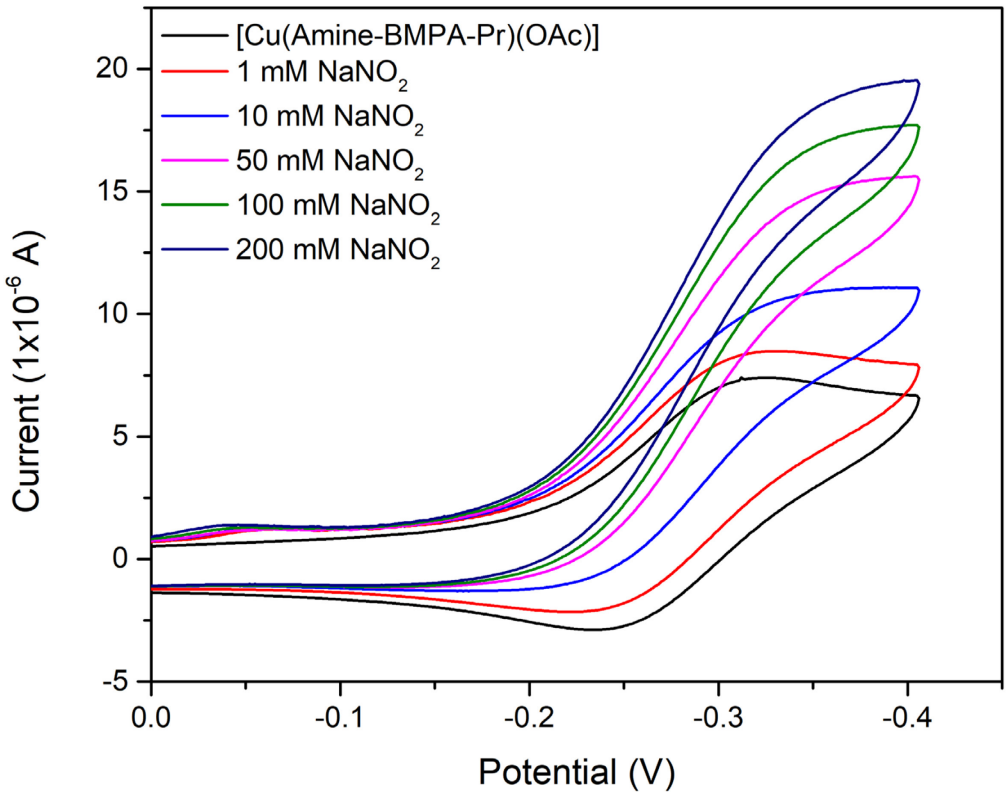

Figure 4.15 CV of 1 mM [Cu(Amine-BMPA-Pr)]$^{+}$ in 0.1 M HEPES buffer at pH 7.4, 0.1 M NaCl, titrated with up to 200 mM $NaNO_2$ at a scan rate of 100 mV/s.

4.5 Bulk Electrolysis in the Presence of Nitrite and Faradaic Efficiency Determination

Next, Faradaic efficiencies were determined by performing bulk electrolysis experiments using 1 mM of the Cu(II) complexes at pH 7.4. The NO generated during the electrochemical reaction was sparged out of the reaction solution and quantified using a chemiluminescence Siever 280i Nitric Oxide Analyzer (NOA). The oxygen sensitivity of the [Cu(BMPA-Pr)(OAc)] and [Cu(Amine-BMPA-Pr)(OAc)] complexes was tested using sparge gases of varying oxygen content and the Faradaic efficiency was determined based on the charge passed and the moles of NO

generated. For each complex, three potentials were studied, including the reduction potential (E_R) and ± 70 mV more positive and negative from this potential. For these potentials, bulk electrolysis experiments performed with the [Cu(BMPA-Pr)(OAc)] were held at -310, -380, and -450 mV, respectively, as previously determined.[82] Since the reduction potential of $[Cu(Amine\text{-}BMPA\text{-}Pr)]^+$ was determined to be -324 mV in the absence of nitrite, bulk electrolysis experiments were carried out -254, -324, and -394 mV. Each potential was held constant for 15 minutes to allow NO generation to stabilize, followed by a waiting period to allow NO detection to return to baseline amounts. The resulting data obtained from the NOA were processed (see Experimental Section) to obtain the moles of NO generated over the course of the reaction. The data obtained by bulk electrolysis were converted to moles of electrons over the course of the experiment resulting in Faradaic efficiency determination. As shown in **Figure 4.16**, sparging the reaction with 100% N_2 resulted in Faradaic efficiencies of 40 and 60% for [Cu(BMPA-Pr)(OAc)] and [Cu(Amine-BMPA-Pr)(OAc)], respectively, when held at the reduction potential (see **Table 4.3**). When switching the sweep gas to 3% O_2, the Faradaic efficiencies decreased to 12.8 and 9.1% for [Cu(BMPA-Pr)(OAc)] and [Cu(Amine-BMPA-Pr)(OAc)], respectively. No further decrease in the Faradaic efficiency was observed when the sparge gas was switched to 10% O_2. Notably, the maximum amount of NO generated decreased significantly when introducing 3% O_2 in the sweep gas.

Table 4.3 Faradaic efficiencies of [Cu(BMPA-Pr)(OAc)] and [Cu(Amine-BMPA-Pr)(OAc)] using sparge gases with varying O_2 content.

[Cu(BMPA-Pr)(OAc)]	**-310 mV**	**-380 mV**	**-450 mV**
N_2	61%	40%	40%
3% O_2	11.5%	12.8%	11.5%
10% O_2	7%	10%	10%
[Cu(Amine-BMPA-Pr)(OAc)]	**-254 mV**	**-324 mV**	**-394 mV**
N_2	58%	68%	70%
3% O_2	9.4%	9.1%	9%
10% O_2	7%	7.2%	7.1%

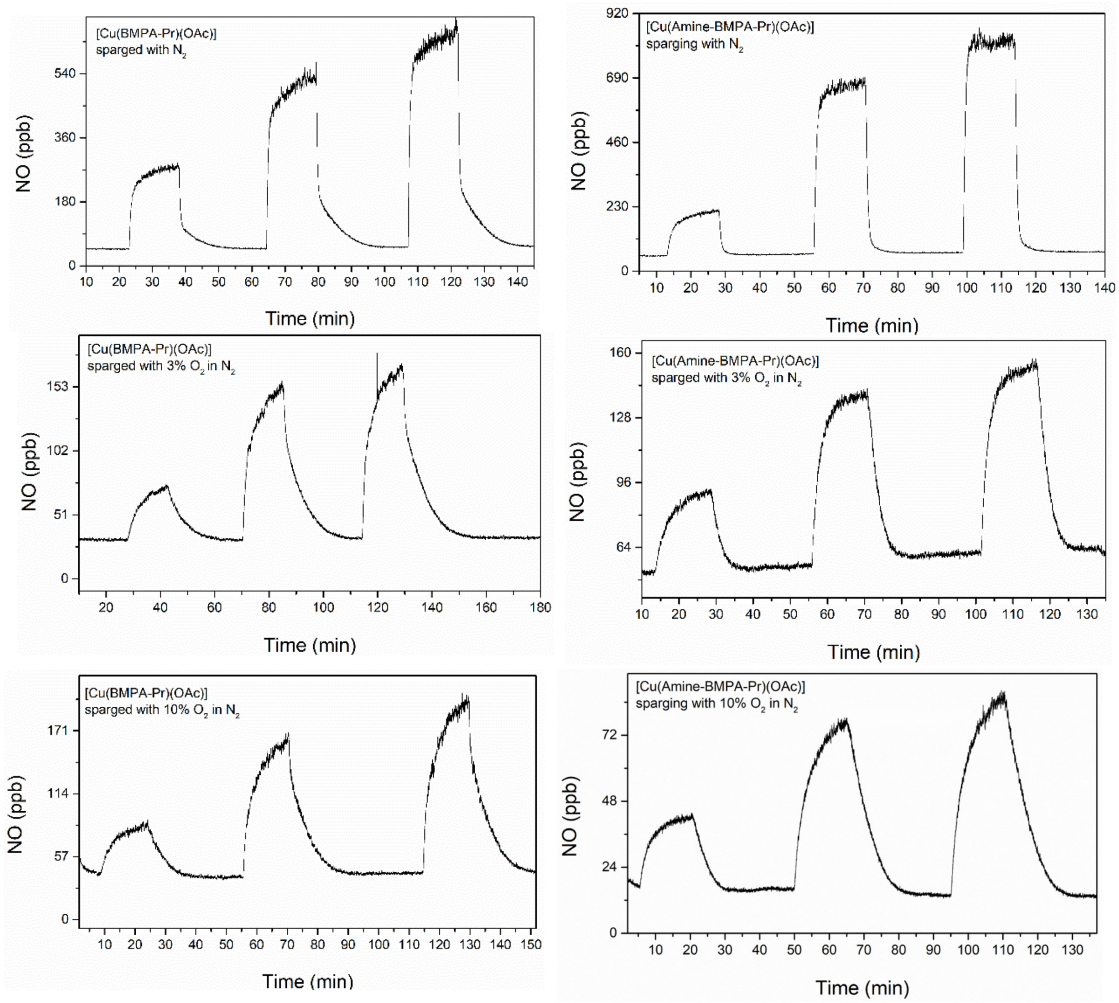

Figure 4.16 Bulk electrolysis experiments of $[Cu(BMPA\text{-}Pr)]^+$ (left) and $[Cu(Amine\text{-}BMPA\text{-}Pr)]^+$ (right). The potentials were held at $E_R \pm 70$ mV. Solutions consisted of 0.1 M HEPES at pH 7.4, 0.1 M NaCl, 1mM catalyst, and 200 mM $NaNO_2$ in 6.5 mL of solution. Experiments were carried out with sparge gases containing varying oxygen content: N_2 (top); 3% O_2 (middle); 10% O_2 (bottom).

4.6 Discussion

In this Chapter, hydrogen bonding derivatives of the BMPA-Pr$^-$ ligand were synthesized according to two synthetic routes. It was determined that the Amide-BMPA-Pr$^-$ ligand could be synthesized using either Route 1 or Route 2. In contrast, Route 2 was determined to be the best synthetic route to obtain Amine-BMPA-Pr$^-$. The ligands were metallated with $Cu(OAc)_2 \cdot H_2O$ to form the

corresponding copper complexes, [Cu(Amide-BMPA-Pr)(OAc)] and [Cu(Amine-BMPA-Pr)(OAc)] and were characterized by UV-vis spectroscopy, CV, and X-ray crystallography. Based on X-ray crystallography, a medium strength hydrogen bond is present between the copper bound acetate and the amide/amine N-H in the second coordinate sphere with a NH-O_{OAc} distance of 2.055 and 2.194 Å, for [Cu(Amide-BMPA-Pr)(OAc)] and [Cu(Amine-BMPA-Pr)(OAc)], respectively.

Despite the presence of the hydrogen bond, UV-vis data demonstrate poor NO_2^- binding to $[Cu(Amide\text{-}BMPA\text{-}Pr)]^+$ despite being in large excess in solution. It is possible that the strength of the hydrogen bond associated with [Cu(Amide-BMPA-Pr)(OAc)] stabilizes acetate binding and therefore prevents its dissociation prior to nitrite binding. In addition to poor nitrite binding to this complex, the [Cu(Amide-BMPA-Pr)(OAc)] appears to be electrochemically unstable by CV since the current associated with the redox couple steadily decreases over the course of 200 sweeps. The combination of poor substrate binding and low electrochemical stability indicates that this complex is not suitable for electrochemical NO generation. On the other hand, the [Cu(Amine-BMPA-Pr)(OAc)] complex was determined to bind NO_2^- as evidenced by a blue shift in the UV-vis spectrum from 637 to 627 nm in the presence of 200 equivalents of $NaNO_2$. Characterization of the [Cu(Amine-BMPA-Pr)(OAc)] by CV demonstrates a slightly more positive E_R and $E_{1/2}$ of -324 and -280 mV, respectively in comparison to those observed for the [Cu(BMPA-Pr)(OAc)] complex with values of -380 and -335 mV, respectively. Based on TOF calculations, nitrite reduction with the [Cu(Amine-BMPA-Pr)(OAc)] complex appears to be faster with a TOF of 6.51 versus 4.78 s^{-1} for the parent complex at 100 mV/s. This change in TOF indicates that the hydrogen bond donor present in [Cu(Amine-BMPA-Pr)(OAc)] appears to provide a proton to facilitate nitrite reduction, and therefore confirms our original hypothesis.

Next, the NO generated via bulk electrolysis was quantified to determine the Faradaic efficiency for nitrite reduction by $[Cu(Amine\text{-}BMPA\text{-}Pr)]^+$. Under inert conditions, the $[Cu(Amine\text{-}BMPA\text{-}Pr)]^+$ catalyst demonstrated a higher Faradaic efficiency of 68% in comparison to that of the parent $[Cu(BMPA\text{-}Pr)]^+$ complex with 40%. Between the higher Faradaic efficiency and TOF reported for the [Cu(Amine-BMPA-Pr)(OAc)] complex, these results demonstrate that the presence of the hydrogen bond in the SCS facilitates nitrite reduction. To further study the effect of a SCS hydrogen bond with respect to oxygen sensitivity, the N_2 sparge gas was swapped with a 3 and 10% O_2 in N_2 mixture. With the increase in O_2 content, the amount of NO produced from nitrite reduction decreased sharply for both [Cu(BMPA-Pr)(OAc)] and [Cu(Amine-BMPA-Pr)(OAc)], with a 75 and 86% decrease in activity, respectively. While the presence of the amine in the second coordination sphere showed an increase in performance under inert conditions, these results indicate that the addition of a hydrogen bond donor in the SCS of the copper catalyst does not decrease O_2 sensitivity. In fact, it appears that the presence of the hydrogen bond increases the O_2 sensitivity to further suppress NO generation. There are several examples in enzymes that demonstrate that hydrogen bonding groups in the SCS stabilize O_2 binding to metal active sites, including superoxide dismutase (SOD), superoxide reductases, as well as heme containing enzymes such as myoglobin and hemoglobin.[145-148] There is literature precedence in synthetic copper complexes showing that the addition of hydrogen bonds in the SCS increases O_2 binding affinity.[149] For example, in 2018 Karlin and coworkers reported TMPA derivatives containing an amide and secondary amines for superoxide stabilization when bubbling solutions of these complexes with O_2 at low temperatures.[150]

Based on the literature precedence, copper catalysts with more positive reduction potentials appear to be less O_2 sensitive and play a key role in selective NO generation. It is also known that

the reduction potential can become too positive, resulting in sluggish catalysis. Therefore, catalysts that contain more positive reduction potentials should be modified with hydrogen bond donors in the SCS going forward, to determine how this effect could aid in facile NO_2^- reduction to NO in the presence of O_2.[82] Recently, a BEPA sulfonate complex, $[Cu(BEPA\text{-}EtSO_3)]^+$, analogous to the $[Cu(BEPA\text{-}Pr)]^+$ parent complex, showed a reduction potential of 55 mV, which is significantly more positive in comparison to the analogous $[Cu(BEPA\text{-}Pr)]^+$ complex with a reduction potential of -80 mV.[151] Bulk electrolysis experiments with the $[Cu(BEPA\text{-}EtSO_3)]^+$ complex showed reduced O_2 sensitivity in the presence of 3 and 10% sparge gases with no changes to the Faradaic efficiency with increasing O_2 content. Future work should explore synthesizing derivatives capable of hydrogen bonding with catalysts containing more positive reduction potentials.

4.7 Experimental Section

General Considerations

All chemicals were purchased from commercial sources, including Sigma Aldrich, Fisher Scientific, and Cambridge Isotope Laboratories Inc., and used without further purification unless noted below. All electrochemical experiments were performed in water obtained from a Milli-Q filtration ultrapure water system. All stocks including 4-(2-hydroxyethyl)-1-piperazineethanesulfonic acid (HEPES) buffer, (pH adjusted to 7.4 with sodium hydroxide and hydrochloric acid if necessary), and sodium chloride electrolyte.

Physical Measurements

UV-vis Spectroscopy. All spectra were recorded using an Agilent Cary Series UV-Vis-NIR Spectrophotometer.

NMR Spectroscopy. A Varian MR 600 MHz instrument was used to record NMR spectra for Route 1 at 25 °C. A Bruker Avance Neo 500 MHz instrument was used to record NMR spectra for Route 2 at 25 °C.

Cyclic Voltammetry (CV). All electrochemical measurements were performed using CH Instruments potentiostats, models 1600E. Small scale CV experiments were performed with 2 mL solutions of 1 mM copper (II) complex in a sealed glass cell. The solution contents included a 1:1.5 ratio of the copper salt, $Cu(OAc)_2 \bullet H_2O$, and either the Amide or Amine BMPA-Pr sodium salt, 0.1 M HEPES buffer (pH 7.4), 0.1 M NaCl in Millipore water. The cell was sparged with 100% N_2 for ~10 minutes to remove oxygen from solution, the reaction was kept under nitrogen atmosphere during data collection. Data was collected using a three-electrode arrangement using a Pt disk working electrode, Pt coiled wire counter electrode, and Ag/AgCl stored in saturated KCl as the reference electrode.

Nitric Oxide Quantification. The nitric oxide produced in the bulk electrolysis experiments was quantified using a Chemiluminescence Sievers 280i Nitric Oxide Analyzer (NOA).The sample gas flow rate was controlled by an Alicat Scientific gas mass flow controller set to 200 SCCM.

Bulk Electrolysis Experiments. A larger electrochemical cell was used to measure 6.5 mL solutions with the same contents as described. Experiments were carried out with 200 mM $NaNO_2$ 100% N_2 and certified O_2/N_2 gas mixtures of 3 and 10% (Metro Welding Supply Corp) to test oxygen sensitivity of the catalysts. CVs were taken before and after bulk electrolysis experiments

to monitor any changes at the electrode surface. The cell was connected to the NOA and the cell was sparged with the appropriate sparge gas to establish a flat baseline for background NO. A potential was applied to the cell by bulk electrolysis for 15 minutes followed by a 15 minute period of rest to allow the signal to return to baseline. The NO generated during this period was quantified by integrating the total peak area for this period. This method was performed at three different potentials including the Cu(II)/Cu(I) reduction potential, with two additional trials ±70 mV.

Density Functional Theory Calculations. All calculations were performed using the program Gaussian 09.[107] All geometry optimizations and frequency calculations were performed using BP86 as the functional and TZVP as the basis set. Calculated frequencies were inspected to ensure the absence of any imaginary frequencies, to confirm that true energy minima were obtained.

Crystal Structure Determination

[Cu(Amide-BMPA-Pr)(OAc)]. Blue crystals of the complex were grown from a 375 mM methanolic solution, layered with diethyl ether and left at room temperature.

[Cu(Amine-BMPA-Pr)(OAc)]. Blue crystals of the complex were grown from a 375 mM methanolic solution, layered with diethyl ether and left at room temperature.

A crystal of dimensions 0.059 x 0.068 x 0.123 for [Cu(Amine-BMPA-Pr)(OAc)] and 0.020 x 0.020 x 0.010 [Cu(Amide-BMPA-Pr)(OAc)] mm was mounted on a Rigaku AFC10K Saturn 944+ CCD-based X-ray diffractometer equipped with a low temperature device and a Micromax-007HF Cu-target micro-focus rotating anode (λ = 1.54187 A) operated at 1.2 kW power (40 kV, 30 mA). The X-ray intensities were measured at 85(1) K with the detector placed at a distance of 42.00 mm from the crystal. A total of 2028 images were collected with an oscillation width of 1.0° in ω. The exposure times were 1 sec for the low angle images, 5 sec for high angle. Rigaku d*TREK images were exported to CrysAlisPro

1.171.43.112a (Rigaku OD, 2024) for [Cu(Amine-BMPA-Pr)(OAc)] and CrysAlisPro 1.171.40.53 (Rigaku OD, 2019) for [Cu(Amide-BMPA-Pr)(OAc)] for processing and corrected for absorption.[103] The integration of the data yielded a total of 63017 for [Cu(Amine-BMPA-Pr)(OAc)] and 19641 [Cu(Amide-BMPA-Pr)(OAc)] reflections to a maximum 2θ value of 138.82° for [Cu(Amine-BMPA-Pr)(OAc)] and 138.95° [Cu(Amide-BMPA-Pr)(OAc)] of which 15091 for amine and 4686 for amide were independent and 13468 for [Cu(Amine-BMPA-Pr)(OAc)] and 3443 [Cu(Amide-BMPA-Pr)(OAc)] were greater than 2σ(I). Analysis of the data showed negligible decay during data collection. The structure was solved using SHELXT 2018[104] and refined with SHELXL-2019/2 (Sheldrick, 2019) for amine[104,105] and [Cu(Amide-BMPA-Pr)(OAc)] the Bruker SHELXTL (version 2016/6) software package was used,[105] using the space group P-1 with Z=4 for amine for the formula C35H44Cu2N8O9 and P-1 with Z = 2 for amide for the formula C24H36CuN4O7. All non-hydrogen atoms were refined anisotropically with the hydrogen atoms placed in a combination of idealized and refined positions using the riding model. [Cu(Amine-BMPA-Pr)(OAc)] featured four solvent molecules (methanol) disordered over several positions. These solvent molecules could not be fully refined and were squeezed using Platon detecting 74 e^- in solvent accessible voids corresponding to approximately four molecules of methanol.[106] Full matrix least-squares refinement based on F2 converged at R1=0.0574 and wR2 =0.1731 for amine and R1 = 0.0594, wR2 = 0.1423 for amide [based on I > 2σ(I)], R1=0.0622 and wR2=0.1845 for [Cu(Amine-BMPA-Pr)(OAc)] and R1 = 0.0866, wR2 = 0.1686 [Cu(Amide-BMPA-Pr)(OAc)] for all data. Additional details are presented in **Table 4.1**.

Synthetic Procedures

Route 1:

Synthesis of 2,2-Dimethyl-*N*-(6-methyl-2-pyridinyl)propenamide (MPP). MPP was synthesized according to a literature procedure.[141] 40g (0.37 mol) of 2-amino-6-methylpyridine

were dissolved in 500 mL of dichloromethane. After the addition of 57 mL (0.41 mol) of triethylamine, the reaction was cooled it 0 °C. Trimethylacetylchloride (50 mL, 0.41 mol) were slowly added to the reaction solution resulting in a white gas and the formation of a white precipitate. The next day, the white precipitate was filtered off and the filtrate was concentrated. The filtrate was washed with 200 mL of 1M hydrochloric acid, followed by 200 mL of saturated sodium bicarbonate solution and 200 mL of saturated sodium chloride solution. The organic layer was then dried by sodium sulfate and rotovapped to a light orange solid. Yield: 50 g (0.26 mol, 70%) ^{1}H NMR ($CDCl_3$): 8.03 (d, 1H); 7.92 (br s, 1H); 7.55 (t, 1H); 6.85 (d, 1H); 2.42 (s, 3H); 1.30 (s, 9H) ppm.

Synthesis of N-[6-(bromomethyl)pyridine-2-yl]-2,2-dimethylpropanamide (BPP). BPP was synthesized according to a literature procedure.[142] 13.97 g (73 mmol) of MPP, 12.71 g (72 mmol) of NBS and 251.3 mg (1.5 mmol) of AIBN were dissolved in 400 mL of carbon tetrachloride in an oven dried Schlenk flask. The reaction was heated to 80 °C and refluxed under N_2 for 7 hour. Reaction was stirred at room temperature overnight. The product was then purified by silica column with 1:4 ethyl acetate to petroleum ether. Yield: 1.48 g (5.4 mmol, 7.5%). ^{1}H NMR ($CDCl_3$): 8.10 (s, 1H); 8.05 (br s, 1H); 7.60 (t, 1H); 7.05 (d, 1H); 4.43 (s, 2H); 1.24 (s, 9H) ppm.

Synthesis of *N*-(2-Pyridinylmethyl)-β-alanine methyl ester (MPA-PrOCH$_3$). MPA-PrOCH$_3$ was synthesized according to a modified literature procedure.[82] 2.5 mL (24.3 mmol) of 2-picolylamine and 2.20 mL (24.3 mmol) of methyl acrylate were dissolved in 36 mL of methanol and stirred at room temperature overnight. Reaction was rotovapped to dryness and used without

further purification. Yield: Quantitative (24.3 mmol) ^{1}H NMR ($CDCl_3$): 8.54 (d, 1H); 7.63 (t, 1H); 7.30 (d, 1H); 7.14 (t, 1H); 3.91 (s, 2H); 3.67 (s, 3H); 2.93 (t, 2H); 2.55 (t, 2H) ppm.

Synthesis of methyl 3-(((6-pivalamidopyridin-2-yl)methyl)(pyridin-2-ylmethyl)amino)propanoate (Amide-BMPA-PrOCH$_3$). Amide-BMPA-PrOCH$_3$ was synthesized according to a literature procedure.[82] 1.16 g (6 mmol) *N*-(2-Pyridinylmethyl)-β-alanine methyl ester, 1.62 g (6 mmol) *N*-[6-(bromomethyl)pyridine-2-yl]-2,2-dimethylpropanamide, and 2.67 g (20 mmol) of potassium carbonate were dissolved in 200 mL of dry acetonitrile. The reaction was refluxed for 2 hours and then allowed to stir at room temperature overnight. The reaction mixture was then filtered to remove white solid and rotovapped to dryness. The product was column purified with 10% hexanes in ethyl acetate on alumina. The resulting red/brown oil was dried under vacuum. Yield: 1.46 g (3.8 mmol, 64%). ^{1}H NMR ($CDCl_3$): 8.43 (d, 1H); 8.01 (d, 1H); 7.90 (s, 1H); 7.57 (t, 2H); 7.39 (d, 1H); 7.12 (d, 1H); 7.06 (t, 1H); 3.75 (s, 2H); 3.63 (s, 2H); 3.54 (s, 3H); 2.84 (t, 2H); 2.49 (t, 2H); 1.24 (s, 9H) ppm.

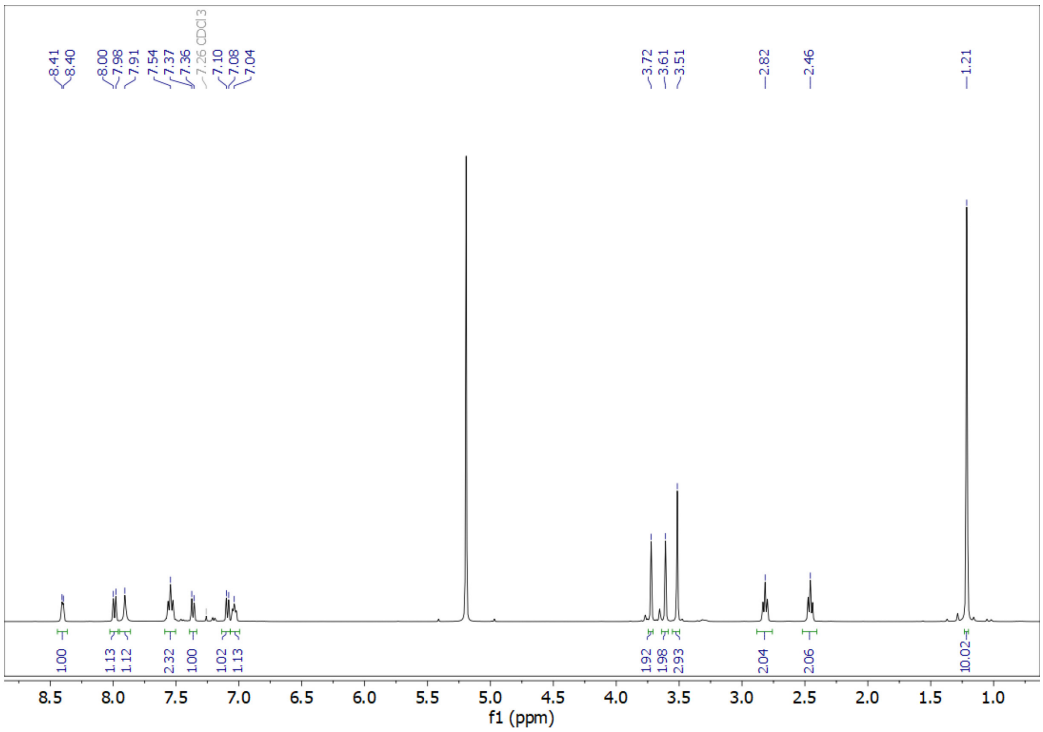

Figure 4.17 ^{1}H NMR spectrum of Amide-BMPA-PrOCH$_3$ in CDCl$_3$ (Route 1).

Route 2:

Synthesis of N-(6-bromopyridin-2-yl)pivalamide. N-(6-bromopyridin-2-yl)pivalamide was synthesized according to a literature procedure.[143] 10 g (58.8 mmol) of 6-bromopyridin-2-amine was dissolved in 200 mL of dichloromethane. Next, 20 mL of triethylamine (0.143 mol, 2.5 eq) was added to the solution. The solution was cooled to 0 °C under N_2 and 8.9 mL of acetyl chloride (72.7 mmol, 1.26 eq) was added dropwise. The reaction was allowed to warm to room temperature and stirred overnight. The reaction mixture was washed with water, followed by saturated sodium bicarbonate, and brine and dried over sodium sulfate. The solution was rotovapped and the resulting solid was washed with hexanes. The solid was collected and dried under vacuum for 3 days. Yield: 13.1 g (50.9 mmol, 88%). ^{1}H NMR (500 MHz, CDCl$_3$): 8.22 (d, 1H); 7.98 (br s, 1H); 7.55 (t, 1H); 7.20 (d, 1H); 1.32 (s, 9H) ppm. ^{13}C NMR (126 MHz, CDCl$_3$): 177.23; 151.82; 140.73; 139.24; 123.55; 112.40; 40.04; 27.54 ppm.

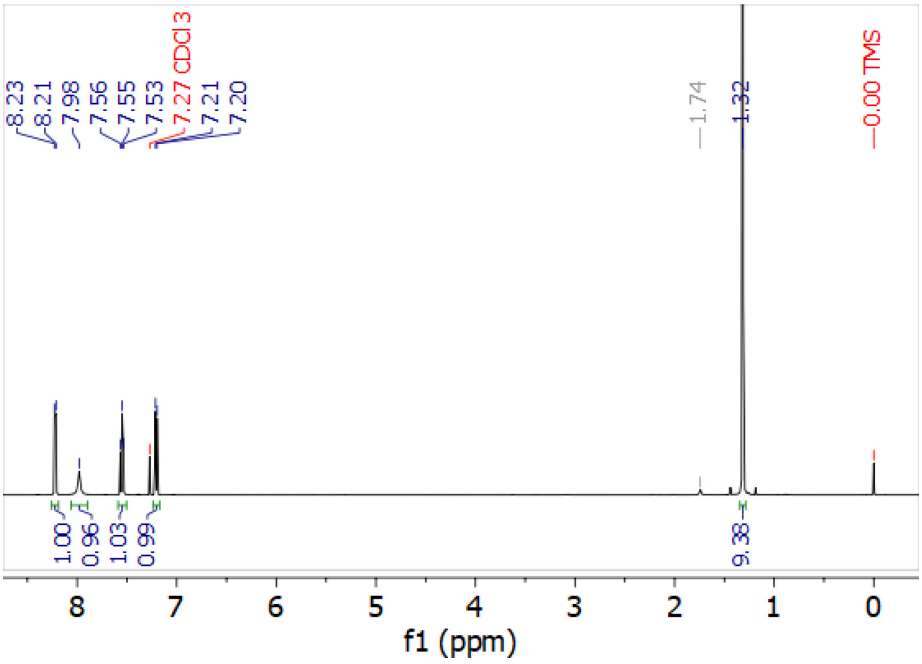

Figure 4.18 ^{1}H NMR spectrum of N-(6-bromopyridin-2-yl)pivalamide in $CDCl_3$.

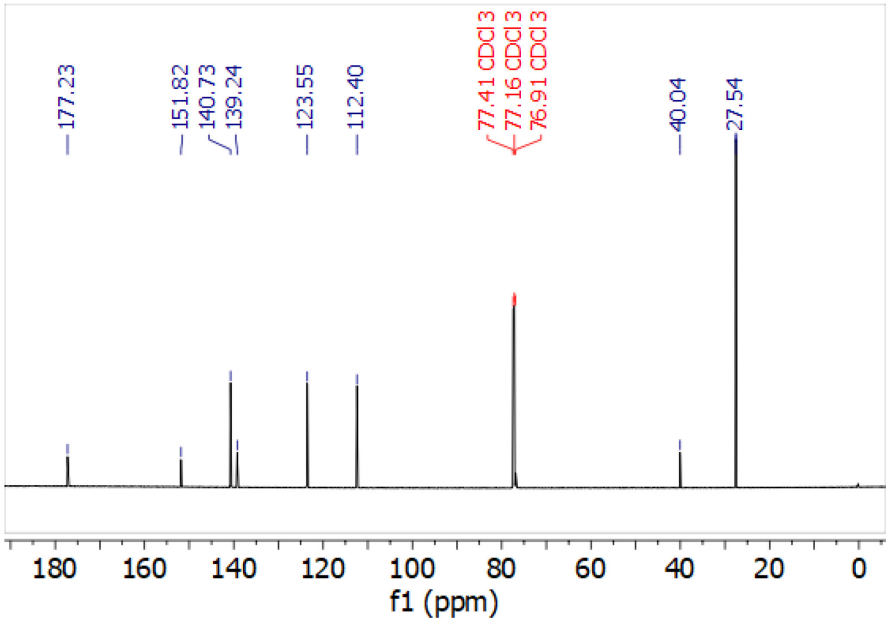

Figure 4.19 ^{13}C NMR spectrum of N-(6-bromopyridin-2-yl)pivalamide in $CDCl_3$.

Synthesis of N-(6-formylpyridin-2-yl)pivalamide. N-(6-formylpyridin-2-yl)pivalamide was synthesized according to a literature procedure.[143] 5.5 g of N-(6-bromopyridin-2-yl)pivalamide (21 mmol) was dissolved in 22 mL of dry toluene and placed in an ice/NaCl water slurry. 25 mL of isopropyl magnesium chloride (50 mmol) was transferred via cannula to an addition funnel attached to the reaction vessel and was added dropwise under N_2 for 1.5 hours. The reaction was left to stir for an additional 23 hours. At this point, 3.25 mL of DMF (42 mmol) was added to the reaction and stirred for 30 minutes. Next, the reaction was placed in an ice bath and was quenched with 50 mL of 10% aqueous acetic acid solution. After 30 minutes, the organic layer was extracted with 10 mL of toluene and stirred with 22 mL of a 0.6 M sodium disulfite solution and stirred an additional 30 minutes. Next, the aqueous layer was extracted and stirred 10 minutes with 30 mL of 1.9 M sodium carbonate solution. The product was extracted with ethyl acetate and dried with magnesium sulfate. The product was rotovapped to dryness and dried under vacuum overnight. Yield: 3.26 g (0.016 mol, 74%). ^{1}H NMR (500 MHz, $CDCl_3$): 9.93 (s, 1H); 8.52 (d, 1H); 8.14 (br s, 1H); 7.89 (t, 1H); 7.68 (d, 1H); 1.36 (s, 9H) ppm. ^{13}C NMR (126 MHz, $CDCl_3$): 192.55; 177.55; 152.23; 150.92; 139.51; 118.68; 40.07; 27.60 ppm.

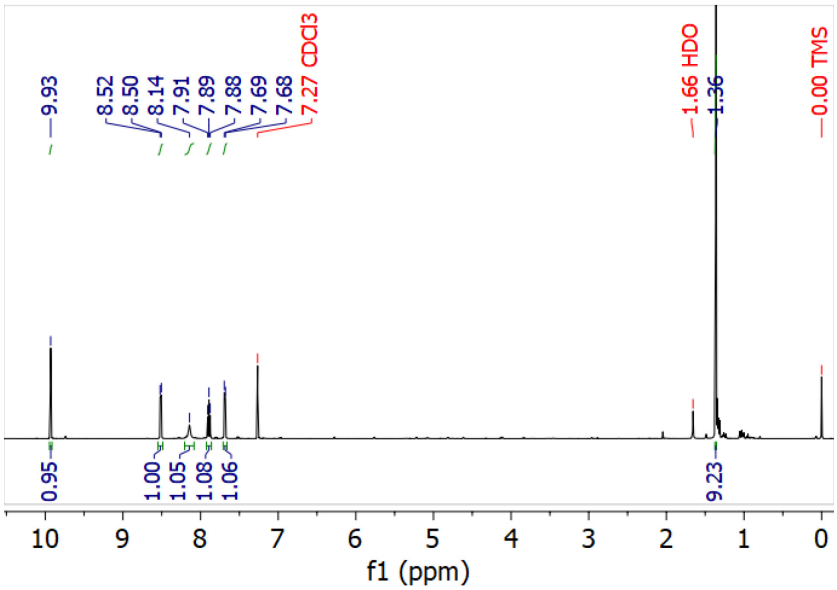

Figure 4.20 ^{1}H NMR spectrum of N-(6-formylpyridin-2-yl)pivalamide in $CDCl_3$.

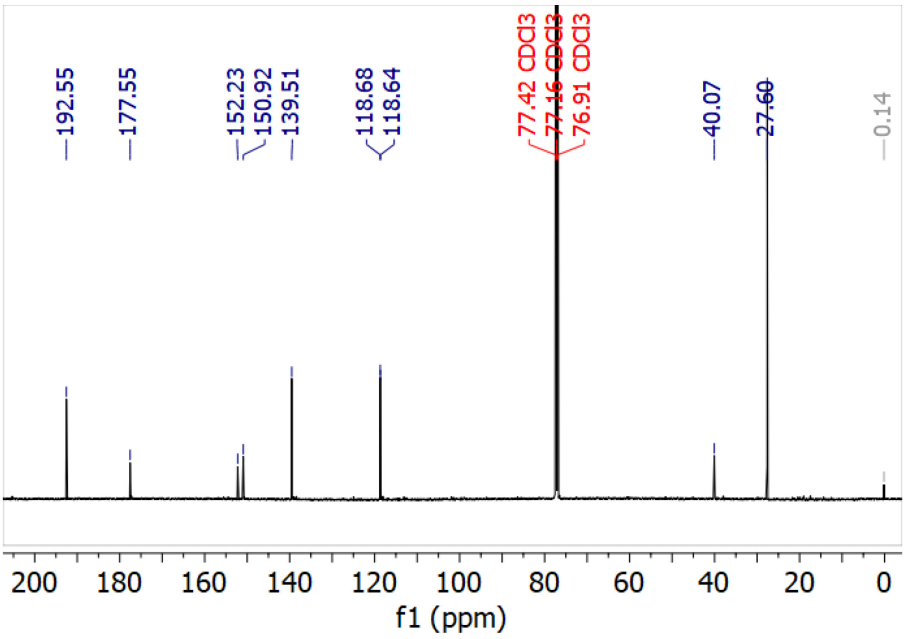

Figure 4.21 ^{13}C NMR spectrum of N-(6-formylpyridin-2-yl)pivalamide in $CDCl_3$.

Synthesis of N-(6-(((pyridin-2-ylmethyl)amino)methyl)pyridin-2-yl)pivalamide (Amide-BMPA). Amide-BMPA was synthesized using a modified literature procedure.[144] 3.74 g of N-(6-formylpyridin-2-yl)pivalamide (18.1 mmol) was dissolved in 75 mL of methanol before adding 2.06 mL of 2-picolylamine (19.9 mmol). After 3.5 hours of stirring, the reaction was cooled to 0 °C prior to adding a total of 1.029 g of $NaBH_4$ (27.2 mmol) in small batches. The reaction was stirred overnight at room temperature. The next day, the reaction was quenched with 100 mL of water and rotovapped to remove methanol. The product was then extracted with ethyl acetate three times and dried with sodium or magnesium sulfate before transferring to a vial to dry under vacuum at room temperature overnight. Yield: 4.99 g (16.7 mmol, 92%). ^{1}H NMR (500 MHz, Chloroform-*d*) δ 8.56 (d, *J* = 4.7 Hz, 1H), 8.12 (d, *J* = 8.3 Hz, 1H), 7.66 – 7.63 (m, 2H), 7.34 (d, *J* = 7.8 Hz, 1H), 7.18 – 7.16 (m, 1H), 7.05 (d, *J* = 7.5 Hz, 1H), 3.97 (s, 2H), 3.87 (s, 2H), 1.33 (s, 8H). ^{13}C

NMR (126 MHz, $CDCl_3$) δ 177.19, 159.77, 158.05, 151.38, 149.49, 138.88, 136.60, 122.50, 122.14, 118.22, 112.14, 54.95, 54.53, 39.94, 27.67.

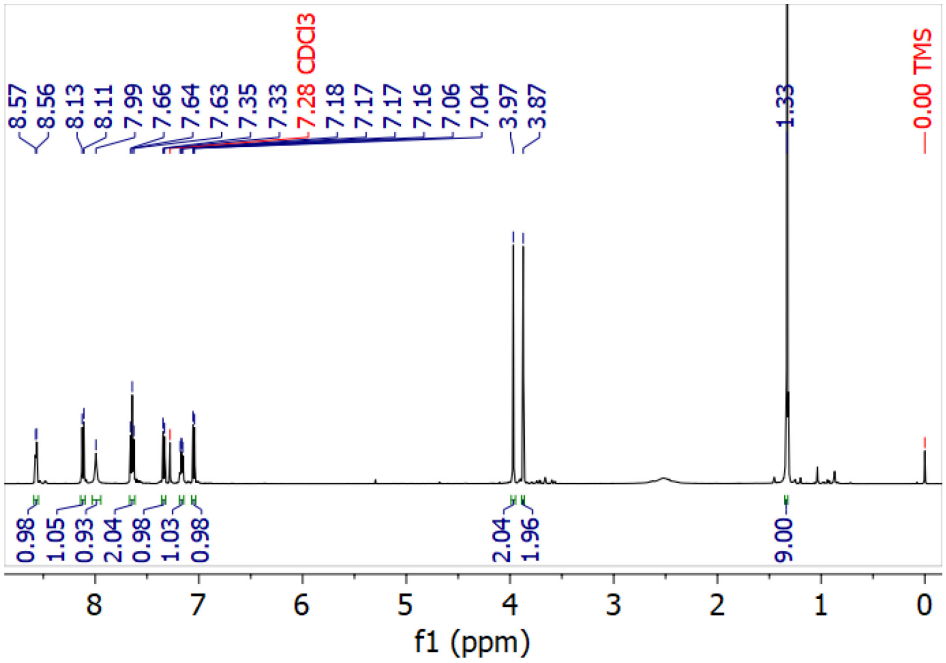

Figure 4.22 ^{1}H NMR spectrum of Amide-BMPA in $CDCl_3$.

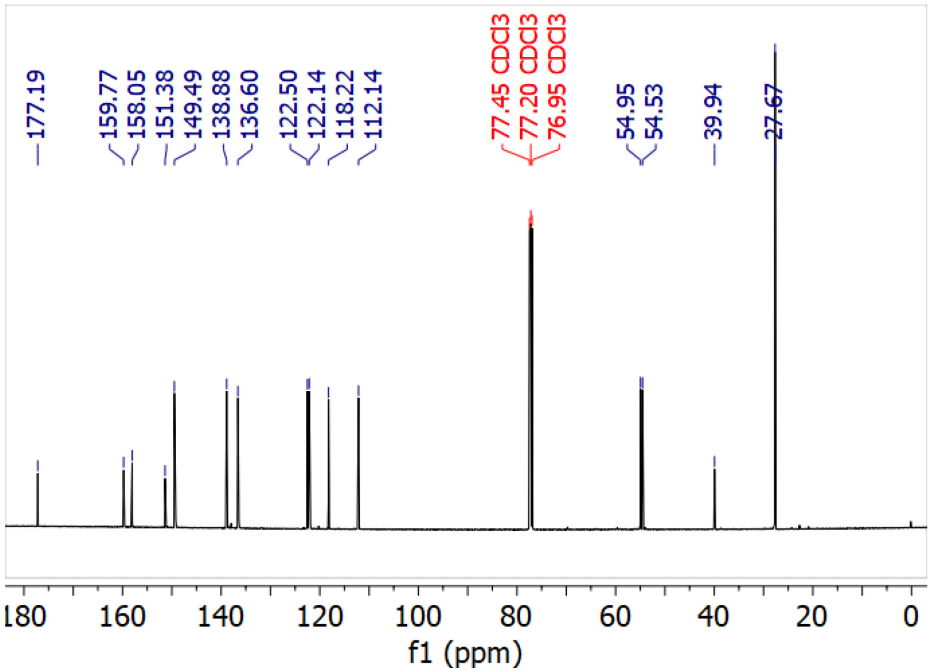

Figure 4.23 ^{13}C NMR spectrum of Amide-BMPA in $CDCl_3$.

Synthesis of 6-(((pyridin-2-ylmethyl)amino)methyl)pyridin-2-amine (Amine-BMPA). The Amine-BMPA was synthesized according to modified literature procedure.[144] 1.2 g of Amide-BMPA (4 mmol) was dissolved in 51 mL of 2 M HCl solution and heated to 85 °C overnight. The next day, the reaction was allowed to cool before adjusting the pH >13 with sodium hydroxide. The product was extracted with dichloromethane four times and dried with sodium sulfate. The solution was evaporated to give the final product which was dried under vacuum overnight at 30 °C. Yield: 0.79 g (3.7 mmol, 92%). ^{1}H NMR (500 MHz, Chloroform-*d*) δ 8.55 (d, *J* = 4.6 Hz, 1H), 7.67 – 7.60 (m, 1H), 7.37 (t, *J* = 7.7 Hz, 2H), 7.19 – 7.13 (m, 1H), 6.66 (d, *J* = 7.3 Hz, 1H), 6.37 (d, *J* = 8.2 Hz, 1H), 4.51 (s, 2H), 3.98 (s, 2H), 3.80 (s, 2H). ^{13}C NMR (126 MHz, $CDCl_3$) δ 159.63, 158.38, 157.68, 149.40, 138.35, 136.60, 122.51, 122.11, 112.38, 107.14, 54.71, 54.49.

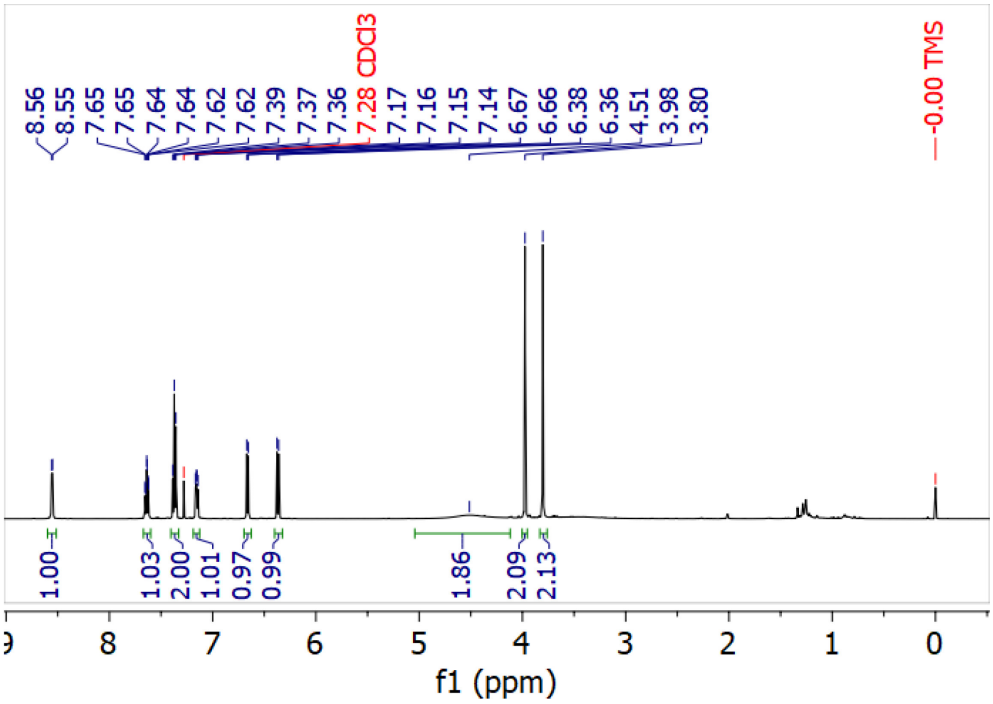

Figure 4.24 ^{1}H NMR spectrum of Amine-BMPA in $CDCl_3$.

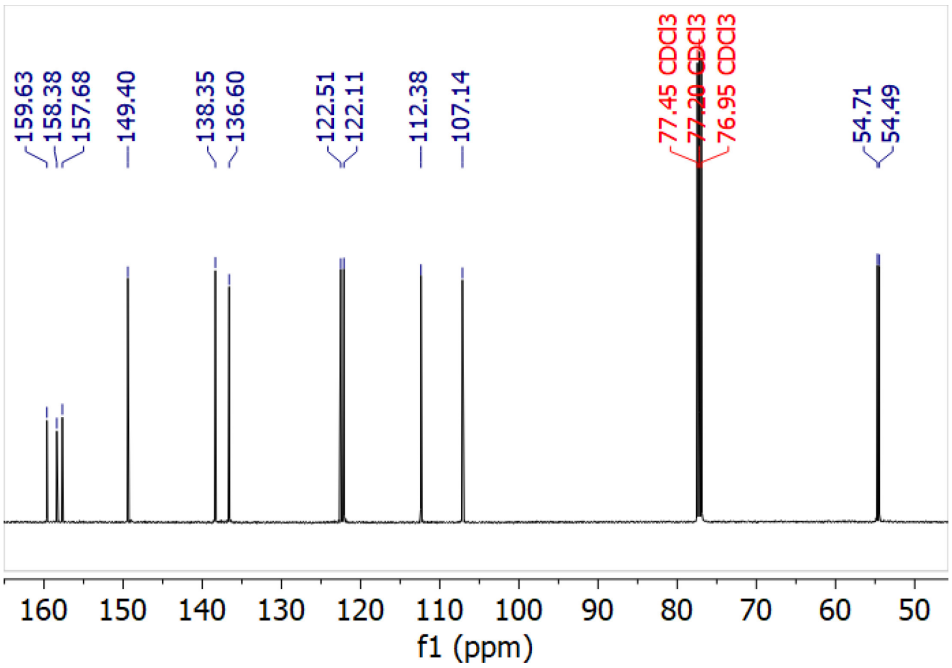

Figure 4.25 ^{13}C NMR spectrum of Amine-BMPA in $CDCl_3$.

Synthesis of methyl 3-(((6-pivalamidopyridin-2-yl)methyl)(pyridin-2-ylmethyl)amino)propanoate (Amide-BMPA-PrOCH$_3$). The Amide-BMPA-PrOCH$_3$ was synthesized according to a modified literature procedure.[82] 100 mg of Amide-BMPA (0.34 mmol) was dissolved in 1 mL of methanol. Next, 71 µL of triethylamine (0.51 mmol) and 56 µL of methyl 3-bromopropanoate (0.51 mmol) were added to the reaction and stirred over night at room temperature. The next day, 1.5 eq of NaOH was added to the reaction and left to stir. The reaction was rotovapped and redissolved in acetonitrile and filtered to remove insoluble salts. The filtrate was dried to give the final product. Yield: 97.8 mg (0.26 mmol, 75%). ^{1}H NMR (500 MHz, Chloroform-*d*) δ 8.51 (d, 1H), 8.09 (d, 1H), 7.97 (s, 1H), 7.65 (t, 2H), 7.47 (d, 1H), 7.19 (d, 1H), 7.15 (m, 1H), 3.83 (s, 2H), 3.71 (s, 2H), 3.63 (s, 3H), 2.93 (t, 2H), 2.57 (t, 2H), 1.33 (s, 3H) ^{13}C NMR (126 MHz, $CDCl_3$) δ 177.22, 173.00, 159.53, 157.85, 151.01, 149.14, 138.85, 136.58, 123.05, 122.22, 118.79, 112.11, 60.39, 59.84, 51.71, 50.06, 32.67, 27.67.

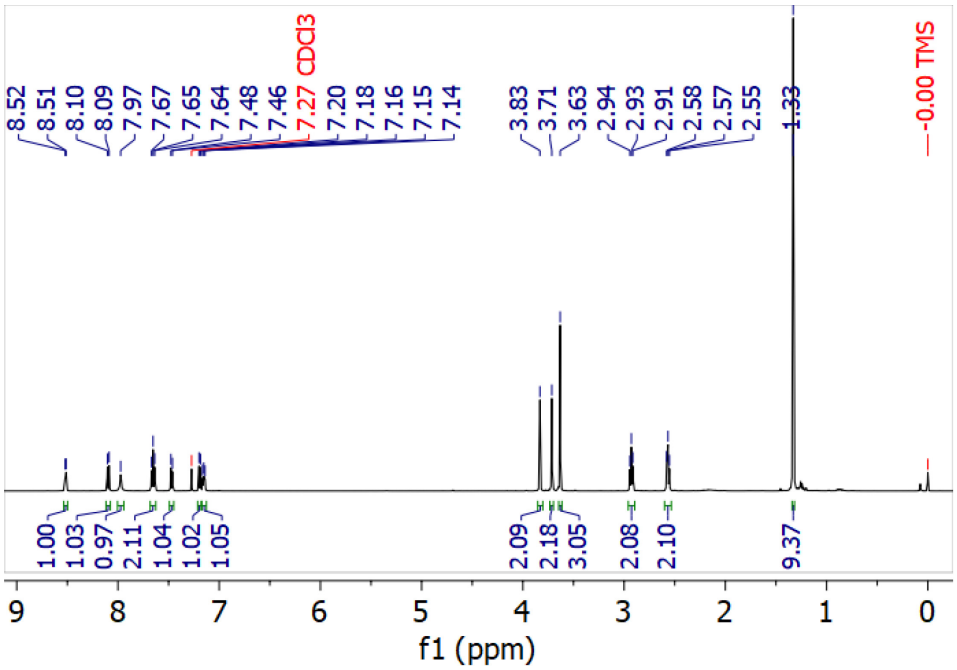

Figure 4.26 ^{1}H NMR spectrum of Amide-BMPA-PrOCH$_3$ in CDCl$_3$. (Route 2)

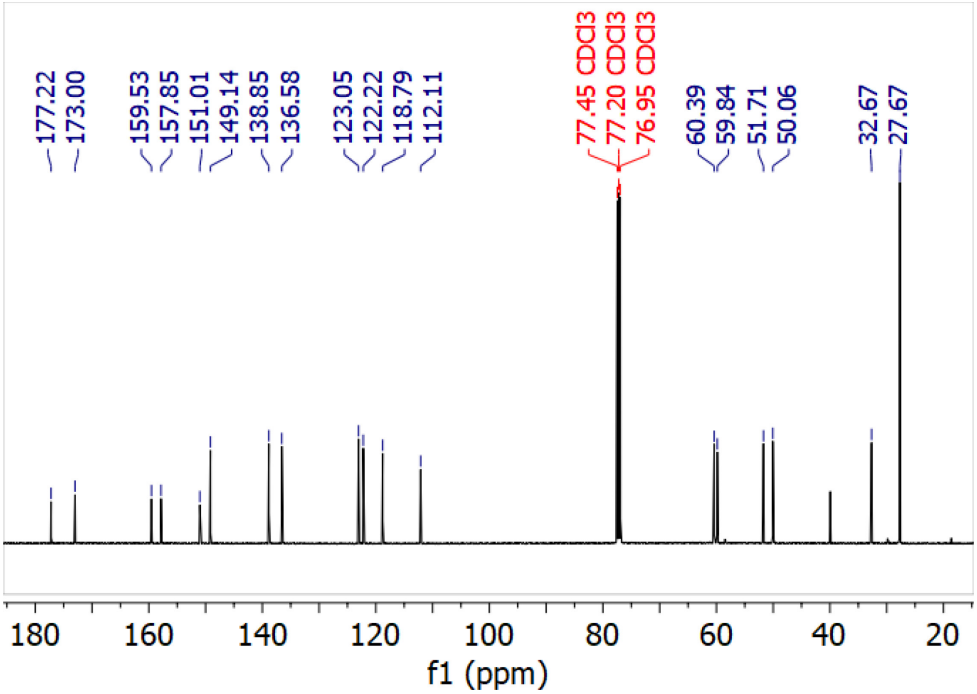

Figure 4.27 ^{13}C NMR spectrum of Amide-BMPA-PrOCH$_3$ in CDCl$_3$. (Route 2)

Synthesis of methyl 3-(((6-aminopyridin-2-yl)methyl)(pyridin-2-ylmethyl)amino)propanoate (Amine-BMPA-PrOCH$_3$). The Amine-BMPA-PrOCH$_3$ was synthesized according to a modified literature procedure.[82] 500 mg of Amine-BMPA (2.3 mmol) was dissolved in 5 mL of methanol. Next, 0.49 mL of triethylamine (3.5 mmol) and 0.38 mL of (3.5 mmol) methyl 3-bromopropanoate were added and the reaction stirred overnight at room temperature. The next day, 1.75 mL of 2M NaOH (1.5 eq) was added and stirred for 20 minutes to reach pH 8.5 to 9. The solution was dried by rotary evaporation to yield a biphasic oil. The product was extracted with dichloromethane and dried with sodium sulfate. The resulting product was dried under vacuum for 2 hours at 60 °C. For further purification, the product was redissolved in acetonitrile and placed in freezer to crash out the triethylamine bromide form during the reaction. Solution was filtered cold and the product was precipitated with diethyl ether and dried under vacuum. Yield: 644 mg (2.1 mmol, 93%). ^{1}H NMR (500 MHz, Chloroform-*d*) δ 8.51 (d, 1H), 7.64 (t, 1H), 7.50 (d, 1H), 7.38 (t, 1H), 7.15 (m, 1H), 6.81 (d, 1H), 6.35 (d, 1H), 4.58 (br s, 2H), 3.83 (s, 2H), 3.65 (s, 2H), 3.62 (s, 3H), 2.91 (t, 2H), 2.55 (t, 2H). ^{13}C NMR (126 MHz, $CDCl_3$) δ 173.05, 159.68, 158.12, 157.74, 149.01, 138.21, 136.48, 123.00, 122.05, 112.77, 106.90, 60.24, 60.03, 51.60, 49.88, 32.51.

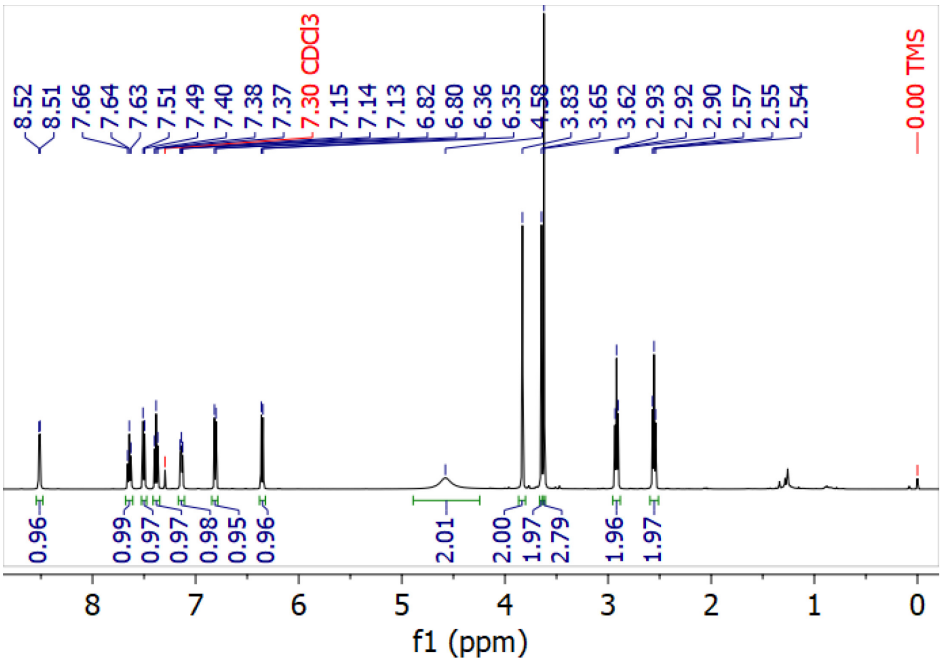

Figure 4.28 ^{1}H NMR spectrum Amine-BMPA-PrOCH$_3$ in CDCl$_3$.

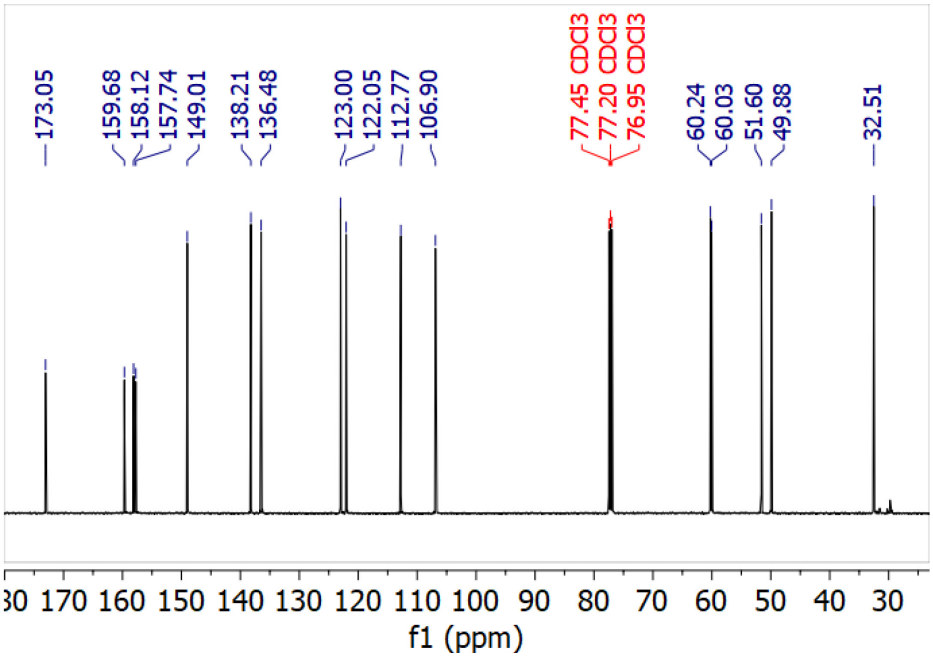

Figure 4.29 ^{13}C NMR spectrum of Amine-BMPA-PrOCH$_3$ in CDCl$_3$.

Hydrolysis Conditions:

Synthesis of sodium 3-(((6-pivalamidopyridin-2-yl)methyl)(pyridin-2-ylmethyl)amino)propanoate [Na(Amide-BMPA-Pr)]. The hydrolysis was performed according to a modified literature procedure.[82] 98.1 mg (0.026 mmol) of Amide-BMPA-PrOCH$_3$ was transferred to a reaction vial and dissolved in 0.25 mL H_2O and 0.45 mL of THF. Next, 0.128 mL of 2M NaOH was added to the solution. The reaction was heated to 60 °C overnight. The next day, the reaction solution was washed with dichloromethane until colorless and the aqueous solution was dried under N_2 flow at 80 °C. Yield: 95.2 mg (0.024 mmol; 93%). ^{1}H NMR (500 MHz, Methanol-d_4) δ 8.40 (d, 2H), 7.86 (d, 1H), 7.76 (t, 2H), 7.69 (t, 1H), 7.64 (d, 1H), 7.27 (d, 1H), 7.24 (m, 2H), 3.82 (s, 2H), 3.71 (s, 2H), 2.88 (m, 2H), 2.44 (m, 2H), 1.31 (s, 9H). ^{13}C NMR (126 MHz, MeOD) δ 181.00, 179.65, 160.86, 159.27, 152.57, 149.38, 139.99, 138.61, 124.97, 123.63, 120.44, 113.89, 60.93, 60.85, 53.32, 40.86, 36.95, 27.64.

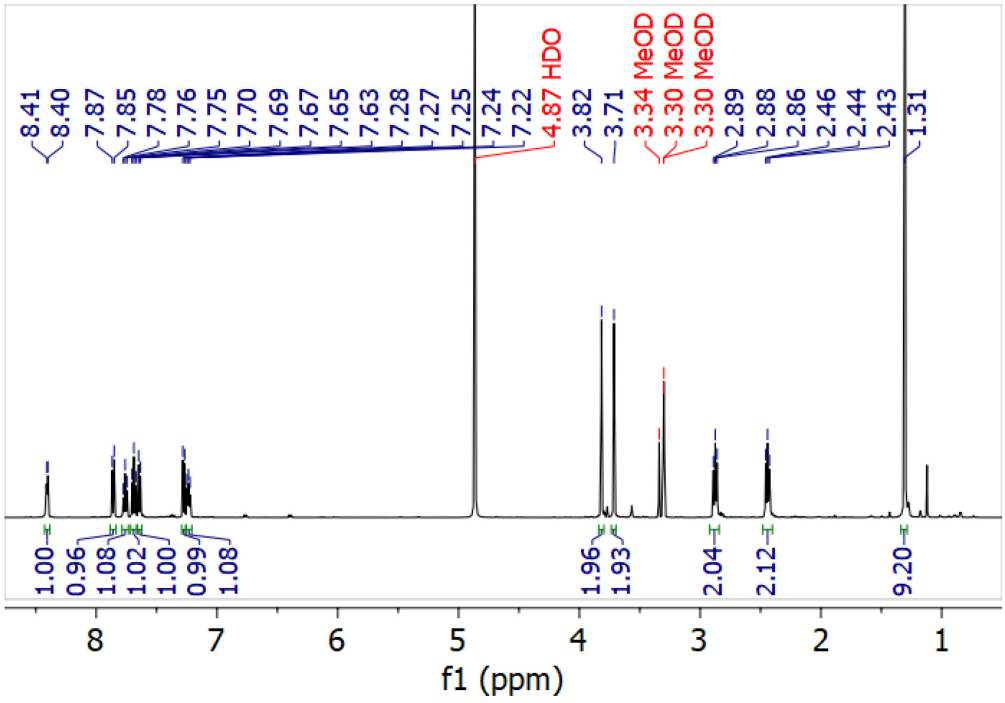

Figure 4.30 ^{1}H NMR spectrum of [Na(Amide-BMPA-Pr)] in CD_3OD.

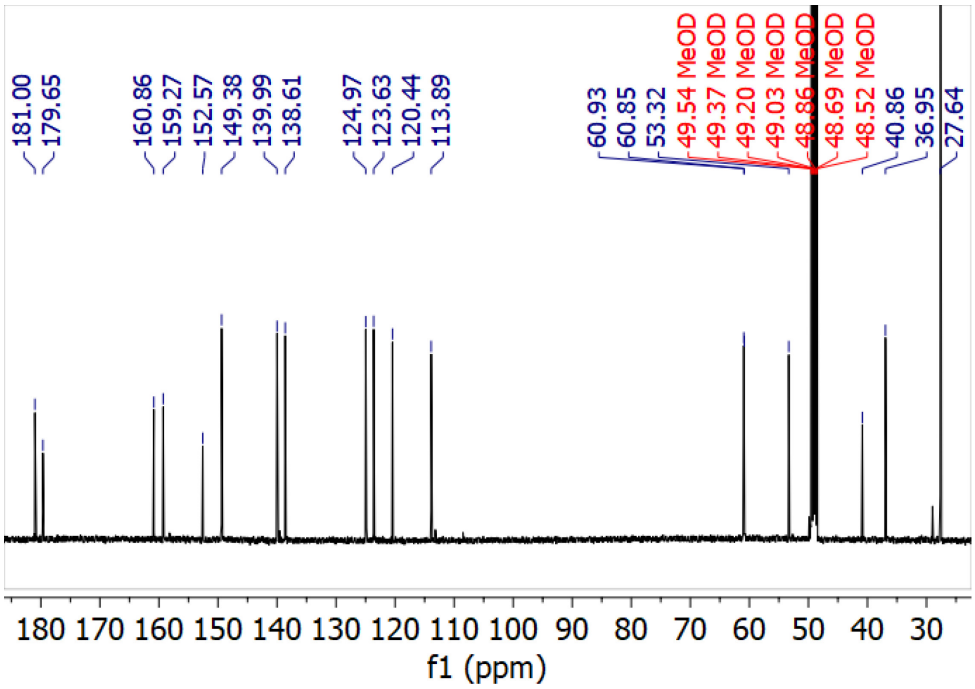

Figure 4.31 ^{13}C NMR spectrum of [Na(Amide-BMPA-Pr)] in CD_3OD.

Synthesis of sodium 3-(((6-aminopyridin-2-yl)methyl)(pyridin-2-ylmethyl)amino)propanoate [Na(Amine-BMPA-Pr)]. Route 1: 139.5 mg (0.364 mmol) of methyl 3-(((6-pivalamidopyridin-2-yl)methyl)(pyridin-2-ylmethyl)amino)propanoate and 5 mL of 1 M (5.45 mmol) sulfuric acid were combined. The reaction mixture was stirred at 50 °C until the reaction was complete by ^{1}H NMR. The reaction mixture was washed with hexanes to remove unreacted starting material. The aqueous layer neutralized with sodium hydroxide to form the desired product as a sodium salt and sodium sulfate. The resulting solution was evaporated and dried under vacuum overnight to remove water. The dried residue was suspended in anhydrous methanol and placed in the freezer at -35 °C resulting in an orange/yellow solution with white precipitate. The white solid was filtered off and the filtrate was evaporated, and the product was column purified on silica and eluted with methanol. Yield: 24.1 mg (0.078 mmol; 21%)

Route 2: The hydrolysis of this ligand followed a modified literature procedure.[82] 98.9 mg of Amine-BMPA-PrOCH_3 (0.033 mmol) was transferred to a 10 mL round bottom flask and dissolved in 0.5 mL of THF:H_2O. Next, 0.16 mL of 2M NaOH solution (0.033 mmol) was added to the reaction. The reaction was heated to 60 °C overnight. The next day, the reaction was washed with dichloromethane three times to remove unreacted starting material. The resulting aqueous layer was dried to yield product which was then stored in the freezer until further use. Yield: 88.4 mg (0.29 mmol, 87%). ^{1}H NMR (CD_3OD): 8.42 (d, 1H); 7.77 (td, 1H); 7.61 (d, 1H); 7.39 (t, 1H); 7.25 (dt, 1H); 6.76 (d, 1H); 6.41 (d, 1H); 3.78 (s, 2H); 3.59 (s, 2H); 2.84 (t, 2H), 2.43 (t, 2H) ppm. ^{13}C NMR (CD_3OD): 181.04; 160.91; 160.64; 149.51; 139.71; 138.61; 124.85; 123.61; 113.13; 108.57; 60.87; 60.83; 53.19 ppm.

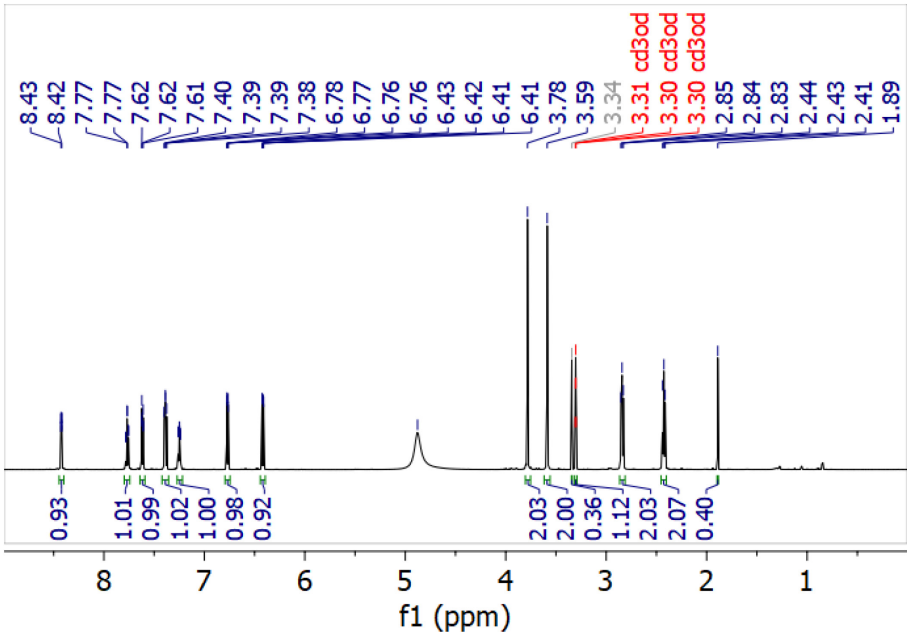

Figure 4.32 ^{1}H NMR spectrum of [Na(Amine-BMPA-Pr)] in CD_3OD.

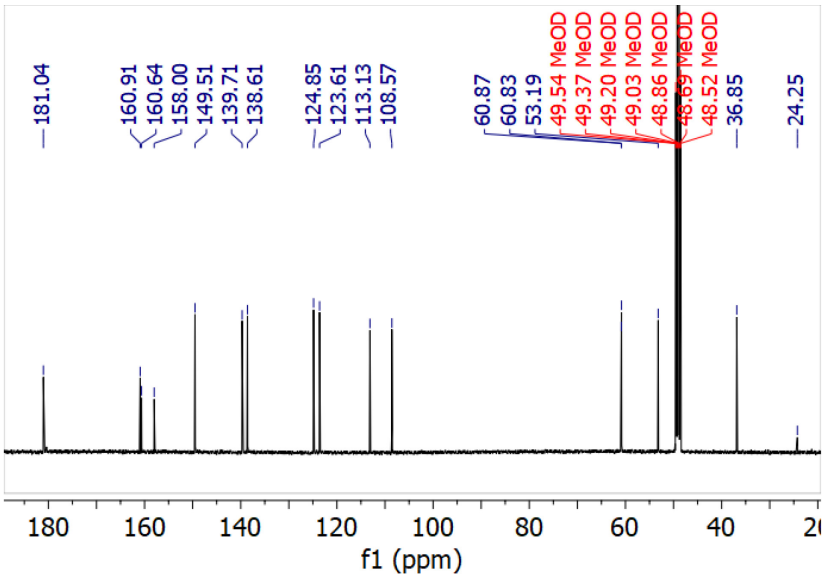

Figure 4.33 ^{13}C NMR spectrum of [Na(Amine-BMPA-Pr)] in CD_3OD.

Copper (II) 3-(((6-aminopyridin-2-yl)methyl)(pyridin-2-ylmethyl)amino)propanoate acetate (Cu(Amine-BMPA-Pr)(OAc)]. 1 equivalent of copper(II) acetate monohydrate ($Cu(OAc)_2$ H_2O) was added to 1.5 equivalents of [Na(Amine-BMPA-Pr)] dissolved in water to give a ~100 mM solution of [Cu(Amine-BMPA-Pr)(OAc)]. UV-vis (H_2O): 298, 637 nm.

Copper (II) 3-(((6-pivalamidopyridin-2-yl)methyl)(pyridin-2-ylmethyl)amino)propanoate acetate (Cu(Amide-BMPA-Pr)(OAc)]. 1 equivalent of copper(II) acetate monohydrate ($Cu(OAc)_2$ H_2O) was added to 1.5 equivalents of [Na(Amide-BMPA-Pr)] dissolved in water to give a ~100 mM solution of [Cu(Amine-BMPA-Pr)(OAc)]. UV-vis (H_2O): 298, 600 nm.

Chapter 5 Conclusions and Future Directions

The denitrification pathway of the nitrogen cycle consists of multiple NO_x interconversions that happen every day in the world around us. Understanding these reactions provides an opportunity to further apply that knowledge to improve our society. From an environmental perspective, 75% of N_2O emissions are predicted to come from agriculture. One source of these emissions is Cyt P450nor, where NO reduction leads to N_2O formation. **Chapter 2** and **Chapter 3** focus on modeling the suspected key intermediate of this enzymatic reaction using a sterically hindered porphyrin that is spectroscopically characterized. These results can be extrapolated in the context of Cyt P450nor to learn more about this reaction. From a medical perspective, inspiration was taken from Nature to improve current biomedical devices like catheters which present risks to patients, such as bacterial infections and blood clots. NO is known to prevent these risks. **Chapter 4** focuses on catalyst development with inspiration from CuNIR, which efficiently reduces NO_2^- to NO. The catalysts made in this chapter were characterized electrochemically in conjunction with NO quantification. These results provide important directions for future copper catalyst developments for this biomedical application.

5.1 Stabilization and Full Characterization of a Sterically Protected Heme-HNO Complex

The work discussed in **Chapter 2** provides a stable heme-nitroxyl adduct with a neutral N donor as the axial ligand in organic solvents. This work is relevant for modeling enzymes proposed to have heme-nitroxyl intermediates. Two examples are hydroxylamine oxidoreductase (HAO)

which contains an axial bound histidine residue, as well as Cytochrome *c* nitrite reductase (C*c*NIR) which contains a lysine residue as the axial ligand. This work focused on full spectroscopic characterization of a six-coordinate ferrous heme-nitroxyl, [Fe(3,5-Me-BAFP)(MI)(NHO)], as well as thorough reactivity studies with NO in the context of Cyt P450nor. Though the axial ligand of the Cyt P450nor active site is a cysteinate residue, the goal of this work was to assess potential electronic structures of Intermediate *I* that promote NO reduction to N_2O.

The formation of [Fe(3,5-Me-BAFP)(MI)(NHO)] was monitored with the addition of [TBA](BH_4) to the corresponding 6C $\{FeNO\}^6$, [Fe(3,5-Me-BAFP)(MI)(NO)](OTf). This reaction models the hydride transfer from NAD(P)H in the Cyt P450nor. The heme-nitroxyl formed from this reaction was found to be stable for hours at -30 °C which was determined to be the most stable heme-nitroxyl complex in organic solvents. The advantage of the prolonged life-time of the heme nitroxyl complex allowed for its isolation as a solid which was found to be stable at room temperature. The vibrational characterization of this complex was coupled with DFT to formally assign the Fe-N stretch and Fe-N-O bend for the first time in the literature. When excess NO gas was added to the heme-nitroxyl complex, N_2O was formed in a 93% yield. The reformation of the $\{FeNO\}^6$ after N_2O formation indicates that a ferric product forms followed by immediate binding from the excess NO in solution. Both results indicate that the Fe(II)-HNO complex contains a viable electronic structure for NO reduction in Cyt P450nor.

5.1.1 Future Directions: Hydrogen Bond Derivatives of the Bulky Bispicket Fence Porphyrin

Water soluble heme nitroxyl models tend to be more stable than those reported in organic solvents. Two water-soluble heme nitroxyl models are reported in the literature. The first model reported was the Mb-HNO and was found to be the most stable heme-nitroxyl complex with no significant

decay. Additionally, a synthetic model $[Fe(TPPS)(NHO)]^{-}$ was found to form and decay at room temperature, which has not yet been observed in organic solvents. Based on the most stable model DFT calculations show that this stability comes from hydrogen bonding between the distal histidine of Mb and the bound HNO, as shown in **Figure 5.1**.

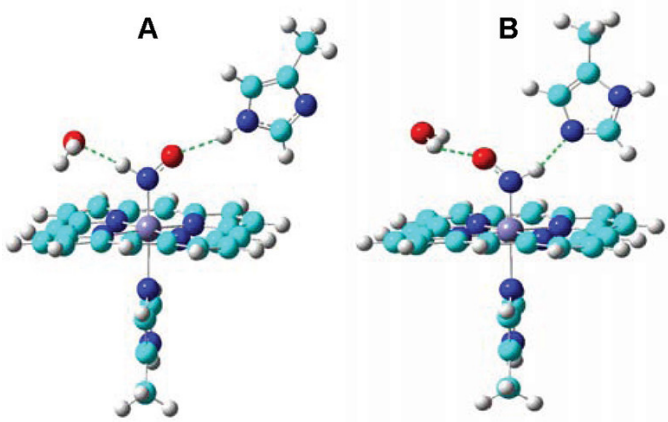

Figure 5.1 Computational models of Mb(II)−NHO, showing a stabilization of the bound HNO ligand by hydrogen-bonding with His64 and a water molecule. Two possible hydrogen-bonding networks are shown (panel A and B). Reprinted with Permission from ref [57]. Copyright 2011 American Chemical Society.

To achieve this type of stability of a heme nitroxyl complex in organic solvents, the bulky bispicket fence porphyrin can be modified to include hydrogen bonding groups in the second coordination sphere of the Fe-HNO moiety. Derivatives of hydrogen bond appended bispicket fence porphyrins were optimized by DFT to determine promising synthetic targets, $[H_2(3\text{-HO-BAFP})]$ and $[H_2(3\text{-NH}_2\text{-BAFP})]$, as shown in **Figure 5.2**. The synthesis of these porphyrins are detailed in **Appendix A**. Despite the symmetry of these porphyrins, the synthesis of both derivatives posed their own challenges. Initially, these porphyrins were synthesized using a modified procedure of the original bulky bispicket fence porphyrin, $[H_2(3,5\text{-Me-BAFP})]$. First, the aldehyde arm is synthesized with either methoxy or nitro phenol via an Ullman condensation. The porphyrin is synthesized using the aldehyde arm and subsequent modifications are made to obtain

the final hydrogen bonding porphyrins. The challenges with this route include difficult purification due to low solubility and low yield for the [H_2(3-NO_2-BAFP)] and [H_2(3-MeO-BAFP)], respectively. Alternatively, the porphyrin was synthesized first to make [H_2(Br_8TPP)] which would be taken forward to the Ullman condensation prior to modifications to yield the desired porphyrins. Unfortunately, this posed issues with unwanted copper metalation of the porphyrins which were difficult to unmetallated. Future students could redesign and optimize the synthesis of these second sphere bispicket fence porphyrin derivatives.

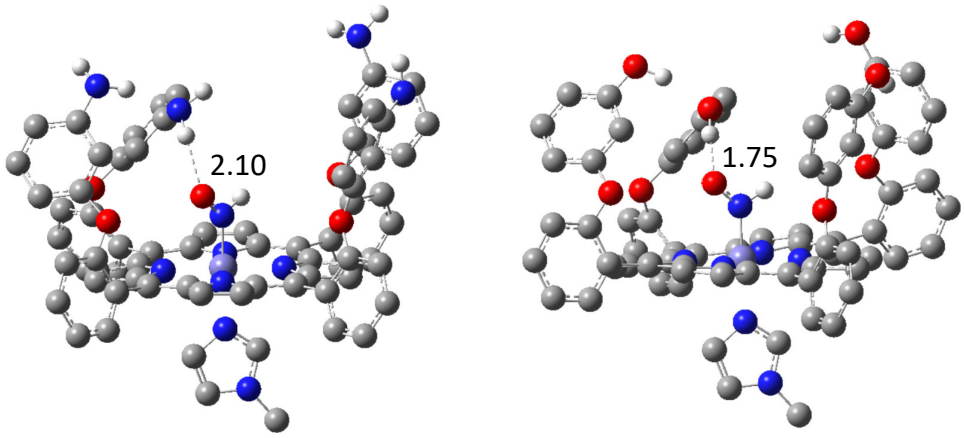

Figure 5.2 BP86/TZVP optimized structures of simplified versions of hydrogen bonding derivatives of [Fe(3,5-Me-BAFP)(MI)(NHO)], where the pickets around the MI ligand have been omitted for simplicity. Left: [Fe(3-NH_2-BAFP)(MI)(NHO)], Right: [Fe(3-OH-BAFP)(MI)(NHO)].

5.2 A Synthetic Model Complex for the Active Site of Cyt P450nor

The contributions from **Chapter 3** include the formation of a thiolate bound heme ls-{FeNO}^{6} model complex using the bulky bis-picket fence porphyrin, followed by hydride addition. Here, the first NMR characterization was obtained for a thiolate bound ls-{FeNO}^{6} synthetic model complex. By vibrational characterization, the thiolate-bound ls-{FeNO}^{6} complex showed Fe-NO and N-O stretching frequencies comparable to those of the native enzyme, indicating that it is a good model for the active site of Cyt P450nor. This work is novel since there is no literature

precedence for hydride addition to a thiolate-bound heme ls-{FeNO}^{6} synthetic model complex. Next, hydride was added to the reaction after forming the thiolate bound ls-{FeNO}^{6} complex at low temperature in situ. Based on solution IR and NMR spectroscopy, the ls-{FeNO}^{6} complex was consumed upon hydride addition which leads to decreased ls-{FeNO}^{7} formation. The results obtained by NMR spectroscopy hint at the undesired reaction between the disulfide present from the initial ls-{FeNO}^{6} complex formation and the hydride source added to the solution.

Due to the side reactions possible between NO, thiol, thiolate, and potential HNO that are generated over the course of this reaction, future work should focus on performing the full control experiments to fully understand these side reactions. The knowledge obtained from these studies will aid in determining the conditions for the successful formation of a synthetic thiolate-bound heme nitroxyl model complex in the future.

5.3 Hydrogen Bond Appended Copper Catalysts for Electrochemical NO Generation

As discussed in **Chapter 4**, two second coordination sphere derivatives of the BMPA-Pr$^-$ ligand were synthesized with either an amide or an amine to make the Amide-BMPA-Pr$^-$ and Amine-BMPA-Pr$^-$ ligands, respectively. The ligands were metallated with $Cu(OAc)_2$ to obtain [Cu(Amide-BMPA-Pr)(OAc)] and [Cu(Amine-BMPA-Pr)(OAc)] complexes, which were subsequently characterized by UV-vis spectroscopy and cyclic voltammetry (CV). It was determined that [Cu(Amide-BMPA-Pr)(OAc)] was not capable of performing nitrite reduction due to poor substrate binding and low electrochemical stability of the complex. On the other hand, [Cu(Amine-BMPA-Pr)(OAc)] was able to outperform the parent complex [Cu(BMPA-Pr)(OAc)] under inert atmosphere. Based on this work, it was determined that the presence of a hydrogen

bond donor in the second coordination sphere does not reduce O_2 sensitivity as previously hypothesized.

Future students could synthesize hydrogen bonding derivatives of catalysts with more positive reduction potentials. Two starting points include BEPA-Pr^- and BEPA-$EtSO_3$, which have reduction potentials of +10 and +55 mV, respectively, which lower the O_2 sensitivity of these copper catalysts. Based on previous work it was determined that catalysts with more positive reduction potentials are more selective toward NO production but are slow with respect to nitrite reduction. In comparison to the parent complex, the presence of hydrogen bond donors in the second coordination sphere appears to improve catalysis in comparison to the parent complex under inert conditions. Therefore, in addition to the appended hydrogen bond donors of the BEPA-Pr^- and BEPA-$EtSO_3$ ligands, a set of asymmetric BMPA/BEPA arms could be synthesized to make a complex with a slightly more negative reduction potential. The addition of the hydrogen bond donors can be used to fine tune the reduction potentials for the lowest O_2 sensitivity with the highest Faradaic efficiency for NO generation.

5.4 Concluding Remarks

The work compiled in this thesis contributes to the knowledge of NO_x interconversions in nature, more specifically, NO reduction to N_2O in Cyt P450nor and NO_2^- reduction to NO in CuNIR. This work provides insight into the reaction mechanism of Cyt P450nor, indicating that a ferrous heme nitroxyl species is capable of NO reduction to N_2O. A new ferric heme thiolate complex was synthesized to better mimic the electronics of the Cyt P450nor active site to study the nitroxyl complex after hydride transfer. This work provides guidelines for monitoring hydride transfer to a thiolate bound $\{FeNO\}^6$ complex in future studies. New copper complexes were synthesized for

NO generation through electrochemical nitrite reduction for biomedical applications. These complexes were synthesized with hydrogen bond donors in the second coordination sphere to reduce the O_2 sensitivity of these types of catalysts. It was determined that the hydrogen bond in the second coordination sphere does not affect O_2 stability, however it does improve catalysis under ambient conditions.

Appendix: Synthesis of Bis-Picket Fence Porphyrins that Carry Hydrogen-Bond Donors in the Second Coordination Sphere

General Considerations

All chemicals were purchased from commercial sources, including Sigma Aldrich, Fisher Scientific, and Cambridge Isotopes, and used without further purification unless noted below. Reactions were performed under inert atmosphere via Schlenk techniques. All solvents were dried and distilled from CaH_2 and freeze pump thawed four times to remove water and dioxygen. Preparation and handling of air-sensitive materials were performed under a dinitrogen atmosphere in an MBraun glovebox, equipped with a circulating purifier (O_2, H_2O <0.1 ppm).

Physical Measurements

UV-vis Spectroscopy. All spectra were recorded using an Analytic Jena Specord S-600 Spectrometer.

^{1}H NMR Spectroscopy. A Varian MR 400 MHz instrument was used to record all NMR spectra at 25 °C.

Mass Spectrometry. All data were collected using an Agilent 6230 time-of-flight high-performance liquid chromatography/mass spectrometer.

Density Functional Theory Calculations. All calculations were performed using the program Gaussian 09.[152] All geometry optimizations and frequency calculations were performed using the

BP86 functional and the TZVP basis set. [107] Calculated frequencies were inspected to ensure the absence of any imaginary frequencies, to confirm that true energy minima were obtained.

A.1 Design of Second Coordination Sphere Bis-Picket Fence Porphyrin Scaffolds

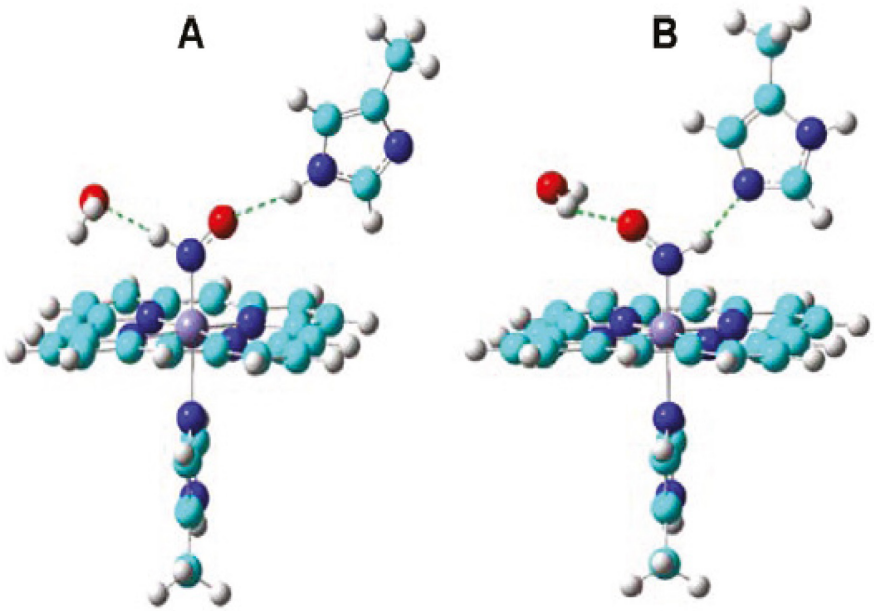

Figure A.1 Computational models of Mb(II)−NHO, showing a stabilization of the bound HNO ligand by hydrogen-bonding with His64 and a water molecule. Two possible hydrogen-bonding networks are shown (panel A and B). Reprinted with Permission from ref [57]. Copyright 2011 American Chemical Society.

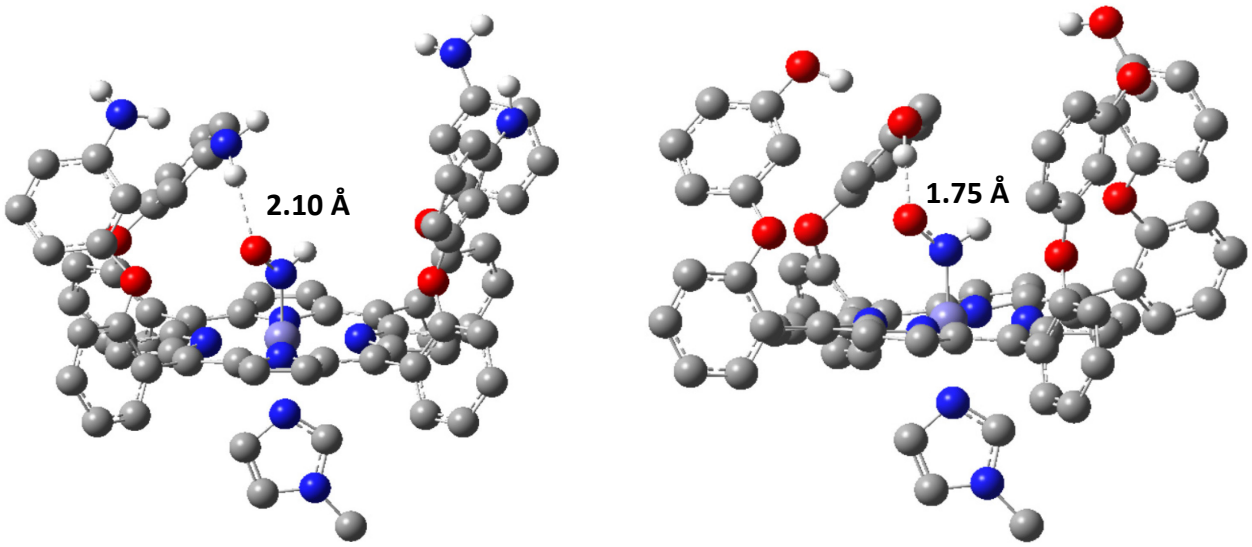

Figure A.2 BP86/TZVP optimized structures of simplified versions of hydrogen bonding derivatives of [Fe(3,5-Me-BAFP)(MI)(NHO)], where the pickets around the MI ligand have been omitted for simplicity. Left: [Fe(3-NH_2-BAFP)(MI)(NHO)], Right: [Fe(3-OH-BAFP)(MI)(NHO)].

The goal of this project was to understand the potential electronic structure effects of hydrogen bonds on the HNO adduct. This work was inspired by the aqueous nitroxyl model, Mb-HNO, which was determined to have unprecedented stability due to two major hydrogen bonding isomers that involve the distal histidine residue present in the Mb active site, as shown in **Figure A.1**.[57] Synthetic model complexes were designed by adding second coordination sphere groups to the pickets of the [H_2(3,5-Me-BAFP)] ligand system, where the methyl substituents can be modified to amine or hydroxyl groups to engage in hydrogen bonding interactions with iron-coordinated molecules, in this case HNO. Computationally, scaffolds employing these hydrogen bonding groups appear to be promising synthetic targets for the goal stated above, as shown in **Figure A.2**. Here, the hydrogen bonding distance between the HNO moiety and the appended hydrogen bonding groups was found to be 2.10 and 1.75 Å for the amine and hydroxyl groups, respectively. The preliminary synthetic pathways for each of these derivatives is discussed below.

A.2 Route 1: Synthesis of Second Coordination Sphere Porphyrin Scaffolds

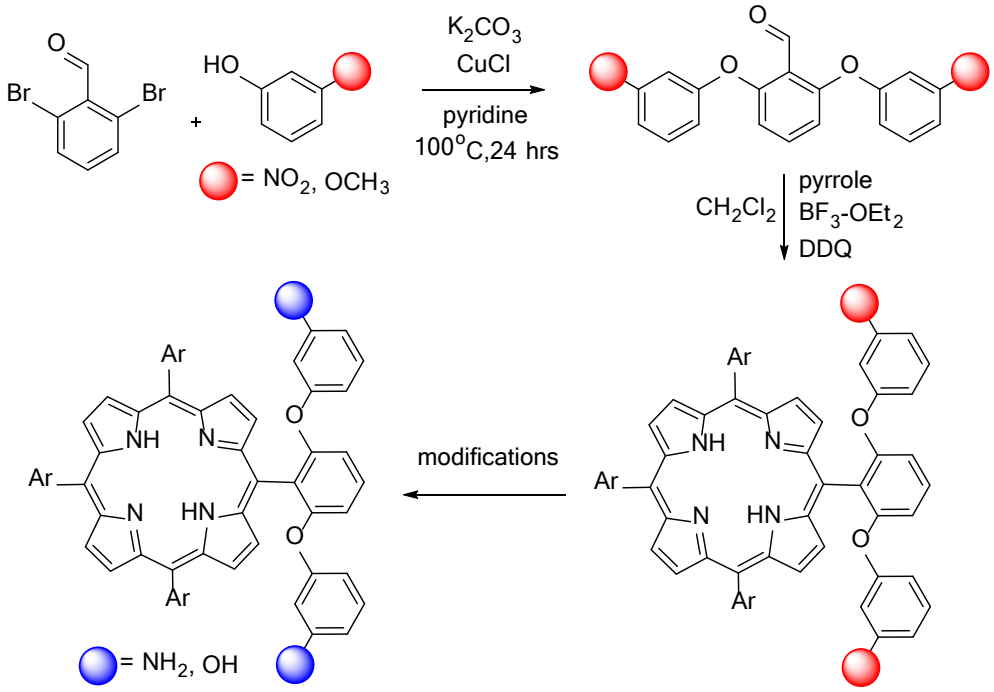

Figure A.3 Synthetic scheme of the modified [H_2(3,5-Me-BAFP)] ligands, where the aldehyde arm is synthesized prior to porphyrin condensation.

This synthetic route is adapted from the original bis-picket fence porphyrin procedure. Here, an Ullman condensation was performed to synthesize the fully substituted aldehyde arm. Although the hydrogen bonding groups are proposed to be an amine or alcohol group, these groups would perform unwanted side reactions in both the Ullman condensation and the subsequent porphyrin condensation. Therefore, nitro and methoxy groups were chosen to act as protecting groups that can be modified to the ideal second coordination sphere groups after the porphyrin is synthesized.

General synthesis of modified BAFP arms. This synthesis follows a modified literature procedure.[63] In the appropriate size Schlenk flask, 4 equivalents of phenol and potassium carbonate (with respect to the aldehyde) were suspended in benzene and stirred for an hour to allow full

deprotonation of the phenol. The solvent was then removed under low pressure. Under an inert atmosphere, the resulting solid was dissolved in pyridine followed by the addition of 1 equivalent 2,6-dibromobenzaldehyde and 17 mol% copper(I) chloride. The reaction was refluxed under nitrogen for 17-24 hours. Once the reaction cooled, the solution was poured over ice and acidified with concentrated hydrochloric acid. The crude product was extracted with dichloromethane and subsequently washed with water, saturated aqueous sodium bicarbonate, and again with water. The organic layer was then concentrated using a rotary evaporator to a thick oil. The crude product was purified by column chromatography on silica eluting typically with dichloromethane, unless otherwise noted. Fractions were evaporated and the product was further purified by recrystallization from methanol.

Synthesis of 2,6-bis(3-nitrophenoxy)benzaldehyde (3-NO_2-BAFP arm). The crude product was column purified with 10% hexanes and dichloromethane as the eluent. Yield: 3.01 g (44%) ^{1}H NMR ($CDCl_3$) δ = 10.48 (1H, s); 8.04 (dd, 2H); 7.88 (2H, t); 7.61 (2H, t); 7.59 (2H, t); 7.46 (2H, dd); 6.88 (2H, d).

Synthesis of 2,6-bis(3-methoxyphenoxy)benzaldehyde (3-MeO-BAFP arm). Yield: 1.8 g (27%). ^{1}H NMR ($CDCl_3$) δ = 10.56 (s, 1H); 7.34 (t, 1H); 7.27 (t, 2H); 6.72 (d, 2H); 6.64 (m, 6H); 3.80 (s, 6H).

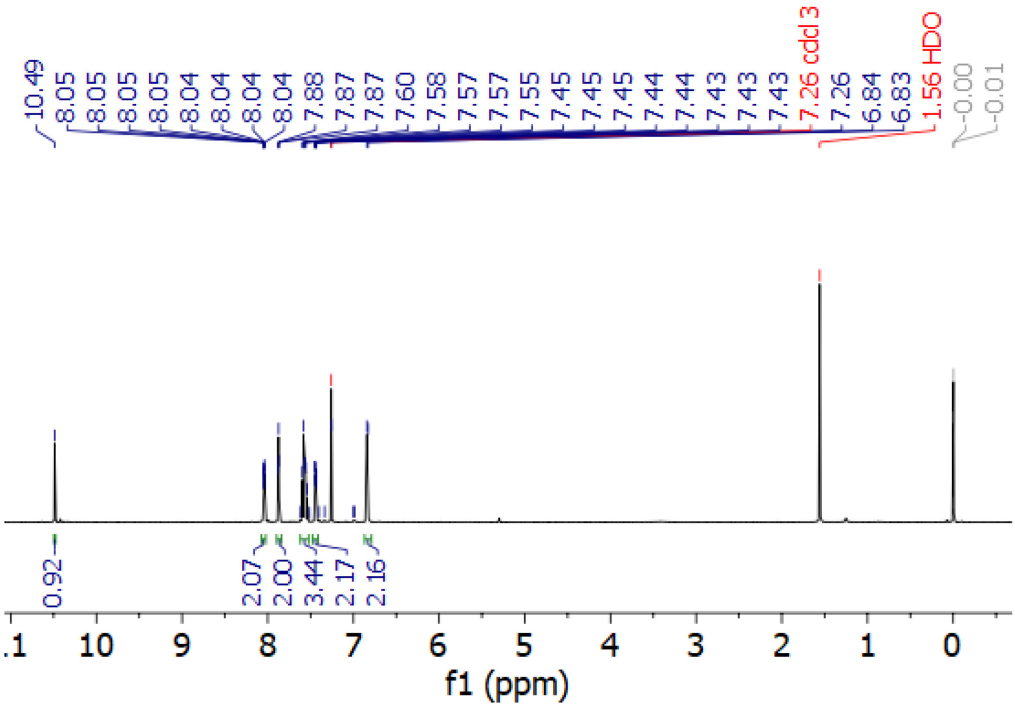

Figure A.4 ^{1}H NMR spectrum of 3-NO_2-BAFP arm in $CDCl_3$.

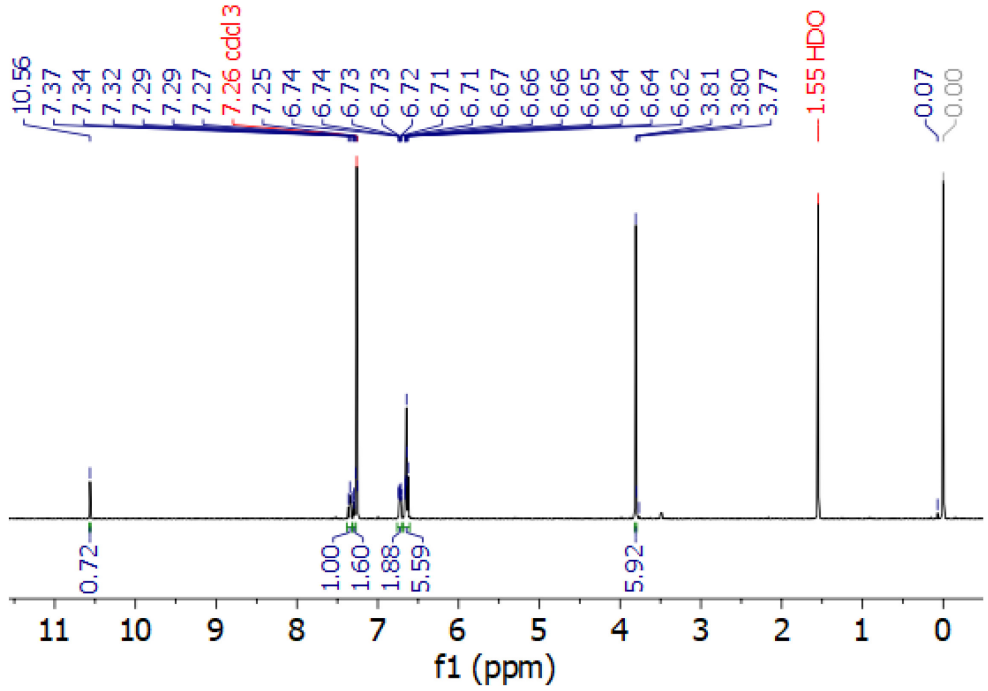

Figure A.5 ^{1}H NMR spectrum of 3-MeO-BAFP arm in $CDCl_3$.

General synthesis of modified bis-picket fence porphyrins. The synthesis of these porphyrins follows a modified literature procedure.[63] In a round bottom flask, typically 1-2 g of modified BAFP arm was dissolved in 300 mL of dry dichloromethane followed by the addition of absolute ethanol making up 5-10% of the reaction mixture by volume. The reaction was sparged with nitrogen for 10 minutes, followed by the dropwise addition of freshly distilled pyrrole (1 equivalent with respect to the aldehyde arm) and allowed to sparge for an additional 5 minutes. Next, 0.16 mL of boron trifluoride diethyl etherate (BF_3OEt_2) was added to the reaction and the mixture was stirred in the dark under nitrogen atmosphere for 1 hour at room temperature. After one hour, the reaction mixture was exposed to oxygen and light, and 0.69 equivalents (with respect to pyrrole) of 2,3-dicyano-4,5-dichlorobenzoquinone (DDQ) were added to form the desired porphyrin, followed by 0.16 mL of triethylamine to quench remaining BF_3OEt_2. The reaction was stirred for one additional hour before it was concentrated by rotary evaporation to a dark oil. The porphyrin was purified on silica eluting with dichloromethane.

Synthesis of 2,6-bis(3-nitrophenoxy)phenylporphyrin ([H_2(3-NO_2-BAFP)]). The general synthesis was performed as outlined above using the 3-NO_2-BAFP arm as the aldehyde. Attempts to purify this porphyrin by column chromatography remained a challenge since the solubility of the porphyrin was low and would result in the product streaking down the column. Multiple solvents were considered to achieve better solubility for cleaner purification including dichloromethane, methanol, ethyl acetate, toluene, hexanes, nitromethane, and nitrobenzene. The crude product was characterized by UV-vis and mass spectrometry to determine if any porphyrin was formed. By UV-vis there wasn't enough heme present to observe a distinct Soret band; however by mass spectrometry there was a peak present indicating that [H_2(3-NO_2-BAFP)] had

indeed been synthesized. Due to the difficult purification conditions, a yield for the [H_2(3-NO_2-BAFP)] product could not be determined and the crude product mixture was brought forward in subsequent synthetic steps. MS: m/z 1713.35 (M+H).

Synthesis of 2,6-bis(3-methoxyphenoxy)phenylporphyrin ([H_2(3-MeO-BAFP)]). The general synthesis was performed as outlined above using the 3-MeO-BAFP arm as the aldehyde. Unfortunately, this method demonstrated very low yields in the first trial. Subsequent attempts showed no product formation by mass spectrometry; therefore, alternate routes were considered to synthesize this porphyrin. Yield: 30 mg (<1 %). ^{1}H NMR (CH_2Cl_2) δ = 8.94 (s, 8H); 7.64 (t, 4H); 7.08 (d, 8H); 6.74 (t, 8H); 6.32 (d, 8H); 6.14 (d, 8H); 6.07 (s, 8H); 3.18 (s, 24H); -2.96 (s, 2H). UV-Vis (CH_2Cl_2): 403, 424, 517, 592, 646 nm. MS: m/z 1592.55 (M+H); 796.7762 (M/2).

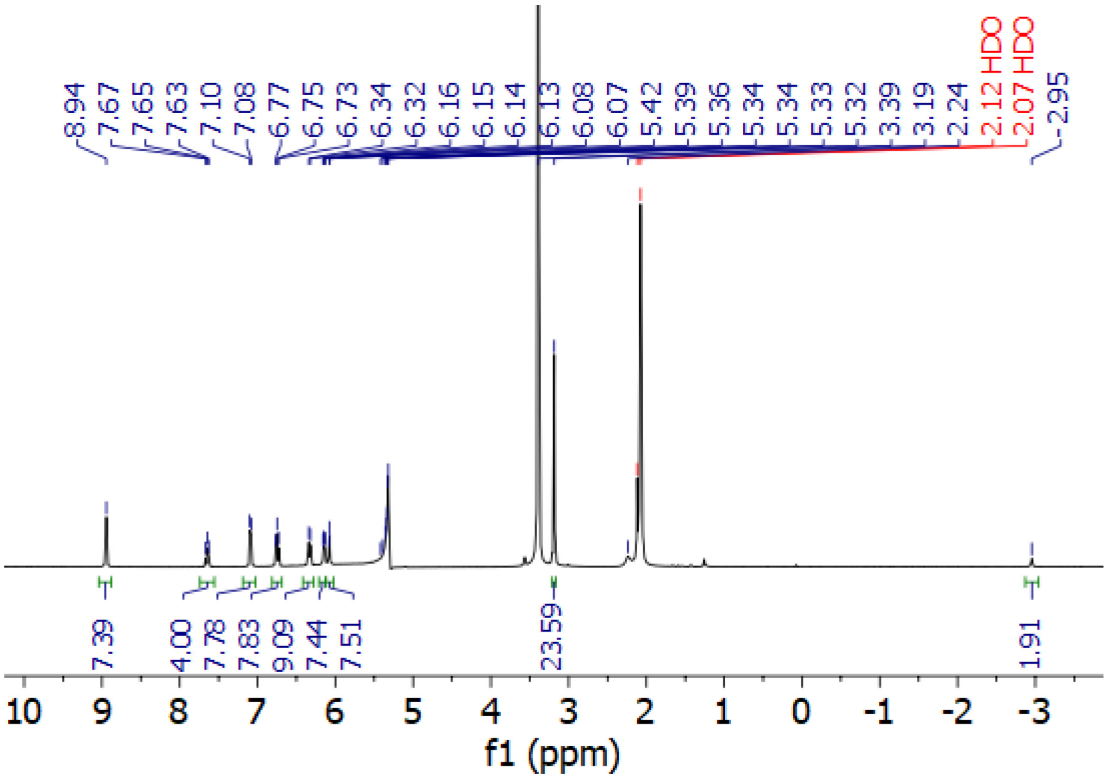

Figure A.6 ^{1}H NMR spectrum of [H_2(3-MeO-BAFP)] in CH_2Cl_2.

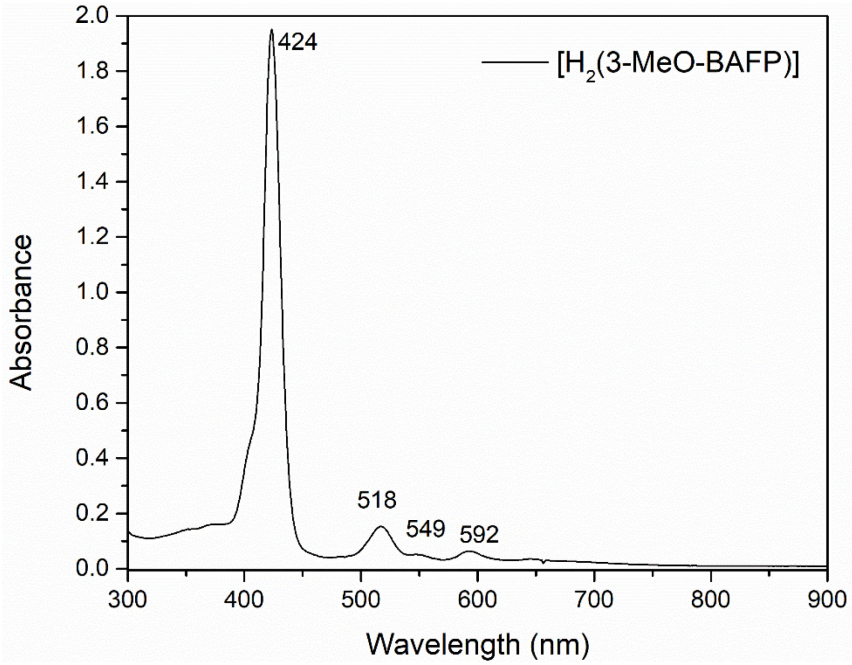

Figure A.7 UV-vis spectrum of [H_2(3-MeO-BAFP)] in CH_2Cl_2.

A.3 Route 2: Synthesis of Second Coordination Sphere Porphyrin Scaffolds

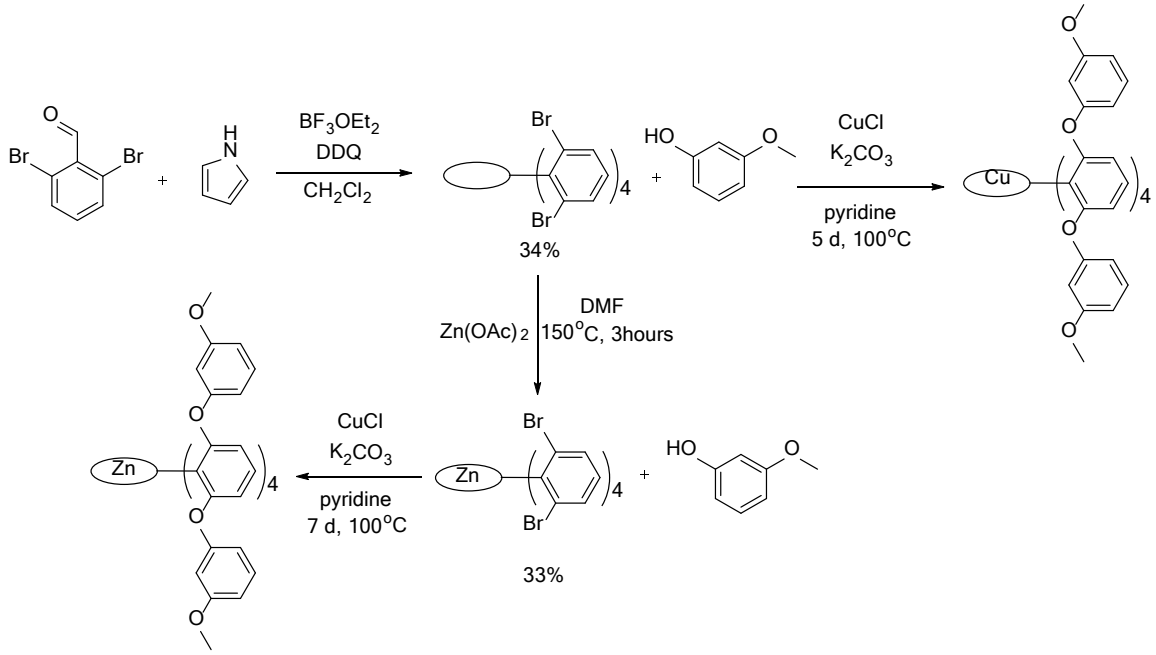

Figure A.8 Synthetic scheme of modified [H_2(3,5-Me-BAFP)], where the porphyrin is synthesized first and metalated with zinc prior to Ullman condensation.

As discussed above, Route 1 lead to unforeseen challenges including the difficult purification of the [H_2(3-NO_2-BAFP)] porphyrin and the very low yields of [H_2(3-MeO-BAFP)]. In Route 2, the porphyrin is initially synthesized to solve both challenges described above. This route allows for the synthesis of one universal porphyrin that can undergo the Ullman condensation with various phenols to yield multiple modified bis-picket fence porphyrins. Because the Ullman condensation requires a copper catalyst, the porphyrin was first metalated with zinc to prevent the unwanted copper metalation.

Synthesis of 5,10,15,20-tetrakis(2,6-dibromophenyl)porphyrin, [H_2(Br_8TPP)]. The synthesis of this porphyrin followed a modified literature procedure.[63] Due to solubility problems with this porphyrin after purification, the ^{1}H NMR spectrum was obtained on a very dilute sample. This

solubility issue can be mitigated by the addition of acid; however, this was not done as it would inhibit the metalation step. Yield: 307 mg (34%). ^{1}H NMR ($CDCl_3$) δ = 8.58 (s, 8H); 7.97 (d, 8H); 7.49 (t, 4H); -2.54 (s, 2H). UV-Vis (CH_2Cl_2) 405, 422, 516, 597 nm. MS 1245.92 [M+H], 623.26 [M/2]

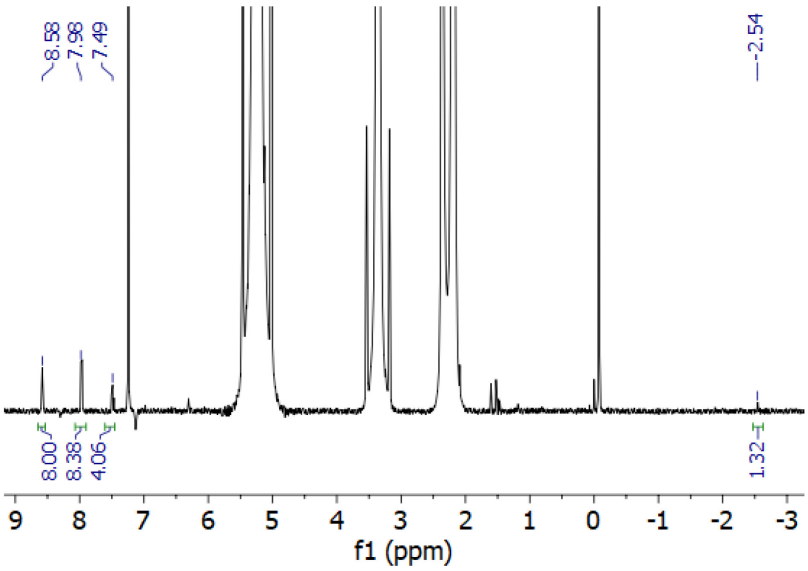

Figure A.9 ^{1}H NMR spectrum of [$H_2(Br_8TPP)$] in $CDCl_3$.

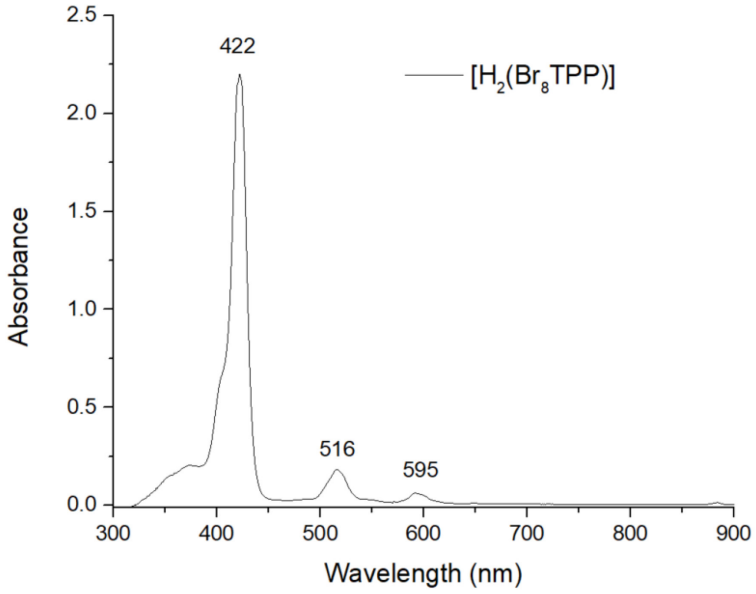

Figure A.10 UV-vis spectrum of [$H_2(Br_8TPP)$] in CH_2Cl_2.

Method A

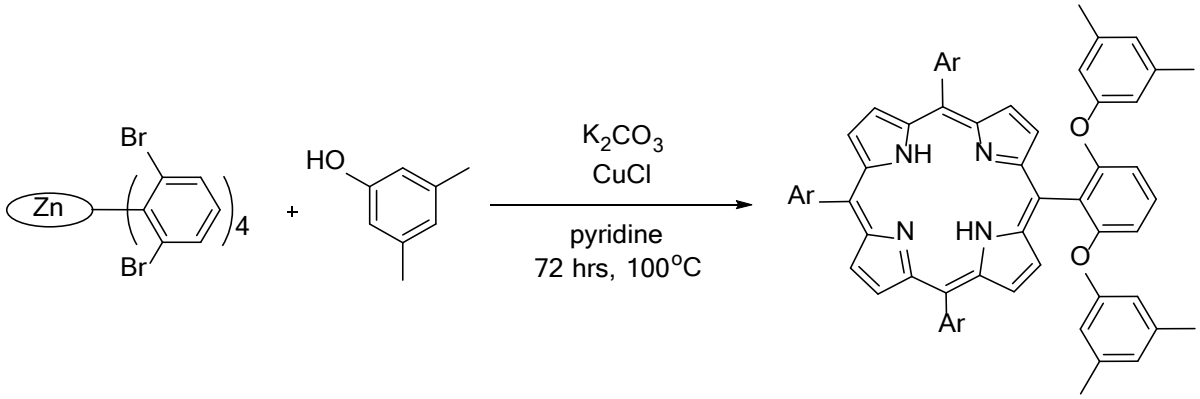

Figure A.11 Synthesis of the [H_2(3,5-Me-BAFP)] porphyrin using Route 2, where the [H_2(Br_8TPP)] ligand was metalated with zinc prior to the Ullman condensation.

Synthesis of zinc 5,10,15,20-tetrakis(2,6-dibromophenyl)porphyrin, [Zn(Br_8TPP)]. In a 250 mL round bottom flask, 307.4 mg (0.247 mmol) of [H_2(Br_8TPP)] and 5.759 g (106 eq) of $Zn(OAc)_2$ were dissolved in 40 mL of DMF. The reaction was refluxed overnight at 150 °C. The next day, the reaction mixture was checked by mass spectrometry to ensure metalation had occurred. The reaction mixture was dried under vacuum and column purified. The fractions were rotary evaporated to yield a bright pink/purple powder. Yield: 106.4 mg, 33%. ^{1}H NMR (CD_2Cl_2) δ = 8.74 (s, 8H); 8.04 (d, 8H); 7.57 (t, 4H). UV-Vis (CH_2Cl_2) 425, 555 nm. MS: 1310 (M+H).

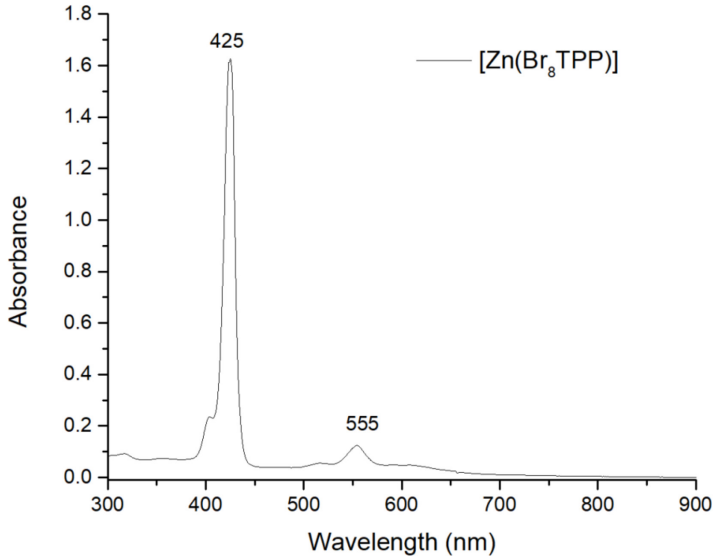

Figure A.12 UV-vis spectrum of [Zn(Br$_8$TPP)] in CH_2Cl_2.

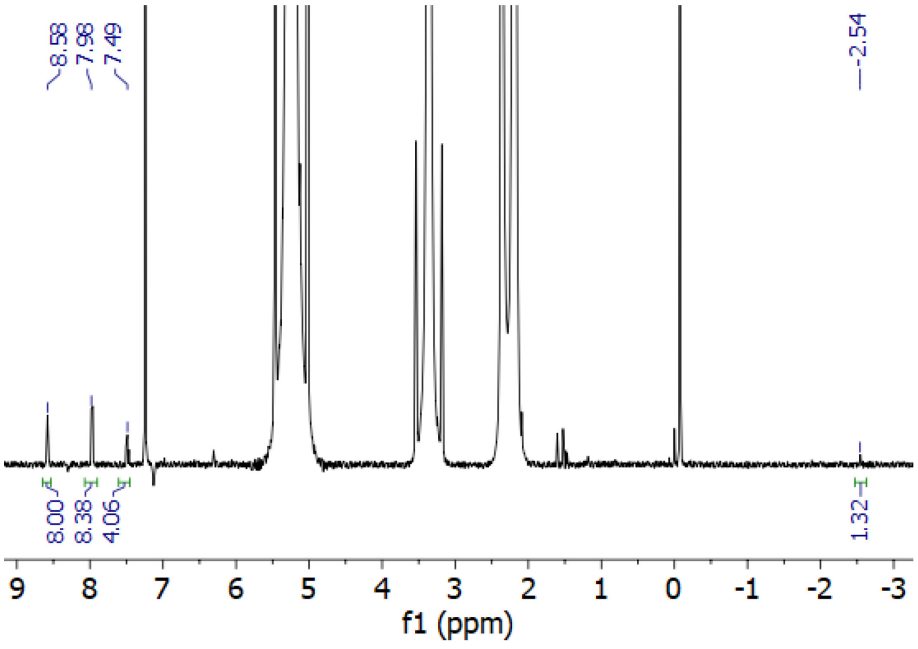

Figure A.13 ^{1}H NMR spectrum of [Zn(Br$_8$TPP)] in CH_2Cl_2.

Synthesis of [Fe(Br$_8$TPP)(X)]. The metalation of the H_2[Br$_8$TPP] ligand was attempted under multiple conditions with little success. These conditions included multiple different iron sources, including $FeCl_3$, $Fe(OTF)_3$, $Fe(AcAc)_3$, as well as different solvents, including the typical solvents used for porphyrin metalation: DMF and THF, as well as pyridine.

Synthesis of 3,5-Dimethyl-bisaryloxyfence porphyrin, [H$_2$(3,5-Me-BAFP)]. This new route was first repeated with the original bis-picket fence porphyrin to determine if this alternative route could be a viable synthetic pathway for the second coordination sphere derivatives. Here, the reaction was adapted based on the synthesis of the 3,5-Me-BAFP arm. In a 10 mL round bottom flask, 3,5-dimethyl phenol (80.5 mg, 0.659 mmol) and K_2CO_3 (101 mg, 0.731 mmol) were dissolved in 5 mL of pyridine. After 15 minutes, [Zn(Br$_8$TPP)] (48.2 mg, 0.0368 mmol) and 17% mol copper(I) chloride was added to the reaction mixture. The resulting solution was refluxed for three days. After removing the reaction mixture from heat, it was poured over ice, and acidified with concentrated hydrochloric acid. The change in pH aided in washing out the copper catalyst after the reaction, but likely also aided in removing the zinc, yielding the free base porphyrin. The product was then extracted with dichloromethane and washed with water followed by saturated aqueous sodium bicarbonate and water. The organic layer was then rotary evaporated to a dark purple solid and column purified on silica with dichloromethane. The purified product was characterized by ^{1}H NMR, UV-Vis, and MS, all of which matched literature values. Yield: <10 mg, 17%. The ^{1}H NMR and MS are shown in **Figure A.14**.

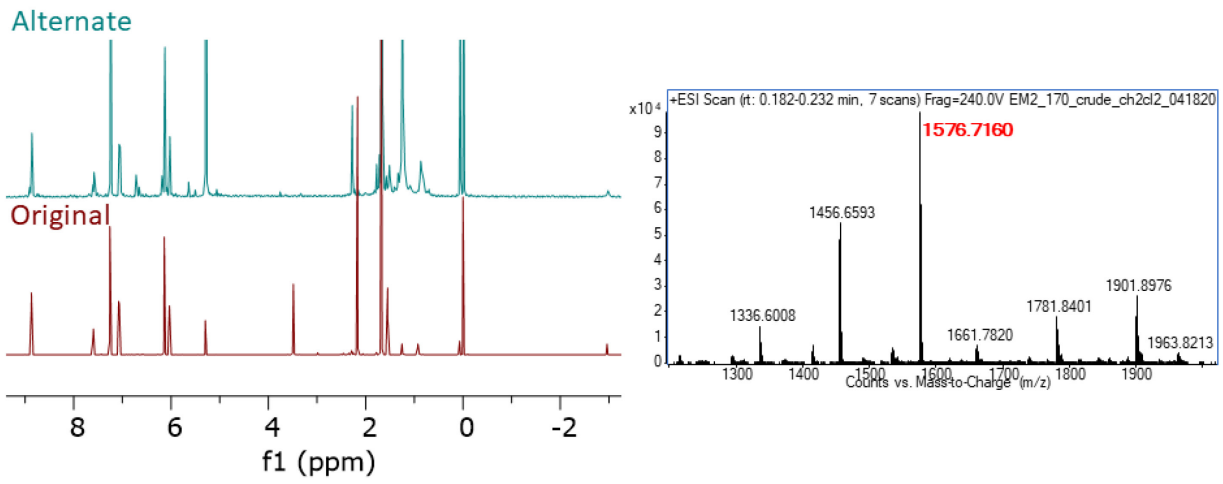

Figure A.14 Left: ^{1}H NMR spectral comparison of the products obtained from the synthesis of [H_2(3,5-Me-BAFP)] by Route 1 (red) and Route 2 (blue). Right: Mass spec of the reaction mixture after 72 hours.

Synthesis of 2,6-bis(3-methoxyphenoxy)phenylporphyrin ([Zn(3-MeO-BAFP)]). The reaction was repeated with 0.16 mL (1.46 mmol) of 3-methoxyphenol and 214 mg (1.5 mmol) of K_2CO_3 in 15 mL of pyridine. Next, 115.4 mg (0.088 mmol) of [Zn(Br_8TPP)] and copper(I) chloride was added to the reaction mixture and refluxed under nitrogen. The resulting solution was monitored by mass spectrometry until no further changes were observed. After 7 days, the reaction mixture was worked up as previously described and was column purified twice on silica, eluting with dichloromethane. Rigorous purification was required for this procedure since a mixture of incompletely substituted porphyrins was obtained as the crude product. Interestingly, despite acidification, the porphyrin remained metalated with zinc as evident by both mass spectrometry, UV-vis and ^{1}H NMR spectroscopy. Yield: 16.3 mg, 11%. UV-vis (CH_2Cl_2) 433, 564 nm. ^{1}H NMR (CH_2Cl_2) δ = 9.01 (s, 8H); 7.85 (s, 2H); 7.65 (t, 4H); 7.44 (s, 2H); 7.11 (d, 8H); 6.71 (t, 8H); 6.33 (d, 8H); 6.06 (d, 8H); 5.99 (s, 4H); 3.18 (s, 24H).

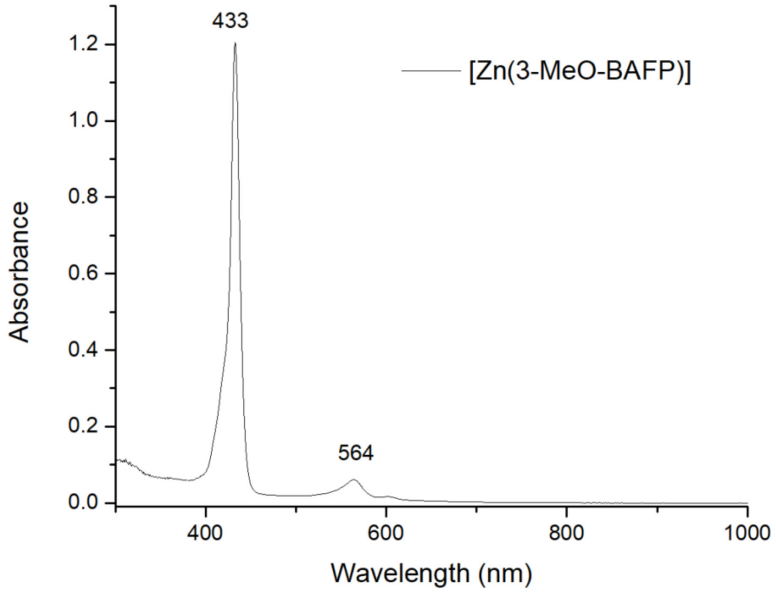

Figure A.15 UV-vis spectrum of [Zn(3-MeO-BAFP)] in CH_2Cl_2.

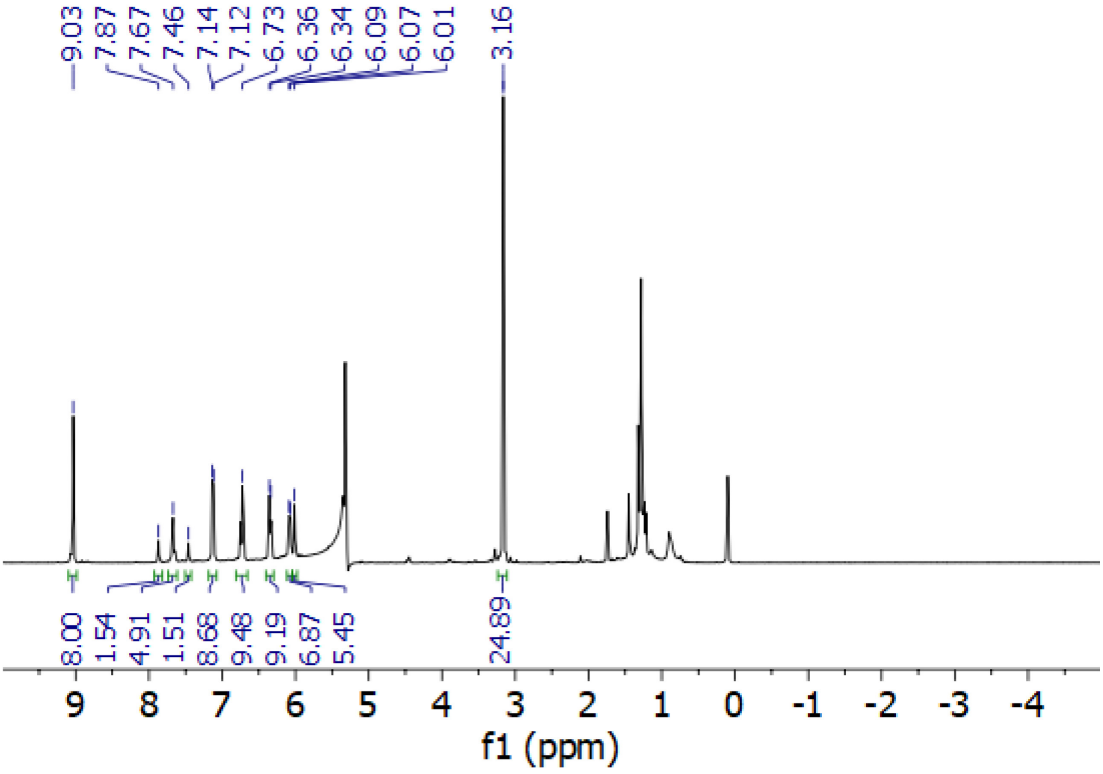

Figure A. 16 ^{1}H NMR spectrum of [Zn(3-MeO-BAFP)] in CH_2Cl_2.

Method B

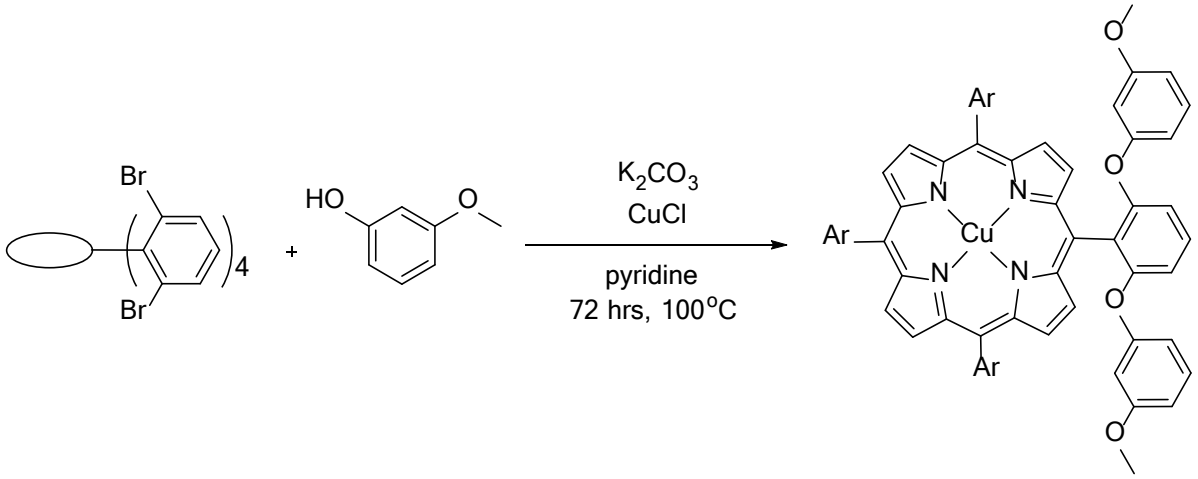

Figure A.17 Synthetic scheme of Route 2, where free base porphyrin, [$H_2(Br_8TPP)$], was used for the Ullman condensation.

Synthesis of 2,6-bis(3-methoxyphenoxy)phenylporphyrin ([Cu(3-MeO-BAFP)]). Method B was performed to compare to the 11% yield obtained by Method A. Here, the reaction was repeated with the unmetalated porphyrin, [$H_2(Br_8TPP)$], in place of the zinc-metalated porphyrin. ^{1}H NMR was not obtained for this procedure because the porphyrin was metalated with copper and the complex was paramagnetic. Yield: 26.6 mg, 36%. UV-vis (CH_2Cl_2) 420, 543 nm. MS: 1653.45 [M+H].

Copper Removal from [Cu(3-MeO-BAFP)]. This synthesis follows a modified synthetic procedure.[153] The reaction was performed at small scale where [Cu(3-MeO-BAFP)] (26 mg, 0.0157 mmol) was added to a 20 mL scintillation vial and cooled to 0 °C. Next, 3 mL of a solution of 2:1 TFA:H_2SO_4 was added, and the reaction mixture changed from a bright pink to a dark blue/green color. At this point, an aliquot of the reaction mixture was removed to obtain a UV-vis spectrum in dichloromethane. Those data indicated that the copper was successfully removed.

Unfortunately, the porphyrin became re-metalated during the work up of this product, which included either neutralizing or diluting the acidic mixture, followed by extraction of the porphyrin with dichloromethane. Based on this result, copper metalation should be avoided by metalating with iron prior to the Ullman condensation.

A.4 Modifications to Form the Second Coordination Sphere Porphyrin Scaffolds

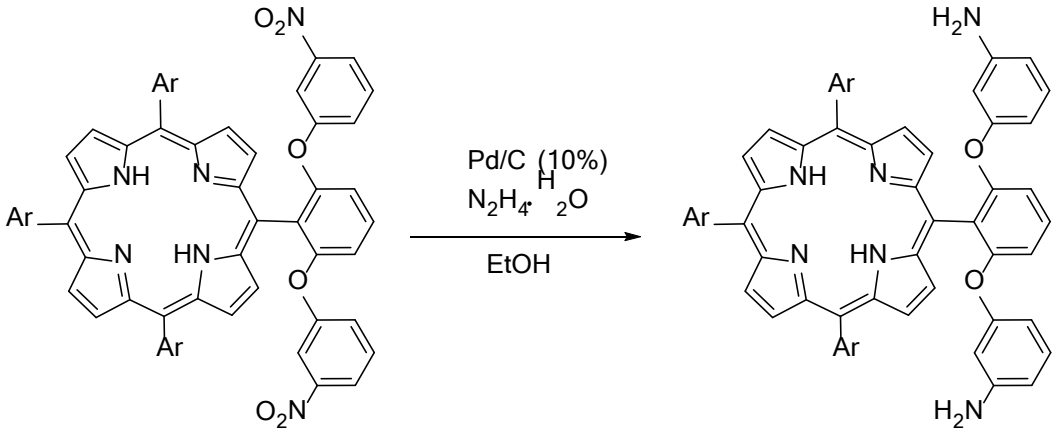

Figure A.18 Synthetic scheme for the reduction of the nitro groups of [H_2(3-NO_2-BAFP)] to amines to yield the desired porphyrin ligand [H_2(3-NH_2-BAFP)].

Synthesis of 2,6-bis(3-aminophenoxy)phenylporphyrin, [H_2(3-NH_2-BAFP)]. This synthesis followed a modified literature procedure.[154] This reaction was performed with crude porphyrin to observe the full reduction of all 8 nitro groups to amines. Here, 63 mg of crude [H_2(3-NO_2-BAFP)] and 63 mg of Pd/C were added to an oven dried Schlenk flask under inert atmosphere. Since the porphyrin could not be purified prior to the reaction, the amount of [H_2(3-NO_2-BAFP)] in the reaction was unfortunately not exactly known. Using Schlenk techniques, materials were dissolved in 7.5 mL of absolute ethanol. While under nitrogen, 0.5 mL of hydrazine monohydrate and 1.5 mL of absolute ethanol were added to an addition funnel and added dropwise to the refluxing solution. The reaction was allowed to reflux overnight. The next day, the solution was filtered over

celite and washed with 100 mL of hot ethanol and dichloromethane. The reaction mixture was checked by mass spectrometry to reveal a large m/z at 1471.55, indicating successful reduction of all 8 amines. Additionally, there were peaks present at 1713.34, 1575, 1558.62, 1534.46, and 1499.80, indicating leftover starting material and partially reduced nitro groups. Unfortunately, further characterization by UV-vis and ^{1}H NMR spectroscopy could not be obtained since the reaction was too crude to properly characterize the product. For this reason, the yield is also unknown.

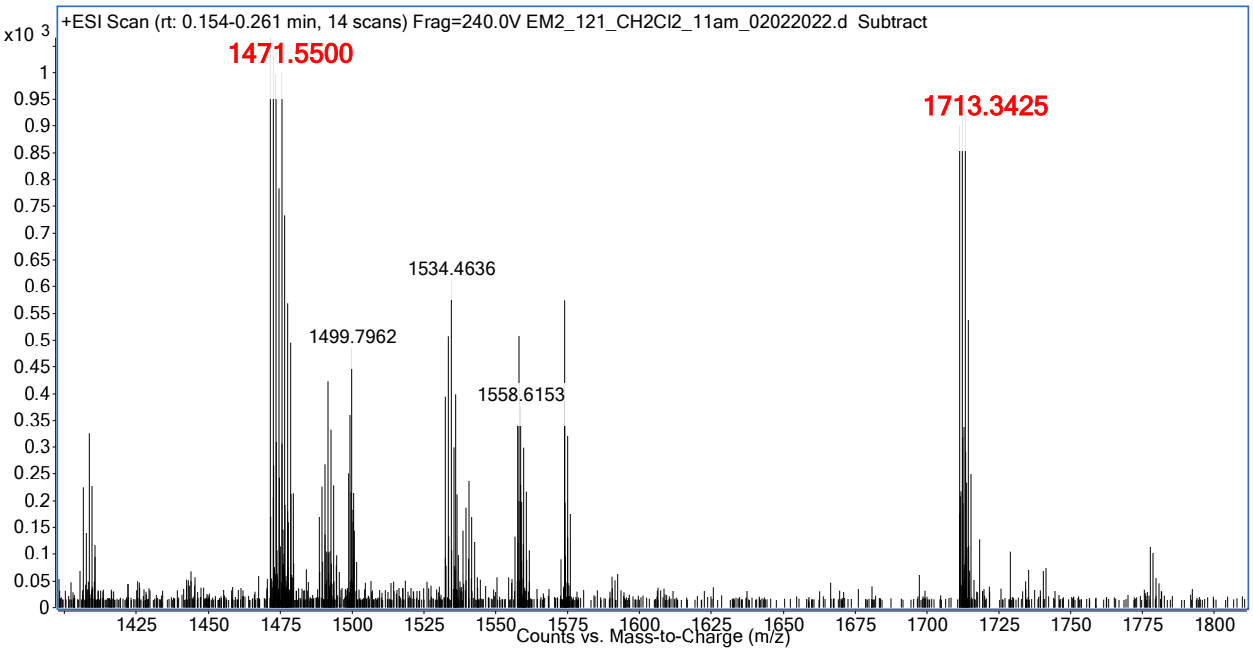

Figure A.19 MS of the reaction mixture en route to [H_2(3-NH_2-BAFP)].

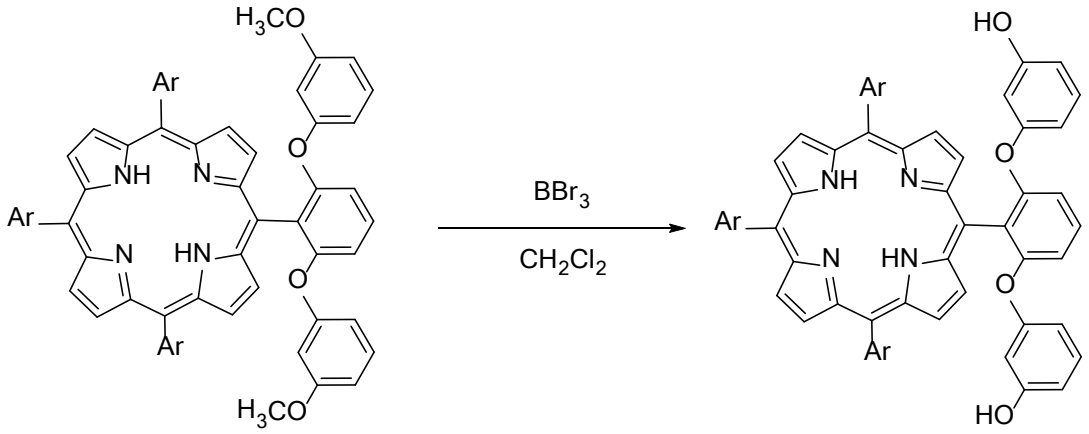

Figure A.20 Synthetic scheme for the hydrolysis of [H_2(3-MeO-BAFP)] to the desired porphyrin ligand [H_2(3-OH-BAFP)].

Synthesis of 2,6-bis(3-hydroxyphenoxy)phenylporphyrin, [H_2(3-OH-BAFP)]. This synthesis followed a modified literature procedure.[155] 20 mg (0.013 mmol) of [H_2(3-OH-BAFP)] was added to a Schlenk flask and dissolved in 1 mL of dichloromethane under inert atmosphere. Next, 0.6 mL of 1 M BBr_3 in dichloromethane was added to the reaction mixture and allowed to stir at room temperature for 8 hours. The reaction mixture was quenched with water followed by the addition of ethyl acetate to extract the product. The organic layer was dried with sodium sulfate and rotary evaporated to dryness. No yield was recorded due to the scale of the reaction; however, the crude product may be purified by chromatography over silica with dichloromethane to elude the starting material [H_2(3-MeO-BAFP)], and with increasing ethyl acetate to elude the product. UV-vis (CH_2Cl_2): 404, 423, 518, 549, 590, 644 nm. ^{1}H NMR (acetone-d_6) δ = 10.43 (br s, 1H); 9.01 (s,

8H); 8.14 (s, 5H); 7.78 (t, 4H); 7.10 (d, 8H); 6.77 (t, 8H); 6.24 (m, 22H); -2.69 (s, 2H). MS: m/z 1480.43 [M+H].

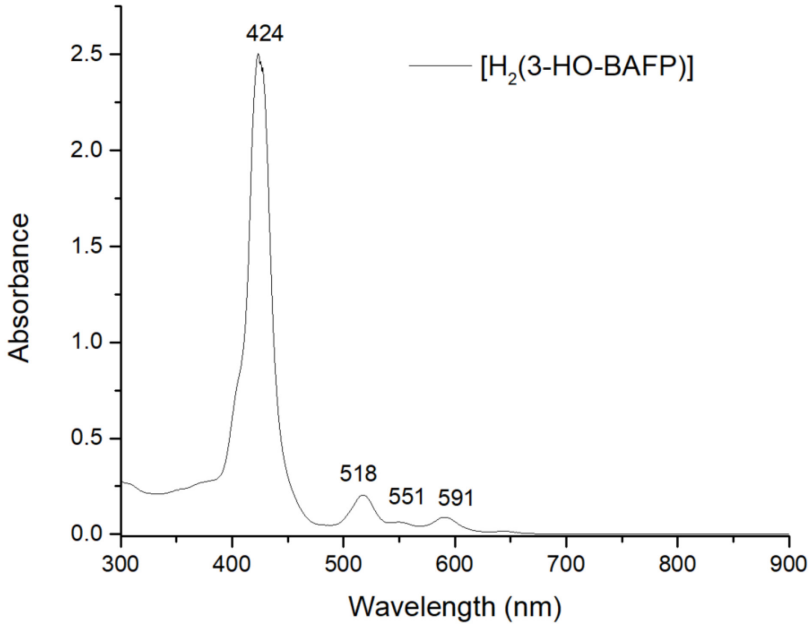

Figure A.21 UV-vis spectrum of [H_2(3-HO-BAFP)] in CH_2Cl_2.

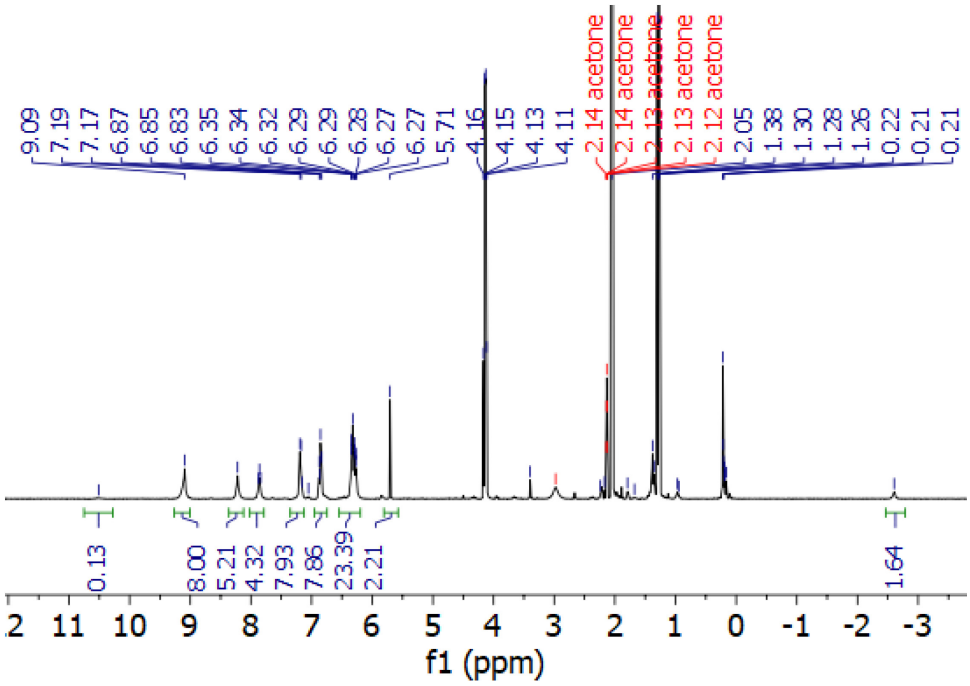

Figure A.22 ^{1}H NMR spectrum of [H_2(3-OH-BAFP)] in acetone-d_6.

As previously stated, the adapted synthetic procedure for the bis-picket fence porphyrin, as shown in Route 1, had unforeseen difficulties with respect to purification and yield. Therefore, Route 2 was pursued where the 2,6-dibrominated version of TPP, [H_2(Br_8TPP)], was synthesized prior to the Ullman condensation to attach the modified bis-picket fence arms. This route ensured that the porphyrin was made in high yield and was easily purified from the crude porphyrin condensation.

Next, two methods were employed in preparation for the subsequent Ullman condensation. In Method A, [H_2(Br_8TPP)] was first metalated with zinc to prevent unwanted copper metalation since the Ullman condensation uses copper to facilitate the reaction. Unfortunately, this step provided its own set of challenges since [H_2(Br_8TPP)] easily loses its metal in the work up conditions, causing the yields to be lower than expected. Successfully metalated [Zn(Br_8TPP)] was taken forward in a control reaction with 3,5-dimethyl phenol to synthesize the well-established 3,5-dimethyl-2,6-bisaryloxyfence porphyrin discussed in **Chapter 2**. Here, a 17% yield was observed where the zinc is easily removed by acidification during the work up. Based on this result, this pathway appeared to be a promising synthetic route. However, when repeated with 3-methoxyphenol, the zinc remained bound to the 3-MeO-$BAFP^{2-}$ despite the acidic work up. Additionally, the 7-day reflux indicated the reaction progression was slow and lead to multiple porphyrins with varying degrees of substitution.

In contrast, Method B carries the reaction forward with the free-base porphyrin, [H_2(Br_8TPP)], and 3-methoxy phenol, which led to differences in reaction progress and yield. Here, the reaction progression appeared cleaner, yielding fewer, less substituted side products and with a higher yield of 36%. In addition, the reaction took less time and was completed within 5 days. As expected, the copper did metalate the product resulting in [Cu(3-MeO-BAFP)] which,

analogous to Method A, did not demetalate post work-up. Based on these two methods, it is proposed that copper metalation generates an active redox catalyst using the porphyrin as a co-ligand that is not accessed when zinc is used. Unfortunately, the methoxy-BAFP seems to have a high affinity for metal ions due to its electron donating substituents, making it difficult to carry out demetallation based on literature procedures.

A.5 Future Directions for the Synthesis Second Coordination Sphere Bis-Picket Fence Porphyrin Scaffolds

Considering the results discussed above, an alternative route can be used to synthesize the second coordination sphere hydrogen bonding bis-picket fence porphyrins. Here, the 5,10,15,20-tetrakis(2,6-dimethoxyphenyl)porphyrin, [H_2(($MeO)_8$TPP)] can be synthesized and metalated according to literature procedure (**Figure A.23**).[155,156] The methoxy arms can then be hydrolyzed to hydroxy groups using BBr_3 to prepare for an Ullman condensation with a substituted bromobenzene derivative (**Figure A.24**). A similar route can be followed to attach the nitro arms to the methoxy porphyrin, as shown in **Figure A.25**. The amine porphyrin can be synthesized by reducing the nitro groups with Pd/C and hydrazine.

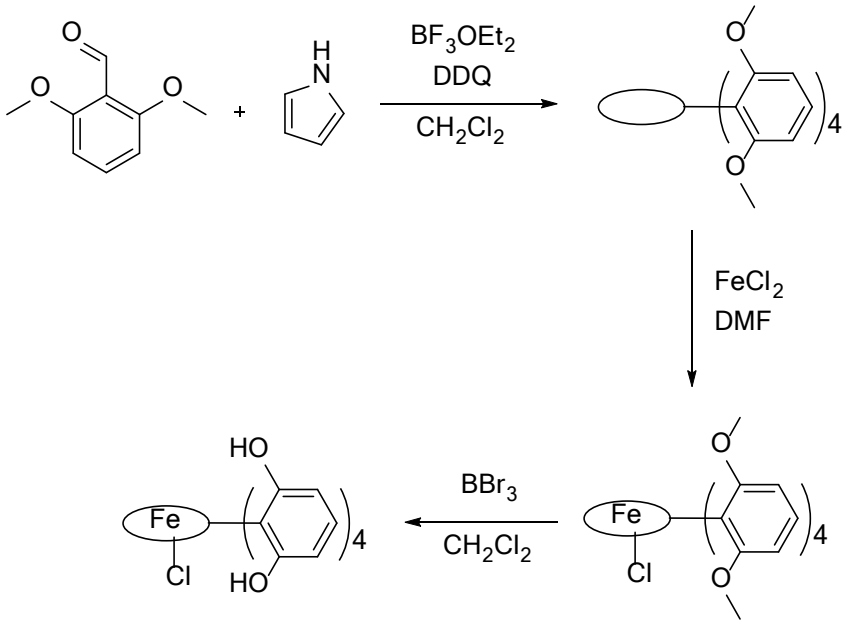

Figure A.23 Overall synthetic scheme of [Fe((OH)$_8$TPP)(Cl)]

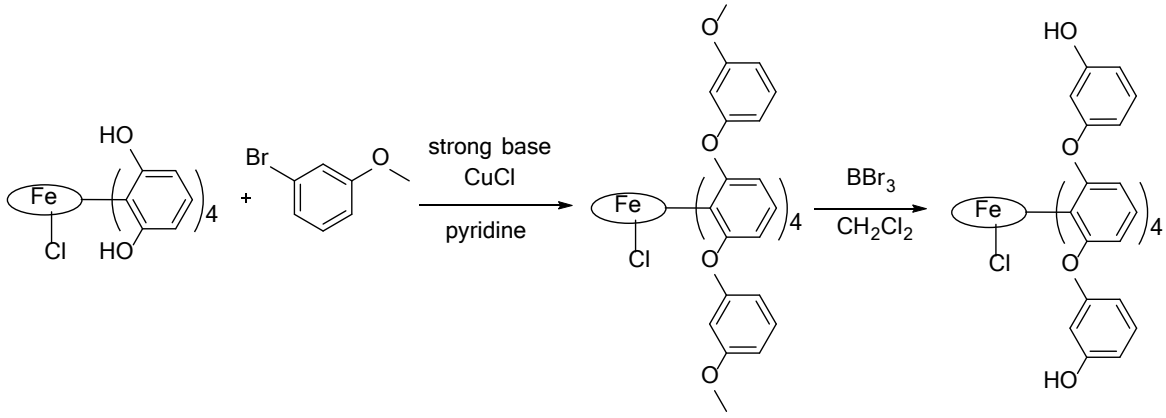

Figure A.24 Proposed synthesis of [Fe(3-OH-BAFP)(Cl)]

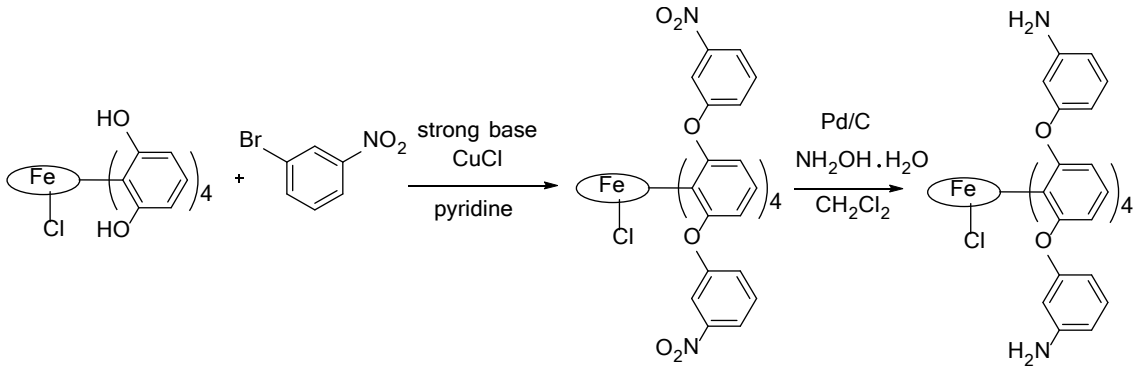

Figure A.25 Proposed synthesis of [Fe(3-NH_2-BAFP)(Cl)]

Bibliography

1. Lehnert, N.; Kim, E.; Dong, H. T.; Harland, J. B.; Hunt, A. P.; Manickas, E. C.; Oakley, K. M.; Pham, J.; Reed, G. C.; Sosa Alfaro, V. The Biologically Relevant Coordination Chemistry of Iron and Nitric Oxide: Electronic Structure and Reactivity. *Chem. Rev.* **2021**, *121*, 14682-14905.
2. Harland, J. B.; Manickas, E. C.; Hunt, A. P.; Lehnert, N. In *Comprehensive Coordination Chemistry III*; Figueroa, J., Ed.; Elsevier: 2021, p 806-874.
3. Manickas, E. C.; LaLonde, A. B.; Hu, M. Y.; Alp, E. E.; Lehnert, N. Stabilization of a Heme-HNO Model Complex Using a Bulky Bis-Picket Fence Porphyrin and Reactivity Studies with NO. *J. Am. Chem. Soc.* **2023**, *145*, 23014-23026.
4. Ignarro, L., ed. *Nitric Oxide: Biology and Pathobiology*; Academic Press: San Diego, 2000.
5. Miranda, K. M. The chemistry of nitroxyl (HNO) and implications in biology. *Coord. Chem. Rev.* **2005**, *249*, 433-455.
6. Basudhar, D.; Bharadwaj, G.; Salmon, A.; Miranda, K.; Doctorovich, F.; Farmer, P. J.; Marti, M. A. *The Chemistry and Biology of Nitroxyl (HNO)*; Elsevier: Amsterdam, Netherlands, 2017.
7. Farmer, P. J.; Sulc, F. Coordination chemistry of the HNO ligand with hemes and synthetic coordination complexes. *J. Inorg. Biochem.* **2005**, *99*, 166-184.
8. Doctorovich, F.; Bikiel, D.; Pellegrino, J.; Suárez, S. A.; Larsen, A.; Martí, M. A. Nitroxyl (azanone) trapping by metalloporphyrins. *Coord. Chem. Rev.* **2011**, *255*, 2764-2784.
9. Paolocci, N.; Jackson, M. I.; Lopez, B. E.; Miranda, K.; Tocchetti, C. G.; Wink, D. A.; Hobbs, A. J.; Fukuto, J. M. The pharmacology of nitroxyl (HNO) and its therapeutic potential: Not just the janus face of NO. *Pharmacol. Ther.* **2007**, *113*, 442-458.
10. Pufahl, R. A.; Wishnok, J. S.; Marletta, M. A. Hydrogen peroxide-supported oxidation of NG-hydroxy-L-arginine by nitric oxide synthase. *Biochem.* **1995**, *34*, 1930-1941.
11. Álvarez, L.; Suárez, S. A.; González, P. J.; Brondino, C. D.; Doctorovich, F.; Martí, M. A. The Underlying Mechanism of HNO Production by the Myoglobin-Mediated Oxidation of Hydroxylamine. *Inorg. Chem.* **2020**, *59*, 7939-7952.
12. Suarez, S. A.; Neuman, N. I.; Muñoz, M.; Álvarez, L.; Bikiel, D. E.; Brondino, C. D.; Ivanović-Burmazović, I.; Miljkovic, J. L.; Filipovic, M. R.; Martí, M. A.; Doctorovich, F. Nitric Oxide Is Reduced to HNO by Proton-Coupled Nucleophilic Attack by Ascorbate, Tyrosine, and Other Alcohols. A New Route to HNO in Biological Media? *J. Am. Chem. Soc.* **2015**, *137*, 4720–4727.
13. Suarez, S. A.; Muñoz, M.; Alvarez, L.; Venâncio, M. F.; Rocha, W. R.; Bikiel, D. E.; Marti, M. A.; Doctorovich, F. HNO Is Produced by the Reaction of NO with Thiols. *J. Am. Chem. Soc.* **2017**, *139*, 14483-14487.
14. Nakagawa, H. Controlled release of HNO from chemical donors for biological applications *J. Inorg. Biochem.* **2013**, *118*, 187-190.

15. Ma, X. L.; Gao, F.; Liu, G.-L.; Lopez, B. L.; Christopher, T. A.; Fukuto, J. M.; Wink, D. A.; Feelisch, M. Opposite effects of nitric oxide and nitroxyl on postischemic myocardial injury. *Proc. Natl. Acad. Sci. U.S.A.* **1999**, *96*, 14617-14622.
16. Pagliaro, P.; Mancardi, D.; Rastaldo, R.; Penna, C.; Gattullo, D.; Miranda, K. M.; Feelisch, M.; Wink, D. A.; Kass, D. A.; Paolocci, N. Nitroxyl affords thiol-sensitive myocardial protective effects akin to early preconditioning. *Free Radic. Biol. Med.* **2003**, *34*, 33-43.
17. Tocchetti, C. G.; Stanley, B. A.; Murray, C. I.; Sivakumaran, V.; Donzelli, S.; Mancardi, D.; Pagliaro, P.; Gao, W. D.; Van Eyk, J.; Kass, D. A. Playing with cardiac "redox switches": the "HNO way" to modulate cardiac function. *Antioxid. Redox Signal.* **2011**, *14*, 1687-1698.
18. Eberhardt, M.; Dux, M.; Namer, B.; Miljkovic, J.; Cordasic, N.; Will, C.; Kichko, T. I.; De La Roche, J.; Fischer, M.; Suárez, S. A. H_2S and NO cooperatively regulate vascular tone by activating a neuroendocrine HNO–TRPA1–CGRP signalling pathway. *Nat. Commun.* **2014**, *5*, 4381.
19. DeMaster, E. G.; Redfern, B.; Nagasawa, H. T. Mechanisms of inhibition of aldehyde dehydrogenase by nitroxyl, the active metabolite of the alcohol deterrent agent cyanamide. *Biochem. Pharmacol.* **1998**, *55*, 2007-2015.
20. Norris, A. J.; Sartippour, M. R.; Lu, M.; Park, T.; Rao, J. Y.; Jackson, M. I.; Fukuto, J. M.; Brooks, M. N. Nitroxyl inhibits breast tumor growth and angiogenesis. *Int. J. Cancer* **2008**, *122*, 1905-1910.
21. Stoyanovsky, D. A.; Schor, N. F.; Nylander, K. D.; Salama, G. Effects of pH on the cytotoxicity of sodium trioxodinitrate (Angeli's salt). *J. Med. Chem.* **2004**, *47*, 210-217.
22. E Shoman, M.; M Aly, O. Nitroxyl (HNO): a possible strategy for fighting cancer. *Curr. Top. Med. Chem.* **2016**, *16*, 2464-2470.
23. Chai, Z.; Liu, D.; Li, X.; Zhao, Y.; Shi, W.; Li, X.; Ma, H. A tumor-targeted near-infrared fluorescent probe for HNO and its application to the real-time monitoring of HNO release in vivo. *Chem. Commun.* **2021**, *57*, 5063-5066.
24. Arasimowicz-Jelonek, M.; Floryszak-Wieczorek, J.; Suarez, S.; Doctorovich, F.; Sobieszczuk-Nowicka, E.; Bruce King, S.; Milczarek, G.; Rębiś, T.; Gajewska, J.; Jagodzik, P. Discovery of endogenous nitroxyl as a new redox player in Arabidopsis thaliana. *Nat. Plants* **2023**, *9*, 36-44.
25. Lehnert, N.; Musselman, B. W.; Seefeldt, L. C. Grand challenges in the nitrogen cycle. *Chem Soc Rev* **2021**, *50*, 3640-3646.
26. Lehnert, N.; Dong, H. T.; Harland, J. B.; Hunt, A. P.; White, C. J. Reversing Nitrogen Fixation. *Nat. Rev. Chem.* **2018**, *2*, 278-289.
27. Ferousi, C.; Majer, S. H.; DiMucci, I. M.; Lancaster, K. M. Biological and Bioinspired Inorganic N−N Bond-Forming Reactions. *Chem. Rev.* **2020**, *120*, 5252-5307.
28. Einsle, O.; Messerschmidt, A.; Stach, P.; Bourenkov, G. P.; Bartunik, H. D.; Huber, R.; Kroneck, P. M. H. Structure of cytochrome *c* nitrite reductase. *Nature* **1999**, *400*, 476-480.
29. Youngblut, M.; Judd, E. T.; Srajer, V.; Sayyed, B.; Goelzer, T.; Elliott, S. J.; Schmidt, M.; Pacheco, A. A. Laue crystal structure of *Shewanella oneidensis* cytochrome *c* nitrite reductase from a high-yield expression system. *J. Biol. Inorg. Chem.* **2012**, *17*, 647-662.
30. Youngblut, M.; Pauly, D. J.; Stein, N.; Walters, D.; Conrad, J. A.; Moran, G. R.; Bennett, B.; Pacheco, A. A. *Shewanella oneidensis* cytochrome *c* nitrite reductase (cc*NiR) does not disproportionate hydroxylamine to ammonia and nitrite, despite a strongly favorable driving force. *Biochemistry* **2014**, *53*, 2136-2144.

31. Stein, N.; Love, D.; Judd, E. T.; Elliott, S. J.; Bennett, B.; Pacheco, A. A. Correlations between the Electronic Properties of *Shewanella oneidensis* Cytochrome *c* Nitrite Reductase (c*c*NiR) and Its Structure: Effects of Heme Oxidation State and Active Site Ligation. *Biochemistry* **2015**, *54*, 3749-3758.
32. Sosa Alfaro, V.; Campeciño, J.; Tracy, M.; Elliott, S. J.; Hegg, E. L.; Lehnert, N. Elucidating Electron Storage and Distribution within the Pentaheme Scaffold of Cytochrome *c* Nitrite Reductase (NrfA). *Biochemistry* **2021**, *60*, 1853-1867.
33. Besson, S.; Almeida, M. G.; Silveira, C. M. Nitrite reduction in bacteria: A comprehensive view of nitrite reductases. *Coord. Chem. Rev.* **2022**, *464*, 214560.
34. Park, S.-Y.; Shimizu, H.; Adachi, S.; Nagagawa, A.; Tanaka, I.; Nakahara, K.; Shoun, H.; Obayashi, E.; Nakamura, H.; Iizuka, T.; Shiro, Y. Crystal structure of nitric oxide reductase from denitrifying fungus *Fusarium oxysporum*. *Nat. Struct. Biol.* **1997**, *4*, 827-832.
35. Shimizu, H.; Park, S. Y.; Lee, D. S.; Shoun, H.; Shiro, Y. Crystal structures of cytochrome P450nor and its mutants (Ser286 Val, Thr) in the ferric resting state at cryogenic temperature: a comparative analysis with monooxygenase cytochrome P450s. *J. Inorg. Biochem.* **2000**, *81*, 191-205.
36. Shimizu, H.; Park, S.-Y.; Shiro, Y.; Adachi, S.-I. Crystal Structure of Nitric Oxide Reductase (Cytochrome P450nor) at Atomic Resolution. *Acta Crystallogr. D* **2002**, *58*, 81.
37. Kudo, T.; Takaya, N.; Park, S. Y.; Shiro, Y.; Shoun, H. A positively charged cluster formed in the heme-distal pocket of cytochrome P450nor is essential for interaction with NADH. *J. Biol. Chem.* **2001**, *276*, 5020-5026.
38. Obayashi, E.; Shimizu, H.; Park, S. Y.; Shoun, H.; Shiro, Y. Mutation effects of a conserved threonine (Thr243) of cytochrome P450nor on its structure and function. *J. Inorg. Biochem.* **2000**, *82*, 103-111.
39. Nakahara, K.; Tanimoto, T.; Hatano, K.; Usuda, K.; Shoun, H. Cytochrome P-450 55A1 (P-450dNIR) acts as nitric oxide reductase employing NADH as the direct electron donor. *J. Biol. Chem.* **1993**, *268*, 8350-8355.
40. Shiro, Y.; Fujii, M.; Iizuka, T.; Adachi, S.; Tsukamoto, K.; Nakahara, K.; Shoun, H. Spectroscopic and Kinetic Studies on Reaction of Cytochrome P450nor with Nitric Oxide. *J. Biol. Chem.* **1995**, *270*, 1617-1623.
41. Kizawa, H.; Tomura, D.; Oda, M.; Fukamizu, A.; Hoshino, T.; Gotoh, O.; Yasui, T.; Shoun, H. Nucleotide sequence of the unique nitrate/nitrite-inducible cytochrome P-450 cDNA from *Fusarium oxysporum*. *J. Biol. Chem.* **1991**, *266*, 10632-10637.
42. Sono, M.; Roach, M. P.; Coulter, E. D.; Dawson, J. H. Heme-Containing Oxygenases. *Chem. Rev.* **1996**, *96*, 2841-2887.
43. Yosca, T. H.; Rittle, J.; Krest, C. M.; Onderko, E. L.; Silakov, A.; Calixto, J. C.; Behan, R. K.; Green, M. T. Understanding C-H Bond Activation in Cytochrome P450: The ferryl pKa and the role of thiolate ligation. *Science* **2013**, *342*, 825-829.
44. Okamoto, N.; Imai, Y.; Shoun, H.; Shiro, Y. Site-Directed Mutagenesis of the Conserved Threonine (Thr243) of the Distal Helix of Fungal Cytochrome P450nor. *Biochemistry* **1998**, *37*, 8839-8847.
45. Hunt, A. P.; Lehnert, N. The Thiolate Trans Effect in Heme $\{FeNO\}^6$ Complexes and Beyond: Insight into the Nature of the Push Effect. *Inorg. Chem.* **2019**, *58*, 11317-11332.
46. Hunt, A. P.; Subhra, S.; Dent, M. R.; Milbauer, M. W.; Burstyn, J. N.; Lehnert, N. Model Complexes Elucidate the Role of the Hydrogen-Bonding Network in Cytochrome P450s. *Inorg. Chem.* **2020**, *59*, 8034-8043.

47. Praneeth, V. K. K.; Paulat, F.; Berto, T. C.; DeBeer George, S.; Näther, C.; Sulok, C. D.; Lehnert, N. Electronic Structure of Six-Coordinate Iron(III)-Porphyrin NO Adducts: the Elusive Iron(III)-NO(radical) State and Its Influence on the Properties of these Complexes. *J. Am. Chem. Soc.* **2008**, *130*, 15288-15303.
48. Enemark, J. H.; Feltham, R. D. Principles of Structure, Bonding, and Reactivity for Metal Nitrosyl Complexes. *Coord. Chem. Rev.* **1974**, *13*, 339-406.
49. Riplinger, C.; Bill, E.; Daiber, A.; Ullrich, V.; Shoun, H.; Neese, F. New Insights into the Nature of Observable Reaction Intermediates in Cytochrome P450 NO Reductase by Using a Combination of Spectroscopy and Quantum Mechanics/Molecular Mechanics Calculations. *Chem. Eur. J.* **2014**, *20*, 1602-1614.
50. Lehnert, N.; Praneeth, V. K. K.; Paulat, F. Electronic Structure of Iron(II)-Porphyrin Nitroxyl Complexes: Molecular Mechanism of Fungal Nitric Oxide Reductase (P450nor) *J. Comp. Chem.* **2006**, *27*, 1338-1351.
51. Riplinger, C.; Neese, F. The Reaction Mechanism of Cytochrome P450 NO reductase: A Detailed Quantum Mechanics/Molecular Mechanics Study. *Chem. Phys. Chem.* **2011**, *12*, 3192-3203.
52. McQuarters, A. B.; Wirgau, N. E.; Lehnert, N. Model Complexes of Key Intermediates in Fungal Cytochrome P450 Nitric Oxide Reductase (P450nor). *Curr. Op. Chem. Biol.* **2014**, *19*, 82-89.
53. McQuarters, A. B.; Blaesi, E. J.; Kampf, J.; Alp, E. E.; Zhao, J.; Hu, M.; Krebs, C.; Lehnert, N. Synthetic Model Complex of the Key Intermediate in Cytochrome P450 Nitric Oxide Reductase. *Inorg. Chem.* **2019**, *58*, 1398-1413.
54. Nomura, T.; Kimura, T.; Kanematsu, Y.; Yamada, D.; Yamashita, K.; Hirata, K.; Ueno, G.; Murakami, H.; Hisano, T.; Yamagiwa, R.; Takeda, H.; Gopalasingam, C.; Kousaka, R.; Yanagisawa, S.; Shoji, O.; Kumasaka, T.; Yamamoto, M.; Takano, Y.; Sugimoto, H.; Kubo, M.; Shiro, Y. Short-lived intermediate in N_2O generation by P450 NO reductase captured by time-resolved IR spectroscopy and XFEL crystallography. *Proc. Natl. Acad. Sci.* **2021**, *118*, e2101481118.
55. Ling, R.; Farmer, P. J. The HNO Adduct of Myoglobin: Synthesis and Charcterization. *J. Am. Chem. Soc.* **2000**, *122*, 2393-2394.
56. Sulc, F.; Immoos, C. E.; Pervitsky, D.; Farmer, P. J. Efficient trapping of HNO by deoxymyoglobin. *J. Am. Chem. Soc.* **2004**, *126*, 1096-1101.
57. Yang, L.; Ling, Y.; Zhang, Y. HNO Binding in a Heme Protein: Structures, Spectroscopic Properties, and Stabilities. *J. Am. Chem. Soc.* **2011**, *133*, 13814–13817.
58. Rahman, M. H.; Ryan, M. D. The use of RRDE voltammetry to study acid-base reactions in unbuffered solutions. *Electrochim. Acta* **2018**, *281*, 17-23.
59. Mazzeo, A. M.; Pellegrino, J.; Doctorovich, F. Water-soluble nitroxyl porphyrin complexes Fe^{II}TPPSHNO and $Fe^{II}TPPSNO^-$ obtained from isolated $Fe^{II}TPPSNO^{\bullet}$. *J. Am. Chem. Soc.* **2019**, *141*, 18521-18530.
60. Goodrich, L. E.; Lehnert, N. The *trans* effect of nitroxyl (HNO) in ferrous heme systems: Implications for soluble guanylate cyclase activation by HNO. *J. Inorg. Biochem.* **2013**, *118*, 179-186.
61. Rahman, M. H.; Ryan, M. D. Redox and Spectroscopic Properties of Iron Porphyrin Nitroxyl in the Presence of Weak Acids. *Inorg. Chem.* **2017**, *56*, 3302-3309.
62. Rahman, M. H.; Liu, Y.; Ryan, M. D. Proton Transfer versus Hydrogen Bonding in a Reduced Iron Porphyrin Nitrosyl Complex. *Inorg. Chem.* **2019**, *58*, 13788-13795.

63. Goodrich, L. E.; Saikat, R.; Alp, E. E.; Zhao, J.; Hu, M. Y.; Lehnert, N. Electronic Structure and Biologically Relevant Reactivity of Low-Spin {FeNO}^{8} Porphyrin Model Complexes: New Insight from a Bis-Picket Fence Porphyrin. *Inorg. Chem.* **2013**, *52*, 7766-7780.
64. Abucayon, E. G.; Khade, R. L.; Powell, D. R.; Zhang, Y.; Richter-Addo, G. B. Hydride Attack on a Coordinated Ferric Nitrosyl: Experimental and DFT Evidence for the Formation of a Heme Model–HNO Derivative. *J. Am. Chem. Soc.* **2016**, *138*, 104-107.
65. Yosca, T. H.; Ledray, A. P.; Ngo, J.; Green, M. T. A new look at the role of thiolate ligation in cytochrome P450. *J. Biol. Inorg. Chem.* **2017**, *22*, 209-220.
66. Buxton, G. V.; Greenstock, C. L.; Helman, W. P.; Ross, A. B. Critical review of rate constants for reactions of hydrated electrons, hydrogen atoms and hydroxyl radicals. *J. Phys. Chem. Ref. Data* **1988**, *17*, 513-886.
67. Daiber, A.; Nauser, T.; Takaya, N.; Kudo, T.; Weber, P.; Hultschig, C.; Shoun, H.; Ullrich, V. Isotope effects and intermediates in the reduction of NO by $P450_{nor}$. *J. Inorg. Biochem.* **2002**, *88*, 343-352.
68. O'grady, N. P.; Alexander, M.; Burns, L. A.; Dellinger, E. P.; Garland, J.; Heard, S. O.; Lipsett, P. A.; Masur, H.; Mermel, L. A.; Pearson, M. L. Guidelines for the prevention of intravascular catheter-related infections. *Clinical infectious diseases* **2011**, *52*, e162-e193.
69. Wang, G.-R.; Zhu, Y.; Halushka, P. V.; Lincoln, T. M.; Mendelsohn, M. E. Mechanism of platelet inhibition by nitric oxide: in vivo phosphorylation of thromboxane receptor by cyclic GMP-dependent protein kinase. *Proc Natl Acad Sci USA* **1998**, *95*, 4888-4893.
70. De Groote, M. A.; Fang, F. C. NO inhibitions: antimicrobial properties of nitric oxide. *Clin. Infect. Dis.* **1995**, *21*, S162-S165.
71. Luo, J.-d.; Chen, A. F. Nitric oxide: a newly discovered function on wound healing. *Acta. Pharmacol. Sin.* **2005**, *26*, 259-264.
72. Fang, F. C. Mechanisms of Nitric Oxide-Related Antimicrobial Activity. *J. Clin. Invest.* **1997**, *99*, 2818-2825.
73. Mellion, B. T.; Ignarro, L. J.; Ohlstein, E. H.; Pontecorvo, E. G.; Hyman, A. L.; Kadowitz, P. J. Evidence for the inhibitory role of guanosine 3′, 5′-monophosphate in ADP-induced human platelet aggregation in the presence of nitric oxide and related vasodilators. *Blood* **1981**, *57*, 946-955.
74. Frost, M. C.; Rudich, S. M.; Zhang, H.; Maraschio, M. A.; Meyerhoff, M. E. In vivo biocompatibility and analytical performance of intravascular amperometric oxygen sensors prepared with improved nitric oxide-releasing silicone rubber coating. *Anal. Chem.* **2002**, *74*, 5942-5947.
75. Major, T. C.; Brant, D. O.; Reynolds, M. M.; Bartlett, R. H.; Meyerhoff, M. E.; Handa, H.; Annich, G. M. The attenuation of platelet and monocyte activation in a rabbit model of extracorporeal circulation by a nitric oxide releasing polymer. *Biomaterials* **2010**, *31*, 2736-2745.
76. Ren, H.; Wu, J.; Xi, C.; Lehnert, N.; Major, T.; Bartlett, R. H.; Meyerhoff, M. E. Electrochemically Modulated Nitric Oxide (NO) Releasing Biomedical Devices via Cu(II)-Tri(2-pyridylmethyl)amine Mediated Reduction of Nitrite. *ACS Appl. Mater. Interfaces* **2014**, *6*, 3779-3783.
77. Merkle, A. C.; Lehnert, N. Binding and Activation of Nitrite and Nitric Oxide by Copper Nitrite Reductase and Corresponding Model Complexes. *Dalton Trans.* **2012**, *41*, 3355-3368.
78. Jacobson, F.; Guo, H.; Olesen, K.; Ökvist, M.; Neutze, R.; Sjölin, L. Structures of the oxidized and reduced forms of nitrite reductase from Rhodobacter sphaeroides 2.4. 3 at high pH:

changes in the interactions of the type 2 copper. *Acta Crystallogr. D Biol. Crystallogr.* **2005**, *61*, 1190-1198.
79. Suzuki, S.; Kataoka, K.; Yamaguchi, K. Metal coordination and mechanism of multicopper nitrite reductase. *Acc. Chem. Res.* **2000**, *33*, 728-735.
80. Li, Y.; Hodak, M.; Bernholc, J. Enzymatic mechanism of copper-containing nitrite reductase. *Biochem.* **2015**, *54*, 1233-1242.
81. Konopińska, K. K.; Schmidt, N. J.; Hunt, A. P.; Lehnert, N.; Wu, J.; Xi, C.; Meyerhoff, M. E. Comparison of Copper(II)-Ligand Complexes as Mediators for Preparing Electrochemically Modulated Nitric Oxide-Releasing Catheters. *ACS Appl. Mater. Interfaces* **2018**, *10*, 25047-25055.
82. Hunt, A. P.; Batka, A. E.; Hosseinzadeh, M.; Gregory, J. D.; Haque, H. K.; Ren, H.; Meyerhoff, M. E.; Lehnert, N. Nitric oxide generation on demand for biomedical applications via electrocatalytic nitrite reduction by copper BMPA-and BEPA-carboxylate complexes. *ACS Catal.* **2019**, *9*, 7746-7758.
83. Woollard-Shore, J. G.; Holland, J. P.; Jones, M. W.; Dilworth, J. R. Nitrite reduction by copper complexes. *Dalton Trans.* **2010**, *39*, 1576-1585.
84. White, C. J.; Lehnert, N.; Meyerhoff, M. E. Electrochemical generation of nitric oxide for medical applications. *Electrochem. Sci. Adv.* **2022**, *2*, e2100156.
85. Mondal, A.; Reddy, K. P.; Som, S.; Chopra, D.; Kundu, S. Nitrate and nitrite reductions at copper (II) sites: Role of noncovalent interactions from second-coordination-sphere. *Inorg. Chem.* **2022**, *61*, 20337-20345.
86. Ferreira, M. P.; Castro, C. B.; Honorato, J.; He, S.; Júnior, W. G. G.; Esmieu, C.; Castellano, E. E.; de Moura, A. F.; Truzzi, D. R.; Nascimento, O. R. Biomimetic catalysis of nitrite reductase enzyme using copper complexes in chemical and electrochemical reduction of nitrite. *Dalton Trans.* **2023**, *52*, 11254-11264.
87. Cioncoloni, G.; Roger, I.; Wheatley, P. S.; Wilson, C.; Morris, R. E.; Sproules, S.; Symes, M. D. Proton-coupled electron transfer enhances the electrocatalytic reduction of nitrite to NO in a bioinspired copper complex. *ACS Catal.* **2018**, *8*, 5070-5084.
88. Mondal, A.; Reddy, K. P.; Bertke, J. A.; Kundu, S. Phenol Reduces Nitrite to NO at Copper(II): Role of a Proton-Responsive Outer Coordination Sphere in Phenol Oxidation. *J. Am. Chem. Soc.* **2020**, *142*, 1726-1730.
89. Abucayon, E. G.; Khade, R. L.; Powell, D. R.; Shaw, M. J.; Zhang, Y.; Richter-Addo, G. B. Over or Under: Hydride Attack at the Metal Versus the Coordinated Nitrosyl Ligand in Ferric Nitrosyl Porphyrins *Dalton Trans.* **2016**, *45*, 18259-18266.
90. McQuarters, A. B.; Kampf, J.; Alp, E. E.; Hu, M. Y.; Zhao, J.; Lehnert, N. Ferric Heme-Nitrosyl Complexes: Kinetically Robust or Unstable Intermediates? *Inorg. Chem.* **2017**, *56*, 10513-10528.
91. Kumar, M. R.; Pervitsky, D.; Chen, L.; Poulos, T.; Kundu, S.; Hargrove, M. S.; Rivera, E. J.; Diaz, A.; Colon, J. L.; Farmer, P. J. Nitrosyl Hydride (HNO) as an O_2 Analogue: Long-Lived HNO Adducts of Ferrous Globins. *Biochemistry* **2009**, *48*, 5018-5025.
92. Immoos, C. E.; Sulc, F.; Farmer, P. J.; Czarnecki, K.; Bocian, D. F.; Levina, A.; Aitken, J. B.; Armstrong, R. S.; Lay, P. A. Bonding in HNO-Myoglobin as Characterized by X-ray Absorption and Resonance Raman Spectroscopies. *J. Am. Chem. Soc.* **2005**, *127*, 814-815.
93. Abucayon, E. G.; Powell, D. R.; Richter-Addo, G. B. Carbon–Nitrogen and Nitrogen–Nitrogen Bond Formation from Nucleophilic Attack at Coordinated Nitrosyls in Fe and Ru Heme Models. *J. Am. Chem. Soc.* **2017**, *139*, 9495-9498.

94. Hoshino, M.; Maeda, M.; Konishi, R.; Seki, H.; Ford, P. C. Studies on the reaction mechanisms for reductive nitrosylation of ferrihemoproteins in buffer solutions. *J. Am. Chem. Soc.* **1996**, *118*, 5702-5707.
95. Fernandez, B. O.; Lorkovic, I. M.; Ford, P. C. Mechanisms of Ferriheme Reduction by Nitric Oxide: Nitrite and General Base Catalysis. *Inorg. Chem.* **2004**, *43*, 5393-5402.
96. Ford, P. C.; Lorkovic, I. M. Mechanistic Aspects of the Reactions of Nitric Oxide with Transition-Metal Complexes. *Chem. Rev.* **2002**, *102*, 993-1017.
97. Lehnert, N.; Scheidt, W. R. Inorganic Chemistry FORUM: The Coordination Chemistry of Nitric Oxide and its Significance for Metabolism, Signaling and Toxicity in Biology. *Inorg. Chem.* **2010**, *49*, 6223-6774.
98. Van Stappen, C.; Goodrich, L. E.; Lehnert, N. In *The Interaction of HNO With Transition Metal Centers and Its Biological Significance. Insight Into Electronic Structure From Theoretical Calculations*; Doctorovich, F., Farmer, P. J., Marti, M. A., Eds.; Elsevier: Amsterdam, Netherlands, 2017, p 155-192.
99. Adler, A. D.; Longo, F. R.; Kampas, F.; Kim, J. On the preparation of metalloporphyrins. *J. Inorg. Nucl. Chem.* **1970**, *32*, 2443-2445.
100. White, C. J.; Lengel, M. O.; Bracken, A. J.; Kampf, J. W.; Speelman, A. L.; Alp, E. E.; Hu, M. Y.; Zhao, J.; Lehnert, N. Distortion of the $[FeNO]_2$ Core in Flavodiiron Nitric Oxide Reductase Models Inhibits N–N Bond Formation and Promotes Formation of Unusual Dinitrosyl Iron Complexes: Implications for Catalysis and Reactivity. *J. Am. Chem. Soc.* **2022**, *144*, 3804-3820.
101. Berto, T. C.; Hoffman, M. B.; Murata, Y.; Landenberger, K. B.; Alp, E. E.; Zhao, J.; Lehnert, N. Structural and Electronic Characterization of Non-Heme Fe(II)-Nitrosyls as Biomimetic Models of the Fe_B Center of Bacterial Nitric Oxide Reductase (NorBC). *J. Am. Chem. Soc.* **2011**, *133*, 16714–16717.
102. Lehnert, N.; Galinato, M. G. I.; Paulat, F.; Richter-Addo, G. B.; Sturhahn, W.; Xu, N.; Zhao, J. Nuclear Resonance Vibrational Spectroscopy applied to [Fe(OEP)(NO)]: the Vibrational Assignments of Five-Coordinate Ferrous Heme Nitrosyls and Implications for Electronic Structure. *Inorg. Chem.* **2010**, *49*, 4133-4148.
103. Expert, C.; Japan.
104. Sheldrick, G. M. SHELXT–Integrated space-group and crystal-structure determination. *Acta Cryst. A* **2015**, *71*, 3-8.
105. Sheldrick, G. M. Crystal structure refinement with SHELXL. *Acta Crystallogr. C Struct. Chem.* **2015**, *71*, 3-8.
106. Spek, A. L. PLATON SQUEEZE: a tool for the calculation of the disordered solvent contribution to the calculated structure factors. *Acta Cryst. C.* **2015**, *71*, 9-18.
107. Frisch, M. J.; Trucks, G. W.; Schlegel, H. B.; Scuseria, G. E.; Robb, M. A.; Cheeseman, J. R.; Scalmani, G.; Barone, V.; Mennucci, B.; Petersson, G. A.; Nakatsuji, H.; Caricato, M.; Li, X.; Hratchian, H. P.; Izmaylov, A. F.; Bloino, J.; Zheng, G.; Sonnenberg, J. L.; Hada, M.; Ehara, M.; Toyota, K.; Fukuda, R.; Hasegawa, J.; Ishida, M.; Nakajima, T.; Honda, Y.; Kitao, O.; Nakai, H.; Vreven, T.; Montgomery, J. A., Jr.; Peralta, J. E.; Ogliaro, F.; Bearpark, M.; Heyd, J. J.; Brothers, E.; Kudin, K. N.; Staroverov, V. N.; Kobayashi, R.; Normand, J.; Raghavachari, K.; Rendell, A.; Burant, J. C.; Iyengar, S. S.; Tomasi, J.; Cossi, M.; Rega, N.; Millam, J. M.; Klene, M.; Knox, J. E.; Cross, J. B.; Bakken, V.; Adamo, C.; Jaramillo, J.; Gomperts, R.; Stratmann, R. E.; Yazyev, O.; Austin, A. J.; Cammi, R.; Pomelli, C.; Ochterski, J. W.; Martin, R. L.; Morokuma, K.; Zakrzewski, V. G.; Voth, G. A.; Salvador, P.; Dannenberg, J. J.; Dapprich, S.;

Daniels, A. D.; Farkas, O.; Foresman, J. B.; Ortiz, J. V.; Cioslowski, J.; Fox, D. J.; Gaussian, Inc.: Wallingford, CT, 2009.
108. Weichsel, A.; Maes, E. M.; Andersen, J. F.; Valenzuela, J. G.; Shokhireva, T. K.; Walker, F. A.; Montfort, W. R. Heme-assisted S-nitrosation of a proximal thiolate in a nitric oxide transport protein. *Proc. Natl. Acad. Sci. U.S.A.* **2005**, *102*, 594–599.
109. Franke, A.; Stochel, G.; Suzuki, N.; Higuchi, T.; Okuzono, K.; van Eldik, R. Mechanistic Studies on the Binding of Nitric Oxide to a Synthetic Heme-Thiolate Complex Relevant to Cytochrome P450 *J. Am. Chem. Soc.* **2005**, *127*, 5360-5375.
110. Hunt, A. Synthesis and Spectroscopic Characterization of Ferric Heme-Thiolate Complexes and Their Reactivity with NO as Models for Cytochrome P450 Nitric Oxide Reductase, University of Michigan, 2019.
111. Ellison, M. K.; Scheidt, W. R. Synthesis, Molecular Structures, and Properties of Six-Coordinate $[Fe(OEP)(L)(NO)]^+$ Derivatives: Elusive Nitrosyl Ferric Porphyrins. *J. Am. Chem. Soc.* **1999**, *121*, 5210-5219.
112. Ellison, M. K.; Schulz, C. E.; Scheidt, W. R. Syntheses, Characterization, and Structural Studies of Several (Nitro)(nitrosyl)iron(III) Porphyrinates: $[Fe(Porph)(NO_2)(NO)]$. *Inorg. Chem.* **1999**, *38*, 100-108.
113. Ellison, M. K.; Schulz, C. E.; Scheidt, W. R. Structural and Electronic Characterization of Nitrosyl(Octaethylporphinato)iron(III) Perchlorate Derivatives. *Inorg. Chem.* **2000**, *39*, 5102-5110.
114. Spiro, T. G.; Wasbotten, I. H. CO as a vibrational probe of heme protein active sites. *J. Inorg. Biochem.* **2005**, *99*, 34-44.
115. Hunt, A. P.; Lehnert, N. Heme-Nitrosyls: Electronic Structure Implications for Function in Biology. *Acc. Chem. Res.* **2015**, *48*, 2117−2125.
116. Dawson, J. H.; Holm, R. H.; Trudell, J. R.; Barth, G.; Linder, R. E.; Bunnenberg, E.; Djerassi, C.; Tang, S. C. Oxidized cytochrome P-450. Magnetic circular dichroism evidence for thiolate ligation in the substrate-bound form. Implications for the catalytic mechanism. *J. Am. Chem. Soc.* **1976**, *98*, 3707-3709.
117. McQuarters, A. B.; Wolf, M. W.; Hunt, A. P.; Lehnert, N. 1958-2014: After 56 Years of Research, Cytochrome P450 Reactivity Finally Explained. *Angew. Chem. Int. Ed.* **2014**, *53*, 4750-4752.
118. Das, P. D.; Samanta, S.; McQuarters, A. B.; Lehnert, N.; Dey, A. Valence Tautomerism in Synthetic Models of Cytochrome P450. *Proc. Natl. Acad. Sci. USA* **2016**, *113*, 6611-6616.
119. Dent, M. R.; Milbauer, M. W.; Hunt, A. P.; Aristov, M. M.; Guzei, I. A.; Lehnert, N.; Burstyn, J. N. Electron Paramagnetic Resonance Spectroscopy as a Probe of Hydrogen Bonding in Heme-Thiolate Proteins. *Inorg. Chem.* **2019**, *58*, 16011-16027.
120. Galinato, M. G. I.; Spolitak, T.; Ballou, D. P.; Lehnert, N. Elucidating the Role of the Hydrogen Bonding Network in Ferric Cytochrome P450cam and corresponding Mutants using Magnetic Circular Dichroism Spectroscopy. *Biochemistry* **2011**, *50*, 1053-1069.
121. Reisz, J. A.; Zink, C. N.; King, S. B. Rapid and selective nitroxyl (HNO) trapping by phosphines: kinetics and new aqueous ligations for HNO detection and quantitation. *J. Am. Chem. Soc.* **2011**, *133*, 11675-11685.
122. Gallego, C. M.; Mazzeo, A.; Vargas, P.; Suárez, S.; Pellegrino, J.; Doctorovich, F. Azanone (HNO): generation, stabilization and detection. *Chem Sci* **2021**, *12*, 10410-10425.
123. Miao, Z.; King, S. B. Recent advances in the chemical biology of nitroxyl (HNO) detection and generation. *Nitric oxide* **2016**, *57*, 1-14.

124. Zarenkiewicz, J.; Khodade, V. S.; Toscano, J. P. Reaction of nitroxyl (HNO) with hydrogen sulfide and hydropersulfides. *J. Org. Chem.* **2020**, *86*, 868-877.
125. Smulik-Izydorczyk, R.; Dębowska, K.; Rostkowski, M.; Adamus, J.; Michalski, R.; Sikora, A. Kinetics of azanone (HNO) reactions with thiols: Effect of pH. *Cell Biochem. Biophys.* **2021**, *79*, 845-856.
126. Zhang, C.; Biggs, T. D.; Devarie-Baez, N. O.; Shuang, S.; Dong, C.; Xian, M. S-Nitrosothiols: chemistry and reactions. *Chem. Commun.* **2017**, *53*, 11266-11277.
127. Melzer, M. M. J., Georgetown University, 2009.
128. Lü, J.-M.; Wittbrodt, J. M.; Wang, K.; Wen, Z.; Schlegel, H. B.; Wang, P. G.; Cheng, J.-P. NO affinities of S-nitrosothiols: a direct experimental and computational investigation of RS− NO bond dissociation energies. *J. Am. Chem. Soc.* **2001**, *123*, 2903-2904.
129. Bredt, D. S.; Snyder, S. H. Nitric Oxide: A Physiologic Messenger Molecule. *Annu. Rev. Biochem.* **1994**, *63*, 175-195.
130. Radomski, M.; Palmer, R.; Moncada, S. Comparative pharmacology of endothelium-derived relaxing factor, nitric oxide and prostacyclin in platelets. *Br. J. Pharmacol.* **1987**, *92*, 181.
131. Gifford, R.; Batchelor, M. M.; Lee, Y.; Gokulrangan, G.; Meyerhoff, M. E.; Wilson, G. S. Mediation ofin vivo glucose sensor inflammatory response via nitric oxide release. *J. Biomed. Mater. Res.* **2005**, *75*, 755-766.
132. Wallis, J. Nitric oxide and blood: a review. *Transfus. Med.* **2005**, *15*, 1-11.
133. Baek, S. H.; Hrabie, J. A.; Keefer, L. K.; Hou, D.; Fineberg, N.; Rhoades, R.; March, K. L. Augmentation of intrapericardial nitric oxide level by a prolonged-release nitric oxide donor reduces luminal narrowing after porcine coronary angioplasty. *Circulation* **2002**, *105*, 2779-2784.
134. Chaux, A.; Ruan, X. M.; Fishbein, M. C.; Ouyang, Y.; Kaul, S.; Pass, J. A.; Matloff, J. M. Perivascular delivery of a nitric oxide donor inhibits neointimal hyperplasia in vein grafts implanted in the arterial circulation. *J. Thorac. Cardiovasc. Surg.* **1998**, *115*, 604-614.
135. Moore, C. M.; Szymczak, N. K. Nitrite reduction by copper through ligand-mediated proton and electron transfer. *Chem. Sci.* **2015**, *6*, 3373-3377.
136. Cardenas, A. J. P.; Ginovska, B.; Kumar, N.; Hou, J.; Raugei, S.; Helm, M. L.; Appel, A. M.; Bullock, R. M.; O'Hagan, M. Controlling proton delivery through catalyst structural dynamics. *Angew. Chem. Int. Ed.* **2016**, *128*, 13707-13711.
137. Wiedner, E. S.; Appel, A. M.; Raugei, S.; Shaw, W. J.; Bullock, R. M. Molecular catalysts with diphosphine ligands containing pendant amines. *Chem. Rev.* **2022**, *122*, 12427-12474.
138. Arnold, P. J.; Davies, S. C.; Durrant, M. C.; Griffiths, D. V.; Hughes, D. L.; Sharpe, P. C. Copper (II) nitrite complexes of tripodal ligands derived from 1, 1, 1-tris (2-pyridyl) methylamine. *Inorg. Chim. Acta* **2003**, *348*, 143-149.
139. Gupta, S.; Arora, S.; Mondal, A.; Stieber, S. C. E.; Gupta, P.; Kundu, S. A Copper (II)-Nitrite Complex Hydrogen-Bonded to a Protonated Amine in the Second-Coordination-Sphere. *Eur. J. Inorg. Chem.* **2022**, *2022*, e202200105.
140. Drover, M. W. A guide to secondary coordination sphere editing. *Chem. Soc. Rev.* **2022**, *51*, 1861-1880.
141. Lv, J.; Chen, X.; Xue, X.-S.; Zhao, B.; Liang, Y.; Wang, M.; Jin, L.; Yuan, Y.; Han, Y.; Zhao, Y. Metal-free directed sp 2-C–H borylation. *Nature* **2019**, *575*, 336-340.

142. Peterson, R. L.; Himes, R. A.; Kotani, H.; Suenobu, T.; Tian, L.; Siegler, M. A.; Solomon, E. I.; Fukuzumi, S.; Karlin, K. D. Cupric superoxo-mediated intermolecular C− H activation chemistry. *J. Am. Chem. Soc.* **2011**, *133*, 1702-1705.
143. Comba, P.; Gahan, L. R.; Mereacre, V.; Hanson, G. R.; Powell, A. K.; Schenk, G.; Zajaczkowski-Fischer, M. Spectroscopic Characterization of the Active $Fe^{III}Fe^{III}$ and $Fe^{III}Fe^{II}$ Forms of a Purple Acid Phosphatase Model System. *Inorg. Chem.* **2012**, *51*, 12195-12209.
144. Mase, T.; Houpis, I. N.; Akao, A.; Dorziotis, I.; Emerson, K.; Hoang, T.; Iida, T.; Itoh, T.; Kamei, K.; Kato, S. Synthesis of a Muscarinic Receptor Antagonist via a Diastereoselective Michael Reaction, Selective Deoxyfluorination and Aromatic Metal− Halogen Exchange Reaction. *J. Org. Chem.* **2001**, *66*, 6775-6786.
145. Sheng, Y.; Abreu, I. A.; Cabelli, D. E.; Maroney, M. J.; Miller, A.-F.; Teixeira, M.; Valentine, J. S. Superoxide dismutases and superoxide reductases. *Chem. Rev.* **2014**, *114*, 3854-3918.
146. Yang, J.; Kloek, A.; Goldberg, D. E.; Mathews, F. S. The structure of Ascaris hemoglobin domain I at 2.2 A resolution: molecular features of oxygen avidity. *Proc. Natl. Acad. Sci.* **1995**, *92*, 4224-4228.
147. Lukin, J. A.; Simplaceanu, V.; Zou, M.; Ho, N. T.; Ho, C. NMR reveals hydrogen bonds between oxygen and distal histidines in oxyhemoglobin. *Proc. Natl. Acad. Sci.* **2000**, *97*, 10354-10358.
148. Arroyo Manez, P.; Lu, C.; Boechi, L.; Martí, M. A.; Shepherd, M.; Wilson, J. L.; Poole, R. K.; Luque, F. J.; Yeh, S.-R.; Estrin, D. A. Role of the distal hydrogen-bonding network in regulating oxygen affinity in the truncated hemoglobin III from Campylobacter jejuni. *Biochem.* **2011**, *50*, 3946-3956.
149. Elwell, C. E.; Gagnon, N. L.; Neisen, B. D.; Dhar, D.; Spaeth, A. D.; Yee, G. M.; Tolman, W. B. Copper–oxygen complexes revisited: structures, spectroscopy, and reactivity. *Chem. Rev.* **2017**, *117*, 2059-2107.
150. Bhadra, M.; Lee, J. Y. C.; Cowley, R. E.; Kim, S.; Siegler, M. A.; Solomon, E. I.; Karlin, K. D. Intramolecular Hydrogen Bonding Enhances Stability and Reactivity of Mononuclear Cupric Superoxide Complexes. *J. Am. Chem. Soc.* **2018**, *140*, 9042-9045.
151. White, C. J.; Schwartz, J. M.; Lehnert, N.; Meyerhoff, M. E. Reducing O2 sensitivity in electrochemical nitric oxide releasing catheters: An O2-tolerant copper (II)-ligand nitrite reduction catalyst and a glucose oxidase catheter coating. *Bioelectrochemistry* **2023**, *152*, 108448.
152. Xu, N.; Richter-Addo, G. B. Interactions of nitrosoalkanes/arenes, nitrosamines, nitrosothiols, and alkyl nitrites with metals. *Progress in Inorganic Chemistry: Volume 59* **2014**, 381-446.
153. Lahaye, D.; Muthukumaran, K.; Hung, C.-H.; Gryko, D.; Rebouças, J. S.; Spasojević, I.; Batinić-Haberle, I.; Lindsey, J. S. Design and synthesis of manganese porphyrins with tailored lipophilicity: investigation of redox properties and superoxide dismutase activity. *Bioorg. Med. Chem.* **2007**, *15*, 7066-7086.
154. Kavanagh, P.; Leech, D. Improved synthesis of 4, 4′-diamino-2, 2′-bipyridine from 4, 4′-dinitro-2, 2′-bipyridine-N, N′-dioxide. *Tetrahedron lett.* **2004**, *45*, 121-123.
155. Huang, L.; Chen, Y.; Gao, G.-Y.; Zhang, X. P. Diastereoselective and Enantioselective Cyclopropanation of Alkenes Catalyzed by Cobalt Porphyrins. *J. Org. Chem.* **2003**, *68*, 8179-8184.

156. Singh, R. Microwave-Assisted Synthesis of Metalloporphyrins. *Asian J. Chem.* **2005**, *17*, 612.